

T 81400
CR-72450

N69-18881
NASA CR-72450

CASE FILE COPY

ANALYTICAL STUDY PROGRAM TO DEVELOP THE THEORETICAL DESIGN OF TRAVELING-WAVE TUBES

by

Dr. O. G. Sauseng , A. Basiulis , Dr. I. Tammaru

prepared for

NATIONAL AERONAUTICS AND SPACE ADMINISTRATION

CONTRACT NAS 3-9719

HUGHES

HUGHES AIRCRAFT COMPANY

ELECTRON DYNAMICS DIVISION
P.O. BOX 2999 TORRANCE, CALIF. 90509

NOTICE

This report was prepared as an account of Government sponsored work. Neither the United States, nor the National Aeronautics and Space Administration (NASA), nor any person acting on behalf of NASA:

- A.) Makes any warranty or representation, expressed or implied, with respect to the accuracy, completeness, or usefulness of the information contained in this report, or that the use of any information, apparatus, method, or process disclosed in this report may not infringe privately owned rights; or
- B.) Assumes any liabilities with respect to the use of, or for damages resulting from the use of any information, apparatus, method or process disclosed in this report.

As used above, "person acting on behalf of NASA" includes any employee or contractor of NASA, or employee of such contractor, to the extent that such employee or contractor of NASA, or employee of such contractor prepares, disseminates, or provides access to, any information pursuant to his employment or contract with NASA, or his employment with such contractor.

Requests for copies of this report should be referred to

National Aeronautics and Space Administration
Office of Scientific and Technical Information
Attention: AFSS-A
Washington, D.C. 20546

CR NO. 72450
HAC EDD W-2646

FINAL REPORT

ANALYTICAL STUDY PROGRAM TO DEVELOP THE
THEORETICAL DESIGN OF TRAVELING-WAVE TUBES

BY

O. G. Sauseng, A. Basiulis, I. Tammaru

prepared for

NATIONAL AERONAUTICS AND SPACE ADMINISTRATION

October 31, 1968

CONTRACT NAS 3-9719

Technical Management
NASA Lewis Research Center
Cleveland, Ohio
SPECIAL PROJECTS OFFICE
Gerald J. Chomos

HUGHES AIRCRAFT COMPANY
ELECTRON DYNAMICS DIVISION
3100 WEST LOMITA BOULEVARD
TORRANCE, CALIFORNIA

ABSTRACT

This report describes an analytical design study for a high efficiency traveling-wave tube amplifier for use in a satellite television transmitter. Several amplifier versions were evaluated with the following frequency, power and modulation specifications:

FREQUENCY	OUTPUT POWER	MODULATION
850 MHz	7.5 kW peak	AM
2 GHz	5 kW peak	AM
2 GHz	5 kW CW	FM
8 GHz	5 kW CW	FM
11 GHz	5 kW CW	FM

The design is based on the coupled cavity structure, which is dielectrically loaded and PPM focused for the 850 MHz and 2 GHz versions to reduce size and weight. The higher frequency versions are solenoid focused. A major emphasis of the studies is placed on achieving very high efficiency. The tube designs include therefore velocity resynchronization using the multiple voltage jump method as well as multistage collector depression, with predicted efficiencies in the range of 70 to 80%.

The design of the tubes with amplitude modulation employs the novel grid modulator technique, which permits linear response over a large dynamic range with very high efficiency.

The cooling system constitutes an integral part of the spacecraft using a combination of dielectric and one way heat pipes.

TABLE OF CONTENTS

<u>Section</u>	<u>Page No.</u>
I. Summary	2
II. Introduction	4
III. State of the Art of Traveling-Wave Tubes	6
A. High Efficiency Achievements	6
B. High Average Power Tubes	24
C. Life Performance of Traveling-Wave Tubes	38
D. Recent Advancements in Heat Pipe Cooling For Microwave Tubes	44
IV. Design Approach and Trade-Off Considerations	58
A. Summary of Major Specifications	58
B. Choice of the Slow-Wave Structure	62
C. High Efficiency Design with Velocity Resynchronization	66
D. Multi Stage Collector Depression	72
E. Gun and Focusing	91
F. High Efficiency AM Signal Amplifier with Traveling-Wave Tube Modulator	99
G. Removal of Heat	115
V. Electronic Design	121
A. Basic Circuit Interaction Considerations	121
B. Circuit Configurations with Multi Voltage Jump Taper	152
C. Efficiency Enhancement with Multi Stage Collector Depression	155
VI. Focusing and Beam Optics	171
A. Focusing	171
B. Gun and Heater	177
C. Launching Conditions for the Gun	179
VII. Collector Design	184
VIII. Thermal Design	191
A. Thermal Circuit Analysis	191
B. Collector Cooling	197
C. Spacecraft Cooling System	200

IX.	Mechanical Design	216
	A. Circuit Construction	216
	B. Gun Construction	221
	C. Special Design Requirements	222
X.	Design Considerations for Long Life	230
	A. Tube Life	230
	B. Life Considerations for Heat Pipe	265
XI.	Power Supply Requirements	269
	A. General	269
	B. Turn-On and Turn-Off Procedures	272
	C. Design Considerations for Electronic Power Conditioner	277
XII.	Traveling-wave Tube Modulator	280
	A. Helix Driver and FM Audio Tubes	280
	B. The Modulation Grid	287
	C. Traveling-Wave Tube Modulator Characteristics	294
XIII.	Summary of Tube Design Parameters	299
	A. Design Assumptions	299
	B. Major Design Parameters	301
XIV.	Critical Design Areas	304
XV.	Conclusions	307
	List of References	309
	Appendix: Television Signal Transmission	312

LIST OF ILLUSTRATIONS

<u>Figure No.</u>		<u>Page No.</u>
1.	Velocity profiles of velocity taper and voltage jump circuit.	7
2.	Spent beam energy distribution (computed).	10
3.	Schematic of double stage collector with single bias voltage.	11
4.	Efficiency of combined voltage jump and two-step velocity taper circuit (measured).	14
5.	Efficiency of combined velocity step and tapered voltage jump circuit (measured).	16
6.	Efficiency of combined velocity step and untapered voltage jump circuit (measured).	17
7.	Efficiency of two-step velocity taper circuit (measured).	18
8.	Efficiency of X-band coupled cavity tube for increased bandwidth with voltage jump (measured).	19
9.	Schematic of helix tube with voltage jump.	22
10.	Efficiency of S-band space type helix tube with voltage jump (measured).	23
11.	High gain 10 kW CW X-band traveling-wave amplifier without solenoid.	27
12.	10 kW CW X-band traveling-wave amplifier packaged in focusing solenoid ready for RF operation.	29
13.	8 kW CW C-band traveling-wave tube without solenoid.	30
14.	8 kW CW C-band traveling-wave tube with solenoid.	30
15.	614H power output vs. frequency for various beam voltages.	31
16.	Finished view of experimental tube 817H, without focusing solenoid.	33
17.	817H beam transmission and efficiency vs. collector depression at 20 kV beam voltage.	33
18.	Pulsed RF power output vs. frequency of 817H. Parameter is cathode voltage.	34

19.	621H - 75 kW PPM focused C-band traveling-wave tube.	35
20.	621H gain vs. frequency.	36
21.	621H power output vs. frequency.	36
22.	50 kW X-band pulsed traveling-wave tube 307H.	38
23.	Schematic of dielectric heat pipe for depressed collector operation.	45
24.	Electric insulation in dielectric heat pipes at low pressures.	47
25.	Effect of temperature on breakdown voltage of dielectric heat pipe systems.	48
26.	Breakdown voltage for dielectric gases.	52
27.	Breakdown voltage for dielectric gas mixtures as a function of pressure.	53
28.	Dielectric heat pipe with gas reservoir.	55
29.	Compact dielectric heat pipe with gas reservoir.	55
30.	Assembly parts of compact dielectric heat pipe with gas reservoir.	58
31.	Dielectric and ohmic losses in dielectrically loaded coupled cavity circuit.	65
32.	Estimated weight reduction of coupled cavity tubes by dielectric loading.	65
33.	Velocity and voltage profiles for combined velocity taper and voltage jump circuit.	68
34.	Schematic of multi voltage jump taper tube.	69
35.	Voltage profile for multi voltage jump taper tube.	70
36.	Spent beam energy distribution and collector depression for high efficiency tubes.	75
37.	Schematic of a triple stage collector with radial velocity sorting.	83
38.	Schematic of four stage collector with radial velocity sorting and electric field suppression of secondaries.	84
39.	Magnetic refocusing of spent beam.	86
40.	Magnetic deflection of the spent beam.	88
41.	Schematic of four stage collector with transverse velocity sorting of spent beam and electric suppression of secondaries.	89

42.	Optimum velocity sorting of spent beam.	90
43.	Schematic of PPM focusing structure for coupled cavity circuit.	93
44.	PPM focusing structure with double period for coupled cavity circuit.	94
45.	Equivalent total weight of solenoid.	97
46.	Separation of FM audio signal from AM signal.	100
47.	Frequency separation for amplitude modulated signal.	102
48.	AM amplifier chain with traveling-wave tube modulator.	102
49.	Instantaneous level of amplitude modulation.	104
50.	Power characteristics with traveling-wave tube modulator.	105
51.	Grid characteristics for traveling-wave tube modulator.	107
52.	Modulation signal chain with linearizer.	109
53.	Combined modulation signal amplifier and linearizer.	109
54.	Automatic gain control for traveling-wave tube modulator.	110
55.	Traveling-wave tube modulator with phase compensator.	112
56.	Automatic phase control for traveling-wave tube modulator.	112
57.	Synchronization of carrier and modulation signal branch for AM signals with PM.	113
58.	Multi-frequency amplitude modulation.	114
59.	Emissive power density as a function of temperature for various thermal emissivities.	117
60.	Tube with dielectric heat pipe for circuit cooling and radiating collector.	118
61.	Fundamental and harmonic beam modulation current at saturation (computed).	125
62.	Equivalent circuit for coupled cavity structure.	127
63.	Equivalent T section of coupled cavity circuit.	127
64.	T section ladder network.	127

65.	Phase deviation of coupled cavity circuit.	129
66.	Phase deviation and bandwidth for coupled cavity circuit.	131
67.	Second order phase deviation for coupled cavity circuit.	132
68.	Second order phase deviation and bandwidth for coupled cavity circuit.	134
69.	Schematic of coupled cavity circuit.	135
70.	Dispersion diagram for 2 GHz coupled cavity circuit (measured).	137
71.	Interaction impedance of 2 GHz coupled cavity circuit (measured).	138
72.	Cold interaction impedance of X-band circuit (measured).	139
73.	Phase diagrams for dielectrically loaded coupled cavity circuits (measured).	142
74.	Schematic of coupled cavity circuit.	148
75.	Voltage jump transition in coupled cavity circuit.	149
76.	Schematic of permanent periodic magnet focusing structure with coupled cavity circuit.	150
77.	Linearized gain profile in multi voltage jump taper traveling-wave tube with sever.	154
78.	Spent beam energy distribution with multi voltage jump taper and with velocity taper - voltage jump for 2 GHz tube (computed).	159
79.	Spent beam energy distribution with multi voltage jump taper and with voltage jump for 8 GHz tube (computed).	160
80.	Effect of velocity sorting efficiency in multi stage collector operation (computed for 850 MHz tube).	164
81.	Effect of backstreaming secondaries on multi stage collector operation (computed for 850 MHz tube).	168
82.	Launching conditions for gun.	182
83.	Beam spread of tilted beam in electrostatic deceleration field with space charge correction.	187
84.	Schematic of four stage collector with beam edge trajectories.	188

85.	Schematic of tube with dielectric heat pipe cooling.	193
86.	Thermal analysis of coupled cavity structure.	194
87.	Schematic of collector with dielectric heat pipe cooling.	198
88.	Spacecraft design using dual panel RF joint concept.	201
89.	Spacecraft design with quad panel slip ring concept.	202
90.	Spacecraft in synchronous orbit (quad panel slip ring concept).	204
91.	Schematic of heat pipe cooling system.	205
92.	Temperature variations on radiator panels during orbit (one-way heat pipe system for 5 kW).	208
93.	Temperature variations of heat pipe cooling system during orbit with 1.5 hours turn-off period.	212
94.	Rate of temperature drop of heat pipe cooling system after turn-off.	213
95.	Schematic of distributor heat pipe system assembly.	215
96.	Typical coupled cavity circuit assemblies for periodic permanent magnet focusing X-band tubes.	217
97.	Typical circuit parts for a PPM focused coupled cavity tube.	218
98.	Typical circuit parts of solenoid focused coupled cavity tube.	219
99.	Typical waveguide coupler parts for solenoid focused coupled cavity tube.	219
100.	Typical sever termination components for coupled cavity tubes.	220
101.	Typical shadow grid electron gun assembly.	221
102.	Voltage jump insulator assembly with iron cavity walls.	224
103.	Voltage jump insulator assembly for solenoid focused tube.	226
104.	Output RF window and dc block assembly.	227
105.	Multi-stage collector design.	229
106.	Schematic of traveling-wave tube and gas pumping tubulations.	233
107.	Remote vacuum opening device.	239

108.	Vapor pressure of vacuum tube materials as a function of temperature.	242
109.	Axial potential profile of tube.	244
110.	Cathode temperatures for space charge limited emission.	246
111.	Life predictions for cathodes as a function of the cathode current loading.	248
112.	Barium arrival rate in oxide coated cathode (computed for 235H cathode).	251
113.	Evaporation rate of cathode materials of impregnated tungsten cathode.	262
114.	Average cumulative mass distribution for interplanetary dust particles in vicinity of earth ²⁴ .	267
115.	Penetration of meteoroids into aluminum skin. ²⁵	268
116.	Power supply diagram for multi-voltage jump taper tubes with four-stage collector.	270
117.	Diagram for switching regulator.	276
118.	Electronic power conditioner with self-regulating dc-dc converter.	279
119.	Helix assembly.	281
120.	Helix PPM focusing configuration.	284
121.	Velocity profiles for helix tube with voltage jump and velocity taper.	285
122.	Power supply diagram for helix tube with voltage jump.	286
123.	Typical shadow grid characteristics (Hughes 116 CG gun).	289
124.	Gain characteristics of traveling-wave tube for very small beam current.	290
125.	Grid input admittance.	291
126.	Beam current characteristics of (multi-voltage jump) traveling-wave tube modulator (computed).	295
127.	Gain characteristics of (multi-voltage jump) TWT modulator (computed).	296
128.	DC power drain of (multi-voltage jump) TWT modulator with modulation drive level (computed).	298

LIST OF TABLES

<u>Table No.</u>		<u>Page No.</u>
I.	Summary of circuit combinations.	20
II.	High average power traveling-wave tubes.	27
III.	Long life tubes for space applications.	39
IV.	Total accumulated hours of life testing for space tubes (7/1/68).	40
V.	Continuous life test data on 384H TWT (7/1/68).	40
VI.	Continuous life test data on 314H TWT.	41
VII.	Continuous life test data on 349H TWT (7/1/68).	42
VIII.	Life test data on high power tubes.	43
IX.	Dielectric heat pipe fluids and gases.	50
X.	Life test data with dielectric heat pipes.	54
XI.	Design requirements for traveling-wave tube amplifiers.	59
XII.	Coupled cavity dimensions for cold tests.	136
XIII.	Comparison of dielectrically loaded circuit with equivalent unloaded circuit.	143
XIV.	Dimensions of coupled cavity structures ($\Delta f_c = 60$ MHz).	151
XV.	Small signal parameters for tubes.	156
XVI.	Multi-voltage jump taper configurations.	157
XVII.	Four-stage collector operation for multi voltage jump taper designs.	170
XVIII.	Focusing design parameters.	176
XIX.	Gun and heater design parameters.	180
XX.	Estimated optimum gun launching conditions into magnetic field.	183
XXI.	Four-stage collector design parameters.	190
XXII.	Thermal circuit analysis.	196
XXIII.	Gas conductances of the three sections of the tubes.	235
XXIV.	Calculated volumes of gun and collector cavities.	236

XXV.	Required tubulation gas conductances	237
XXVI.	Maximum permissible tubulation lengths for gun and collector sections.	237
XXVII.	Materials used in vacuum tubes.	241
XXVIII.	Failure causes for oxide coated cathodes and their prevention.	255
XXIX.	Recommended cathodes.	264
XXX.	Power supplies for voltage jump taper tubes with four-stage collector.	271
XXXI.	Voltage regulation requirements.	273
XXXII.	Design parameters for helix driver and FM audio tubes.	288
XXXIII.	Major design parameters for coupled cavity tubes.	302

FOREWORD

This final technical report was prepared by the Hughes Aircraft Company, Electron Dynamics Division, 3100 West Lomita Boulevard, Torrance, California on a contract of the NASA, Lewis Research Center, Cleveland, Ohio, number NAS 3-9719, entitled "Analytical Study Program to Develop the Theoretical Design of Traveling-wave Tubes." It summarizes the results of a six month study effort on this subject. The work was directed by Mr. G. J. Chomos of the NASA, Lewis Research Center.

The studies reported here were performed by the Electron Dynamics Division of Hughes Aircraft Company with Dr. O. G. Sauseng as project manager. Others working on the project included Mr. A. Basiulis, thermal design, Dr. I. Tammaru, electronic design, Mr. A. L. Rousseau, mechanical design, Miss Janet G. Dahlstrom, computer analysis and Mr. R. Lewis, circuit cold tests. Others working on the program included Mr. R. A. Brennan, Mr. B. Langford, Dr. U. J. Pittack, Mr. A. S. Rostad, and Mr. R. K. E. Weebe.

General technical and administrative assistance was provided during the program by Dr. J. T. Mendel, Division Manager of the Electron Dynamics Division, by Mr. K. P. Grabowski, Head Research and Development Laboratories, and by Mr. H. M. Griffin.

This report contains no classified information extracted from other classified documents.

ANALYTICAL STUDY PROGRAM TO DEVELOP THE
THEORETICAL DESIGN OF TRAVELING-WAVE TUBES

by O. G. Sauseng, A. Basiulis, I. Tammaru

Hughes Aircraft Company
Electron Dynamics Division

I. SUMMARY

The theoretical design of high CW power traveling-wave tubes for satellite television transmission is described. These tubes include a 7.5 kW peak power amplifier for amplitude modulation at 850 MHz, a 5 kW peak power amplifier for amplitude modulation at 2 GHz, and 5 kW amplifiers for frequency modulation at 2 GHz, at 8 GHz and at 11 GHz.

The tubes are designed for a life expectancy of more than 5 years and for maximum efficiencies in the range of 70 to 80%. This is achieved with the novel multiple voltage jump method for velocity resynchronization and collector depression in four stages. The four-stage collector uses transverse magnetic velocity sorting and electrostatic suppression of secondaries.

The amplifiers for amplitude modulation employ a new grid modulator technique, which permits linear response over a dynamic range of 20 dB with very high efficiency.

The coupled cavity structure is used as the slow wave structure, which is dielectrically loaded for the 850 MHz and 2 GHz tubes to achieve a substantial reduction of their diameter and weight. These tubes also use a light weight periodic permanent magnet focusing structure, while the 8 GHz and 11 GHz tube are focused with a wrapped-on solenoid.

A multiple heat pipe system, which constitutes an integral part of the spacecraft vehicle, provides cooling for the tubes. The heat pipe system uses dielectric heat pipes and one way heat pipes for low temperature cooling and high reliability.

The report includes a state of the art review of high efficiency achievements for traveling-wave tubes, of high average power traveling-wave tubes, and of life performance data of medium power space type traveling-wave tubes. Also listed are recent heat pipe achievements for microwave tubes.

II. INTRODUCTION

This report describes an analytic design study for a high efficiency traveling-wave tube amplifier for use in a satellite television transmitter. Prime design objectives are long life, maximum overall efficiency and minimum weight.

The estimated time of the launch is post 1975. This time frame permits exploring new concepts, methods, and techniques which promise significant improvements beyond the present state-of-the art.

The scope of these studies was therefore primarily directed to explore and evaluate new ideas rather than to provide hardware designs in meticulous detail. As a result of these studies, several new concepts were incorporated into the tube designs representing advancements in the state of the art.

These new design concepts include:

1. A multiple voltage jump taper for improved efficiency enhancement.
2. A new design concept for multi stage collector depression using transverse magnetic velocity sorting and electrostatic suppression of backstreaming secondaries.
3. A new grid modulation method for linear amplification of amplitude modulated signals with very high efficiency.
4. Dielectric loading of the coupled cavity circuit structure to achieve a substantial reduction of the tube diameter and weight for the lower frequency tubes.

5. A new cooling system using both dielectric and one way heat pipes for superior heat transfer and low temperature tube operation.

Some of these schemes have not yet been demonstrated and an experimental evaluation of their feasibility will therefore be required in order to incorporate them into tube hardware.

In the following a review is given of the state of the art of traveling-wave tubes which establishes a reference for the advanced tube designs described here. The review covers efficiency achievements for traveling-wave tubes, the performance characteristics of a list of typical high average power traveling-wave tubes, and long life performance data on medium power space tubes. Recent heat pipe developments for microwave tube cooling are also described.

This review is based on data obtained at the Electron Dynamics Division of the Hughes Aircraft Company, but these data can be considered typical for the present state of the art of traveling-wave tubes.

III. STATE OF THE ART OF TRAVELING-WAVE TUBES PRIOR TO BEGINNING OF CONTRACT

A. HIGH EFFICIENCY ACHIEVEMENTS¹

Methods for velocity resynchronization of the beam modulation with the circuit phase velocity at large signal levels have been studied and evaluated. With these methods, in particular with the voltage jump technique and with velocity tapering of the slow wave circuit, it has become possible to achieve efficiencies up to 63% on experimental X-band coupled cavity tubes at the 5 to 10 kW power level. Recently these methods were also applied to space type helix tubes at S-band, resulting in 55% efficiency with 30 watt power output. This compares to 30 to 40% efficiency previously possible for conventional traveling-wave tubes.

The design of these methods is rather critical and a large signal computer program was found to be essential in analyzing the rather complex interaction process of a traveling-wave tube. These programs were continuously evaluated and compared with the experimental results and thus they became important design tools for advanced efficiency designs.

The two velocity resynchronization schemes are illustrated with the velocity profiles of Figure 1.

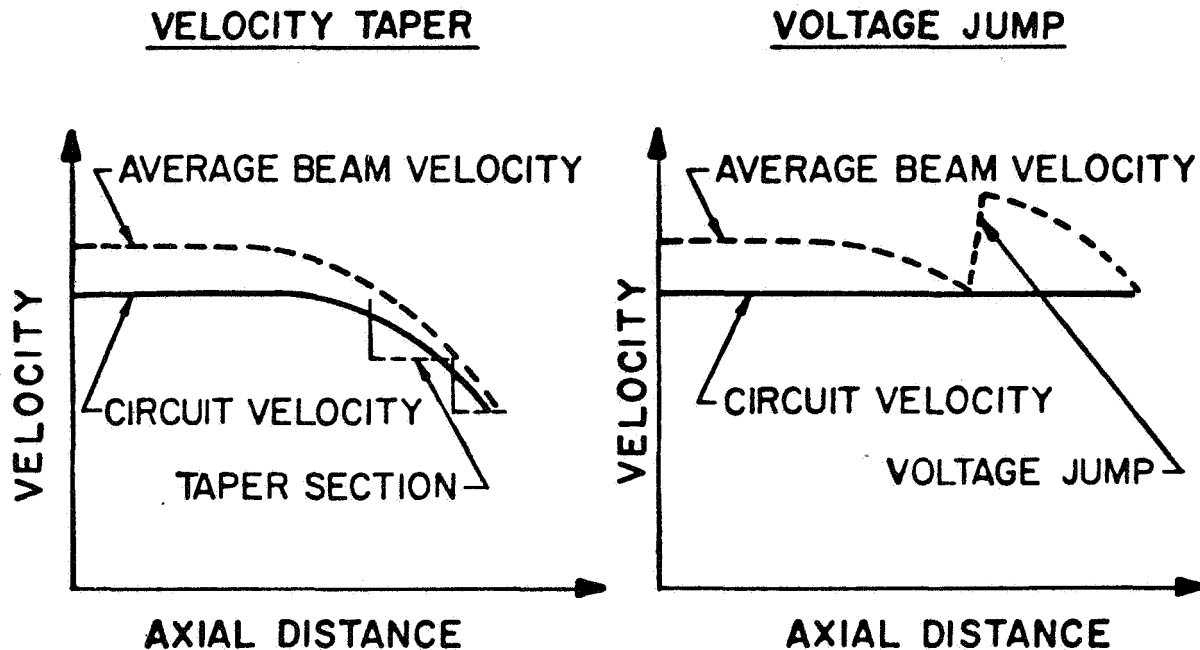


Figure 1 Velocity profiles of velocity taper and voltage jump circuit.

The velocity taper achieves resynchronization by reducing the circuit phase velocity along the axis at the same rate as the average beam velocity.

Velocity tapering can be applied continuously when a helix circuit is used.

For filter type circuits, such as the coupled cavity structure, velocity tapering is only possible in steps. In a voltage jump, on the other hand, the circuit phase velocity remains unchanged, while the beam is reaccelerated near the output end of the tube with a voltage jump on the circuit.

In comparing these two methods, the velocity taper could be expected to be more effective, since it can be gradually applied, so that velocity synchronization is feasible over a longer distance than with the rather abrupt voltage jump. It was found, however, that the voltage jump method is usually more powerful. This becomes plausible when one considers that velocity tapering is generally associated with a reduction of the interaction impedance. The energy transfer becomes therefore weaker in a velocity taper, but not in a voltage jump circuit. Moreover, the

voltage jump causes a reduction of the space charge forces in the beam. These space charge forces generally have a degrading effect on the beam modulation.

Both methods, the velocity step tapers and the even more effective voltage jump technique, have been extensively investigated in these studies.

The following are some findings of these investigations:

1. The velocity profile (for instance linear, quadratic or step taper) is not critical.
2. The optimum position of tapers is given so that the input end of the taper is located at the saturation point of the driver section of the circuit.
3. The optimum velocity reduction of the taper was about 50%.
4. The optimum length of a taper or voltage jump section is the most critical design parameter. Its length must accurately be correlated to the electron beam modulation to be effective. The large signal computer program made it possible to arrive rather quickly at its optimum design.
5. The choice of the relative beam velocity (voltage) of the driver section deserves special consideration. This parameter determines the efficiency of the driver section, but also the beam modulation which enters the resynchronization section. This beam modulation is a rather important factor in making the velocity resynchronization effective. The beam modulation of a modulated electron beam at large signal levels is generally rather complex, but of significance is primarily the beam modulation current at the fundamental frequency. This is the only component of the beam modulation which is capable of energy transfer to the slow wave circuit.

It is found that the fundamental component of the beam modulation current becomes larger at lower voltages, until it reaches a maximum at the "optimum beam bunching voltage", which is lower than the maximum gain voltage.

This "optimum beam bunching voltage" in the driver section of the circuit provides indeed the largest efficiency enhancement with velocity resynchronization, even though the initial efficiency is then rather low. At this voltage, the harmonic beam current is comparatively small. At the "optimum overvoltage," on the other hand, the fundamental beam current is rather small, and practically no further efficiency improvement is possible with velocity resynchronization, at least not with the methods described here. At this voltage the harmonic beam modulation current is comparatively large.

Conventional traveling-wave tubes are frequently designed for depressed collector operation.² In this case the spent beam is decelerated and collected at a lower potential for further efficiency enhancement. The efficiency improvement with such conventional depressed collectors, however is found to be limited.^{3,4} Limitations on the collector depression are primarily imposed by the beam modulation of the spent beam. Of concern is the average velocity of the spent beam, as well as the velocity modulation. The velocity distribution of the spent beam, or rather the velocity of the slowest electrons of the beam determine the limit of collector depressing before backstreaming of these low energy electrons occurs.

The velocity modulation of a spent beam generally exhibits very little correlation with the beam modulation currents. However, it is generally found that the average velocity spread of the spent beam is proportional to the basic (conversion) efficiency. Tubes with high conversion efficiencies will therefore contain very slow electrons in the spent beam, and less efficiency improvement with conventional depressed collectors will therefore be possible for such tubes.

This is especially true for tube which employ velocity resynchronization for efficiency improvement. Theoretical and experimental investigation on the velocity distribution of such tubes¹ showed, that the average beam velocity is lower and the velocity spread of the spent beam is larger than is in conventional tubes. This is illustrated in Figure 2 of the computed spent beam velocity characteristics of a velocity taper tube and a conventional tube with similar tube parameters.¹ From Figure 2 it can be seen, that the velocities of the slowest spent beam electrons of the velocity taper tube are almost zero. A conventional collector will therefore not permit any depression without backstreaming. The velocities of the slowest spent beam electrons of the conventional tube (with the same parameters) on the other hand are seen to be fast enough to permit 45% collector depression (with respect to the circuit potential V_0), before backstreaming with a conventional collector occurs. (Figure 2)

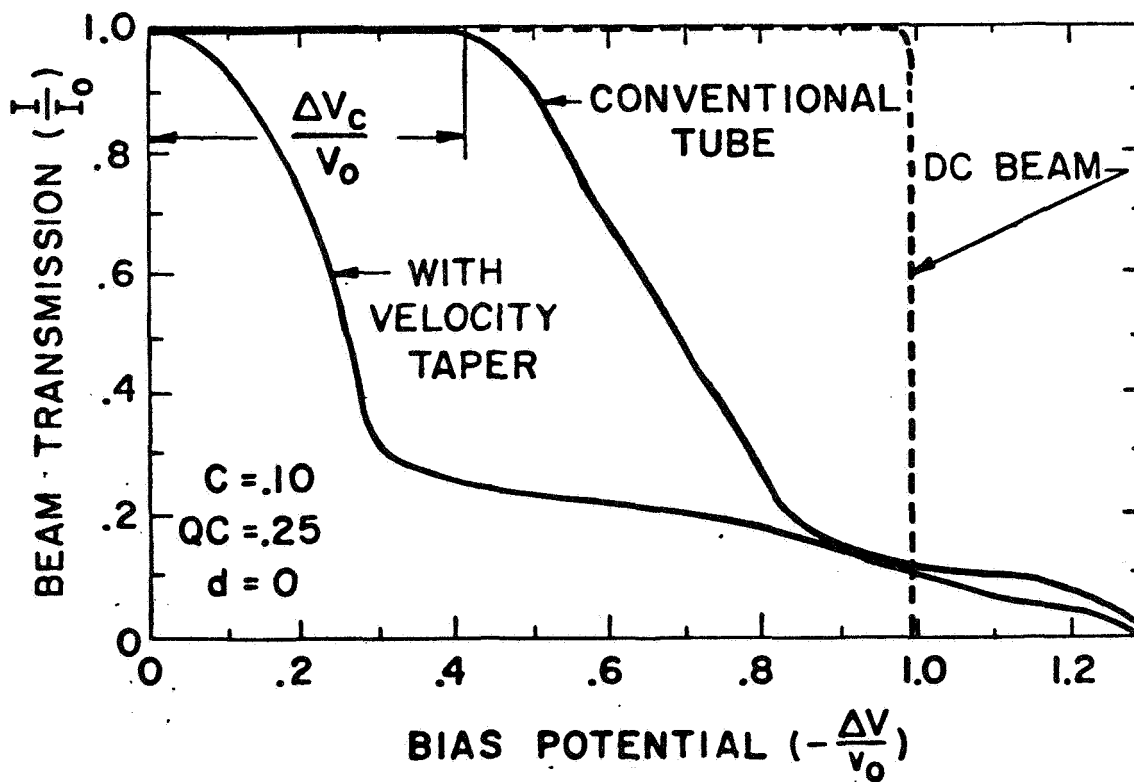


Figure 2 Spent beam energy distribution (computed).

For high efficiency tube, however, which have a large velocity spread of the spent beam, double stage collector depression permits to achieve additional efficiency improvements. The spent beam is then separated into two velocity groups and is collected in two stages.¹ The faster electrons of the spent beam are depressed further and are collected at a lower potential than the slower velocity group.

The design of such double stage collectors can be relatively simple. The first collector stage is kept at the circuit potential (V_o), while the second stage collector only is biased, as shown schematically in Figure 3.

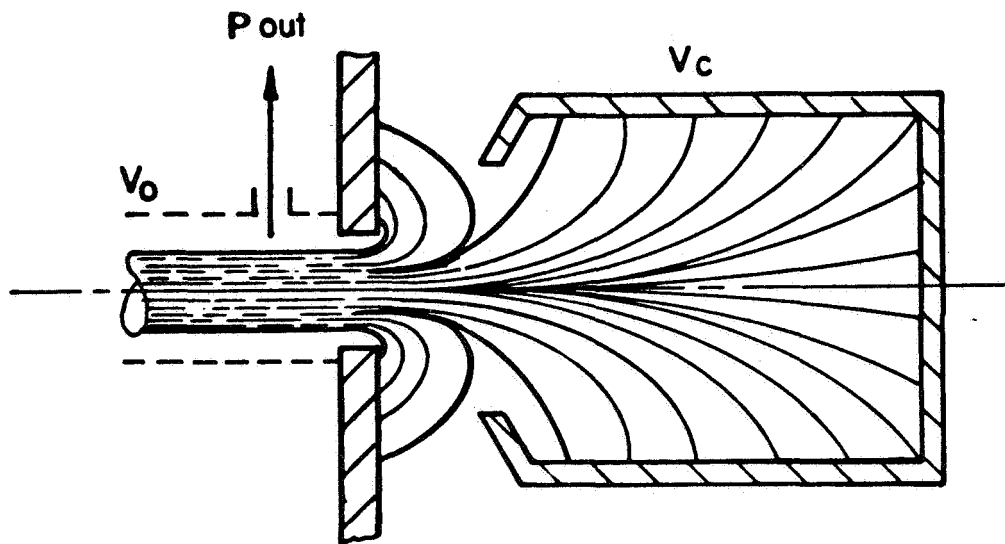


Figure 3 Schematic of double stage collector with single bias voltage.

This type of collector has been generally used with the tubes described here. The optimum collector depression is found in most tubes approximately at half the circuit potential V_o , or

$$V_c \approx .5 V_o$$

The beam current is then collected in nearly equal amounts in both collector stages.

Coupled Cavity Tubes¹

The velocity resynchronization methods described above have been applied to the coupled cavity slow wave structure. Velocity tapering is achieved by reducing the cavity period, while care must be taken not to change the cut-off frequencies of the taper cavities. The voltage jump method can be applied by separating a cavity with electric insulation, such as mica. A conventional choke design can be applied to compensate for the RF perturbations of the insulation.

The velocity resynchronization schemes were investigated to a considerable extent with experimental coupled cavity tubes at X-band.

A demountable test apparatus was used for this purpose to facilitate design changes of the velocity resynchronization methods. These tubes had the following common design characteristics:

Frequency	X-band
Cold Circuit Bandwidth	6%
Focusing	Solenoid
Gun Perveance	.5 μ p
Beam Voltage	14 kV
Output Power	5 to 10 kW (pulsed)
Collector	Double stage collector with single bias voltage

The tubes were built without sever to avoid possible degrading effects of the sever on the efficiency. The gain had therefore to be restricted to less than 20 dB to assure stable tube operation. The efficiency η was therefore defined as

$$\eta = \frac{P_{out} - P_{in}'}{P_o}$$

to correct for low gain effects.

Where

P_{out} = RF output power

P_{in}' = Input power reduced by cold loss of circuit

P_o = Sum of applied dc power to tube (excluding heater and solenoid).

The investigations were not limited to the voltage jump and the velocity step taper method, but were extended to combinations of these methods as well. Such voltage jump-velocity taper combinations resulted in higher efficiencies than was possible with either voltage jump or velocity taper only. The following circuit combinations have been evaluated;

- A. Voltage jump
- B. Two-step velocity taper
- C. Combination voltage jump two-step velocity taper
- D. Combinations of a voltage jump and single step velocity taper

Figure 4 gives the results of a voltage jump followed by a two-step velocity taper with an end velocity of 70% of the initial circuit phase velocity. This figure also shows a schematic of the velocity profiles for the circuit phase velocity and the beam voltage, including the collector region (collector grounded or depressed).

These velocities are defined as follows:

- v_o = circuit phase velocity in driver section
- v_1 = circuit phase velocity in first step velocity taper section
- v_2 = circuit phase velocity in second step velocity taper section
- u_o = dc beam velocity in driver section and in undeprressed collector
- u_j = dc beam velocity in voltage jump section
- u_c = dc beam velocity in depressed collector

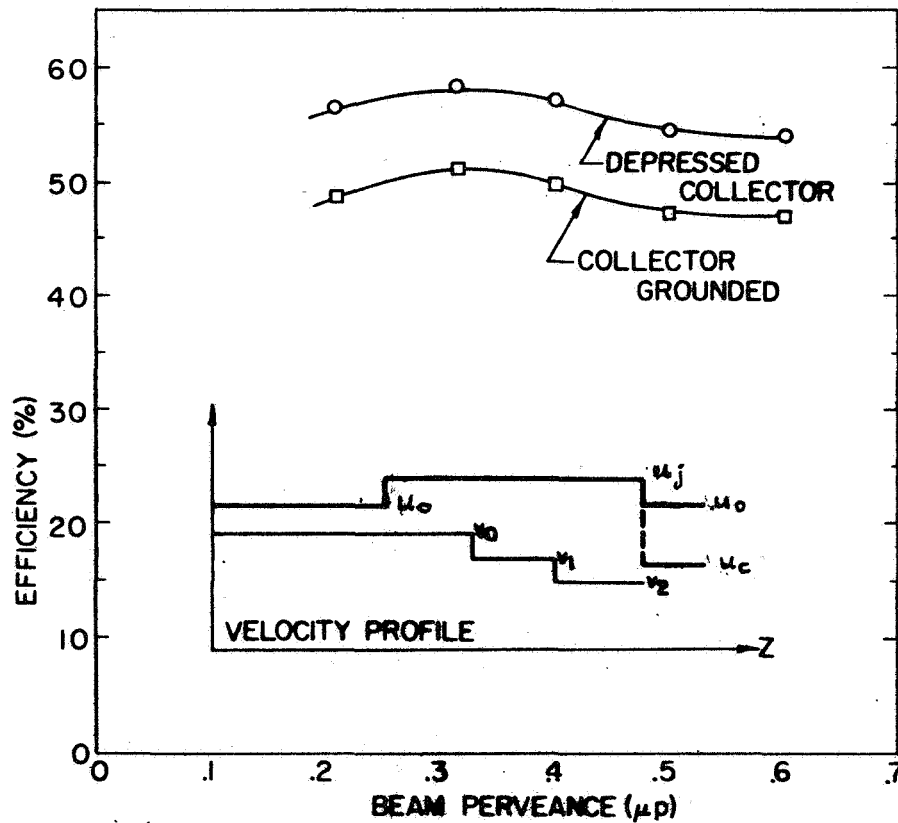


Figure 4 Efficiency of combined voltage jump and two-step velocity taper circuit (measured).

The beam current is the variable in this plot. The frequency was held constant in the measurements. All voltages, with the exception of the anode voltage, were also held constant. The drive level was optimized at each beam current value. The saturation gain was 20 dB for the optimum efficiency point. The efficiency reaches 58% with collector depression; more than 50% efficiency is achieved with a grounded collector. We note one efficiency behavior peculiarity associated with these taper methods: efficiency will increase with about the third root of the beam current in typical traveling-wave tubes. Here, however, we see that an efficiency maximum is reached with a specific value of the beam current (corresponding to a beam perveance of $.3\mu p$).

The circuit combination shown consists of a voltage jump and a two-step velocity taper. Very good efficiencies, however, can also be obtained with a simpler combination of a voltage jump and only a single velocity step taper.

Figure 5 shows results from such a combination: As indicated on the velocity profile, there is a velocity step taper first -- with a velocity reduction of 12%. The velocity taper is followed by the voltage jump. The frequency is the variable in this efficiency plot. The current and all voltages are kept constant; the drive level was optimized at each frequency. The saturation gain was about 18 dB. The efficiency (with a depressed collector) is about 50% over a 200 MHz frequency range. With a grounded collector, 45% efficiency is achieved at the center frequency. We note that the voltage jump in this configuration is applied to a tapered circuit section which already had a reduced phase velocity. This is a disadvantage because the interaction impedance of a circuit with a reduced phase velocity is inherently lower; a lower interaction impedance reduces the effectiveness of a voltage jump. Therefore, it appears attractive to apply the voltage jump to a circuit section without phase velocity reduction so that sacrifices are unnecessary

in the interaction impedance. The velocity profile in Figure 6 shows how this can be done in such a combination. The higher phase velocity in the untapered voltage jump section is then compensated by an equivalent increase of the voltage jump magnitude to maintain the required synchronism between circuit wave and beam velocity in the voltage jump section.

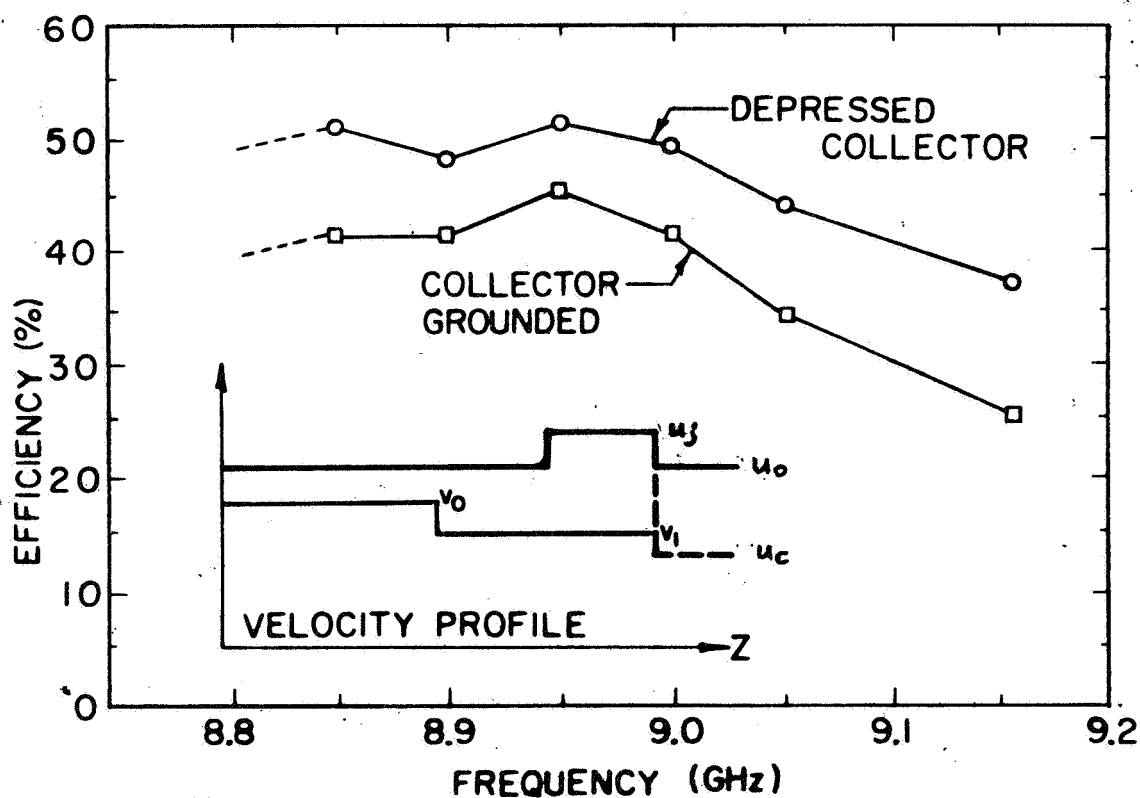


Figure 5 Efficiency of combined velocity step and tapered voltage jump circuit (measured).

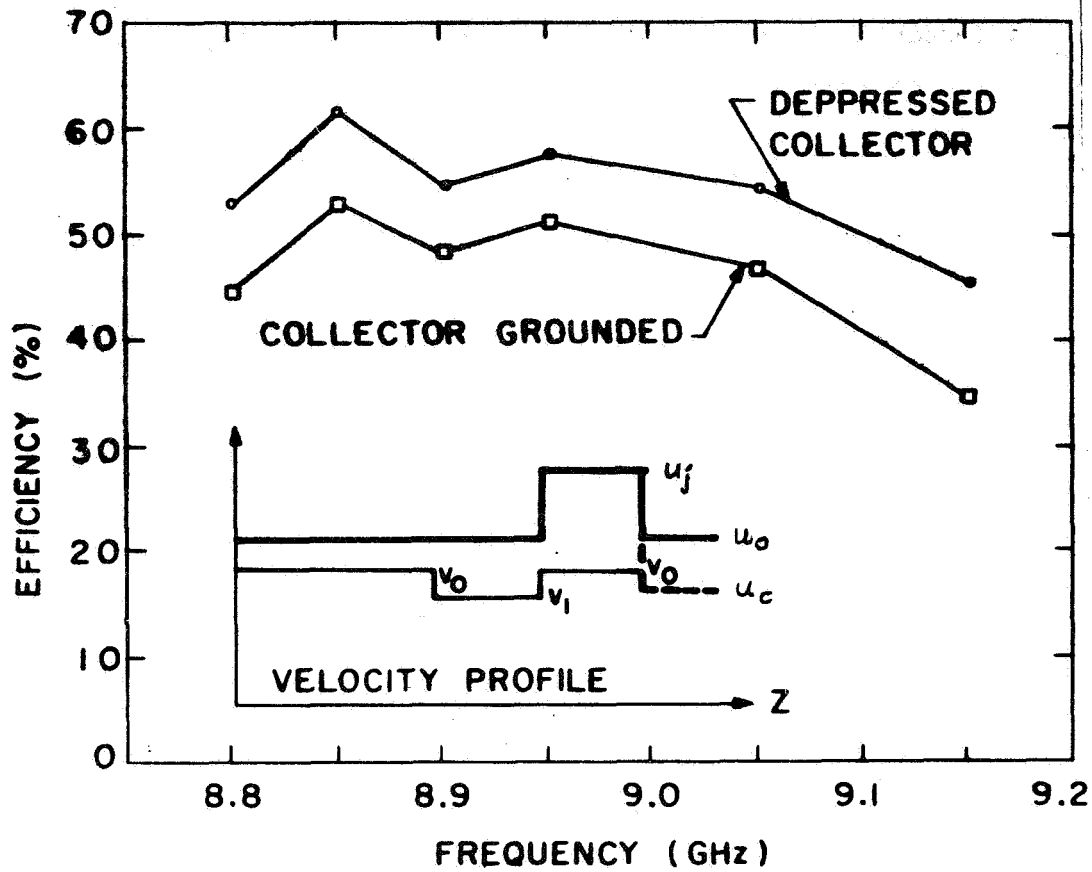


Figure 6 Efficiency of combined velocity step and untapered voltage jump circuit (measured).

These data were taken as a function of frequency. The current and all voltages were kept constant. The drive level was optimized at each frequency. The gain was then about 18 dB at saturation. As expected, the efficiency is higher, up to 62% with depressed collector and up to 53% with a grounded collector. The overall efficiency is higher than 50% over a frequency range of 350 MHz. This is more than half the "cold" bandwidth of this circuit (600 MHz). Although this is a relatively small bandwidth, these results are indicative of the large bandwidth capabilities of the taper methods. It is well known that such coupled cavity circuits can only operate efficiently for less than half the "cold"

bandwidth. Thus, no bandwidth limitations have been imposed by the taper methods and the bandwidth is limited only by the limitations of the basic circuit.

In Figure 7 the performance of a velocity step taper is shown. The velocity profile in Figure 7 shows its configuration: a two-step velocity taper with a total phase velocity reduction of 30%.

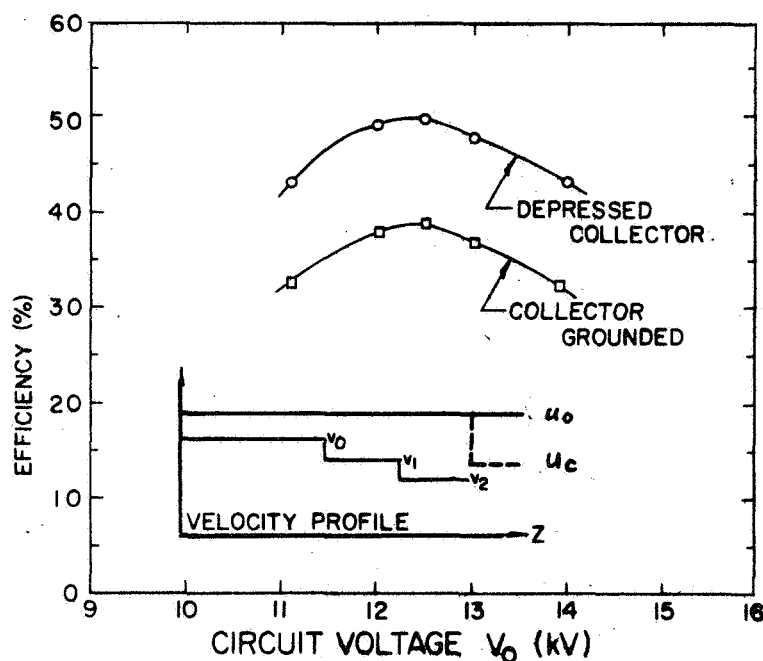


Figure 7 Efficiency of two-step velocity taper circuit (measured).

The variable in this case was the circuit voltage. Current and frequency were kept constant, and the drive level was optimized at each voltage. This gave a gain of about 20 dB at saturation. Note that the efficiency becomes a maximum with a voltage of 12.5 kV to produce enhanced beam bunching in the driver section. This compares to a maximum gain voltage of 16 kV, and about 19 kV optimum overvoltage to obtain maximum efficiency without tapering. The tube achieves 38% efficiency with the grounded collector and 50% with collector depression.

These results have been tabulated in Table I.

The cases I, IIA and IIB are the voltage jump velocity taper combinations discussed previously. Case III is the straight two step velocity taper and IVA and IVB are the two voltage jump circuits used in our combinations. One has a lower and the other a higher interaction impedance.

The experimental tubes described above operate over a comparatively small bandwidth (3%). However, the velocity resynchronization methods are not restricted to such small bandwidths.

An increased bandwidth version of the voltage jump tube was therefore evaluated with the demountable test apparatus. The efficiency data are shown in Figure 8.

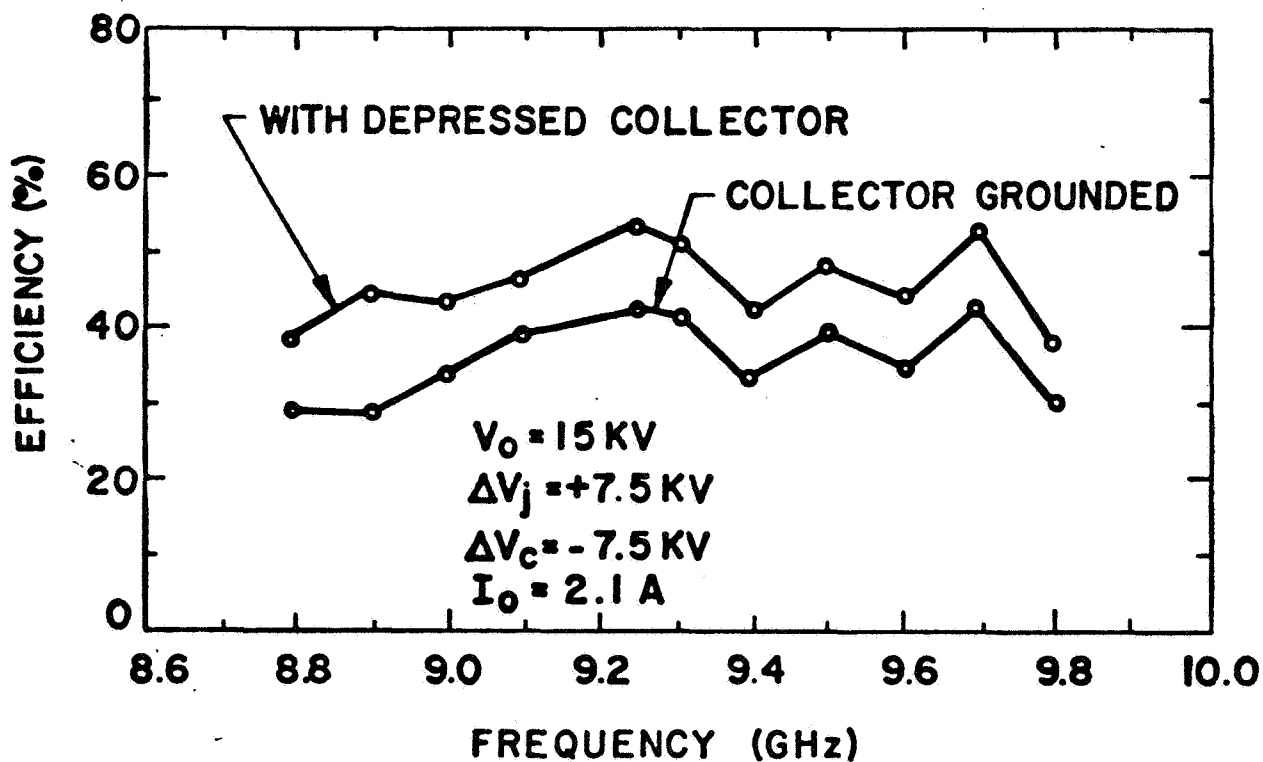


Figure 8 Efficiency of X-band coupled cavity tube for increased bandwidth with voltage jump (measured).

TABLE I Summary of circuit combinations.

COMBINATION	SECTION	PERIOD (INCHES)	VOLTAGE (V_o)	EFFICIENCY COLLECTOR GROUNDED ($V_c = V_o$)	EFFICIENCY COLLECTOR DEPRESSED ($V_c < V_o$)
I	driver	.175	1	51%	58%
	voltage jump	.175	1.3		
	step velocity taper	.140	1.3		
	step velocity taper	.120	1.3		
IIA	driver	.200	1	45%	51%
	step velocity taper	.175	1		
	voltage jump	.175	1.4		
IIB	driver	.200	1	53%	62%
	step velocity taper	.175	1		
	voltage jump	.200	1.6		
III	driver	.175	1	38%	50%
	step velocity taper	.140	1		
	step velocity taper	.120	1		
IVA	driver	.175	1	40%	57%
	voltage jump	.175	1.4		
IVB	driver	.200	1	47%	57%
	voltage jump	.200	1.4		

Nearly 10% bandwidth have been achieved with this tube with approximately 50% efficiency. This tube has an increased perveance of $1.15 \mu p$ to provide output power of 10 kW. The gain of this tube is approximately 18 dB, since no sever is used.

The voltage jump and velocity taper method are not the only velocity resynchronization schemes available for efficiency enhancement on coupled cavity tubes. It has been found that multi-voltage jump tapers, which consists of a series of small voltage jump sections with increasing beam voltage result in superior efficiency improvements compared to the velocity resynchronization methods described here. This new method has been used for the efficiency design of the proposed tubes.

Helix Tubes

The velocity resynchronization methods can be applied to the helix slow wave structure or other circuits. The helix circuit offers the advantage that the desired length of a helix taper or voltage jump section can be accurately obtained, while the lengths of coupled cavity sections are variable only in steps due to the periodicity of this structure.

Helix circuits can easily be designed with a continuous velocity taper by varying the helix pitch accordingly.

Voltage jump circuits however have the problem that an internal helix coupling between the driver helix and the voltage jump helix can not easily be achieved. It is possible however to bypass this problem with an external helix coupling through coaxial windows as shown schematically in Figure 9.

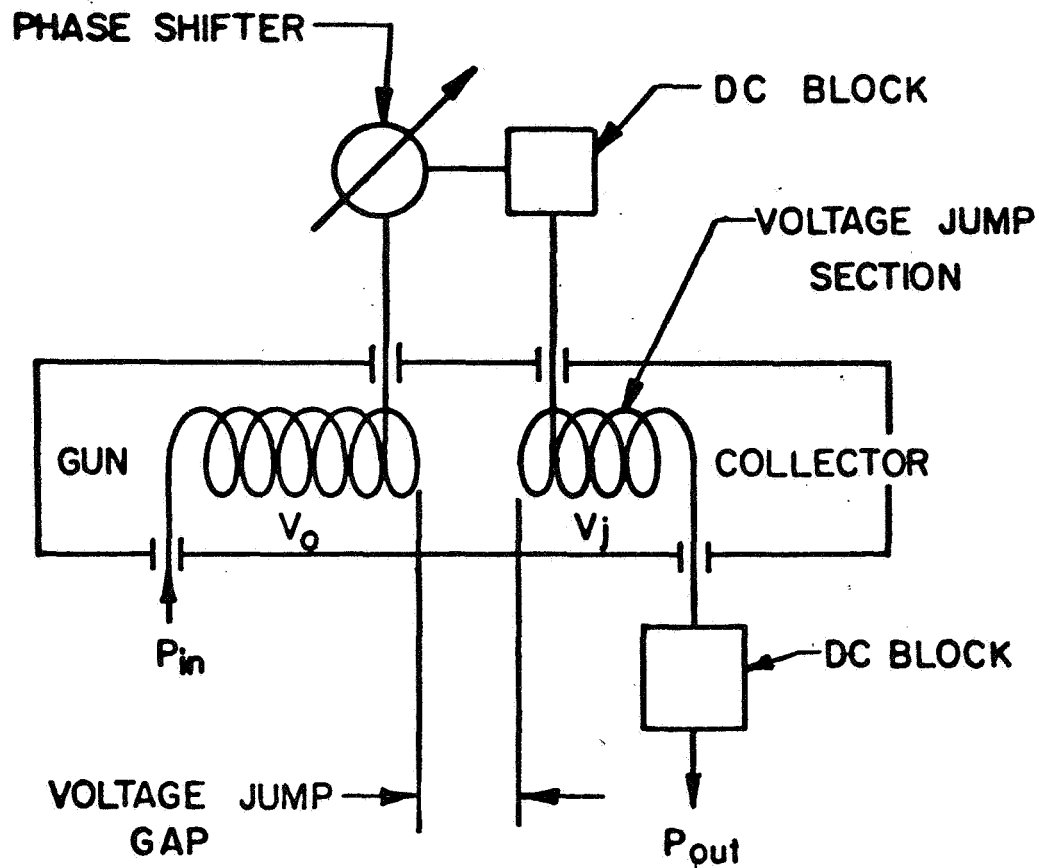


Figure 9 Schematic of helix tube with voltage jump.

The voltage jump helix is electrically insulated by two dc blocks at its input and output. These dc blocks permit undisturbed RF transmission and allow to apply a higher voltage to the helix. A phase shifter has to be inserted between driver and voltage jump helix to compensate for undesired phase shifts of the circuit wave in the transition path.

The gap in the voltage jump transition is exposed to a dc acceleration field, which may cause a perturbation of the beam focusing if the gap is too small. If the gap is too large, on the other hand, the beam modulation may deteriorate in the transition of the gap and may thus cause an efficiency degradation.

The large signal computer program was modified to analyze the effect of such voltage jump gaps with a linear voltage gradient assumption.

The space type helix tube with PPM focusing for S-band was designed with a voltage jump and a single biased double stage collector with data obtained from the large signal computer analysis. The efficiency data of this tube, shown in Figure 10, demonstrate the feasibility of this technique for helix tubes.

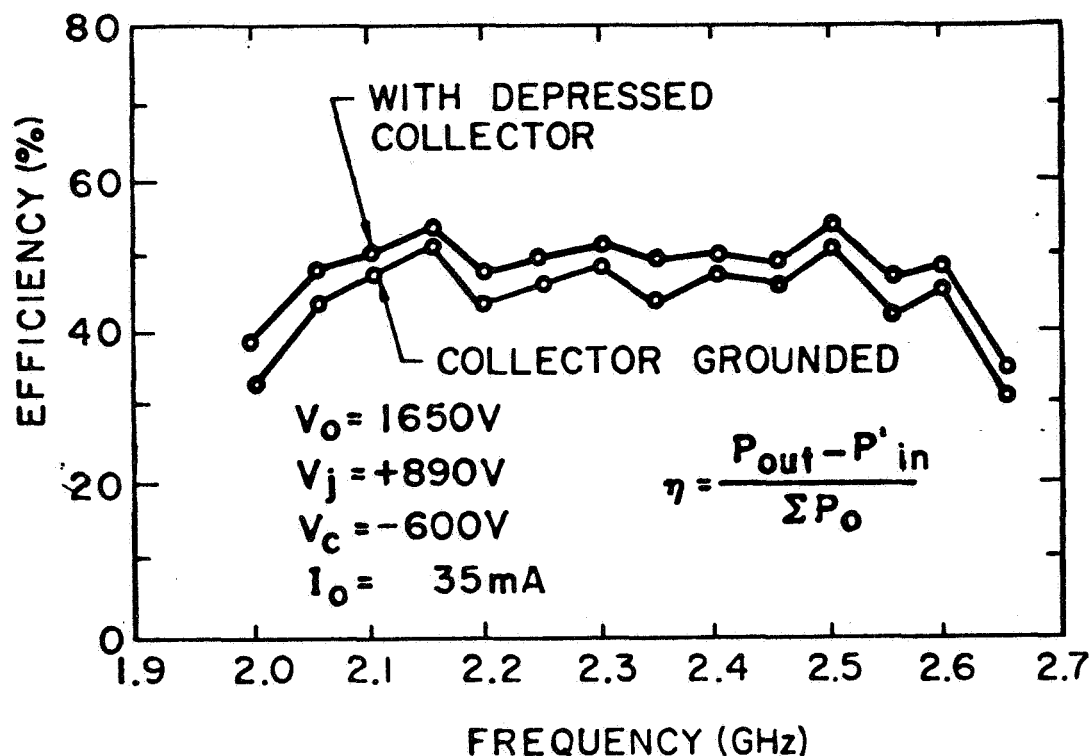


Figure 10 Efficiency of S-band space type helix tube with voltage jump (measured).

The efficiency with depressed collector is approximately 50% from 2.1 GHz to 2.6 GHz, with a power output of 30 watts. The tube was built without an attenuator to avoid possible degrading effects on the efficiency. The saturation gain was approximately 12 dB. The drive level and the phase

in the voltage jump transition was optimized for each frequency (Figure 9). The required phase changes correspond to those which would be produced by a helix line with the length of the gap.

The distortion characteristics of space tubes which are used for communication purposes is of concern. These data were therefore evaluated for the described tube. At saturation the AM - PM conversion was measured to $1^{\circ}/\text{dB}$, the third order intermodulation distortion to -12 dB. These data compared favorably to those of conventional traveling-wave tubes.

The intermodulation distortion of such velocity resynchronization tubes can be expected to be low, since these tubes operate with enhanced beam bunching, where the harmonic beam modulation current is suppressed.

It appears possible to apply a velocity taper or a combination of a voltage jump and a velocity taper to a helix tube. Significant efficiency improvements can then be expected also.

B. HIGH AVERAGE POWER TUBES

The Electron Dynamics Division of Hughes Aircraft Company has been engaged for many years in the development and production of high average power traveling-wave amplifiers with operating frequencies ranging from C-band to Ku-band. Several of these tubes are used for satellite ground communication transmitters. These tubes use the coupled cavity slow wave structure.

This bandpass filter structure has many advantages for high power traveling-wave amplifiers:

The high interaction impedance of this circuit assures high gain per unit length and high efficiency. It has become the standard for multi-kilowatt traveling-wave tubes above S-band. Its advantages are a large thermal mass (because of the all metallic construction) and its ease of adjustment from very narrow to almost 40% bandwidth.

In the past, operation has been limited to a few percent bandwidth because of bandedge oscillations. This is due to the bandpass characteristics of this type of circuit, with its high reflection and impedance at the upper and lower cutoffs. A technique of including lossy elements, resonant at the cutoffs, within the circuit, was developed.

The resulting tubes have wide, oscillation-free operating ranges that aid in trouble free operation. The all metallic construction assures the good thermal path to the cooling medium necessary in high power devices.

This technique has been employed for several years on low duty pulsed tubes. However, a careful study of materials, methods and techniques was required to prevent over-heating and gassing for tubes, to be operated at CW.

The coupled cavity circuit structure is uniquely suitable for the design of a highly effective, light weight magnetic focusing structure, which uses periodic permanent magnets. This focusing structure can be incorporated as an integral part of the circuit structure and offers a high quality focusing system with substantial weight and size reductions when compared to solenoid focusing.

Stable high gain is achieved by dividing the circuit into separate sections which are completely isolated from each other in an RF sense. The only coupling from one section to the next is through the modulated electron beam which can travel in one direction only. Consequently, there can be no feedback from the output to the input to cause regeneration --

even if more sections are added to give still higher values of RF gain. This technique allows a straightforward design approach for arbitrarily high gains. High gains are achieved merely by adding length to the circuit of the tube.

The coupled cavity structure is also extremely rugged and can withstand severe shock and vibration. It is suitable for space applications. As the reliability of these tubes was being improved, the power level and gain were also being raised to the present level of 10 kW CW at X-band with 55 dB of small signal gain.

In Table II a variety of these tubes with their performance characteristics are listed. These tubes can be considered representative for presently available high average power traveling-wave tubes.

The design and performance features of several of these tubes are described below:

10 kW CW X-band Traveling-Wave Tube (710H)

The high gain 10 kW CW traveling-wave amplifier is one of a variety of high average power X-band tubes. Some of these have been in pilot production for a number of years. More than 200 models of the 10 kW level tube have been fabricated. This indicates both the advanced nature of the refinement of this device and the valuable experience gained in identifying its critical problem areas.

Figure 11 shows the tube after processing and before being packaged in its focusing solenoid. The circuit is severed into three separate sections to obtain the 55 dB of stable gain. The two extra waveguide windows are used to install external loads to terminate each side of the last sever.

Table II High average power traveling-wave tubes.

TUBE	FREQUENCY RANGE GHz	POWER OUTPUT		GAIN dB	EFFICIENCY WITH DEPRESSED COLLECTOR	TYPE FOCUSING
		PEAK kW	AVERAGE kW			
614H	5.9 - 6.4	8 CW	8	45	35%	Solenoid
622H	5.4 - 5.9	75	2	50	22% (No collector depression)	PPM
635H	5.4 - 5.9	200	8	50	25% (No collector depression)	Solenoid
636H*	4.4 - 5.0	10 CW	10	11	50%	Solenoid
745H	7.9 - 8.4	1.2 CW	1.2	35	30%	Solenoid
722H	8.4 - 9.2	1.5 CW	1.5	40	18% (No collector depression)	Solenoid
307H	8.5 - 9.5	75	1	50	37%	PPM
750H	9.0 - 10.0	25	.5	50	40%	PPM
710H	8.7 - 9.3	10 CW	10	50	40%	Solenoid
817H	15.3 - 16.5	8 CW	8	40	35%	Solenoid
828H	16.0 - 16.5	100	.5	53	35%	PPM

* in development

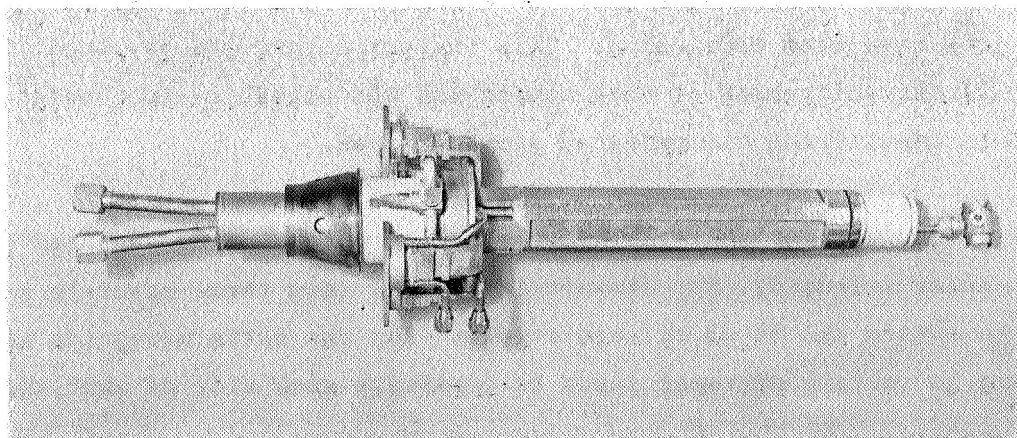


Figure 11 High gain 10 kW CW X-band traveling-wave amplifier without solenoid.

Recently, an internal termination capable of absorbing over 700 W has been developed for this tube. This allows up to 3 kW average output power with an internal type of termination rather than the external sever connections.

The collector, with a large insulator to permit collector depression, projects between the waveguide flanges. Coolant connectors are attached to the body and the collector. Appendage ion pumps are included at the exhaust manifold between the waveguide extensions and at the gun to assure good pressure during preliminary tests. Figure 12 shows the tube packaged for operation within the focusing solenoid. Various detailed operating results were presented in earlier sections of this discussion. Some of the pertinent parameters are:

Frequency	X-band
Bandwidth	10%
Gain (saturated)	53 dB typical
Power output	10 kW
Power input	10 - 100 mW
Efficiency	25%
Efficiency (with depressed collector)	35 - 40%
Cathode voltage	-20 kV
Cathode current	2.5 A
Perveance	$.88 \times 10^{-6}$
Focusing	Solenoid

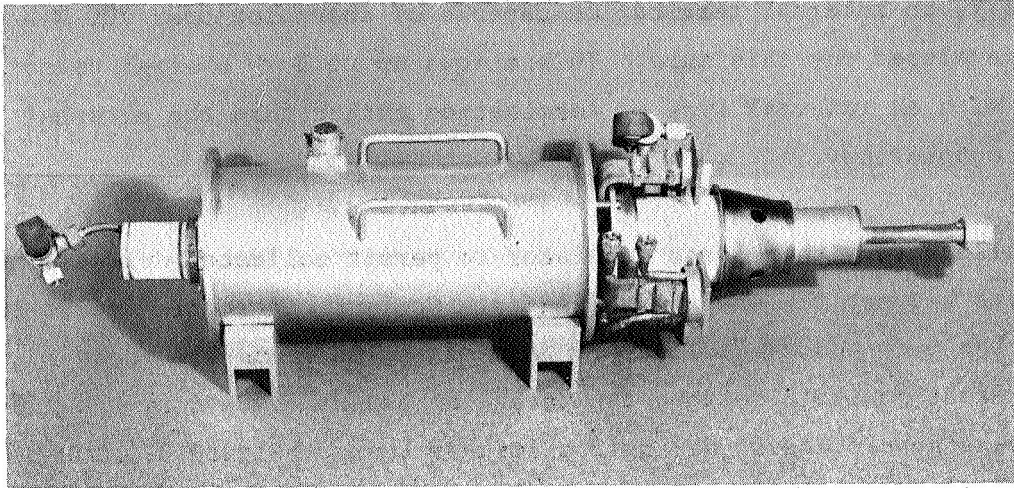


Figure 12 10 kW CW X-band traveling-wave amplifier packaged in focusing solenoid ready for RF operation.

8 kW CW X-band Traveling-Wave Tube (614H)

The C-band CW traveling-wave amplifier (614H) was developed from experience gained on the X-band tube. A summary of the major specifications is included below:

Frequency range	5.9 - 6.4 GHz
Gain	40 dB
Power Output	8 kW
Efficiency	18%
Efficiency (with depressed collector)	35%
Cathode voltage	-18.6 kV
Cathode current	2.9 A
Perveance	1.2×10^{-6}
Focusing	Solenoid

Figure 13 is a photograph of the 614H without its focusing solenoid. Note the similarities (except size) in layout with the X-band tube. This indicates the degree to which prior experience is utilized.

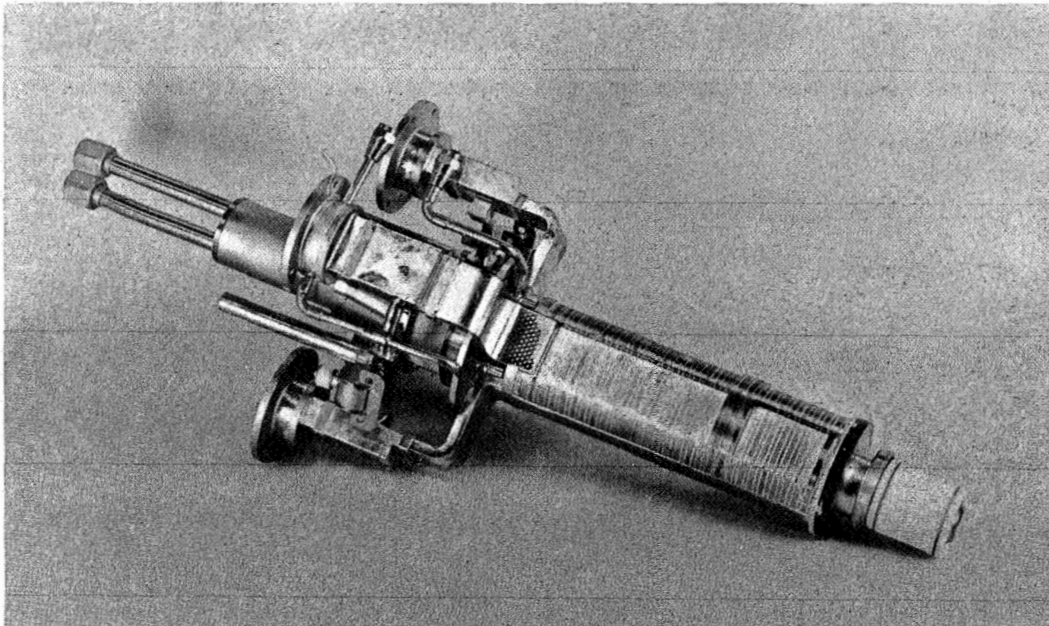


Figure 13 8 kW CW C-band traveling-wave tube without solenoid.

Figure 14 shows the 614H as it would appear in a completed package with solenoid.

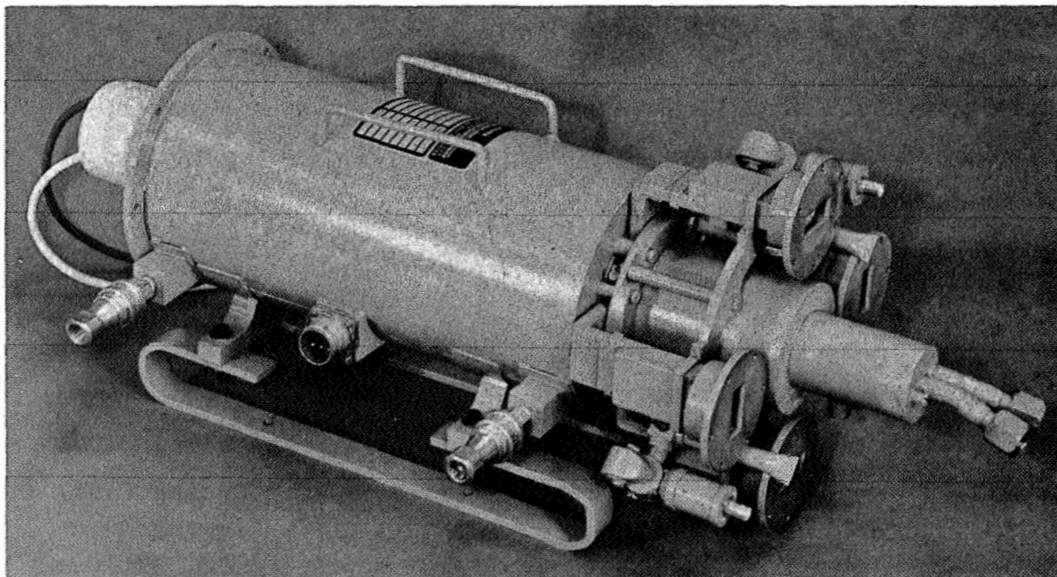


Figure 14 8 kW CW C-band traveling-wave tube with solenoid.

Figure 15 shows the power output versus frequency for the latest tube of this type.

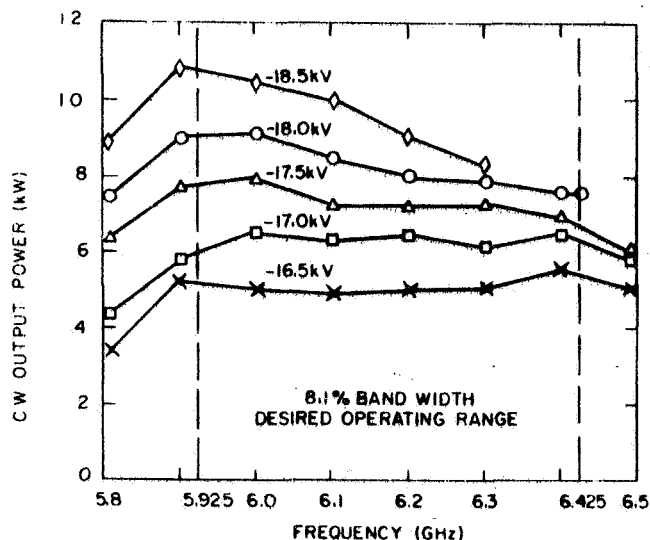


Figure 15
614H power output vs.
frequency for various
beam voltages.

Ku-band 10 kW CW Traveling-wave Tube (817H)

Recently the Hughes Electron Dynamics Division conducted a study of high power transmission tubes above X-band for use in satellite communication ground terminals for the U. S. Army Electronics Command (Contract No. DA 28-043 AMG-00234(e)). This study shows that coupled cavity traveling-wave tubes are feasible for operation at the 15 to 16 GHz and 31 to 32.3 GHz frequency bands at power levels of 10 kW and 25 kW CW.

As a part of this program, one experimental tube (817H) was constructed. This tube was operated to 8.7 kW CW at 15.54 GHz. Although the limited scope of the experimental portion of the study program allowed only one tube to be built, the capability of the coupled cavity traveling-wave tube approach to high average power, even at Ku-band frequencies, was demonstrated.

The basic design features and mechanical construction of the 817H are closely related to the more fully developed X-band tube (710H), discussed before. The 817H is essentially a more narrow band version of the 710H scaled to operate at Ku-band.

The 817H uses a cathode modulated electron gun and is solenoid focused. The beam perveance is 0.9×10^{-6} . The beam diameter is 0.059 inch and the resulting γa is approximately 1.45. To obtain a gain of 40 dB the interaction circuit is severed into three sections. The terminations at the first sever are provided internally. Because of the very high RF power of this tube, the relatively small internal terminations can not handle the power at the second sever. Therefore, the circuit is matched to external waveguide and the terminations for this sever are provided externally. For this reason four RF windows are required on the 817H.

Figure 16 shows the completely assembled 817H after vacuum processing and pinch-off but prior to placing it in the focusing solenoid. As can be seen, appendage vacuum pumps remain on each end of the tube. It has been found that with proper processing, the pump at the gun end is not essential.

Figure 17 shows a typical curve of efficiency and beam transmission as functions of collector depression voltage taken under pulsed conditions at a frequency of 15.33 GHz. The RF output power was approximately 11.6 kW.

The 817H was operated both pulsed and CW over a wide range of operating conditions. It was oscillation free for a cathode voltage range of -13 kV to -24 kV. Figure 18 shows saturated power output versus frequency under pulsed conditions.

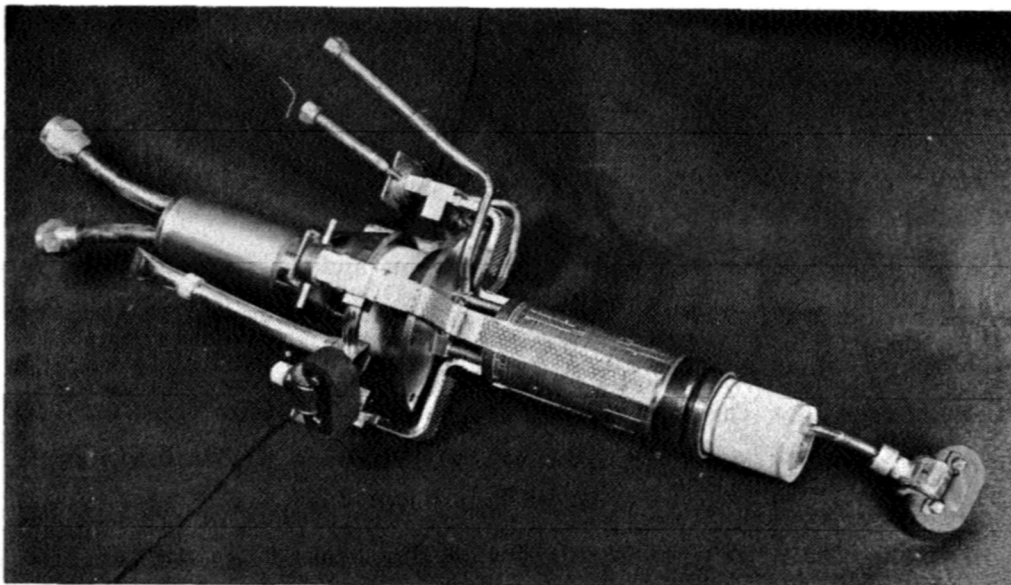


Figure 16 Finished view of experimental tube 817H, without focusing solenoid.

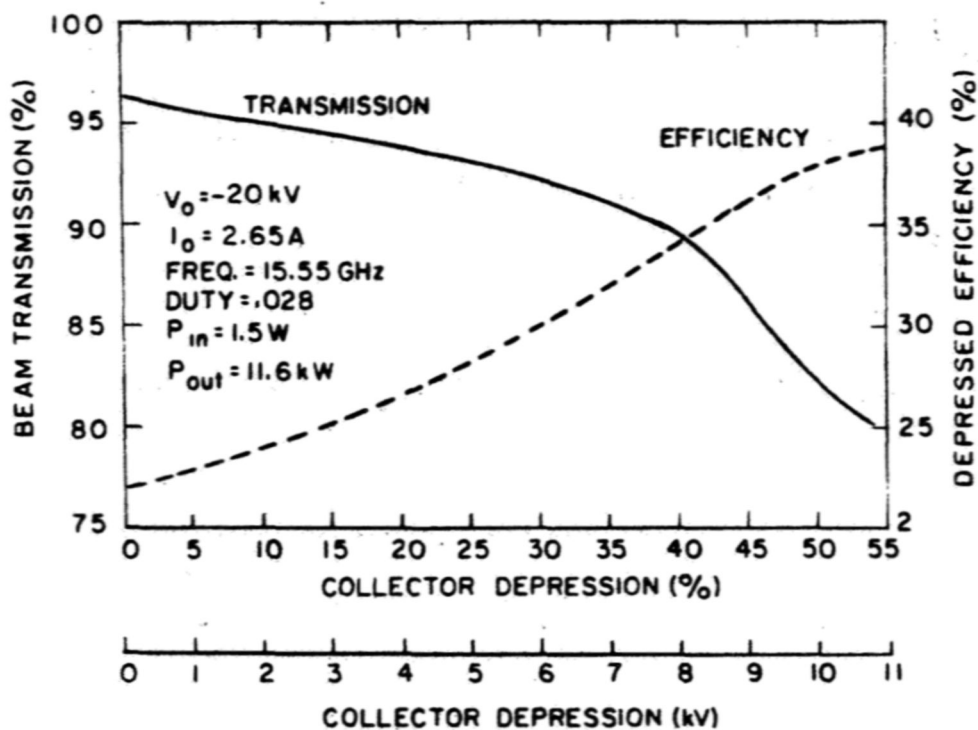


Figure 17 817H beam transmission and efficiency vs. collector depression at -20 kV beam voltage.

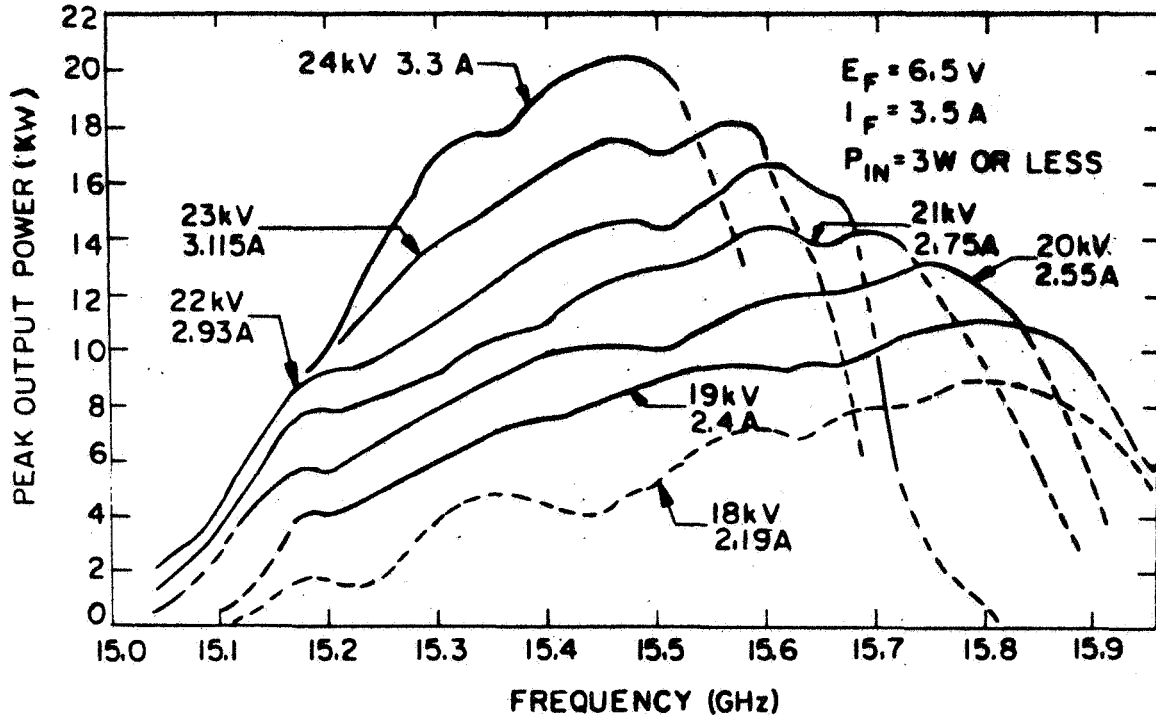


Figure 18 Pulsed RF power output vs. frequency of 817H. Parameter is cathode voltage. The dashed portions of the curves indicate that the drive level is not sufficient for saturation.

75 kW, Gridded, Periodically Focused, C-band TWT (621H)

The 621H is shown in first packaged form in Figure 19. It uses a "shadow" grid electron gun. The 621H is designed to meet the following requirements:

Frequency range	5.4 to 5.9 GHz
Small signal gain	50 dB
Peak output power	75 kW
Duty cycle	.02
Cathode voltage	-36 kV dc
Beam current	10 amp peak
Perveance	1.5×10^{-6}
Grid voltage (with respect to cathode)	400 V peak
Grid bias	-800 V dc

Focusing

Periodic permanent magnet

Cooling

Liquid

Weight

36-1/2 pounds

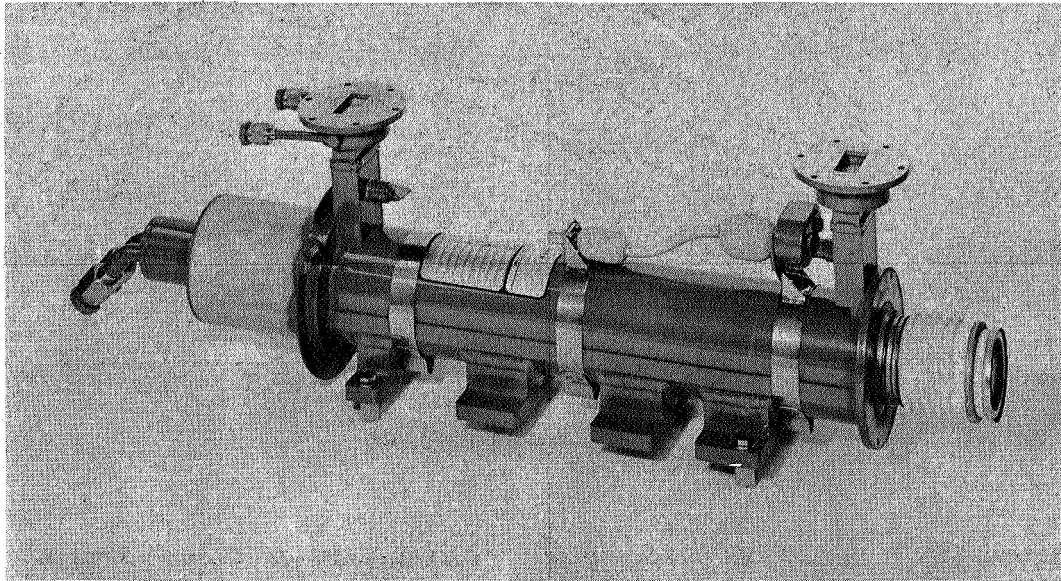


Figure 19 621H - 75 kW PPM focused C-band traveling-wave tube.

Figures 20 and 21 show typical small signal gain and saturated output power versus frequency curves of one of the early developmental models of the 621H for several values of beam voltage.

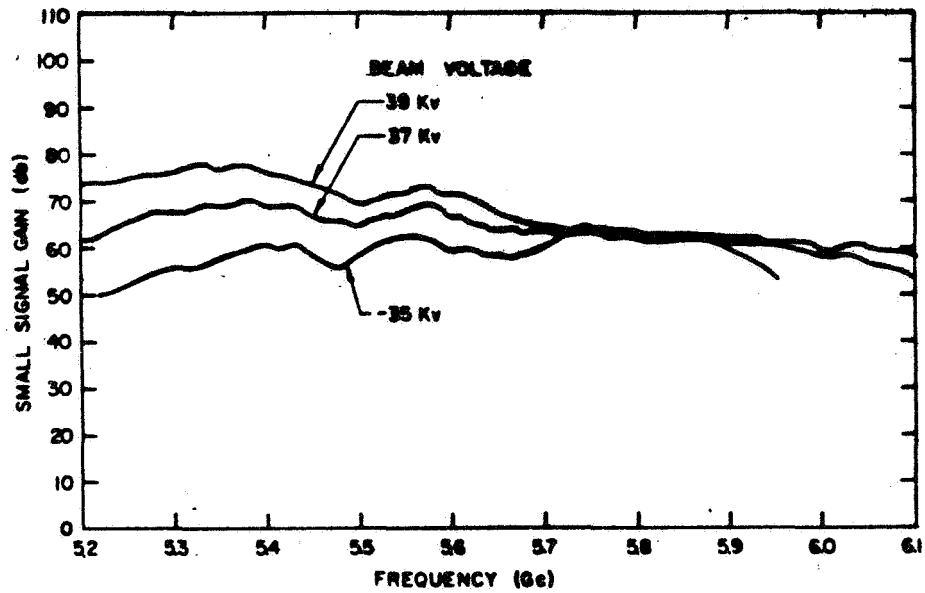


Figure 20 621H gain vs. frequency.

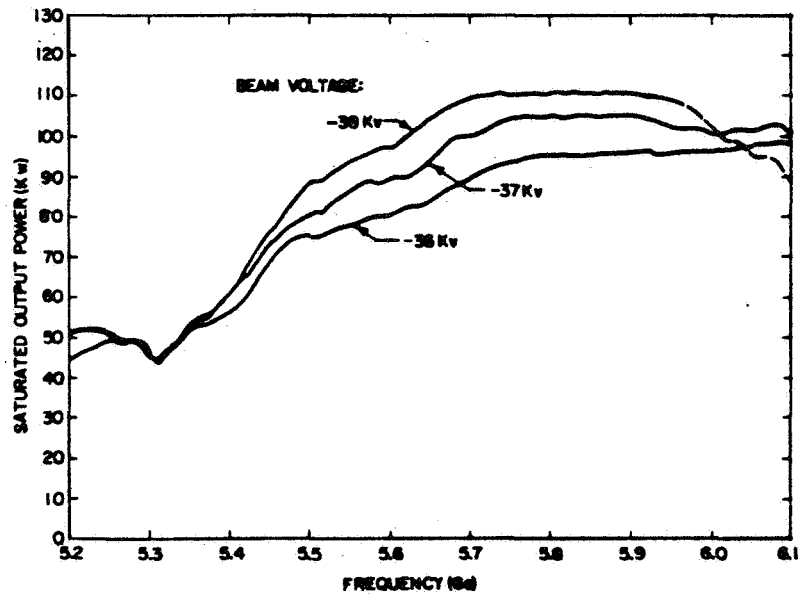


Figure 21 621H power output vs. frequency.

307H High Average Power X-band PPM Tube

The 307H is a broadband, high power traveling-wave tube. This production tube has high efficiency with high gain per unit length; 50 kW peak power is attained in this lightweight, periodic permanent magnet focused traveling-wave tube. A photograph of the 307H is shown in Figure 22. A summary of the major specifications is included below:

Frequency	8.55 - 9.45 GHz
Power output	50 kW minimum
Duty	1% (tested to 4%)
Gain (saturated)	50 dB
Gain (small signal)	56 dB
Cathode voltage	-36 kV
Cathode current	10 A
Anode voltage	0
Anode voltage (cutoff)	-37 kV
Heater voltage	11 V ac
Heater Current	5.5 A
Cooling - Collector	1.5 GPM H ₂ O
Body	.5 GPM H ₂ O
Length	22-1/6 inches
Diameter	3-1/2 inches OD
Weight	25 pounds
Efficiency	37%

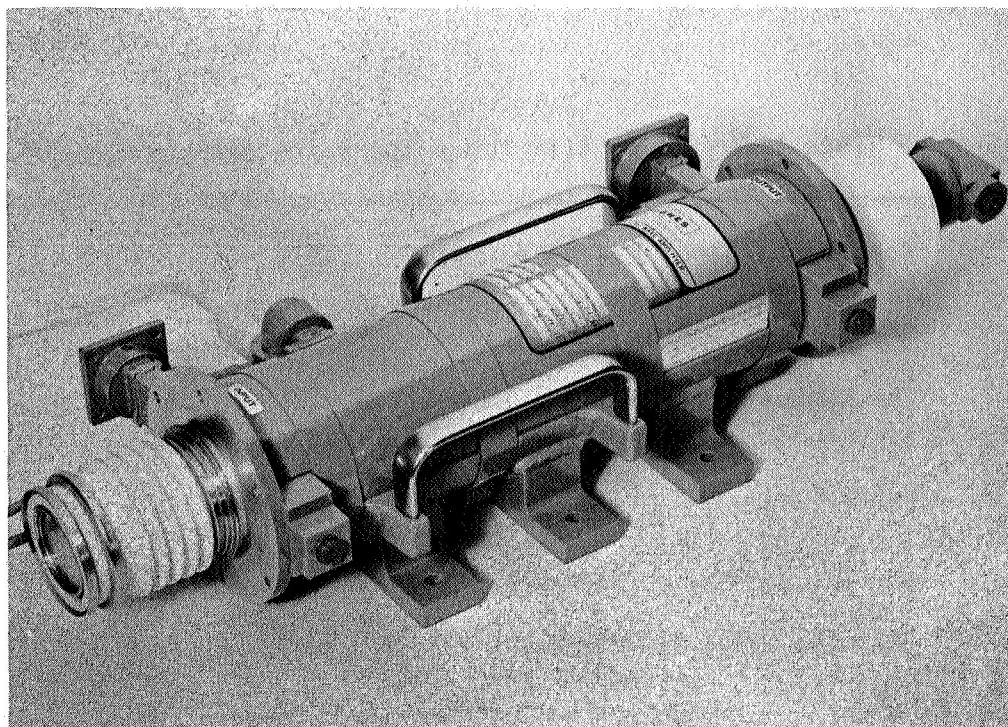


Figure 22 50 kW X-band pulsed traveling-wave tube 307H.

C. LIFE PERFORMANCE OF TRAVELING-WAVE TUBES

Medium Power Tubes for Space Applications

The Electron Dynamics Division of Hughes Aircraft Company has been the supplier of approximately 80% of the traveling-wave tubes used in space applications. Substantial efforts have been devoted over a number of years to develop the technology and the special facilities necessary to manufacture traveling-wave tubes with the required extreme reliability in space environment. These tubes are generally very rugged, very efficient, light weight and small with PPM focusing and a helix slow wave structure. Their operating frequencies range from S-band through Ku-band with power levels up to 30 watts.

In order to evaluate the life expectancy of these tubes, extensive life tests were initiated a number of years ago, which are still continuing. In Table III several of these tubes are listed as well as their application in space.

Table III Long life tubes for space applications.

1. The Hughes 314H, a 2 to 5 watt CW, 1.5 to 2.5 GHz tube, is the Syncom I Satellite Transponder Output Amplifier.
2. The Hughes 349H, a 10 to 12 watt CW, 1.8 to 3.2 GHz tube for the Surveyor Telecommunications System (Mariner and Lunar Orbiter).
3. The Hughes 384HA, a 4 watt CW, 3.0 to 5.0 GHz tube, is the Applications Technology Satellite Transponder Output Amplifier.
4. The Hughes 384H, a 4 watt CW, 3.0 to 5.0 GHz tube, is the Advanced Syncom Satellite Transponder Amplifier (now ATS).
5. The Hughes 394H, a 5 or 20 watt CW, 1.8 to 3.0 GHz tube for NASA's Apollo Spacecraft Transponder.
6. The Hughes 214H, an 8 watt CW, 2.2 to 2.4 GHz tube for the Pioneer Telecommunications System.
7. The Hughes 215H, a 6 watt CW, 3.0 to 5.0 GHz tube for the Early Bird Communications Satellite Transponder.
8. The Hughes 226H, a 50 mW CW, 3.0 to 5.0 GHz tube is the driver tube for the Intelsat II Communications Transponder Output Amplifier.

These tubes have accumulated a very substantial amount of successful total life test hours as shown in Table IV.

Table IV Total accumulated hours of life testing for space tubes (7/1/68).

TUBE TYPE	NUMBER OF TUBES	TOTAL HOURS
384H	12	431,300
384HA	13	161,500
215H	10	112,560
394H	5	55,585
314H	9	484,100
349H	8	247,200
214H	2	32,025
226H	<u>3</u>	<u>46,880</u>
	62	1,571,150

The life testing includes emission evaluation, failure-mode evaluation, an evaluation of on-off switching, filament warm-up, of cold starts without a filament warm-up period temperature cycling, and of the storage time effects under operational conditions.

In Table V, VI and VII the individual accumulated hours of successful life testing for several of these tubes are listed.

Table V Continuous life test data on 384H TWT (7/1/68).

TUBE TYPE	SERIAL NUMBER	TOTAL OPERATING TIME (hours)
384H	39	37,900
384H	45	36,000
384H	48	38,800
384H	49	37,300
384H	53	37,800
384H	55*	17,100
384H	67	38,500
384H	68	36,400

Table V Continued.

TUBE TYPE	SERIAL NUMBER	TOTAL OPERATING TIME (hours)
384H	70	38,400
384H	74	37,600
384H	76	37,500
384H	78	<u>38,000</u>
TOTAL OPERATING TIME (12 TWTs)		431,300
* Removed from test - equipment malfunction		

Table VI Continuous life test data on 314H TWT (7/1/68).

TUBE TYPE	SERIAL NUMBER	TOTAL OPERATING TIME (hours)
314H	6	54,100
314H	11	54,300
314H	12	54,300
314H	14	58,500
314H	18	53,600
314H	20	55,600
314H	37	54,400
314H	39	53,400
314H	55	<u>45,900</u>
TOTAL OPERATING TIME (9 TWTs)		484,100

Table VII. Continuous life test data on 349H TWT (7/1/68).

TUBE TYPE	SERIAL NUMBER	TOTAL OPERATING HOURS	CYCLES
349H	25 *	24,400	
349H	51	51,300	
349H	52 *	23,800	
349H	56 *	26,000	
349H	69	51,900	
349H	97 *	20,500	
349H	101 *	19,200	
349H	110	<u>30,100</u>	<u>45,150</u>
TOTAL OPERATING TIME (8 - 349H TWT)		247,200	45,150
* Removed from test due to end-of-life.			

It can be seen that a number of these continue to perform after continuous life testing of approximately 50,000 hours. Although these data are restricted to tubes made by the Hughes Aircraft Company, they can be considered representative for these low powered tube types.

Life Tests on High Power Tubes

Life tests have been carried out on several pulsed kilowatt power level traveling-wave tubes, which use either coupled cavity circuit or helix slow wave structure. These tubes are generally designed for 2000 to 3000 hours operation. The life tests had to be discontinued due to limitations of the test equipment. These life test data are listed in Table VIII.

Table VIII Life test data on high power tubes.

TUBE	QUANTITY	TOTAL ACCUMULATED LIFE TEST HOURS	FAILURES	OUTPUT POWER	DUTY %	FREQUENCY BAND	CIRCUIT TYPE	COOLING
310H	4	4,337	0	1 kW	2.0	X	Helix	Air
538H	4	4,000	0	1.5 kW	1.0	S - C	Helix	Air
740H	6	5,077	1 - gassy	1.5 kW	2.0	X	Coupled Cavity	Air
350H	18	17,995	2 - Open heater	1.5 kW	1.0	S	Helix	Air
362H	3	10,575	0	500 watts	.5	S	Helix	Air
313H	5	2,871	2	1 kW	.6	S	Helix	Air
518H	1	2,000	0	1.25 kW	.02	S	Helix	Liquid
611H	2	4,000	0	1.25 kW	.02	C	Helix	Liquid

D. RECENT ADVANCEMENTS IN HEAT PIPE COOLING FOR MICROWAVE TUBES

The Electron Dynamics Division of Hughes Aircraft Company is actively investigating new concepts and methods of heat transfer and cooling for traveling-wave tubes, especially heat pipe cooling. Heat pipe cooling utilizes the evaporation heat of fluids for cooling purposes. This method provides superior heat transfer characteristics when compared to conventional liquid cooling techniques. This cooling method requires no pumps, since the transport of the fluids is accomplished by capillary action. Power is therefore saved and the tube can operate more efficiently than a tube with conventional liquid cooling. The capillary pumping method is gravity-independent and thus it is ideally suitable for space applications. A heat pipe cooling system operates at nearly isothermal conditions over large areas and thus can be considered more reliable than other heat transfer methods.

Design methods for heat pipes are now well established^{2,3,4}. Recent efforts in this area at Hughes Aircraft Company led to the development of one-way heat pipes and of dielectric heat pipes for depressed collector operation. These devices are described here.

1. Dielectric Heat Pipe

The dielectric heat pipe is a device which has the ability to remove heat from a heat source (traveling-wave tube) while, at the same time, serving as an electrical insulator. To date these devices have been capable of removing up to 1000 watts of dissipated power from the collector while the voltage was depressed 12,000 volts. Figure 23 shows a heat pipe built around a traveling-wave tube collector. In this particular heat pipe the working fluid and the wick are dielectric materials and, thus, the device is also a good electrical insulator.

However, the dielectric strength of the device drops off very fast, according to Paschen's Law⁵, when the operating temperature is reduced, since the pressure inside the device drops exponentially with temperature.

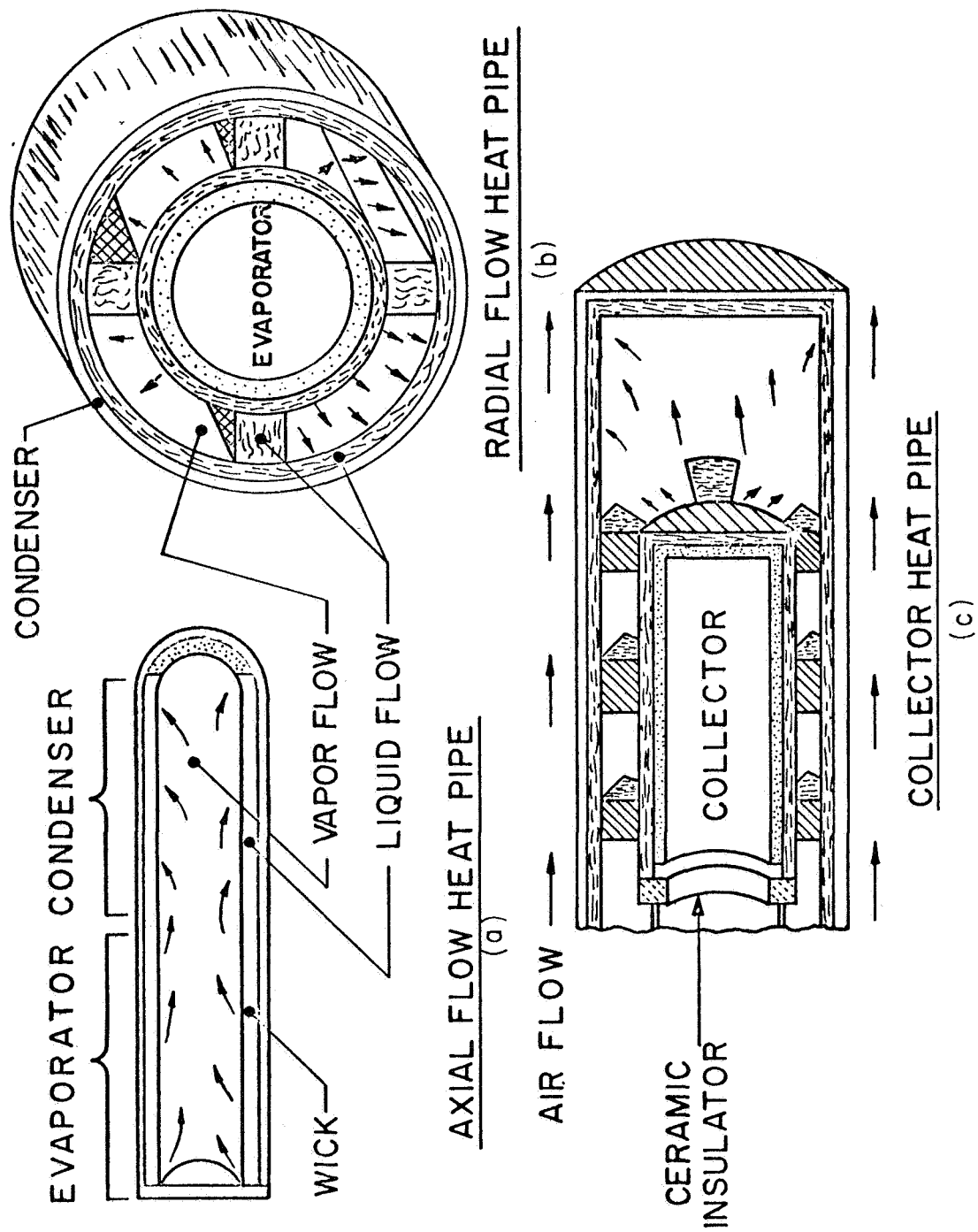


Figure 23 Schematic of dielectric heat pipe for depressed collector operation.

There are several methods to compensate for this effect. Among these are gas displacement, liquid displacement, and preheating. In the gas displacement method (shown in Figure 24a) inert gas at room temperature and atmospheric pressure is introduced above the working fluid. During operation, vapor displaces the inert gas in the condenser area and the inert gas is displaced into the expanding bellows. A similar approach is used in the liquid displacement system (Figure 24b). In this case, the chamber is filled at room temperature with working fluid. As the device begins to operate, vapor will displace the excess liquid from the condenser to the expanding bellows. During shutdown the bellows will force the fluid back into the condenser maintaining the desired pressure upon cooling and, consequently, voltage breakdown strength.. This, however, would result in a rather bulky and stationary device. Another possibility to solve the start-up problem at low pressures would be to preheat the heat pipe before the operation begins.

The dielectric heat pipe employs the technique of introducing dielectric gas into the vapor space (Figure 24c). The dielectric gas can maintain the required dielectric strength at low pressures, which exist below operating temperatures. Thus, the dielectric strength is maintained by gas at low temperatures and by the vapor of the heat pipe fluid at higher temperatures. This is illustrated by the curves of Figure 25, where the breakdown voltage is plotted as a function of temperature for a heat pipe charged with Dowtherm A working fluid. It can be seen that the dielectric strength of the system falls off very rapidly with lower temperatures. However, when a dielectric gas such as SF_6 at 300 mm Hg pressure is introduced, the system can withstand voltages up to 15 kV even at low temperatures.

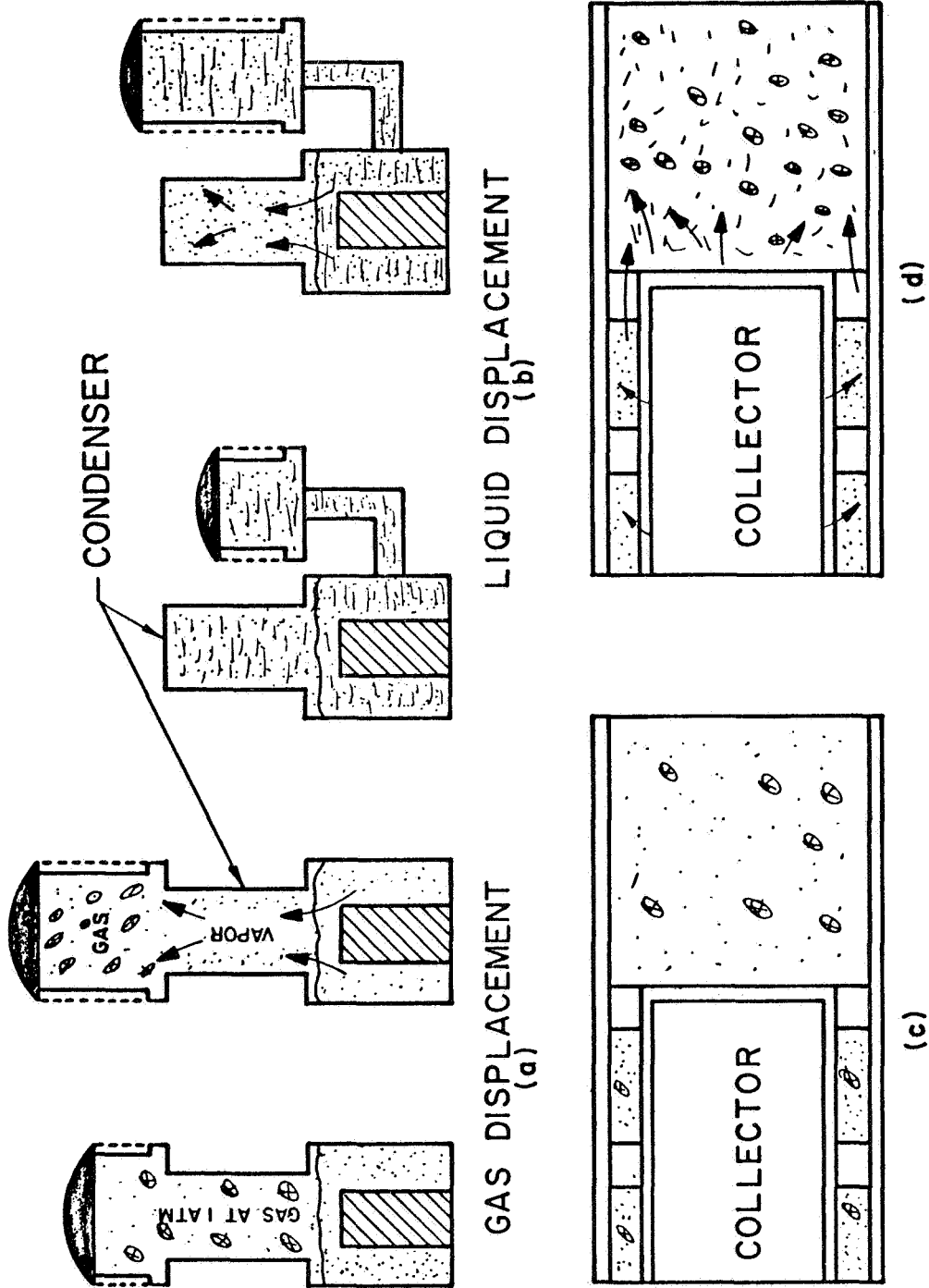


Figure 24 Electric insulation in dielectric heat pipes at low pressures.

BREAKDOWN VOLTAGE IN WORKING FLUID - DIELECTRIC GAS MIXTURE TEST MODEL;
 PARALLEL KOVAR WELD FLANGES 2 3/8" OD, 2" ID SEPARATED BY BRAZED ON
 CERAMIC INSULATOR 2 1/4" OD, 2" ID X .200 THICK

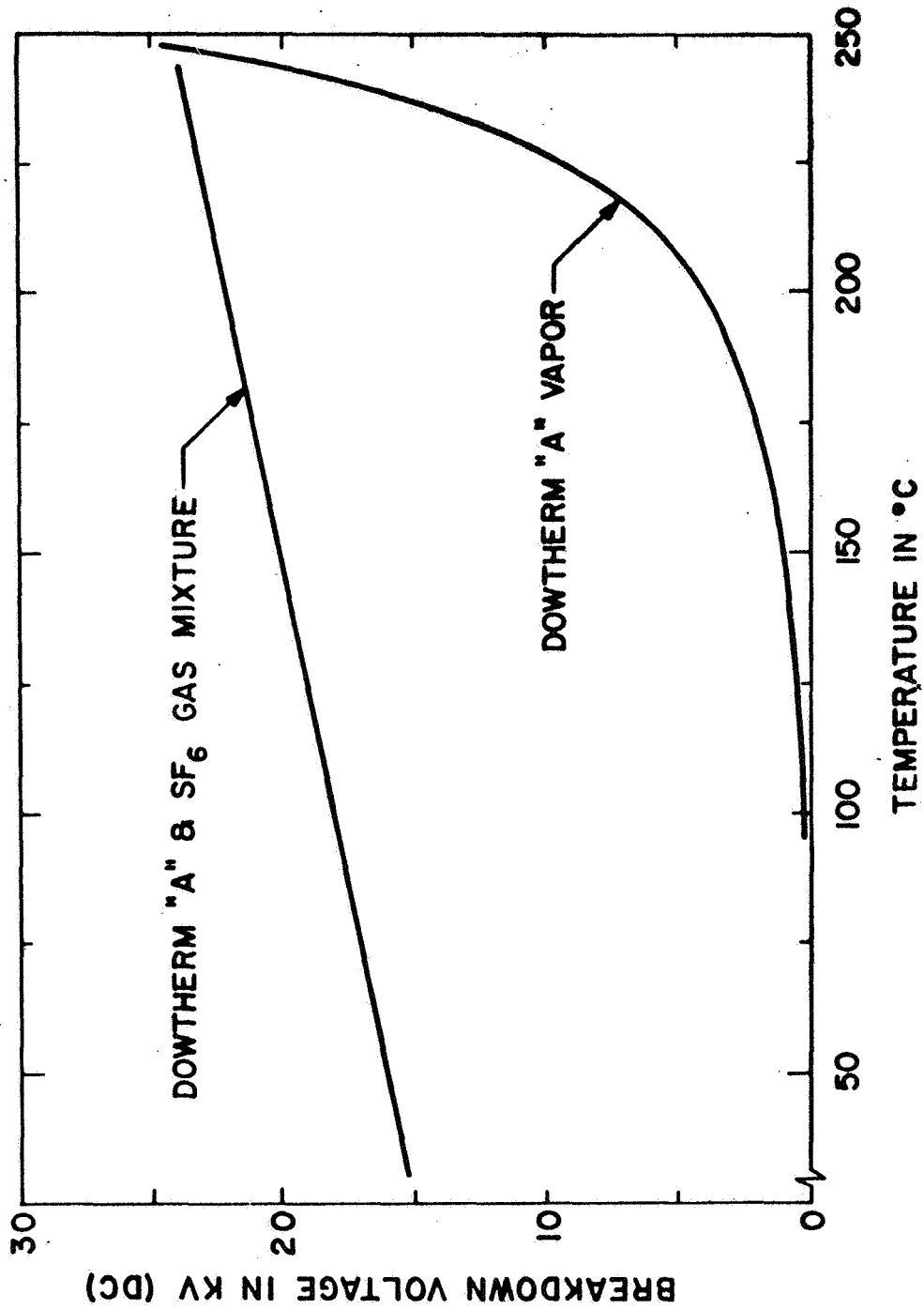


Figure 25 Effect of temperature on breakdown voltage of dielectric heat pipe systems.

The dielectric gas pressure is chosen high enough to provide adequate voltage breakdown insulation for the lower limit of the temperature range of the system.

The principle of this method is illustrated in Figure 24c and 24d. Without any application of heat, the volume inside the heat pipe is filled with a mixture of gas and vapor (Figure 24c). The gas pressure is approximately 300 mm of mercury. At high voltage, the gas has sufficient dielectric strength to prevent breakdown, whereas the vapor alone would not. Hence, the device can be operated at high voltage from a cold start. As heat is applied, the pressure in the heat pipe increases because of boiling of the working fluid and, to a lesser degree, because of thermal expansion of the gas. Both vapor and gas molecules are forced to carry their energy to the cold portion of the device. The heat pipe vapor condenses on the wick surface where the condensate is drawn into the wick and returned toward the heated end by capillary action to replace the fluid being removed by evaporation. The gas molecules, however, being non-condensable, are not absorbed into the wick. They are trying to migrate in all directions according to kinetic theory, but their progress toward the hot end of the heat pipe is impeded and reversed by collision with the large number of molecules in the vapor driven off from the heated sections. Accordingly, as more heat is applied, the gas molecules are crowded into the cold end of the heat pipe. It is seen that the effective condenser area (Figure 24d) becomes larger until, at steady state, the required condenser area to give up the heat to the outside is achieved.

Table IX characterizes typical working fluids and dielectric gases suitable for operation in dielectric heat pipes. Choice of a working fluid and gas demands consideration of several characteristics. The first is compatibility of the fluid with the gas and in combination with heat pipe materials. Operating temperature requirements

Table IX Dielectric heat pipe fluids and gases.

WORKING FLUID	HEAT OF VAPORIZATION CAL/G	SURFACE TENSION DYNES/CM	VISCOSITY CS	BOILING POINT °C	MELTING POINT °C
DC - 200	52.4*	15.9	.65	100	-67
DOWTHERM A	71.3	40.1	3.46	257.7	12
CP-9	67.0	38.0	4.5	297.0	-65
CP-63	68.4	41.0	2.8	296.0	-40
FC-43	16.7	16.0	2.6	173	-50

DIELECTRIC GAS	BOILING POINT	RELATIVE BREAKDOWN	TEMPERATURE STABILITY	TOXICITY
Nitrogen	-195.8	1.0	Very good	Nontoxic
Sulphur Hexafluoride	-63.8	2.3	>150°	Nontoxic
Perfluoropropane	-36.7	2.2	>250°	Nontoxic
Octafluorocyclobutane	-6.0	2.8	>300°	Nontoxic
Perfluorobutane	-2.0	2.8	Unknown	Nontoxic
Hexafluoroethane	-78.0	2.11	>300°	Low

* Estimated value

define the choice of fluid; its atmospheric boiling point should be within $\pm 10\%$ (in degrees) of the desired operating temperature. The choice of heat pipe fluid and gas is further narrowed by requirements for highest possible latent heat of vaporization, highest possible surface tension, and the lowest possible viscosity. The dielectric, or electronegative gas, must be stable at operating temperatures; it must have sufficiently high dielectric strength at design pressure; and its boiling point must be below the lowest heat pipe start-up temperature. Preferably, the gas should also be nontoxic. Typical breakdown voltage curves for dielectric gases at 300 mm Hg pressure are presented in Figure 26 and 27. Figure 27 plots the breakdown voltage as a function of pressure for several mixtures of cooling fluids and SF_6 .

The life performance of dielectric heat pipes has been evaluated in life tests for various heat pipe fluids with and without dielectric gases. These life test data have been compiled in Table X. Dielectric heat pipe operation in excess of 10,000 hours has been achieved so far.

Figure 28 shows a picture of a dielectric heat pipe collector tested with electron beam heating. This heat pipe has a gas reservoir with baffles. It operates with a beam power load of 860 watts on the collector and with 12 kV collector depression. This tester is still being life tested with full operational conditions and random turn-on-and-off cycling.

Figure 29 and Figure 30 show a more compact heat pipe and its assembly parts. The gas reservoir of this dielectric heat pipe is connected to the vapor chamber by an orifice. This dielectric heat pipe collector operates with a thermal power load of 1,000 watts on the collector, and can hold 15 kV collector depression even at room temperature and lower. A modified design of this dielectric

BREAKDOWN VOLTAGE IN DIELECTRIC GASES; APPARATUS,
 ROUND ROBIN ASTM CELL; PRESSURE, 300 MM Hg;
 TEMPERATURE 78° F

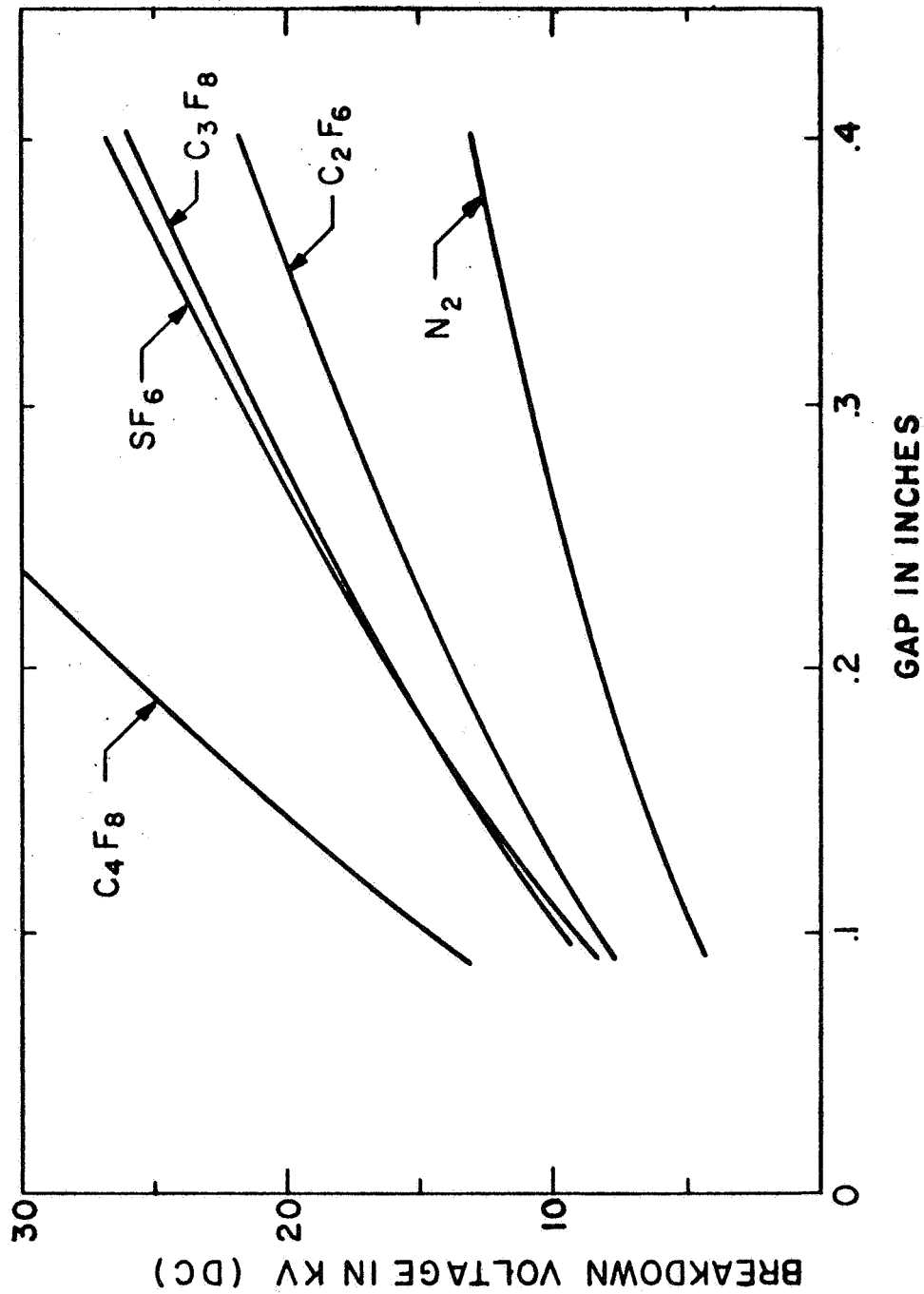


Figure 26 Breakdown voltage for dielectric gases.

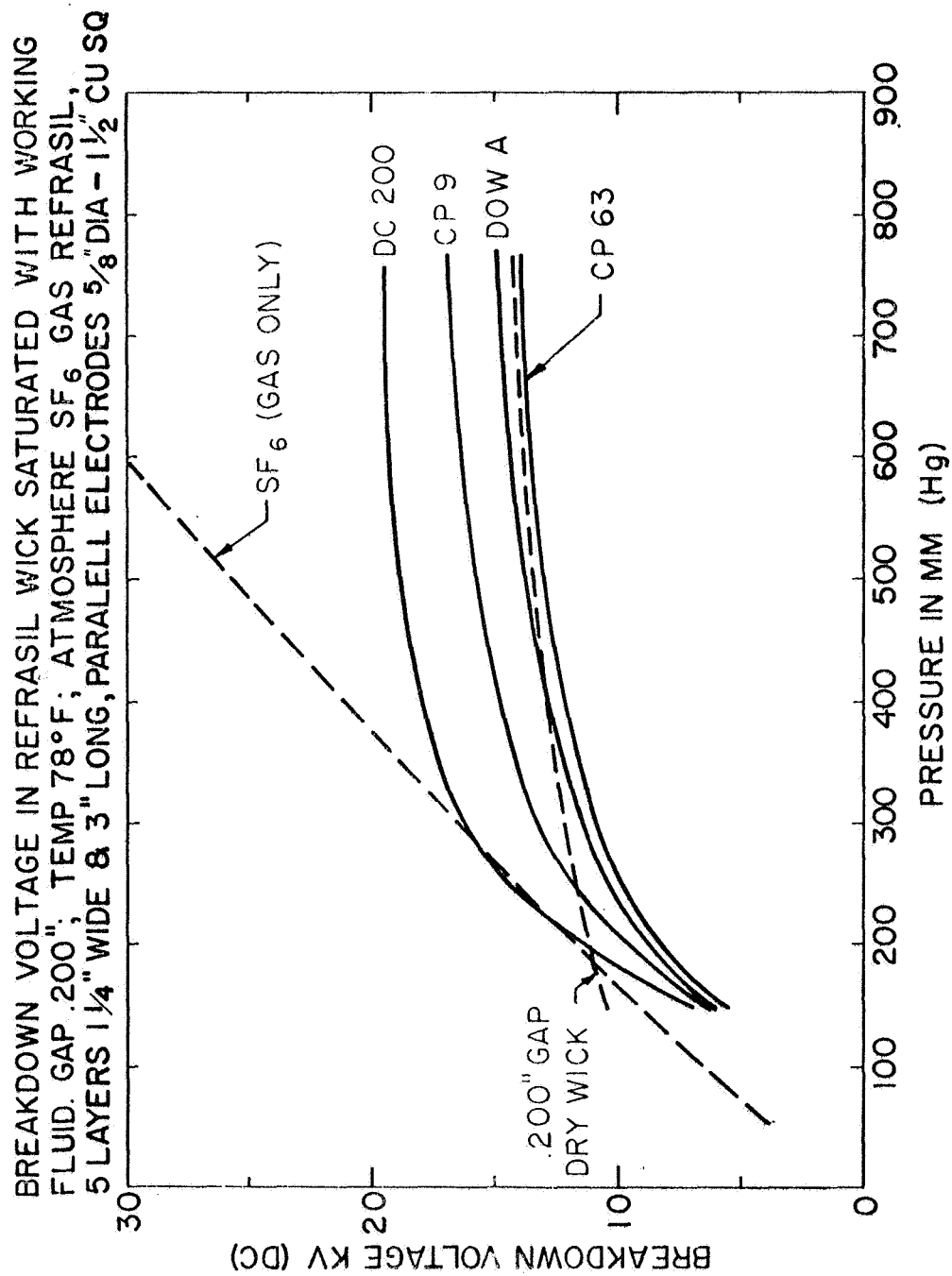


Figure 27 Breakdown voltage for dielectric gas mixtures as a function of pressure.

Table X Life test data with dielectric heat pipes.

HP NO.	TYPE	HP MATERIAL	WICK	FLUID	GAS RESERVOIR	DEPRESSION	HOURS	STATUS
HP-1	Axial	Cu	SS	DC-200	NO	NONE	10163	Life Test
HP-8	Radial	Cu	Refrasil	DOW-A	NO	6 kV	1750	T.A.
HP-10	Axial	Cu	Refrasil	DOW-A	NO	NONE	6207	Life Test
HP-11	Axial	Cu	Refrasil	CP-9	NO	NONE	1422	Life Test
HP-12	Radial	Cu	Refrasil	DOW-A	YES	12 kV	1500	T.A.
HP-13	Radial	Cu	Cu and Refrasil	DOW-A	YES	12 kV	850	Life Test
T.A. = Termination of Life Test for Analysis								

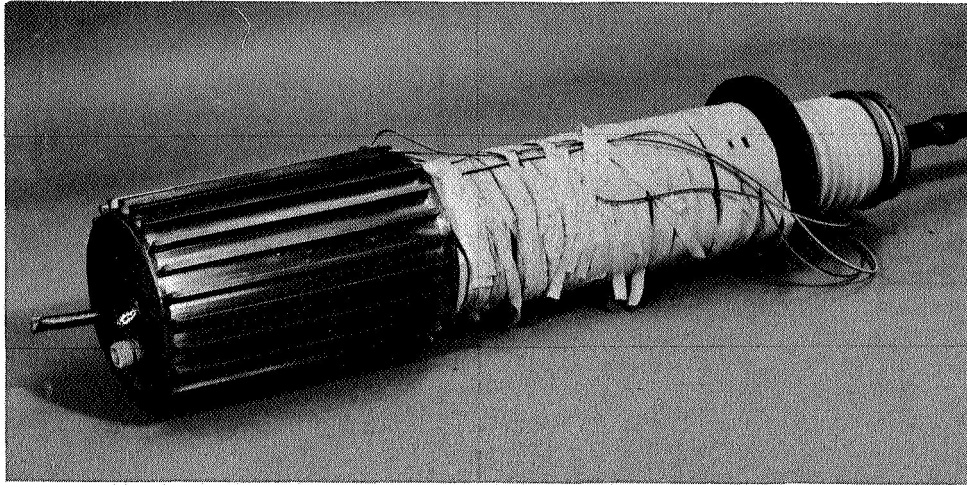


Figure 28 Dielectric heat pipe with gas reservoir.

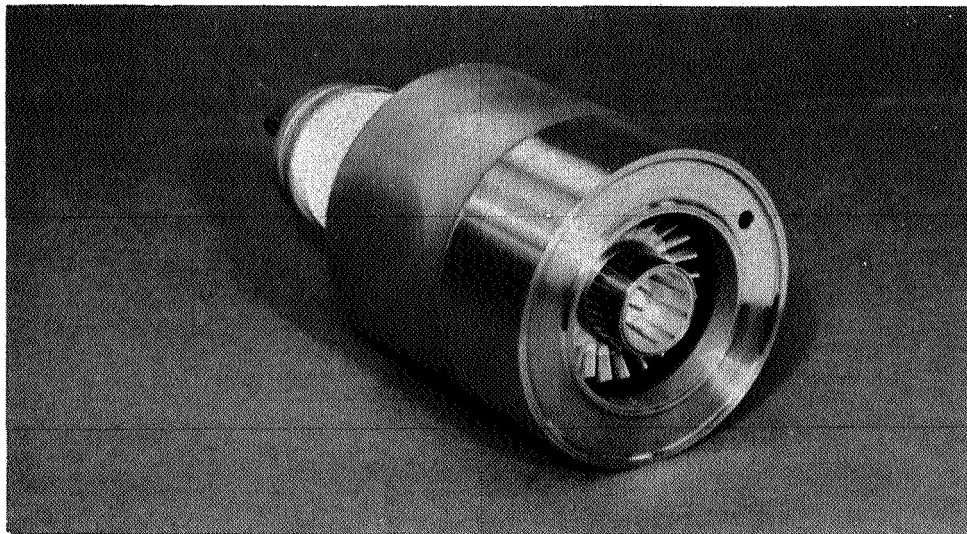


Figure 29 Compact dielectric heat pipe with gas reservoir.

heat pipe collector will operate with a thermal load of 1500 watts (14 watts/cm^2) and a collector voltage depression of 20 kV within the same envelope.

The advantages of collectors using dielectric heat pipes are therefore:

1. The collector can operate at higher thermal power densities.
2. The collector insulator is not exposed to the cooling air and failures due to dirt, moisture or high altitudes are eliminated.
3. The configuration provides complete RF shielding.

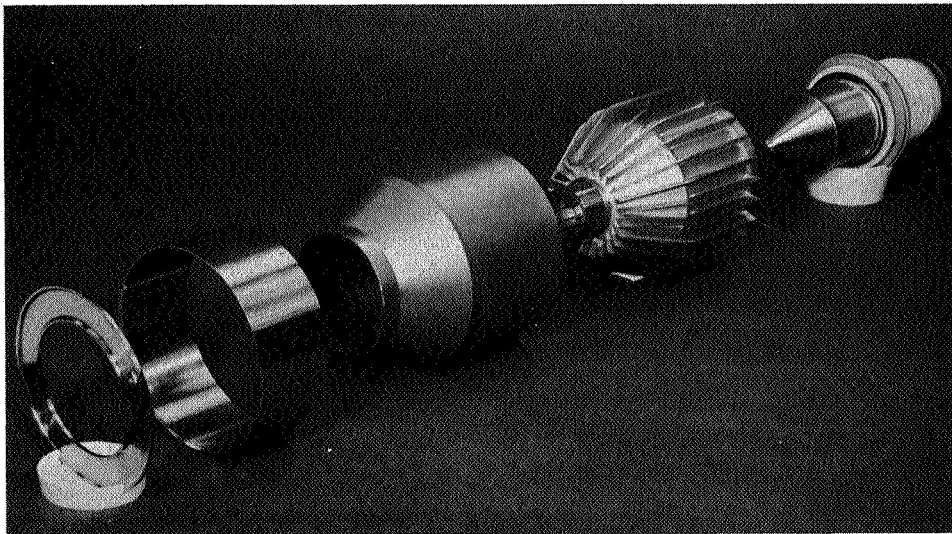


Figure 30 Assembly parts of compact dielectric heat pipe with gas reservoir.

2. One-Way Heat Pipe

The one-way heat pipe is a device which permits heat flow in one direction but acts as a thermal insulator when heat is applied from the opposite direction.

Such one-way heat pipes will provide good thermal insulation for the spacecraft when the radiator is exposed to the sun and thus protect the spacecraft from being heated by the sun. However when the radiator is not exposed to the sun, the one-way heat pipe will provide good heat transfer from the heat source of the spacecraft (tube) to the radiator. Thus the one-way heat pipe acts as an automatic thermal switch for the radiators. This permits to utilize a larger number of radiators which may temporarily be exposed to the sun.

Several such one-way heat pipes have been built and were operated successfully.

IV. DESIGN APPROACH AND ~~TRADE-OFF~~ CONSIDERATIONS

A. SUMMARY OF MAJOR SPECIFICATIONS

The following requirements have been specified for the tube design analysis:

Tube Application: Output stage traveling-wave tube amplifier for satellite television transmitter.

Tube design objectives in order of importance:

1. Expected tube life: 20,000 hours minimum.
2. Maximum overall efficiency, and driver stage efficiency.
3. Minimum weight, including focusing, driver stages and filters, if any.

The factor relating weight and efficiency is given to be

100 lbs/kW .

The design of five traveling-wave tube amplifiers with the specifications given in Table XI is required.

The amplitude modulated tubes (I and II) are required to provide a linear dynamic range of

20 dB minimum

with a maximum deviation from linearity Δg_{\max} of $\Delta g_{\max} = \pm .5$ dB at 3 dB below saturation.

Their maximum permissible deviation from phase linearity $\Delta \phi_{\max}$ has been specified to:

$\Delta \phi (\omega)_{\max} = \pm 1.2^\circ$ over the bandwidth.

Table XI Design requirements for traveling-wave tube amplifiers.

TUBE	I	II	III	IV	V
Frequency	850 MHz	2 GHz	2 GHz	8 GHz	11 GHz
Modulation	AM Vestigial Side- band only	AM Vestigial Side- band only	FM	FM	FM
Peak Synchronism Power	7.5 kW	5.0 kW			
Peak Picture Power	3.5 kW CW	2.3 kW CW			
Average Picture Power	2.6 - 3.0 kW	1.75 - 2.0 kW	5 kW CW	5 kW CW	5 kW CW
Minimum Picture Power	1.3 kW	.9 kW			
Sound Power	.75 kW	.5 kW			
Total Gain	40 dB minimum	40 dB minimum	40 dB min.	40 dB min.	40 dB min.
Bandwidth (3 dB points)	6 MHz	6 MHz	30 MHz	30 MHz	30 MHz
Thermal Capability	2.05 - 3.25 kW	1.4 kW - 2.8 kW	5 kW CW	5 kW CW	5 kW CW
Cooling Method	Radiation into space				

Their signal to noise ratio S/N over the AM bandwidth is required to

$$\begin{aligned} S/N &= 42 \text{ dB minimum} \\ &= 55 \text{ dB desirable.} \end{aligned}$$

The FM tubes (III, IV and V) require their second order phase deviation not to exceed

$$\begin{aligned} \frac{d^2 \phi(\omega)}{d\omega^2} &= - .05^\circ / (\text{MHz})^2 \text{ maximum} \\ &= - .015^\circ / (\text{MHz})^2 \text{ desired} \end{aligned}$$

and a signal to noise ratio of

$$\begin{aligned} S/N &= 32 \text{ dB minimum} \\ &= 45 \text{ dB desirable.} \end{aligned}$$

The tubes have to withstand the following vibration conditions:

FREQUENCY (SINUSOIDAL)	PEAK AMPLITUDE	RANDOM DENSITY	RMS ACC.
20 - 400 (cps)	5.0 g	.082 g ² /cps	5.4
400 - 3000 (cps)	15.0 g	.15 g ² /cps	17.9

as well as a shock of

$$\begin{aligned} &30 \text{ g minimum with} \\ &8 \text{ msec duration.} \end{aligned}$$

The satellite's altitude (synchronous orbit) is given to 19,300 N.M. in the equatorial plane. The gravitational environment is less than

$$5 \times 10^{-7} \text{ g}$$

and the background pressure

less than 10^{-12} torr.

It may be assumed for the purposes of this study that heat may be rejected (radiated) over a solid angle of 2π into a background at a very low absolute temperature.

Relative orientation of satellite components:

Antenna: toward earth

Solar array: toward sun

The mode of operation in space has been specified as

22.5 hours minimum per 24 hours

24 hours maximum per 24 hours

with a maximum required restarting period of

once in 24 hours within less than five minutes following a command signal.

Number of restarts in life time

180 minimum.

Some of these specifications have to be considered preliminary and are subject to modifications as a result of more detailed system design analysis.

In the following sections the design approach and design trade-off considerations are discussed for the design requirements given above. In these trade-off considerations the choice of the slow-wave structure, the high efficiency design, the choice of the focusing configurations

and the choice of the cooling method are discussed with regard to long life and reliability, to maximum overall efficiency and minimum overall weight.

B. CHOICE OF THE SLOW-WAVE STRUCTURE

Two types of circuit structures were considered for traveling-wave tubes: the helix type circuit and the coupled cavity structure. The helix circuit has considerable bandwidth capability, and is comparatively small in size and weight. However, its power handling capability is limited due to its dielectric support structure and, for a conventional helix circuit, due to a tendency for backward-wave oscillations at high operating voltages. Although advancements in the power handling of the helix circuit are being made, the power requirements of the design tubes are still beyond the present state of the art of these tubes. Therefore the coupled cavity circuit is chosen as the slow wave structure. This circuit can safely handle at least an order of magnitude higher power levels than the helix circuit due to its massive copper structure. The required power levels are well within the capability of this circuit. The structure is also very rugged. The diameter and weight of a coupled cavity tube is comparatively large, however, especially at low frequencies. The coupled cavity structure is a bandpass filter type circuit, and unlike the helix circuit, it can be designed for a precisely chosen bandwidth. Therefore its bandwidth can be decreased to the relatively small frequency ranges required for the tube designs. This offer the advantage of achieving a very high interaction impedance, since the interaction impedance of this circuit is inversely proportional to the bandwidth. A high interaction impedance is desirable for high efficiency, and it also results in a very high gain per unit length, so that the tube can be rather short. The coupled cavity has a tendency to oscillate at its cut-off frequencies unless precautionary measures (such as tuned "loss buttons") are taken. Very narrow band coupled cavity tubes however are generally more stable. The coupled cavity structure also lends itself

to the design of a light-weight high quality periodic permanent focusing configuration, which constitutes an integral part of the circuit. This circuit is also uniquely suitable for advanced efficiency enhancement schemes such as the multiple voltage jump taper.

Nevertheless, the helix circuit is not ruled out since a dual tube approach is conceivable with a low power, light weight helix tube as a driver and a high power coupled cavity output tube. A new concept is proposed for the AM tubes (tubes I and II) which requires a dual tube design for the picture signal, comprised of a helix tube preamplifier and a coupled cavity tube modulator, as well as a helix tube amplifier for the FM audio signal. This approach provides very high overall efficiency (in the range of 60 to 70%) for amplitude modulated signals.

The dual tube approach with a helix driver tube offers the possibility of an overall weight reduction, when compared to a high gain single coupled cavity tube. However, calculations for these tubes have shown that such overall weight reductions can only be achieved for amplifiers with frequencies lower than 2 GHz. Therefore the dual tube approach is not used for the FM tubes (tubes III, IV and V), since it offers no advantages for these tube designs.

The diameter of coupled cavity circuits can be substantially reduced by dielectric loading of the cavity, resulting in a major weight reduction of the circuit. Extensive cold tests with dielectric loading have shown that such diameter reductions can be achieved without any sacrifices of the interaction impedance. However, the dielectric loading of the coupled cavity circuit introduces dielectric losses in addition to the ohmic losses. At low frequencies (up to 2 GHz) both

of these losses are extremely small and their effect on the efficiency is negligible. These losses increase with frequency. The ohmic loss increase is proportional to the square root of the frequency, but the dielectric losses increase in proportion with the frequency, as illustrated in Figure 31 for alumina loading. At high frequencies the diameter and weight reduction due to the dielectric loading is accompanied by a degradation of the efficiency due to the increased losses. Only the low frequency tubes (850 MHz and 2 GHz) are therefore designed with dielectric loading. The dielectric loading becomes more effective with a larger value of the dielectric constant. This is illustrated in Figure 32 with the estimated weight reduction as a function of the dielectric constant. Alumina has therefore been chosen as the dielectric loading material. This material is frequently used in vacuum tubes; it has a large value of the dielectric constant ($\epsilon = 9$) and its losses are very low.

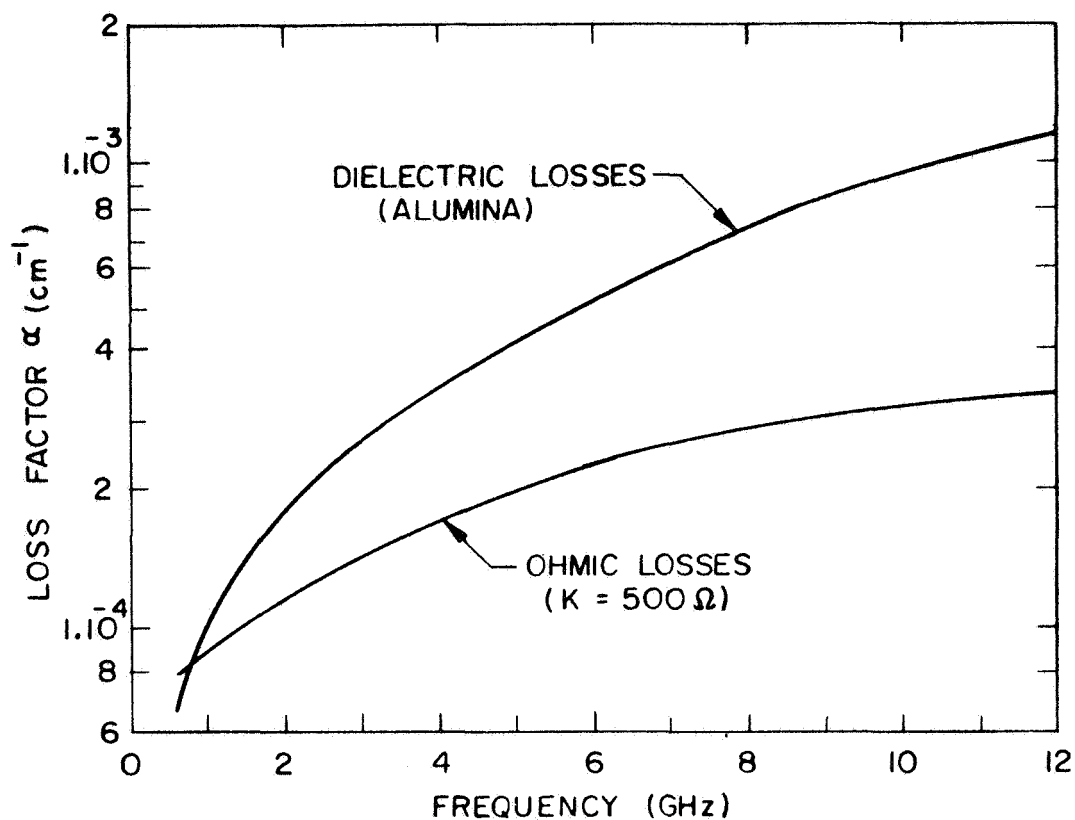


Figure 31 Dielectric and ohmic losses in dielectrically loaded coupled cavity circuit.

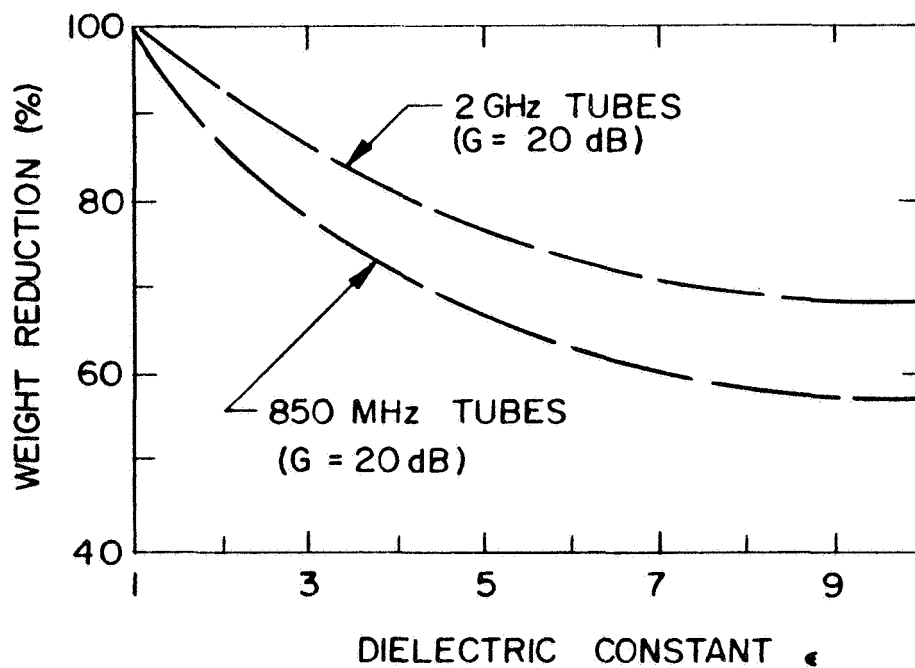


Figure 32 Estimated weight reduction of coupled cavity tubes by dielectric loading.

C. HIGH EFFICIENCY DESIGN WITH VELOCITY RESYNCHRONIZATION

Generally, there are three steps in the process of energy conversion from the dc energy of the power supply to the RF output energy of a traveling-wave tube:

1. The acceleration of the electron beam to a specified level of kinetic energy. This is primarily an electron optical problem in designing the electron gun and the beam focusing and is generally well in hand.
2. The basic energy conversion process of the traveling-wave tube. In this step the RF signal to be amplified produces a traveling electromagnetic wave in the slow wave structure which interacts with the electron beam. The electron beam becomes modulated and a part of its kinetic energy is converted into RF energy of the signal wave.
3. The kinetic energy of the spent beam is reduced by depressing the collector potential below that of the slow wave structure. The electrons are decelerated and the beam is collected at a lower kinetic energy. The resultant electrical energy recovery provides additional efficiency improvement.

The efficiency of conventional traveling-wave tubes is found to be limited to approximately 45%, assuming a conventional single stage collector is used, and provided that all design parameters are optimized. In this case, the overall efficiency was found to be practically independent of the (basic) conversion efficiency. A higher basic efficiency will therefore permit a small efficiency improvement with collector depression than a lower basic efficiency.

Previous studies have shown that the conversion efficiency of traveling-wave tubes can be substantially increased by using velocity resynchronization between the modulated beam and the circuit wave at large signal levels. This method will therefore be used for the tube designs. In previous investigations¹ it was found that the velocity taper method (of the circuit) and the voltage jump method (of the beam) can be combined into one tube, resulting in a higher efficiency than is possible with either a voltage jump or a velocity taper alone. This scheme is illustrated in the velocity profiles of Figure 33. This circuit uses a velocity taper with a velocity reduction v_1 to

$$v_1 = .85 v_o$$

and a voltage jump potential V_j of

$$V_j = 1.6 V_o.$$

This combination resulted in a conversion efficiency of 53% without depression and 62% with collector depression. It had been intended to use this efficiency design approach for the tubes. However, it was found that this approach was not as effective for very narrow bandwidth circuits, such as some of the tubes considered here. The high frequency tubes at 8 GHz and 11 GHz (tubes IV and V) yield a rather high interaction impedance and a very high efficiency improvement with a voltage jump technique, but no further efficiency improvement due to the velocity taper method. Detailed computer evaluations showed, however, that efficiencies of 70% to 75% can be achieved with these methods for all tubes at saturation. Optimization of the design would have probably resulted in even higher efficiencies, but theoretical studies with the large signal computer program have provided a new and superior efficiency enhancement scheme referred to as multivoltage jump taper, which is used for the efficiency enhancement design for

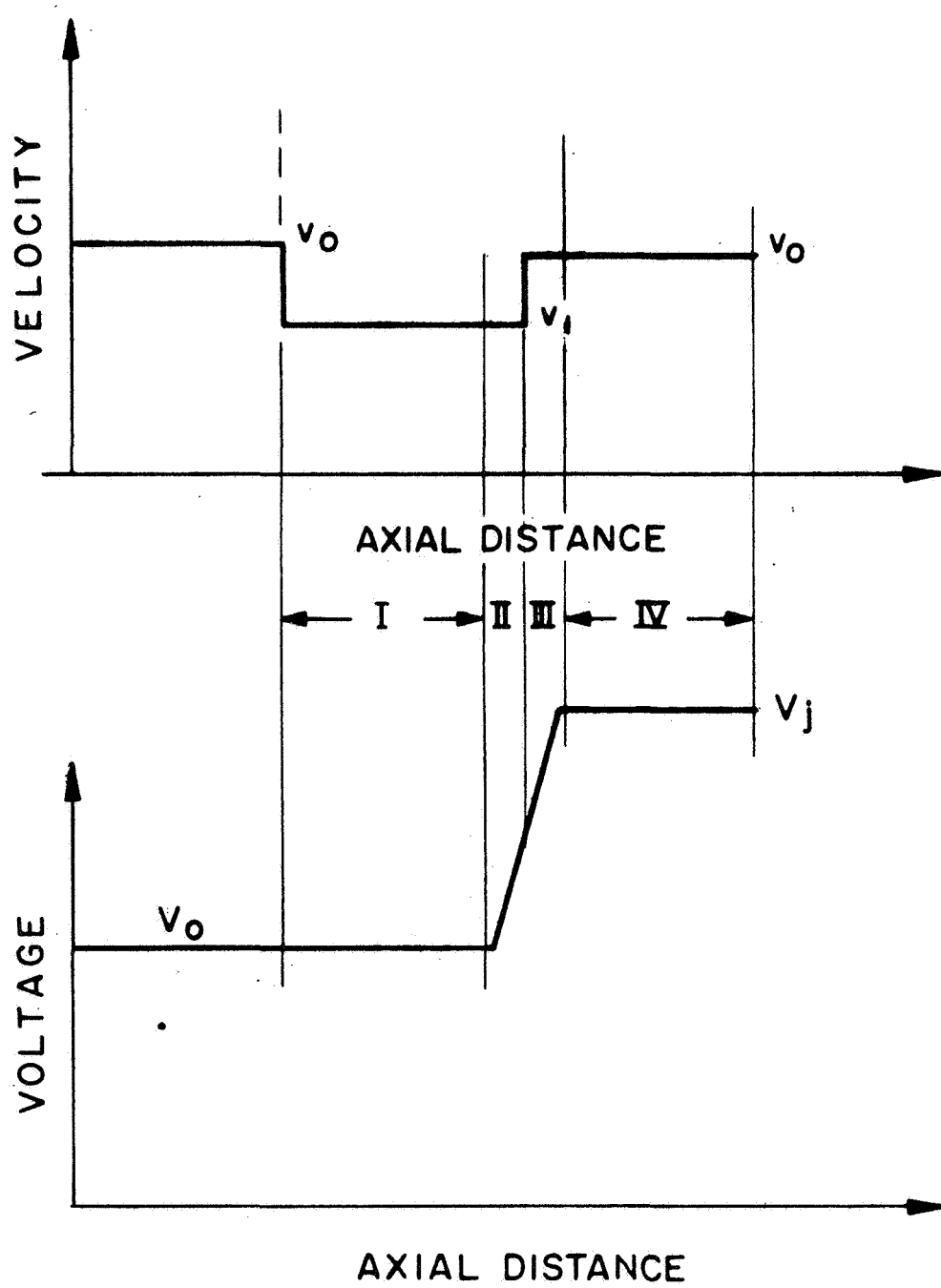


Figure 33 Velocity and voltage profiles for combined velocity taper and voltage jump circuit.

the tubes. This method is uniquely suitable for the coupled cavity circuit structure. It uses a series of voltage jump cavities, such that a gradual voltage increase is applied in the efficiency enhancement section as illustrated in Figure 34 and 35. This scheme is therefore the equivalent to a multi step velocity taper. In this scheme, however, the average electron beam velocity is gradually reaccelerated to maintain synchronism between circuit wave and beam modulation. The interaction impedance is not reduced as in a velocity taper (for coupled cavity circuits) and this resynchronization method is therefore more effective.

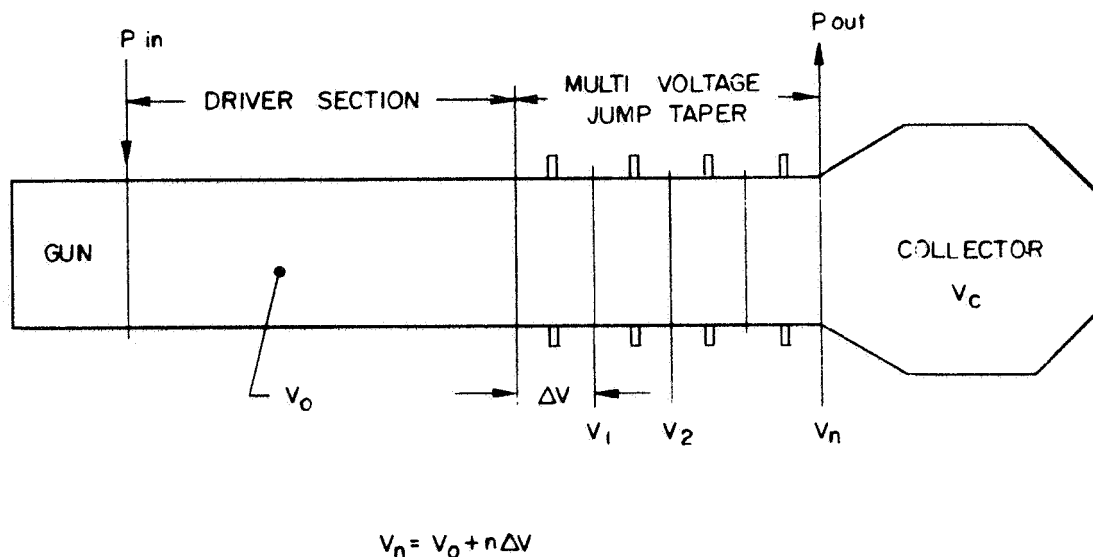


Figure 34 Schematic of multivoltage jump taper tube.

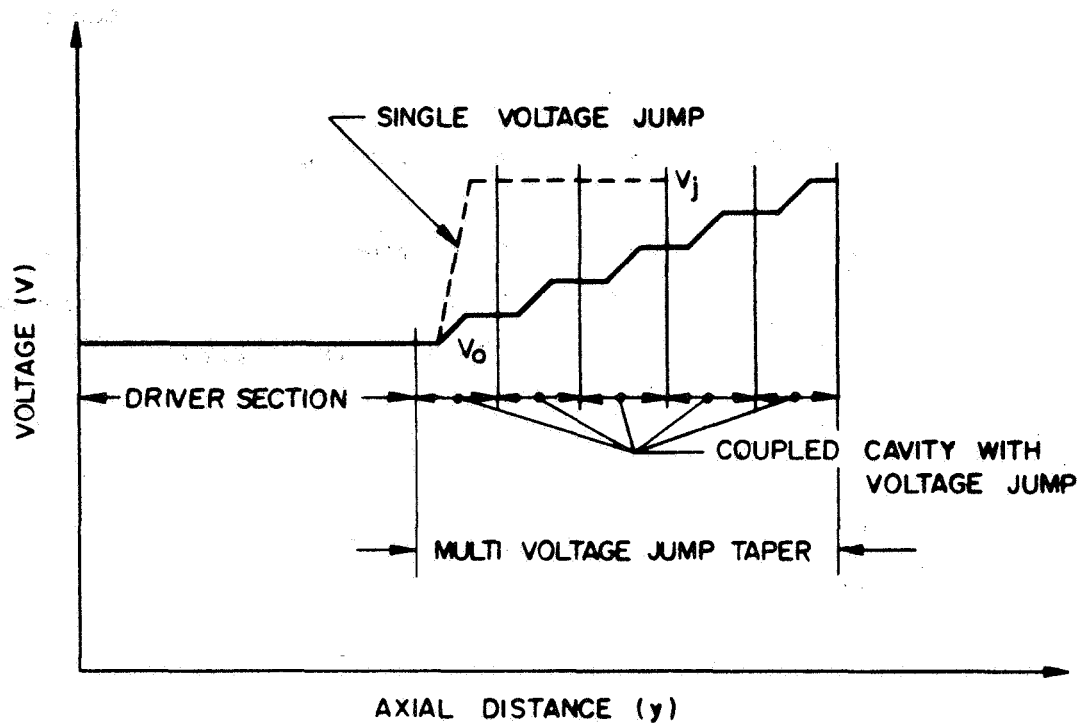


Figure 35 Voltage profile for multi-voltage jump taper tube.

Moreover, the increase of the beam potential with this method reduces the degrading effects (velocity spread) of the beam space charge, and better beam bunching can be maintained. This manifests itself generally in higher values of the fundamental beam modulation current.

The tube designs with this scheme resulted in higher efficiencies than was possible with the previously considered methods, assuming the same collector configuration. The overall efficiency is then generally approximately 3 to 6 percentage points higher, or in the range of 75% to 80% for all tubes.

In comparing this new method with the previously considered schemes, several important advantages become apparent:

1. A higher conversion and overall efficiency can be achieved.
2. The beam voltage and therefore the beam power is considerably increased in the multivoltage jump section. The design approach is flexible with respect to the choice of the voltage increase. A total voltage increase by approximately a factor of 2 was chosen, or

$$V_j \approx 2 V_o .$$

This substantial beam voltage and power increase has several significant advantages:

- a. The beam power in the driver section and gun can be lowered. A lower voltage or a lower current (perveance) gun design can therefore be used, resulting in a more reliable gun with longer life capability. For grid modulated tubes (tubes I and II) the grid power drive can be lowered.
 - b. The lower beam power makes the focusing requirements of the driver section easier, but more importantly, the focusing of the multivoltage jump efficiency enhancement section can be much better due to the substantial voltage increases with resultant reduction of the space charge densities. For solenoid focused tubes (tubes IV and V) this will provide significant solenoid power reductions.
3. Since the voltage increase is applied gradually over a number of coupled cavities, the voltage gradient in one cavity can be lower than with a single voltage jump circuit, where the total voltage

increase is applied on one cavity only. Tubes of this design can therefore be considered more reliable, especially at frequencies in the X and Ku-bands, where the voltage gradients are generally high due to the smaller tube dimensions.

The basic design considerations (insulation and choke design) for multivoltage jump cavities are the same as for a single voltage jump cavity circuit.

4. The multivoltage jump circuit has considerable flexibility with the voltage adjustments and therefore it is likely that optimum efficiency performance can be achieved. This is not the case with the velocity step taper or the single voltage jump method, where the section lengths are extremely critical for optimum efficiency enhancement, especially when narrow bandwidth circuits with high interaction impedances are used. It may therefore be rather difficult in this case to attain the predicted efficiency with a practical circuit, since the section lengths are restricted to multiples of one cavity period.

D. MULTISTAGE COLLECTOR DEPRESSION

1. Conventional Depressed Collector Operation

The efficiency of conventional traveling-wave tubes can be significantly improved by collector depression. The collector is electrically insulated from the circuit or body of the traveling-wave tube and is operated at a positive potential less than that of the circuit or body. Thus, the spent beam electrons are decelerated and the kinetic energy of the beam is reduced at the collector. This results in a power saving. This process is limited by the inherent velocity modulation of the spent beam. A part of the kinetic beam energy, which serves as the energy source for the

traveling-wave tube, is converted into RF power in the interaction region. As a result, the spent electron beam will have a velocity spread and its average velocity will be reduced. When the collector potential is depressed to a greater degree than the corresponding velocity of the slowest spent beam electrons, these electrons have insufficient energy to penetrate into the collector. Therefore, their flow will be reversed. Backstreaming current is then initiated. Such backstreaming is generally undesirable. Not only will it defeat the power saving purpose of collector depression, but it may also produce an excessive thermal load on the circuit. It may also interfere with the RF performance and cause instabilities. The maximum useful collector depression is then limited by the velocity spread of the spent beam.

There are effects other than the velocity spread of the spent beam which can also cause undesirable backstreaming from the collector. It can be caused by space charge blocking of the depressed beam, or by magnetic mirror effects.^{6,7,8} However, by the far the most important source are secondaries produced on the collector surfaces. Their number is rather large, since the secondary emission more than equals the number of the electrons of the striking primary beam. Thus, the stricken collector surfaces resemble a hot cathode emitter. With a depressed collector, the electrostatic deceleration fields serve as an acceleration field for the secondaries which may be pulled out of the collector in great numbers by these fields and thus render the collector depression ineffective.

Conventional depressed collectors can be designed such that these effects are small compared to the velocity spread effects. Space charge blocking and magnetic mirror effects can be kept small by minimizing the potential depression of the beam space charge in the collector region and by magnetically shielding the collector

region so that the rotational beam energy is small in this region. Backstreaming of secondaries can be avoided if a collector is designed such that the beam stricken collector surfaces are removed from the collector acceleration (deceleration) fields.

The design analysis of a depressed collector, where these effects are minimized requires therefore to determine the collector trajectories of the spent beam.

2. Double Stage Collector Depression for Traveling-Wave Tubes with Velocity Resynchronization

The velocity modulation (velocity spread) of the spent beam is relatively small in conventional traveling-wave tubes and a significant reduction of the spent beam kinetic energy can therefore be achieved with conventional depressed collectors. However for tubes which are designed for high electronic (basic) efficiency the velocity spread of the spent beam becomes large and hence the efficiency improvement with a conventional depressed collector is then small.

This is especially true for traveling-wave tubes with velocity resynchronization (voltage jump or velocity taper), which achieve very high electronic (basic) efficiencies. The velocity modulation of the spent beam in such tubes becomes so large that collector depression with a conventional collector is no longer possible without backstreaming of beam current into the circuit section.¹

In such tubes the average kinetic energy of the spent beam is substantially reduced, while the energy spread of the spent is also very large. The velocity of some beam electrons will therefore be close to zero as illustrated in Figure 2 and 36.

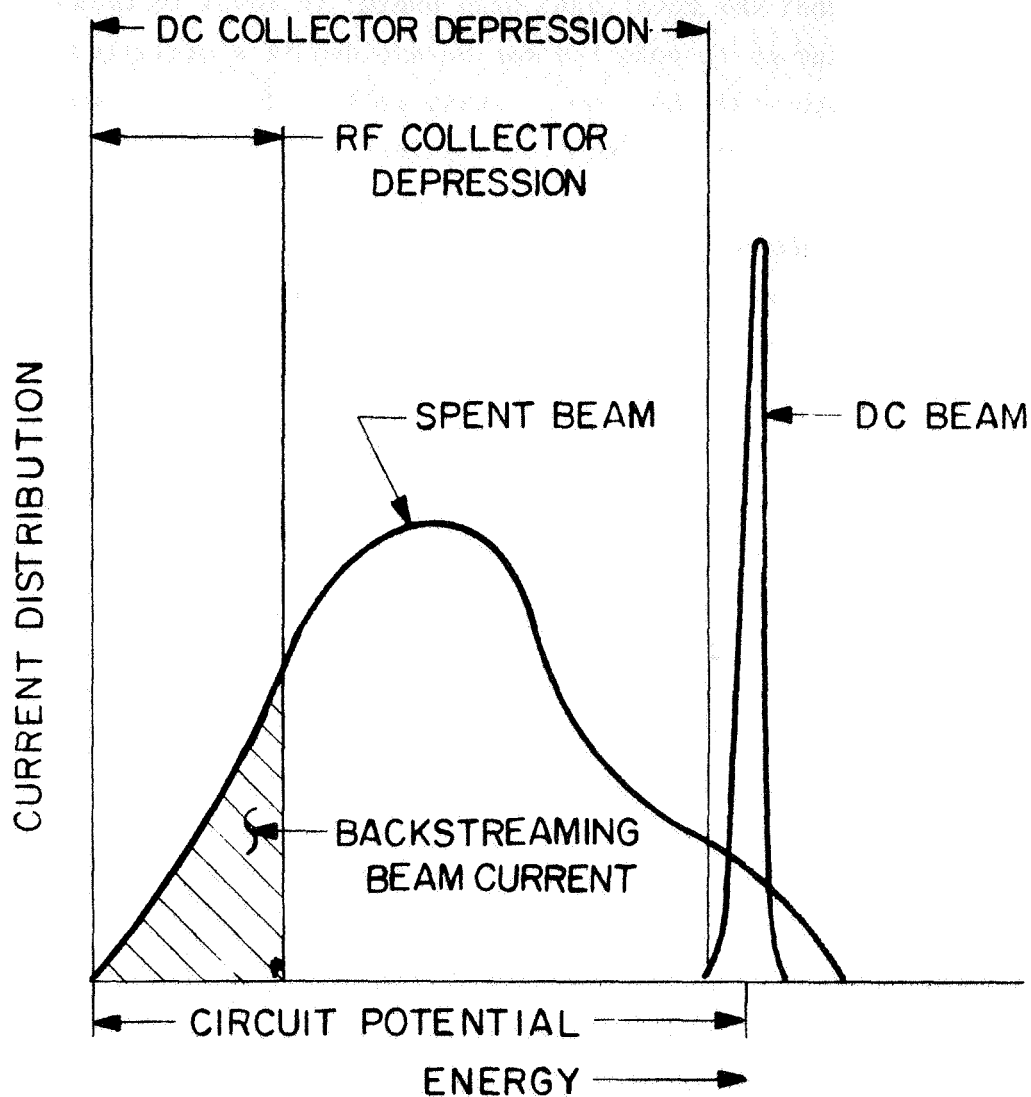


Figure 36 Spent beam energy distribution and collector depression for high efficiency tubes.

Multistage collector operation, however, will provide additional efficiency improvements for such tubes. The simplest version of a multistage collector is a double stage collector where the beam is collected in two stages at two different potentials. This requires a sorting of the spent beam in two velocity groups so that the faster beam electrons are depressed further in the second collector.

One simple double stage collector configuration is shown schematically in Figure 3. This design consists of a coaxial collector assembly, where the velocity separation is intended to occur in radial direction.

Radial velocity sorting of the spent beam is attractive because the spent beam is already in a radially presorted condition at the output due to the interaction mechanism of the traveling-wave tube. At large signal levels a radial velocity distribution is observed in the beam cross section such that the axial electron velocity becomes slower with increased radius.⁹ This is primarily caused by the circuit wave acting upon electrons with larger radii.

The spent beam is also exposed to strong radial defocusing fields from the circuit wave at the output coupler. This causes radial deflections of the beam trajectories,¹⁰ which are larger for the slower electrons toward the outer boundary of the beam. Since the

The spent beam is also exposed to strong radial defocusing fields which from the circuit wave at the output coupler. This causes radial deflections of the beam trajectories,¹⁰ which are larger for the slower electrons toward the outer boundary of the beam. Since the magnetic focusing field is generally terminated near the output coupler, the spent beam will expand such that the radial velocity sorting of the spent beam is increased. The electron trajectories are also exposed to the radial deflection forces of the beam space charge and of the electrostatic collector deceleration region, resulting in enhanced radial velocity sorting.

The slower electron group is deflected radially outward more than the faster group, so that it will be collected at the outer (first) collector at a higher potential. The faster electrons are deflected less and remain in the inner core of the beam. They can penetrate into the smaller second collector, which is more depressed.

Double stage collectors for velocity resynchronization tubes offer the advantage of being designed with the potential of one collector stage undepressed (or grounded). The design, therefore, does not differ from that of a single stage collector (See Figure 3). In concept it has all the advantages of a double stage collector, since a significant part of the spent beam is collected at the undepressed collector stage.

Efficiency improvements of about 25% (factor 1.25) compared to the grounded collector operation have been typical for velocity resynchronization tubes with double stage collectors.

3. Multistage Collector Depression

For traveling-wave tubes with very high electronic (basic) efficiency and thus with a very large velocity spread of the spent beam multistage collector depression becomes more effective.

The spent beam is separated into a number of velocity groups, and each of these velocity groups of the beam is individually decelerated by a maximum possible amount and collected at its collector stage. The faster part of the beam current is therefore more decelerated, when it is collected, than the slower part of the spent beam. This makes it possible to achieve additional efficiency improvements with an increased number of collector stages.

It is a difficult task, however, to accomplish an effective separation of the spent beam electrons into a number of energy groups for multistage collector depression. This is primarily because the velocity sorting mechanism being used is subject to deficiencies leading to errors of the velocity sorting. It is possible to define such errors

in terms of a sorting "sharpness" such that the separation of two energy groups is accomplished over a finite kinetic energy range dV_k rather than at a discrete energy level V_k . If the "sorting sharpness" is expressed by

$$S_k = \frac{dV_k}{\Delta V_k}$$

where ΔV_k = energy range of velocity group k, one can conclude that the sorting sharpness S should be small in order for the velocity sorting of collector stage k to be effective.

Since the individual energy ranges ΔV_k of the velocity groups become smaller with a larger number of collector stages, the sorting sharpness will deteriorate. Therefore, there is a practical limit to the number of useful collector stages and to the associated efficiency improvements due to velocity sorting deficiencies.

It is for this reason that attempts to develop multistage collectors for conventional traveling-wave tubes with more than two stages have not been very successful in the past. For traveling-wave tubes with velocity resynchronization however the velocity spread of the spent beam is significantly larger than for conventional tubes (Figure 2) and the useful number of collector stages should be higher, assuming the same sorting sharpness as for conventional tubes. It should therefore be possible to design a three-stage collector for such tubes with the same sorting techniques as the two stage collectors of conventional tubes.

The state of the art for spent beam velocity sorting methods has not yet been advanced. If improved velocity sorting schemes can be developed, it should be possible to design multistage collectors with more than three useful collector stages for advanced efficiency tubes.

In addition to the problems of an effective velocity sorting scheme, the design of multistage collectors has also been concerned with other problems and limitations. These are backstreaming secondary electrons, residual space charge potential energy, and residual rotational energy.

Of these, the problem of backstreaming secondaries presents by far the most severe limitation to the design of multistage collectors.

A large number of secondaries is produced on the collector surfaces by the impinging primary electron beam. The secondary emission coefficient is in the order of one for most metals, and, therefore, the collector surfaces resemble the hot emitter surfaces of a cathode. These secondaries can easily be accelerated and then be collected at higher potentials, thus degrading the efficiency improvement of a depressed collector. Secondary emission can be somewhat reduced by the use of collector surface materials with a smaller secondary emission coefficient. Carbon and titanium have been used in the past with moderate success. Carbon is a poor thermal and electrical conductor and thus it is very restricted in its power handling capability, this material also has adherence problems when attached to a metal structure. Titanium ($\delta = .9$) achieves only a small reduction of the secondary emission compared to conventional collector metals. There are, however, more effective electron optical methods to reduce or eliminate backstreaming of secondaries.

Residual Space Charge Potential Energy

Electron beams of high power tubes usually have a fairly high space charge density, especially for tubes with velocity resynchronization. In this case the average velocity of the spent beam is considerably reduced due to a large amount of energy extraction, and due to a

high degree of beam bunching in such tubes. An accumulation of space charge has potential energy, which has been derived from the kinetic energy of the beam. An electron beam with high space charge density will thus be slower and hence can not be decelerated as much. Moreover, such beams are known to suffer flow instabilities even before the deceleration limits are reached⁷ ("Space Charge Blocking"). It is, therefore, common practice to let the beam expand in the collector region. It is then generally possible to keep the space charge potential depression small.

Residual Rotational Energy

The presence of magnetic fields force the electron trajectories into a spiralling motion, and, therefore, some of the kinetic energy of the beam is rotational, at the expense of translational energy. The beam is slower and can not be depressed as much ("Magnetic Mirror Effects"). Good magnetic shielding of the depressed collector region is therefore generally desirable. In the transition region where the magnetic focusing fields are terminated, the rotational beam energy is reconverted into translational kinetic energy. For ideal "Brillouin flow" focusing (cathode magnetically shielded), the rotational energy is converted into a corresponding increase of the axial beam velocity. With "confined flow" focusing (a portion of the magnetic focusing flux penetrates the cathode surface), the rotational energy is converted into translational energy with a radial and azimuthal velocity component. This manifests itself as a radial deflection of the beam contour.

Velocity Sorting of the Spent Beam

In a multistage collector with N stages, the spent beam must be separated physically into N velocity groups such that each velocity group contains all beam electrons within a specified energy range. For each velocity group which has been removed from the beam, a velocity sorting process has taken place, and, therefore, there

are N velocity sorting processes required for N collector stages. It can be shown that there is an optimum partition of energy levels which separate two adjacent velocity groups. This optimum partition of velocity groups depends on the specific velocity distribution of the spent beam and the number of required collector stages.

Velocity sorting of modulated electron beams is generally accomplished with a radial or transverse deflection scheme. For slower electrons the deflection is stronger and therefore the radial or transverse displacement for these electrons is larger, resulting in a radial or transverse separation of the velocity groups. The effectiveness of such velocity sorting schemes is contingent on the absence of radial velocity components of the spent beam trajectories at the entrance into the deflection device. However, the assumption of a parallel flow spent beam is idealized. Generally the spent beam trajectories deviate from a parallel flow, resulting in sorting errors, such that a fraction of higher energy electrons is sorted into the "wrong" velocity group (with lower kinetic energy) and these electrons are not as much decelerated as they could be.

Radial velocity components in spent beam trajectories are induced by RF defocusing fields, by focusing deficiencies, and by non-laminar flow conditions. Non-laminar flow is generally caused by imperfect beam launching conditions from the gun into the focusing field.

Good multistage collector performance requires therefore high quality focusing and good beam launching conditions of the gun.

The design of multistage collectors has to incorporate several functions: Velocity sorting, collector deceleration and suppression of backstreaming secondaries. There is a variety of schemes conceivable for each of these functions. Frequently these schemes combine several functions into one.

For velocity sorting the following schemes are feasible:

- radial electrostatic sorting
- transverse electrostatic sorting
- transverse magnetic sorting
- combination of transverse electric and magnetic sorting.

Collector deceleration is generally achieved with a combined axial and radial electrostatic deceleration field, however, transverse electrostatic deceleration is possible also.

The simplest method for the electron optical suppression of backstreaming secondaries uses electrostatic shielding of the collector interception region. The application of this method for multistage collectors is rather restricted and more advanced methods, such as electric or magnetic field suppression have to be used. These methods take advantage of the very low kinetic energy (~ 20 eV) of most of the secondaries. Electric field suppression provides an electrostatic potential barrier, while magnetic field suppression uses a transverse magnetic deflection field in the path of the secondary trajectories.

Effective multistage collectors with more than two stages have not yet been developed for high efficiency tubes. Several design approaches are available, but of particular interest is the design concept for double stage collectors (Figure 3).

These collectors use radial velocity sorting and secondary suppression by shielding. Radial velocity sorting appeared particularly attractive for these collectors since the spent beam is already in a radially presorted condition as a result of the RF interaction (D2).

When this design concept is applied to a triple stage collector a configuration as shown in Figure 37 is obtained. Secondary suppression of this triple stage collector is in the first and second stage by electric field suppression (as in the first stage of the double stage collector, Figure 3, however the secondary suppression of the second stage will be less effective due to its snout configuration.

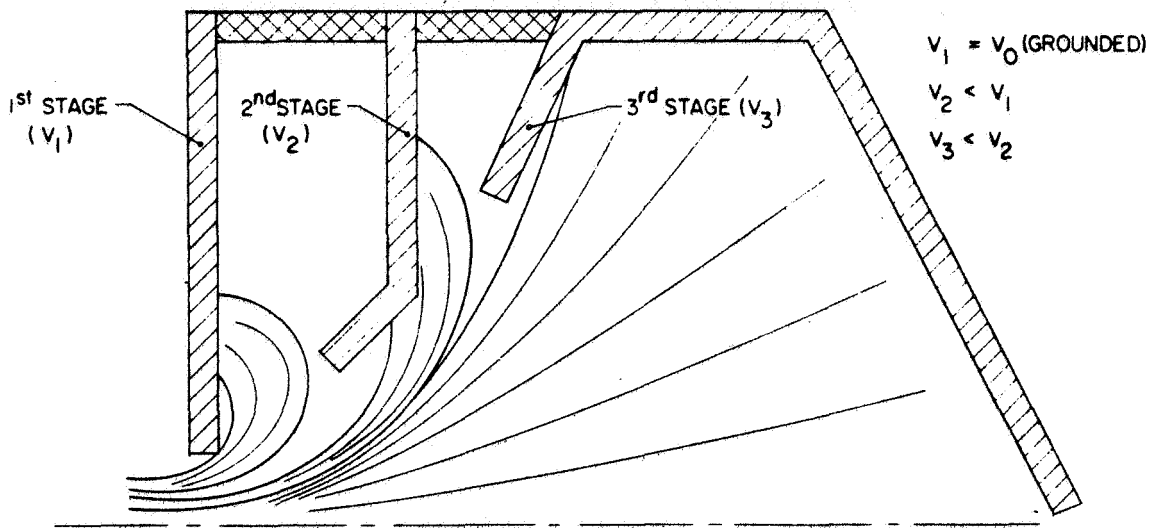
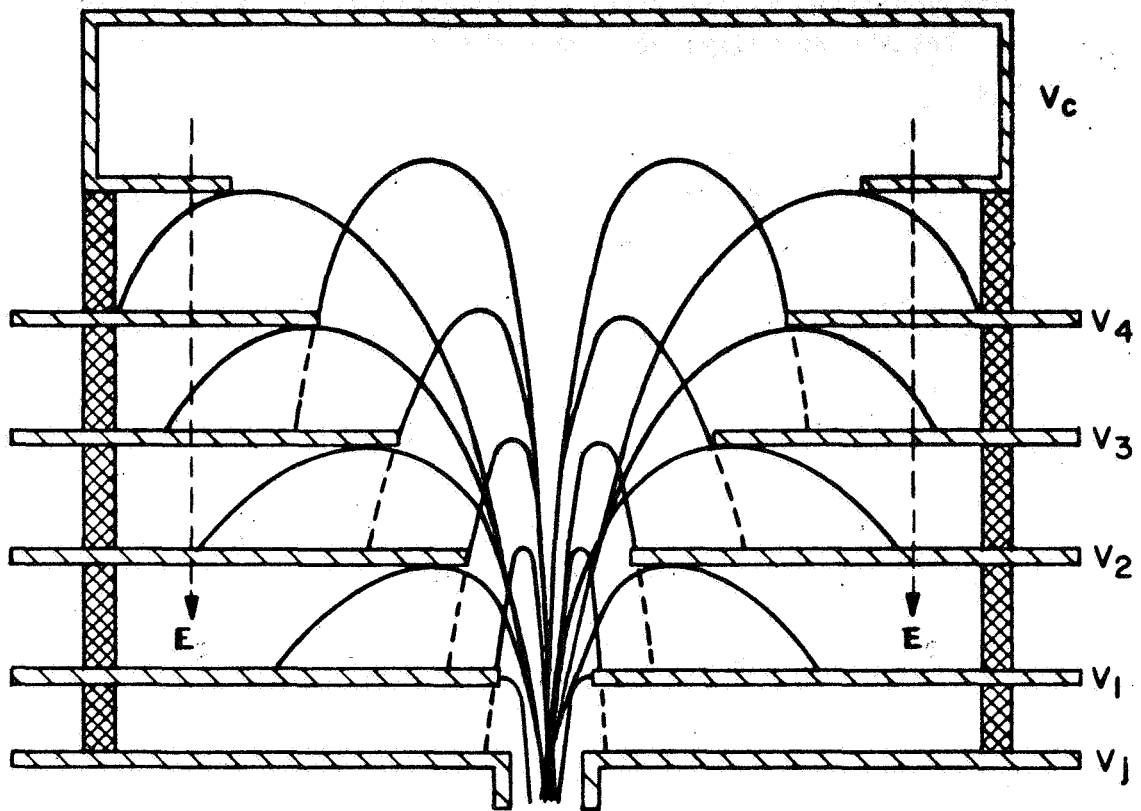


Figure 37 Schematic of a triple stage collector with radial velocity sorting.

The secondary suppression of the third stage is expected to be provided by shielding (as in the second stage of the double stage collector Figure 3). It appears however, that adequate shielding cannot be achieved, because the third collector snout hole has to be rather large due to the very rapid beam spread.

Much better secondary suppression can be expected when electric field suppression is used throughout all collector stages. An additional electrode has to be attached beyond the last collector electrode with the lowest potential. This field electrode is conveniently kept at cathode potential V_c . A schematic of such a configuration is shown in Figure 38 for a four stage collector with radial velocity sorting.



$$V_j > V_1 > V_2 > V_3 > V_4 > V_c$$

Figure 38 Schematic of four stage collector with radial velocity sorting and electric field suppression of secondaries.

The RF defocusing fields at the output coupler provide the initial radial deflection, while the collector deceleration field completes the radial velocity sorting.

It is desirable to provide a fairly uniform deceleration field in the collector region in order to minimize lens effects which may cause sorting errors. This can be accomplished by placing the collector electrodes, which have prescribed potentials, at their respective equipotentials in the uniform field.

The apertures of the collector electrodes are chosen large enough to let the spreading beam pass through. The collection of the spent beam takes therefore place only at one side of the collector electrodes. The electrostatic potential in front of the intercepting collector surface becomes increasingly more negative with respect to the collector potential.

The average kinetic energy V_s of the secondaries is very small, in the order of

$$V_s \approx 20 \text{ eV}$$

The secondaries will therefore be reflected back to the collector surface at a equipotential surface in the vicinity of 20 V below the collector potential. This reflection surface will be very close to the collector surface, so that the secondaries are practically prevented from ever leaving the collector surfaces. Only secondaries from the aperture edges or from their close vicinity may be able to escape and to produce backstreaming.

Although the radial velocity sorting scheme is convenient in view of the radial presorting mechanism produced by the beam interaction, it is obvious that it is inherently deficient. This is because the radial sorting fields diminish toward the beam axis. The center portion of the beam is therefore not exposed to the radial sorting fields and cannot be properly sorted with the collector configuration of Figure 38.

Uniform transverse electric or magnetic fields on the other hand are capable of effective transverse velocity sorting, provided the spent electron beam enters the deflection region in parallel flow. Only magnetic velocity sorting however, will then provide deflection

angles which are inversely proportional to the electron velocity. With electric deflection a sorting error is introduced due to the transverse energy gradient which is produced by the transverse electric field.

Transverse magnetic deflection will therefore be used for the sorting design of all tubes. The spent beam, however, is exposed to the radial RF defocusing field at the output coupler and the resultant radial beam deflections can generate serious sorting errors for a transverse sorting scheme, especially in high impedance circuits, where the RF fields are very strong. Such radially deflected trajectories can be restored to parallel flow by magnetic refocusing, at least for laminar beam flow conditions. This is accomplished by adding a drift space beyond the output coupler, over which the full magnetic focusing field is maintained. In the drift space the electron trajectories will scallop as a result of the radial RF perturbation at the output coupler. If the drift length is chosen to be approximately one quarter (or a multiple of one quarter) of the scalloping wavelength λ_s of the beam, as illustrated in Figure 39.

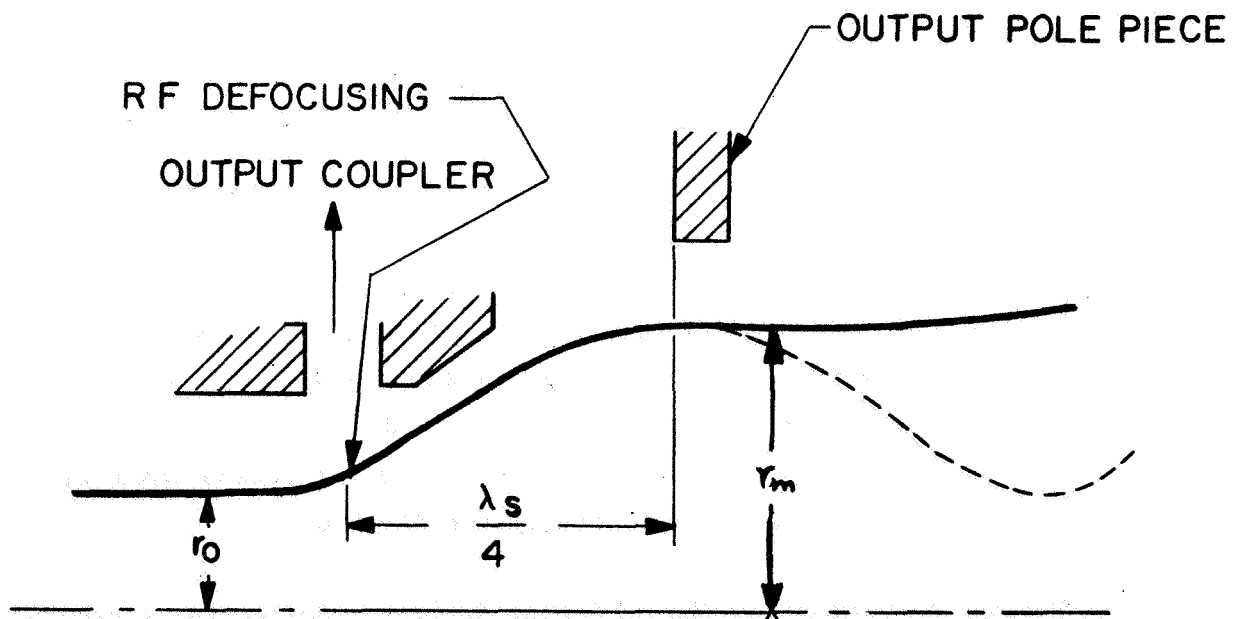


Figure 39 Magnetic refocusing of spent beam.

The beam trajectories will reach a maximum of their radial excursion (radius r_m) and the beam is in parallel flow at this point. If the focusing field is terminated at this point with the output pole piece, the spent beam will leave the magnetic refocusing region in parallel flow, even if the radial RF perturbation has been large. In this case the maximum beam radius r_m will be much larger than the beam radius r_0 in the interaction region. The scalloping wavelength λ_s of the perturbed beam is related to the cyclotron wavelength of an electron in a magnetic field, but it is considerably modified by the space charge effects of the beam.¹¹

The same magnetic refocusing procedure is applicable with periodic magnetic focusing as well, because a PPM focused beam will also exhibit a scalloping of the beam trajectories when exposed to a radial perturbation. In practice one additional magnet period with a modified length will be sufficient for the beam trajectories to reach a maximum radius with parallel flow at the terminating pole piece.

The velocity sorting scheme to be used for the tubes consists of a transverse magnetic deflector, followed by the electrostatic collector deceleration region, where the velocity sorting is completed. The deceleration region is magnetically shielded to avoid magnetic mirror effects. The magnitude of the initial magnetic deflection angle should be small in order to keep the transverse kinetic energy component small, since this component will not be extracted in the axial decelerator. With small deflections, however, a deceleration with large dimensions will be required, and the sorting errors due to non-parallel beam entrance conditions will be relatively large. An optimum choice of the deflection angle can only be made if the beam entrance conditions are known.

For the deflectors of the collector designs a deflection strength corresponding to that of the radial defocusing fields was chosen.

The deflector consists of a constant magnetic field B_T , which is produced by a pair of external magnets as illustrated in Figure 40. The deflection length ℓ_m is determined by the magnetic deflection field B_T and the required deflection strength.

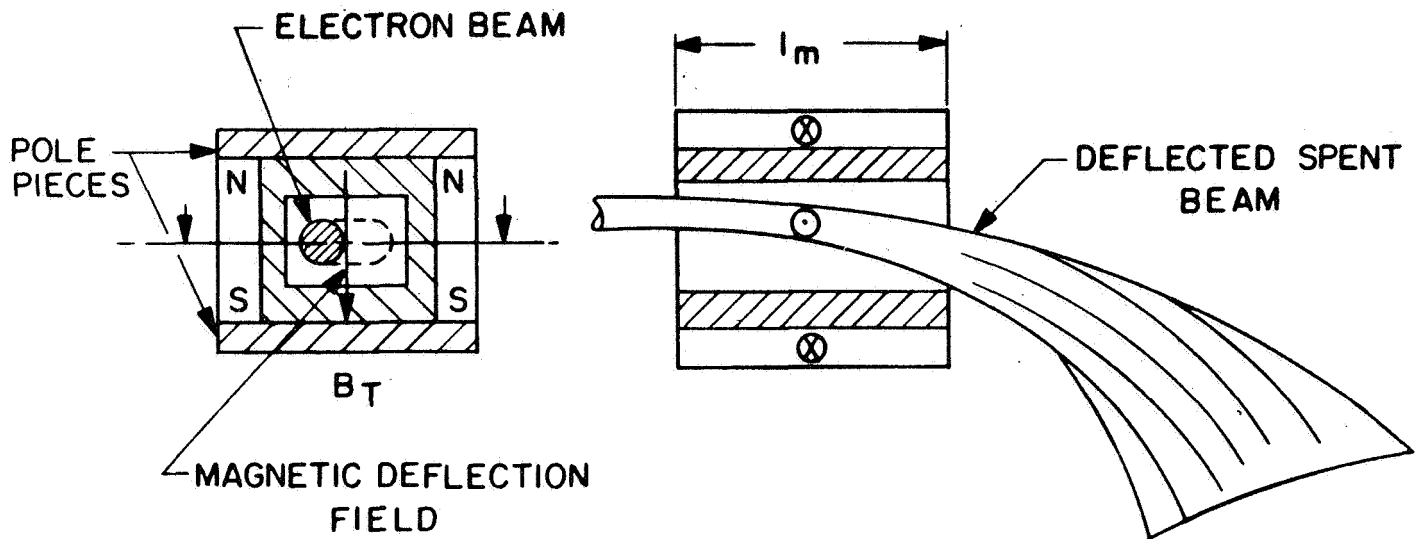


Figure 40 Magnetic deflection of the spent beam.

The decelerator following the deflector uses a uniform deceleration field to minimize sorting errors due to lens effects and electric field suppression as described for the collector configuration with radial velocity sorting (Figure 38), requiring one additional deceleration electrode of cathode potential V_c . The collector configuration is shown schematically in Figure 41 for a four stage collector. The collector apertures are designed large enough to let the deflected beam pass through, so that the beam collection can take place only at one side of the collector electrodes. This assures electric secondary suppression except for the aperture edges.

The collector electrodes with their prescribed potential are positioned in the deceleration field at their respective equipotentials to achieve uniformity of the deceleration field.

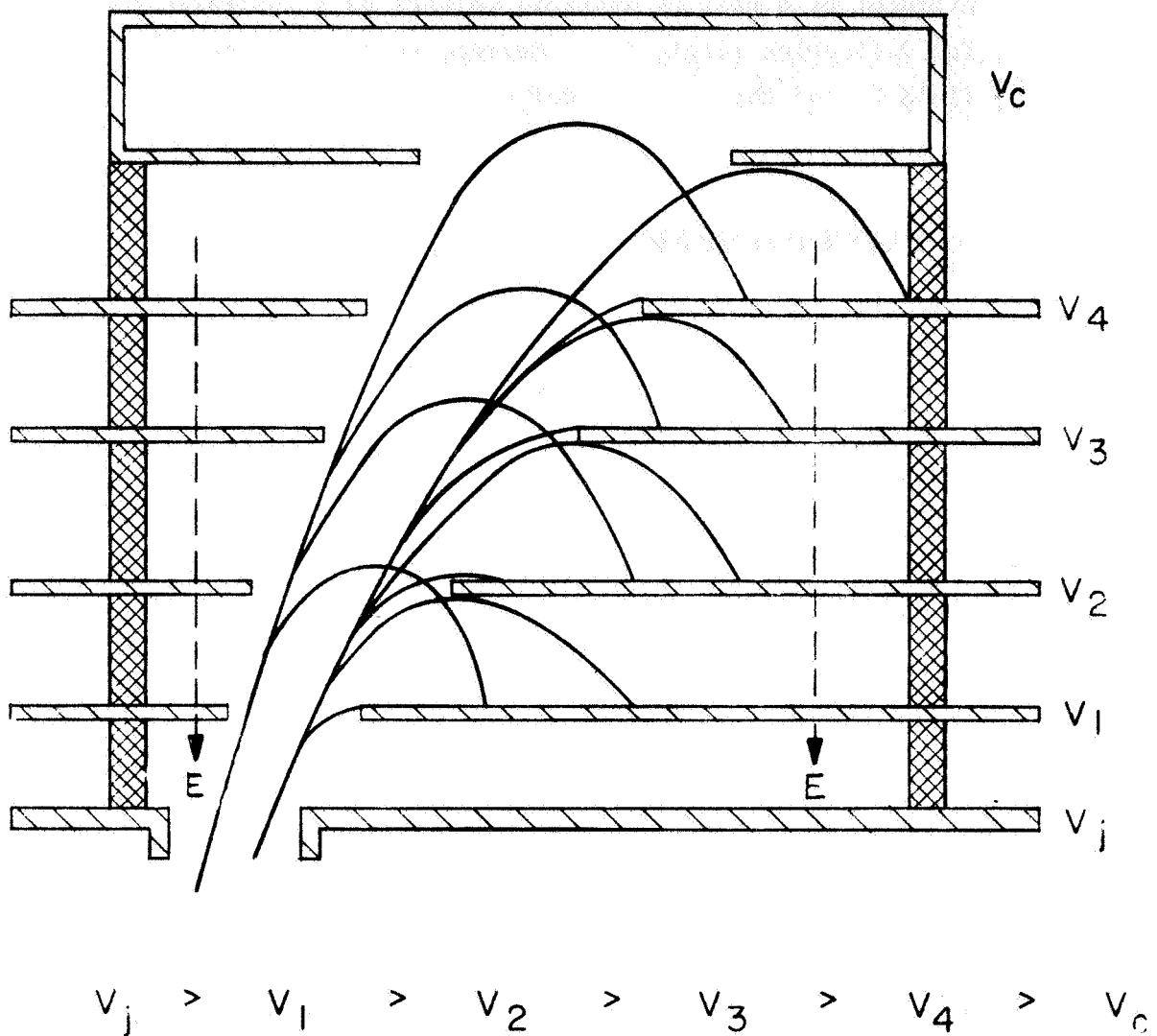


Figure 41 Schematic of four stage collector with transverse velocity sorting of spent beam and electric suppression of secondaries.

The choice of the respective collector potentials for optimum efficiency improvement depends on the kinetic energy distribution of the spent beam for each of the tubes. This energy distribution is obtained by the large signal computer analysis and an optimum choice of collector potential (for a given number of collector stages) is derived, for which maximum efficiency improvements are

obtained, assuming no sorting errors and no secondary backstreaming. The energy separation levels and the respective deceleration magnitudes are indicated schematically in Figure 42.

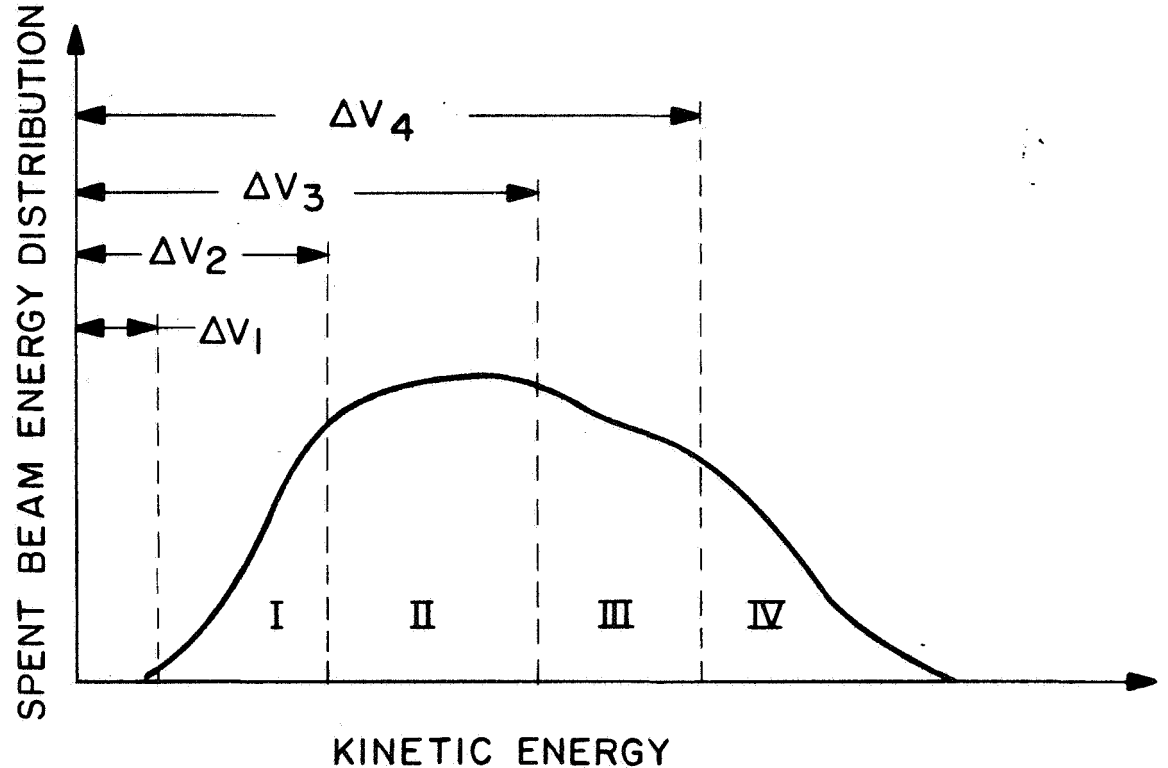


Figure 42 Optimum velocity sorting of spent beam.

It is possible to take imperfect velocity sorting into account, as well as partial secondary backstreaming. It was found that the useful number of collector stages is reduced, when such deficiencies are taken into account.

E. GUN AND FOCUSING

1. Gun

The life expectancy of a traveling-wave tube is primarily determined by the cathode and to some extent by the gun design. The electron beam will be produced by a conventional Pierce type convergent gun.¹² These types of gun designs have been used for a long time for traveling-wave tubes. Their design techniques have continuously been improved and very high quality beams can now be produced with these guns over a large range of perveances, voltages and beam compression ratios. A high quality beam with a low percentage of translaminar electron trajectories is important to achieve good beam transmission. Good beam transmission is essential for the effectiveness of the depressed collector, especially with many stages. Good beam transmission is also important for long tube life.

The beam compression ratio also has an important effect on the tube life, since it determines the cathode loading (current density on the cathode). The cathode loading must be small for a long cathode life. The beam area compression ratio has therefore been chosen high enough to keep the cathode loading i_c to less than

$$i_c < 500 \text{ mA/cm}^2 .$$

With this limit for cathode loading, long cathode life can be achieved even with oxide coated cathodes. This is of concern for the 8 GHz and 11 GHz tubes (tubes IV and V), while the low frequency tubes required a much lower cathode loading even with small area compression ratios.

2. Focusing

Traveling-wave tubes employ either permanent magnets, periodic permanent magnets, or solenoid magnetic focusing, while periodic electrostatic focusing has never been successful for these tubes, especially not for tubes with long life requirements or high power levels. This is primarily because electrostatic focusing generally does not achieve the high quality of beam focusing that is now possible with magnetic focusing. The electrostatic beam focusing is less stiff and tends to easily become unstable when perturbed.^{11,13}

Permanent magnetic focusing is used in a number of low and medium power traveling-wave tubes. However, in comparing it to permanent periodic magnetic focusing, this method requires much larger and heavier focusing structures, especially for low frequency tubes. This method is also more restricted with respect to the maximum field strength which can be produced. The maximum available focusing field is approximately 900 gauss¹⁴ with presently available materials. This limitation excludes this technique to be used for most high power high frequency tubes.

Periodic magnetic focusing is generally used for high reliability space tubes with very long life. This type of focusing is readily adaptable for high power coupled cavity tubes, where it is also frequently used. Since PPM focusing is much smaller and requires much less weight than a solenoid, which also needs additional power, PPM focusing is usually preferable to solenoid focusing from the efficiency point of view. This conclusion has to be qualified, however. Figure 43 shows schematically the PPM configuration with the coupled cavity circuit.

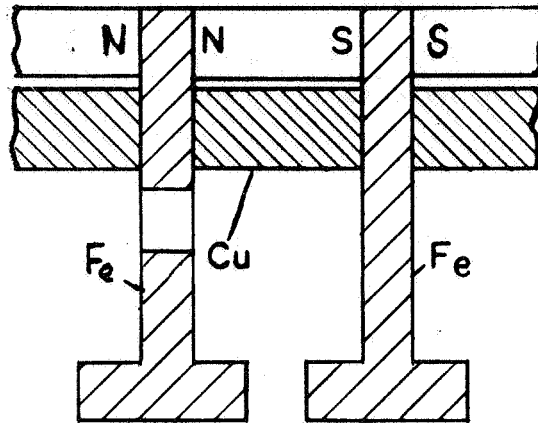


Figure 43 Schematic of PPM focusing structure for coupled cavity circuit.

The pole piece is thus integrated into the coupled cavity and the focusing period (L) is tied to the cavity period. For large bandwidth coupled cavity tubes the coupling slot width has to be large and may cause a perturbation of the magnetic symmetry of the magnetic circuit, which results in undesirable transverse perturbation fields on the beam. In this case the double period focusing system is generally used, shown in Figure 44.

This double period system has been found to eliminate such transverse perturbation effects, while its focusing performance and stability are identical to the single period system (Figure 43).

These focusing structures provide excellent beam focusing; however, the beam contour exhibits inherently a ripple with this focusing method, which has half the focusing magnet period. This beam ripple can be rather small, when the electron optical launching conditions of the gun into the focusing field are optimized. These launching conditions can readily be optimized, provided the gun, and especially the cathode, is magnetically shielded.

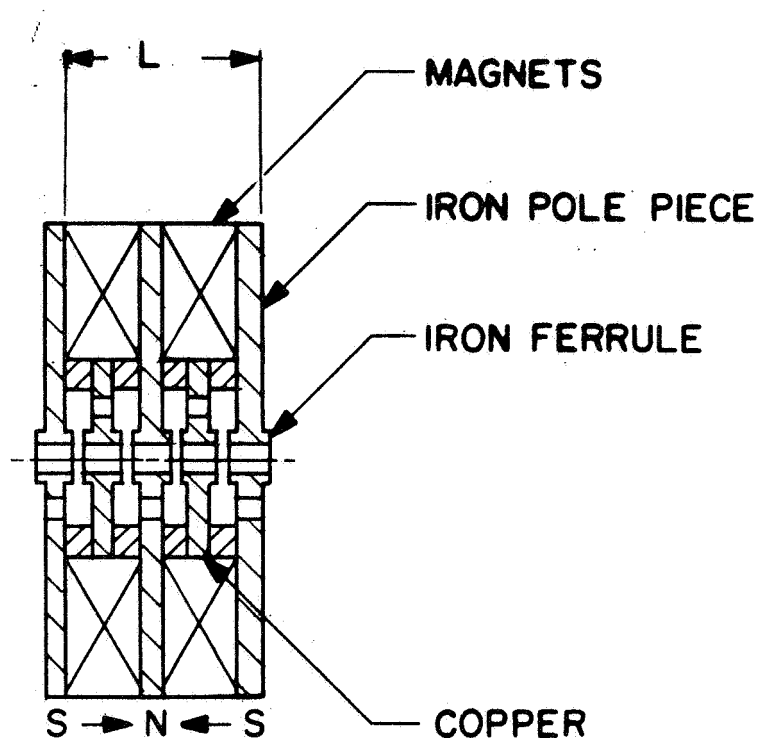


Figure 44

PPM focusing structure with double period for coupled cavity circuit.

The PPM focusing method, due to its periodic field configuration, has stability limitations. The beam focusing will break down when the stability limits are reached. The stability limits can be expressed by the $\frac{\lambda_p}{L}$ parameter, where

λ_p = Plasma wavelength of electron beam

and

L = magnetic focusing period.

It can be shown that the focusing stability for a beam in "paraxial" approximation (Mathieu-type equation) is limited by

$$\left[\frac{\lambda_p}{L} \right]_{\min} \geq 1.3 \text{ (paraxial theory).}$$

In practice, however, it is found that larger $\frac{\lambda_p}{L}$ values are required to achieve stable PPM focusing. Good focusing is generally obtained for

$$\left[\frac{\lambda_p}{L} \right]_{\min} \geq 2 \text{ (empirical).}$$

For very high efficiency tubes, however, the high degree of beam bunching and large velocity reduction of the beam with RF has to be taken into account. This will substantially reduce the $\frac{\lambda_p}{L}$ value with RF, and stable focusing with RF is only assured when an adequate design margin for $\frac{\lambda_p}{L}$ is provided.

This requirement imposes a restriction on the design of the coupled cavity circuit with PPM focusing. In order to keep $\frac{\lambda_p}{L}$ large enough, it may be necessary to increase λ_p by increasing the beam voltage and reducing the beam current (thereby reducing beam perveance). Such a design change will increase the tube length and it may not be consistent with an optimum efficiency design. In this case solenoid focusing has to be considered too, since it does not restrict the coupled cavity circuit design. Due to the absence of pole pieces in the structure, the thickness of the cavity walls ("webs") can be smaller, resulting in a higher interaction impedance.

Solenoid focusing for high efficiency tubes is generally designed for "confined flow." In this case a large portion of the magnetic beam flux is allowed to penetrate the cathode surface. This will require a higher magnetic field, but the resultant beam focusing is then very stiff,¹³ and superior beam focusing can be achieved. For an assumed relative magnetic cathode flux K_c of

$$K_c = .85$$

the magnetic field B has to be

$$B = 2B_0$$

with

$$B_0 = \text{"Brillouin" field.}$$

This focusing condition has been assumed for the solenoid focusing design.

Recent strides in very light weight high performance solenoid design for airborne high power tubes (at the 2 kW CW power level at S-band) have been made at the Hughes Electron Dynamics Division. This was accomplished by developing methods of winding the solenoid directly on the tube body ("wrapped-on solenoids"). The inner core of the solenoid is then reduced to a minimum and a considerable reduction of the solenoid weight, size and power consumption is achieved. These new solenoids are not much larger than an equivalent PPM system: for a beam power of 10 kW and 12 dB gain a focusing power of only 300 watts was required.

These solenoids can be designed for either minimum weight or minimum power consumption. In the first case, aluminum is the preferable foil material; in the latter case copper is preferable. It is possible to arrive at an optimum solenoid design by using the equivalent power - weight conversion of

100 lbs/kW .

The equivalent weight of the power supply and the solenoid weight can be calculated as a function of the solenoid outer diameter. The total weight will then exhibit a minimum at an optimum solenoid outer diameter as indicated in Figure 45.

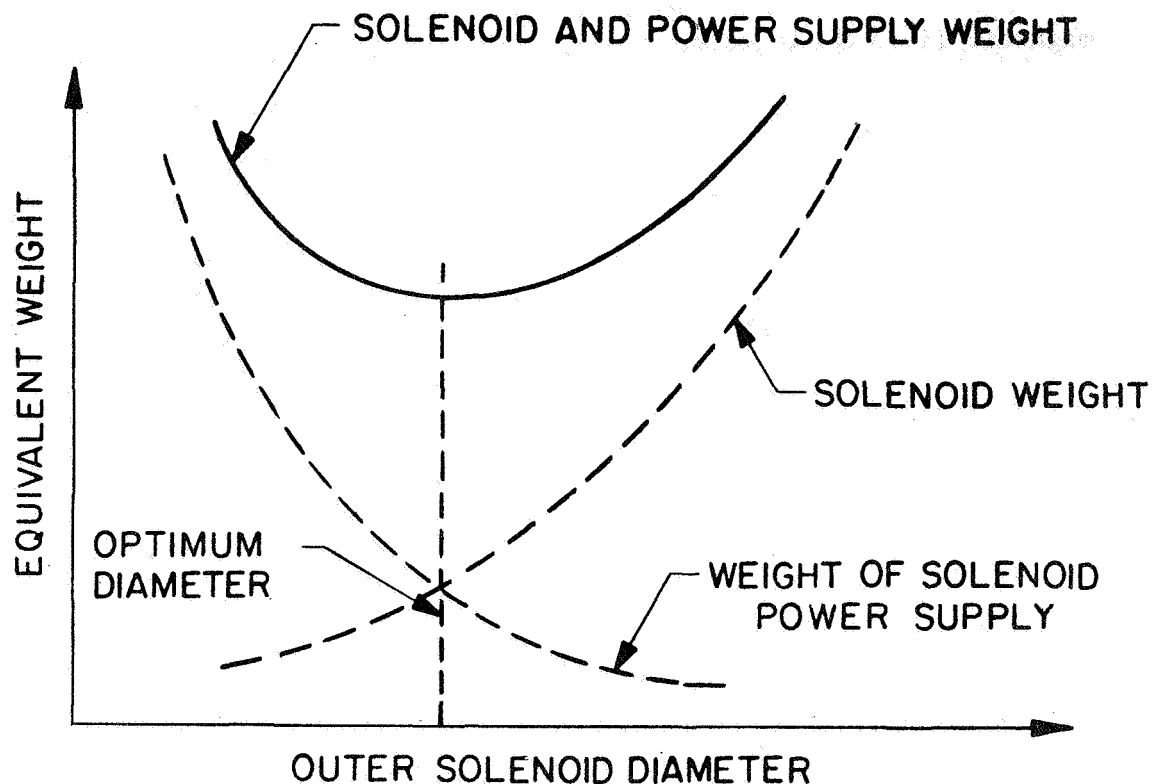


Figure 45 Equivalent total weight of solenoid.

Comparison of PPM Focusing and Solenoid Focusing

All tube designs were evaluated both for PPM focusing and solenoid focusing, taking stability criteria into account. The total equivalent weight for both focusing versions was evaluated, consisting of:

weight of the circuit

weight of the focusing structure (solenoid or PPM focusing structure)

equivalent weight of the solenoid power supply

equivalent weight of the tube power supply

using the power-weight conversion factor of

$$1 \text{ watt} = .1 \text{ lbs.}$$

The weight of the gun and collector are not included since these can be considered equal for solenoid and PPM focusing.

It was found that the 850 MHz and 2 GHz tubes (tubes I, II, and III) resulted in a lower total weight with PPM focusing, while the 8 GHz and 11 GHz tubes with PPM focusing suffered significant efficiency reductions and required therefore a higher equivalent total weight than the solenoid focused versions. It should also be mentioned that PPM focusing for these frequencies (8 GHz and 11 GHz) and the power levels (5 kW CW) is not yet within the present state of the art, and these PPM designs could not yet be considered reliable for long life operation. Solenoid focusing, on the other hand, is generally superior to PPM focusing and well within the present state of the art for these higher frequency tubes.

The 850 MHz, 2 GHz AM and 2 GHz FM tubes are therefore designed with PPM focusing with axial ringmagnets, while the 8 GHz and 11 GHz tubes are designed with a wrapped-on copper solenoid.

F. HIGH EFFICIENCY AM SIGNAL AMPLIFIER WITH TRAVELING-WAVE TUBE MODULATOR

The amplifiers for AM signals (850 MHz and 2 GHz) are designed with the traveling-wave tube modulator concept, which permits linear AM signal amplification with very high efficiency. This is in contrast with conventional amplifiers for AM signals. These amplifiers must be operated well below saturation in order to avoid distortions and to achieve the required phase and amplitude linearity. The amplifier will then be very inefficient, especially at low modulation amplitudes. Conventional (single stage) collector depression will improve the efficiency, but this improvement is impaired by the inherent velocity spread of the spent beam, which is significant even at low signal levels. Therefore, it is not possible to achieve good depressed collector efficiency with a conventional traveling-wave tube amplifier operating below saturation, as is required for the amplification of AM signals.

The advantage of the new concept is:

1. traveling-wave tube amplification of AM signals with very high efficiency is achieved
2. the efficiency remains high over the specified dynamic range of the AM signal.

This is accomplished by varying the beam current of the traveling-wave tube modulator in proportion to the signal level, so that the tube operation remains near saturation over the dynamic range of the AM signal.

However, since the new scheme is useful only for AM signals with greatly varying amplitudes, the FM modulated signal for audio, which has a constant magnitude, must be removed from the AM signal with filters and be amplified separately as indicated in Figure 46. The

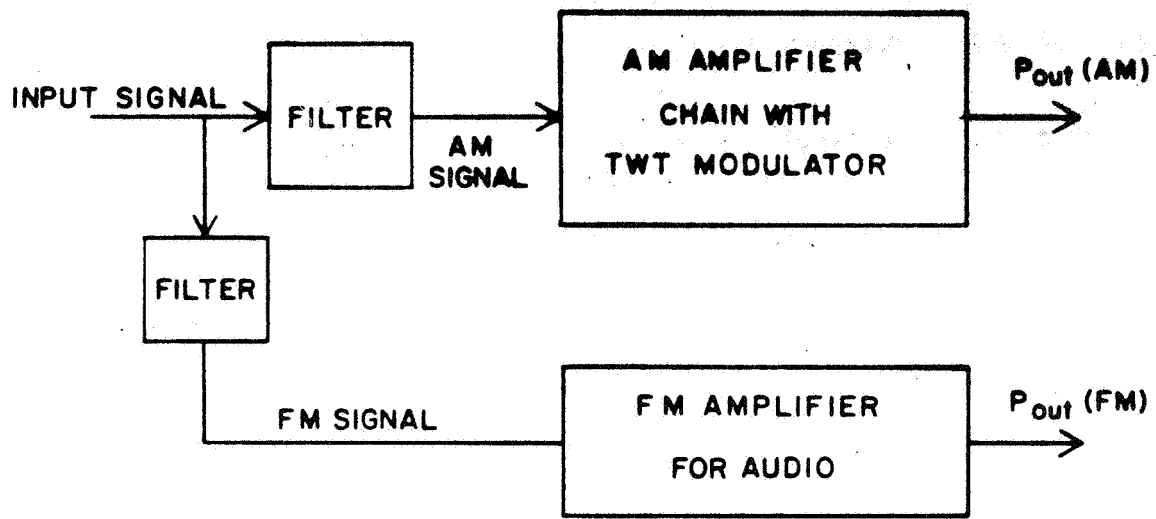


Figure 46 Separation of FM audio signal from AM signal.

required power levels for the FM audio signal are considerably lower than the required peak AM power levels (750 watt for 850 GHz, 500 watt for 2 GHz), it is therefore possible to design the amplifiers for the FM audio signal with a highly efficient, light weight helix tube.

Both the FM audio signal and the AM signal can be recombined with a power coupler into a common antenna feed.

In the AM amplifier chain it is required to remove the amplitude modulation from the carrier, to amplify the demodulated carrier signal with a preamplifier, and to add the amplitude modulation back on to the amplified carrier signal with the traveling-wave tube modulator. Both the preamplifier and the TWT modulator can be designed for high efficiency, so that highly efficient amplification of the AM signal is obtained. In addition, circuitry can be added to achieve a high degree of amplitude and phase linearity of the output signal.

The following processes are provided for this purpose:

- 1) Separation of amplitude modulation and carrier signal
- 2) Amplification of carrier signal
- 3) Recombination of amplitude modulation and carrier signal
- 4) Amplitude and phase linearization.

1. Separation of Amplitude Modulation and Carrier Signal

This can be accomplished with a power splitter, a limiter for the carrier signal, and a detector for the modulation signal as indicated in Figure 47. The limiter is designed to provide a constant level of the carrier frequency (f_o) signal, which drives the carrier signal preamplifier. The maximum available carrier frequency level is then determined by the lower amplitude modulation limit S_2 (Figure 47). For double sideband AM signals it would be possible to generate the driver signal for the carrier signal preamplifier by an independent oscillator, which generally can be a solid state device with low power consumption. In this case the power splitter and limiter (Figure 47) could be eliminated and the available input power for the modulation signal chain would be twice as large.

For vestigial AM signals, however, this is not permissible. Such signals carry also a phase modulation signal, in addition to their AM signal, which must be preserved through the AM amplifier chain.

The modulation signal drives the grid of the TWT modulator. It will generally be necessary to provide a modulation amplifier and a dc grid bias voltage to achieve the desired grid voltage for the TWT modulator.

A schematic of this scheme is shown in Figure 48.

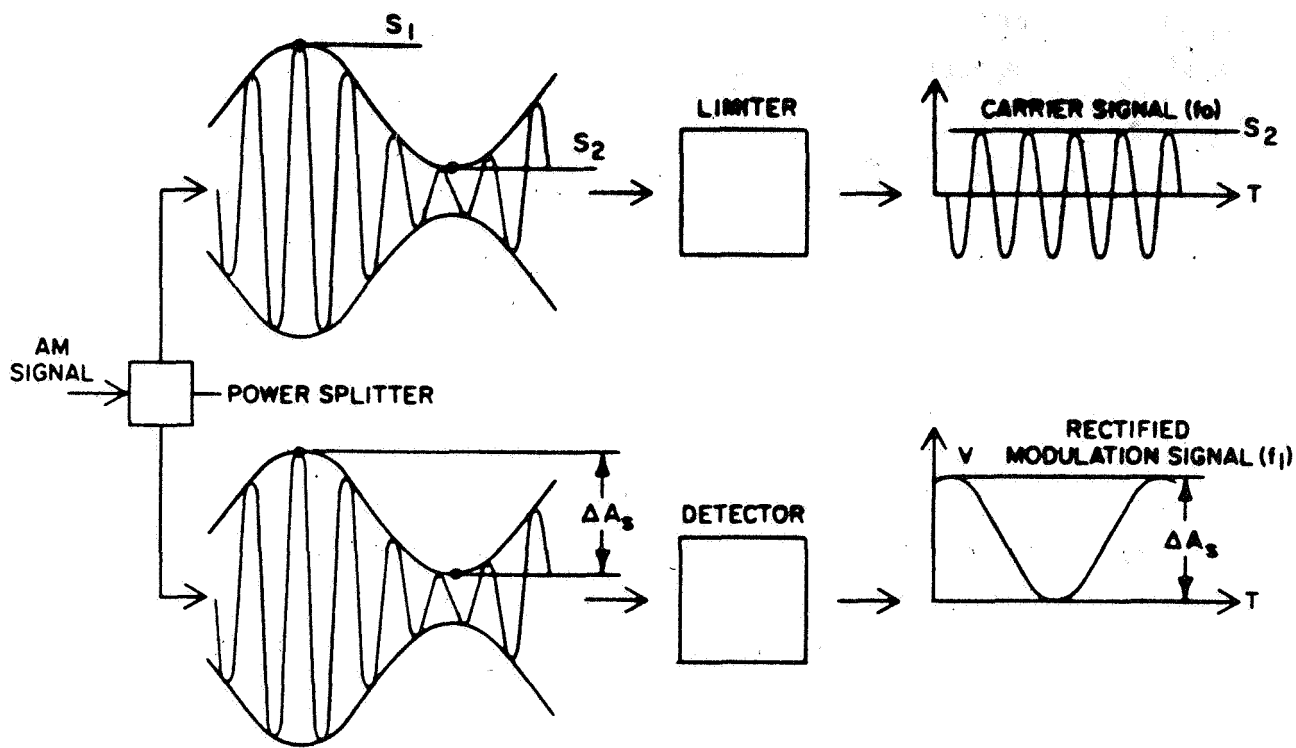


Figure 47 Frequency separation for amplitude modulated signal.

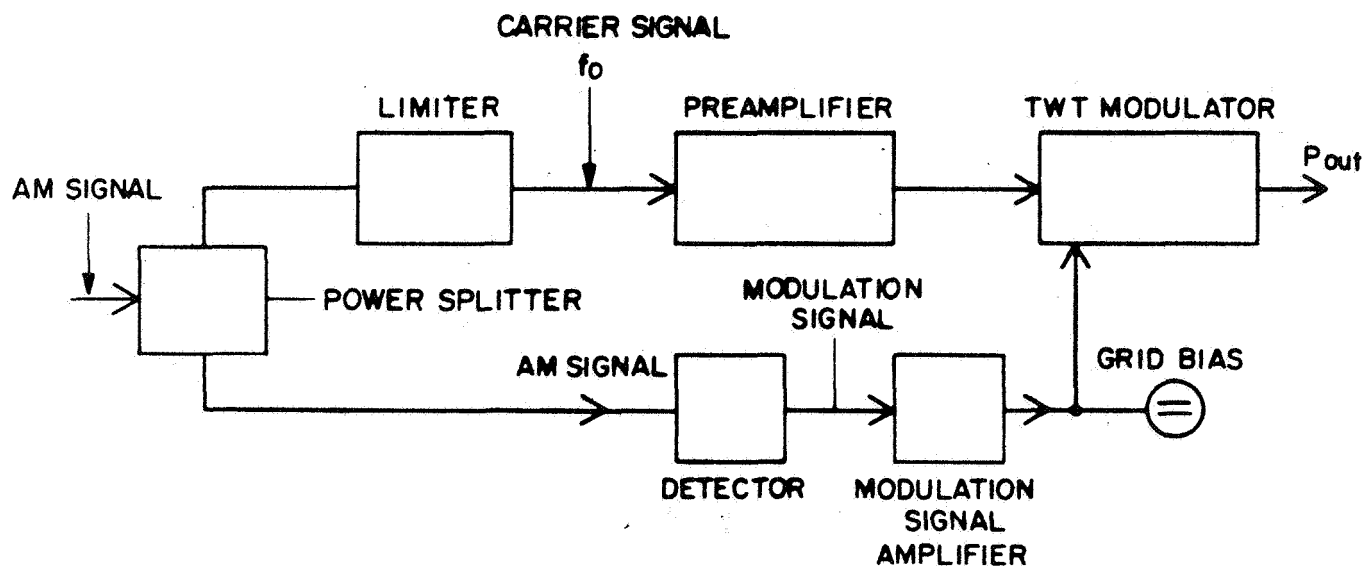


Figure 48 AM amplifier chain with traveling-wave tube modulator.

2. Amplification of Carrier Signal

The preamplifier is designed to boost the demodulated carrier frequency signal S_2 to a specified level P_2' , such that

$$P_2' \text{ (dB)} = P_2 \text{ (dB)} + G_o \text{ (dB)}.$$

where

$$P_2 \text{ (dB)} = \text{power level of demodulated signal } S_2$$

$$G_o \text{ (dB)} = \text{specified gain for AM signal}.$$

The input and output power levels P_2 and P_2' of the preamplifier do not vary. Therefore the preamplifier can be designed to operate at saturation and with high efficiency. The required output power levels for these preamplifiers are low enough (75 watts for the 850 MHz amplifier and 50 watts for the 2 GHz amplifier) to use highly efficient PPM focused light weight helix tubes for these preamplifiers.

3. Recombination of Carrier Signal and Amplitude Modulation

The amplitude modulation is added back on to the carrier signal with the traveling-wave tube modulator. The TWT modulator provides a variable gain ΔG_{mi} for the carrier signal with a level P_2 , which is proportional to the instantaneous relative modulation level ΔP_i of the AM signal to be amplified (Figure 49), or

$$\Delta G_{mi} \text{ (dB)} = \Delta P_i \text{ (dB)}.$$

The instantaneous gain of the TWT modulator varies therefore from

$$\Delta G_m \text{ (min)} = 0$$

for the lowest level ($P_i = P_2$) of the AM signal (Figure 49), to

$$\Delta G_m \text{ (max)} = \Delta P = 20 \text{ dB}$$

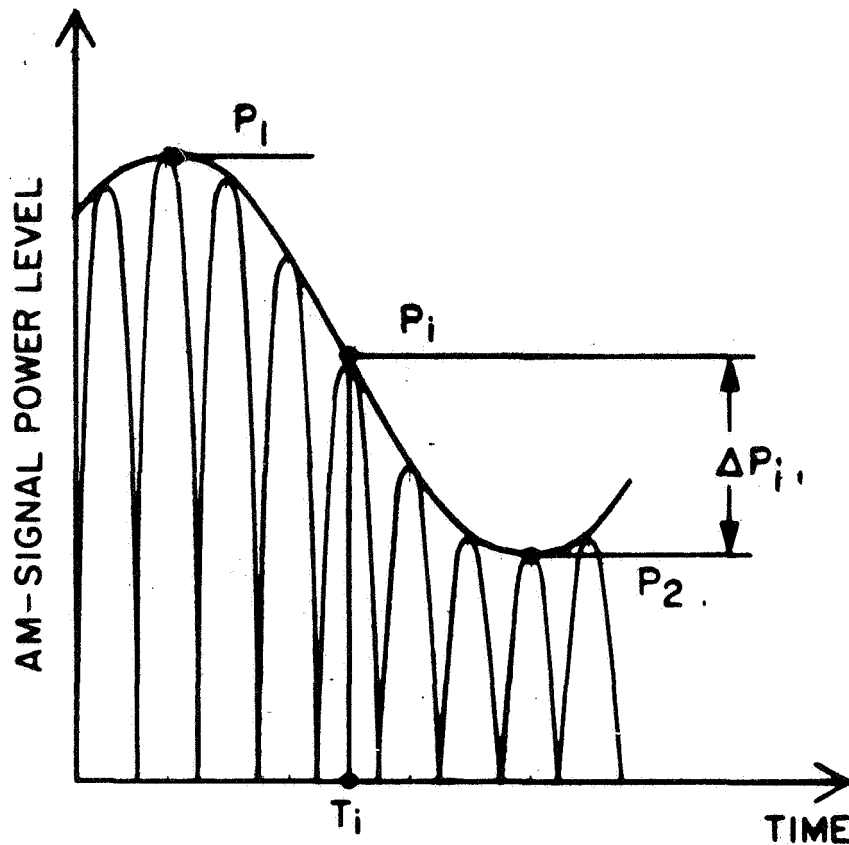


Figure 49 Instantaneous level of amplitude modulation..

where ΔP (dB) = maximum value of the AM modulation (20 dB) corresponding to the dynamic range of the AM signal. The overall gain of the system is therefore constant with a value of 40 dB, and the system is linear, even though its components are not. This is shown schematically in Figure 50.

The variable gain ΔG_{mi} of the TWT modulator is achieved by varying the beam current I_i accordingly, while the beam voltage of the TWT modulator is kept constant as in conventional traveling-wave tubes.

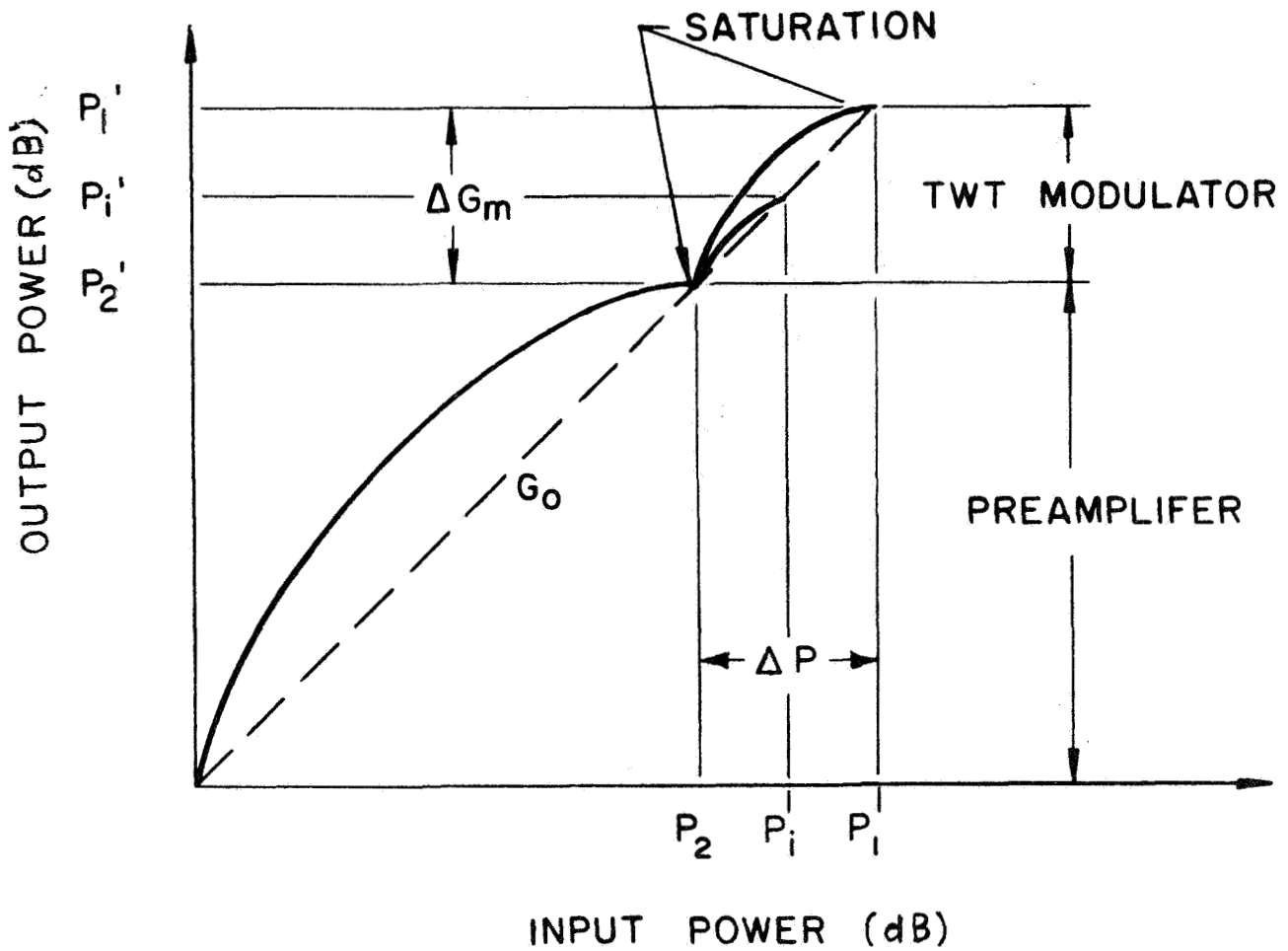


Figure 50 Power characteristics with traveling-wave tube modulator.

The beam current can conveniently be varied by a modulation grid near the cathode of the gun. A variable grid modulation voltage V_{go} , which is generated by the modulation signal (Figure 48), will produce the desired beam current variation I_i . At low modulation levels the beam power will thus be small, and it will increase with the modulation level. Therefore the TWT modulator will operate at or near saturation over the entire dynamic range of the AM signal, and its efficiency can be expected to be high for all power levels of the AM signal (Figure 50).

The pertinent design considerations for the modulation grid of the TWT modulator may be illustrated for several modulation levels (Figure 47).

The grid may either be a conventional modulation grid, or a shadow grid, which has a substantially higher power handling capability. This is because the grid interception current I_g of a shadow grid is extremely small:

$$I_g \text{ (shadow grid)} \approx .0005 I_o$$

as compared to a conventional grid:

$$I_g \text{ (conventional grid)} \approx .10 \text{ to } .15 I_o \text{ with } I_o \text{ beam (cathode) current.}$$

For the case of the lower modulation limit P_2 (Figure 49) the corresponding TWT gain has to be zero. However, this requires a small beam current I_o in the TWT modulator in view of the gain characteristics of a TWT at small beam currents. This (zero gain) beam current I_o is supplied with a positive dc grid bias voltage V_{go} as indicated in Figure 48.

For the upper modulation level limit P_1 (Figure 49) the gain of the traveling-wave tube modulator ΔG_m is required to be

$$\Delta G_m = \Delta P = 20 \text{ dB} .$$

The traveling-wave tube modulator is to be designed to achieve this gain at saturation so that its efficiency will be high. This will require a beam current I , which can be produced with a grid voltage V_{gl} , or, taking the bias voltage V_{go} into account, a grid modulation voltage ΔV_{gl} of

$$\Delta V_{gl} = V_{gl} - V_{go} .$$

The gain of the modulation signal chain (Figure 48) must therefore be adjusted to produce a grid modulation voltage of (Figure 50).

$$\Delta V_{gi} = 0 \quad \text{for} \quad P_i = P_2$$

$$\Delta V_{gi} = \Delta V_{gl} \quad \text{for} \quad P_i = P_1.$$

For intermediate power levels P_i the required traveling-wave tube modulator gain G_{mi} is

$$G_{mi} = \Delta P_i \text{ (dB)}$$

corresponding to a beam current I_i and a grid modulation voltage V_{gi} (Figure 51).

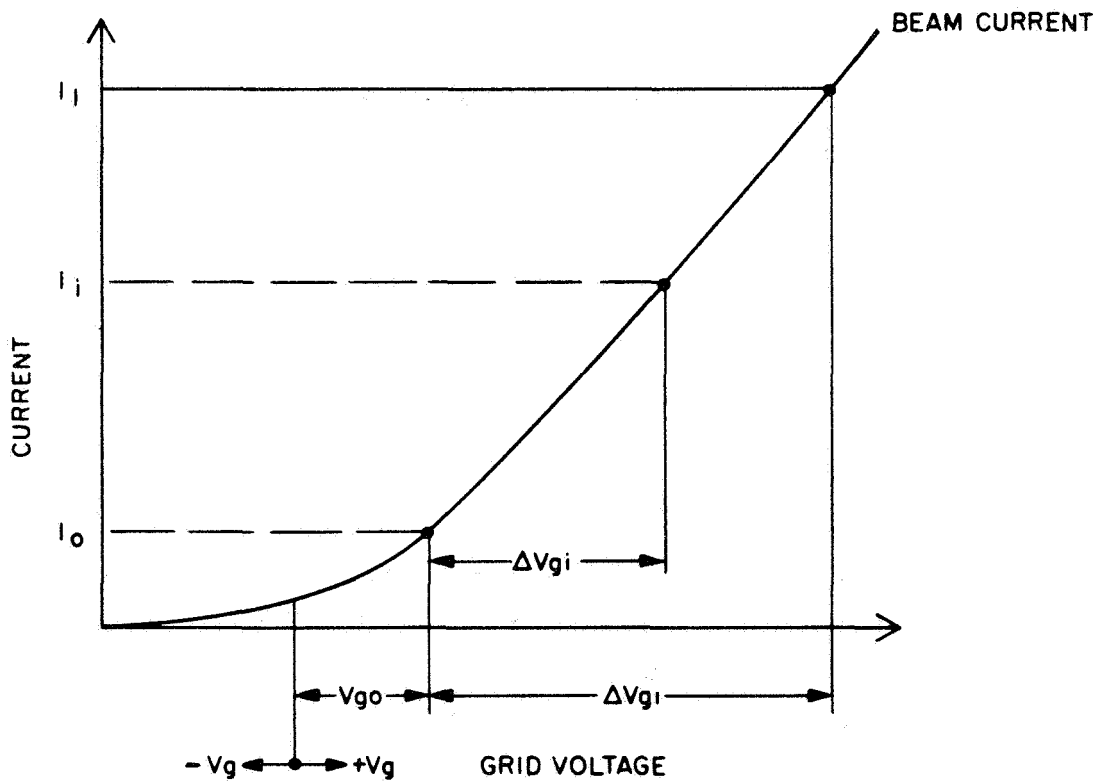


Figure 51 Grid characteristics for traveling-wave tube modulator.

4. Linearization

The amplitude linearity of the described AM signal amplification depends on how closely the required gain characteristics of the traveling-wave tube modulator

$$\Delta G_{mi} = \Delta P_i \text{ (dB)}$$

are achieved over the dynamic range of $\Delta P = 20$ dB. This is primarily a function of the characteristics of the modulation signal chain. It is possible to determine the resultant linearity deviations when the characteristics of the modulation chain are known.

The gain characteristics of the traveling-wave tube modulator have been computed with the large signal computer program both for the 850 MHz and the 2 GHz amplifiers as a function of the beam current, taking the beam diameter variations with beam current into account.

These deviations from amplitude linearity are found not to be large, and it appears possible to apply corrective circuitry in the modulation signal chain to linearize the power characteristics of the TWT modulator. Such a compensation is possible in a number of ways. Two possible methods of gain equalization can be considered; a programmed linearization scheme, and an automatic gain control method.

The linearizer method is shown schematically in Figure 52. A "linearizer" is inserted to process the modulation signal in such a way that linear gain is achieved with the traveling-wave tube modulator. The linearizer provides, therefore, a modulator transfer characteristics which is a function of the modulation signal level. It may be convenient to combine the modulation signal amplifier and linearizer into one device as indicated in Figure 53.

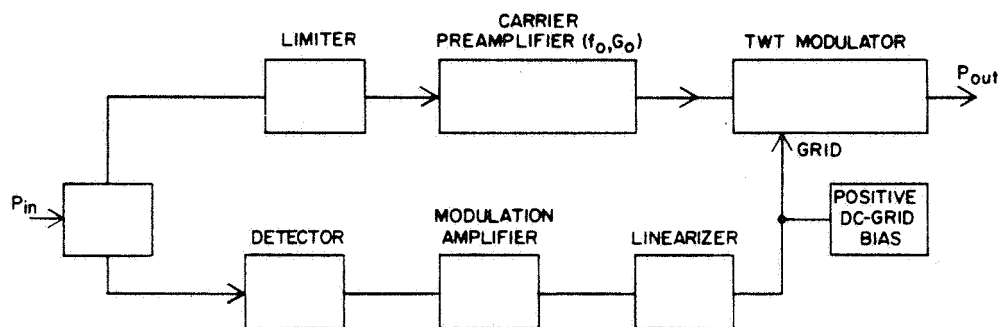


Figure 52 Modulation signal chain with linearizer.

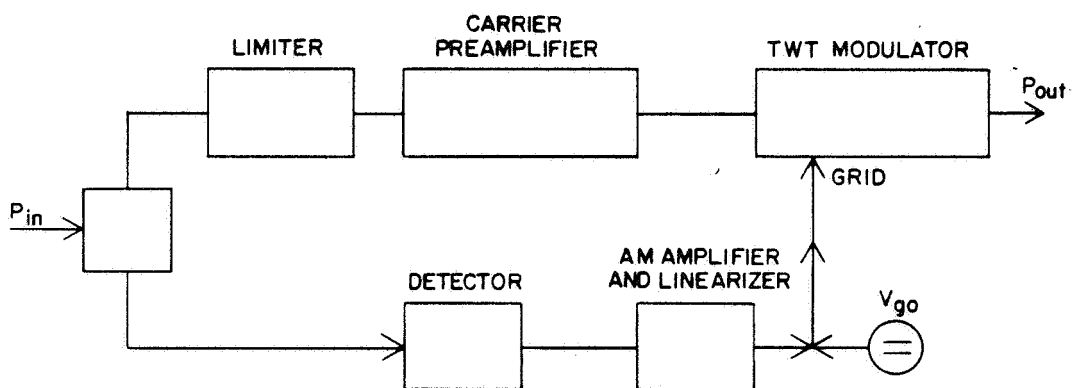


Figure 53 Combined modulation signal amplifier and linearizer.

The automatic gain control system is shown schematically in Figure 54. This system compares the AM signal levels of input and output of the system in a gain comparator, which may be a bridge-type circuit.

The detected gain deviation signal of the gain comparator drives the gain regulator, which provides a variable gain to the modulation signal. The regulator gain is a function of the detected gain deviation.

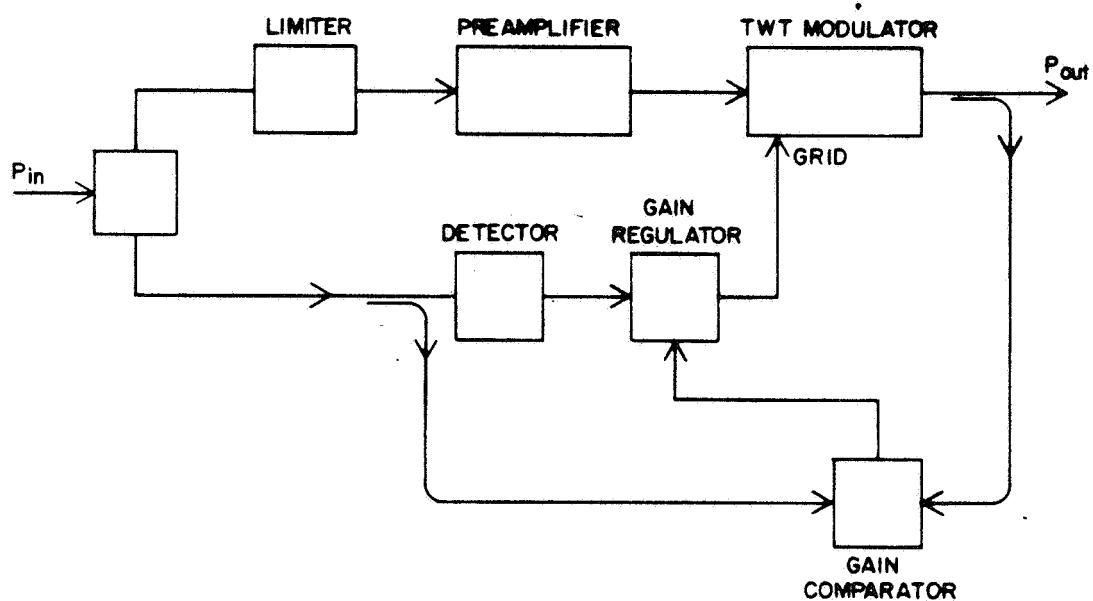


Figure 54 Automatic gain control for traveling-wave tube modulator.

The traveling-wave tube modulator can not be expected to precisely reproduce the phase relations of the original carrier signal in the amplification process. This would be of no consequence for pure (double sideband) amplitude modulation. For vestigial sideband AM signals, however, the signal is phase modulated as well, and this phase modulation must be preserved in the amplification process. Two requirements are therefore imposed on the system for phase modulated AM signals:

1. The phase relations of the input signal must be reproduced for the amplified output signal.
2. The recombination of the carrier signal and the amplitude modulation signal at the modulation grid must be synchronized.

This can be accomplished with a number of phase linearization schemes for the carrier frequency signal and a delay line for the modulation signal chain. Two possible methods for phase linearization are:

- i) Programmed phase compensation
- ii) Automatic phase control .

The phase compensator method is schematically shown in Figure 55. A phase shifter is inserted in the carrier signal line, which produces a prescribed phase shift as a function of the AM signal.

An alternate method, using automatic phase control, is shown schematically in Figure 56. The carrier signal phase changes from output to input of the system are compared in a phase comparator, which may be a bridge-type circuit. The phase comparator produces a signal proportional to the phase deviation between output and input. This deviation signal drives a phase shifter which compensates for the detected phase deviation.

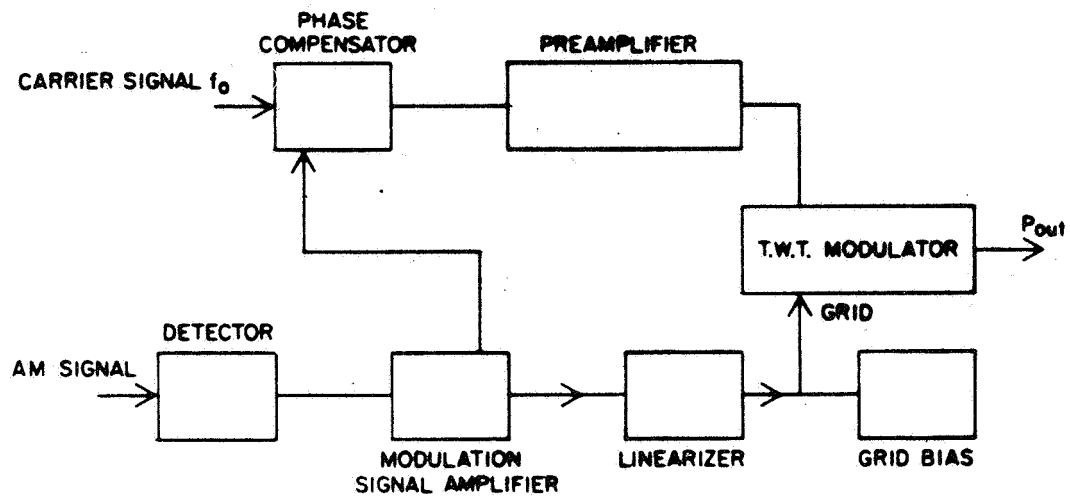


Figure 55 Traveling-wave tube modulator with phase compensator.

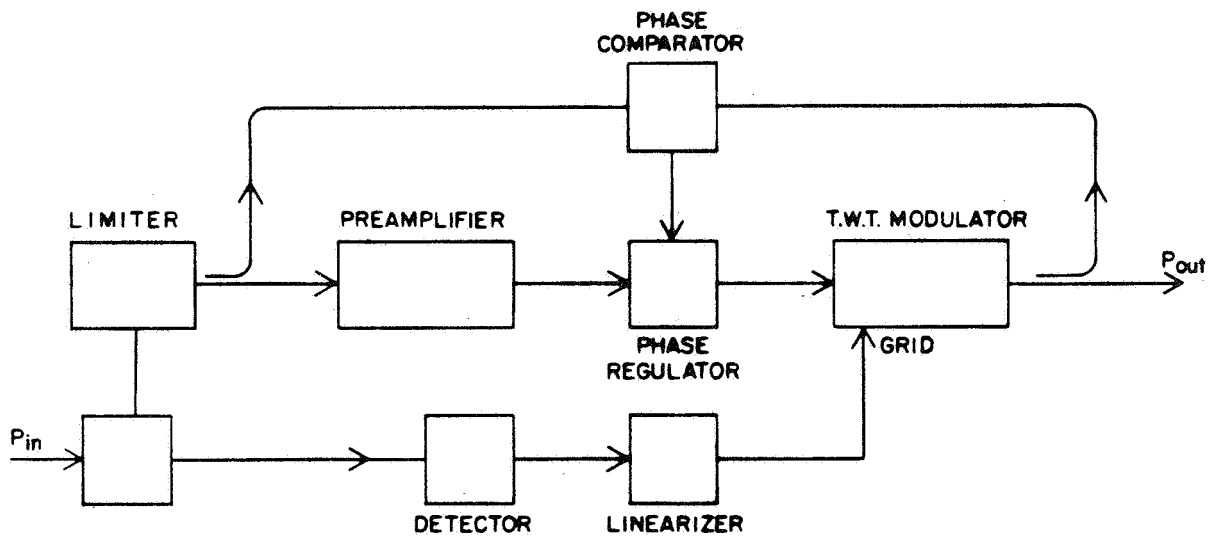


Figure 56 Automatic phase control for traveling-wave tube modulator.

The amplitude modulation is phase correlated with the phase modulation of the carrier signal. It is therefore necessary in this case to resynchronize the amplitude and phase modulation in the recombination process of the signal in the traveling-wave tube modulator. This can be accomplished by making the time delays ΔT_0 and ΔT_1 of the carrier signal and modulation signal chains from their recombination equal, or

$$\Delta T_0 = \Delta T_1.$$

These time delays do not vary with time; therefore, a delay time in the modulation signal chain will provide the required synchronism at the recombination point (Figure 57).

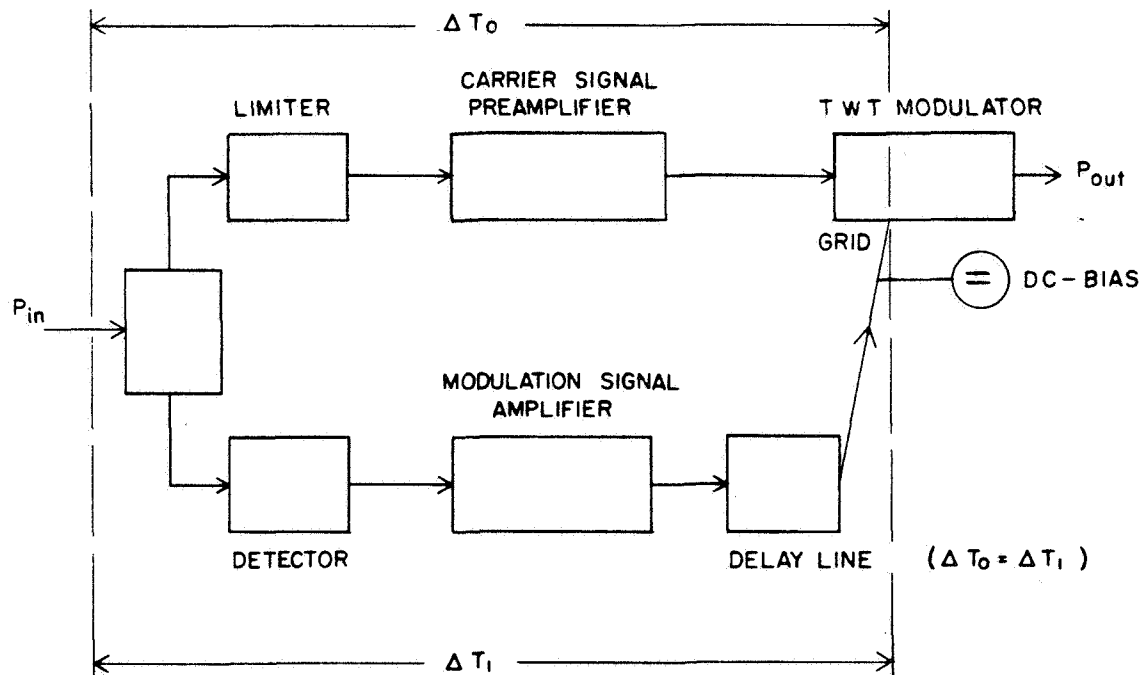


Figure 57 Synchronization of carrier and modulation signal branch for AM signals with PM.

Bandwidth Considerations

In the discussion of the traveling-wave tube modulator method it was assumed that the carrier is amplitude modulated with a single frequency f_1 (Figure 48 and 49). However, in practical applications the amplitude modulation will extend over a frequency range Δf_1 with a nonsinusoidal modulation envelope as pictured in Figure 58. In order to preserve the modulation envelope with the described scheme, it is necessary to preserve the phase relations in the modulation frequency range Δf_1 in all components and devices involved with the modulation. Such phase linearity is generally obtained when the bandwidth Δf_d of the devices are considerably larger than the frequency range Δf_1 of the signals to be handled, or

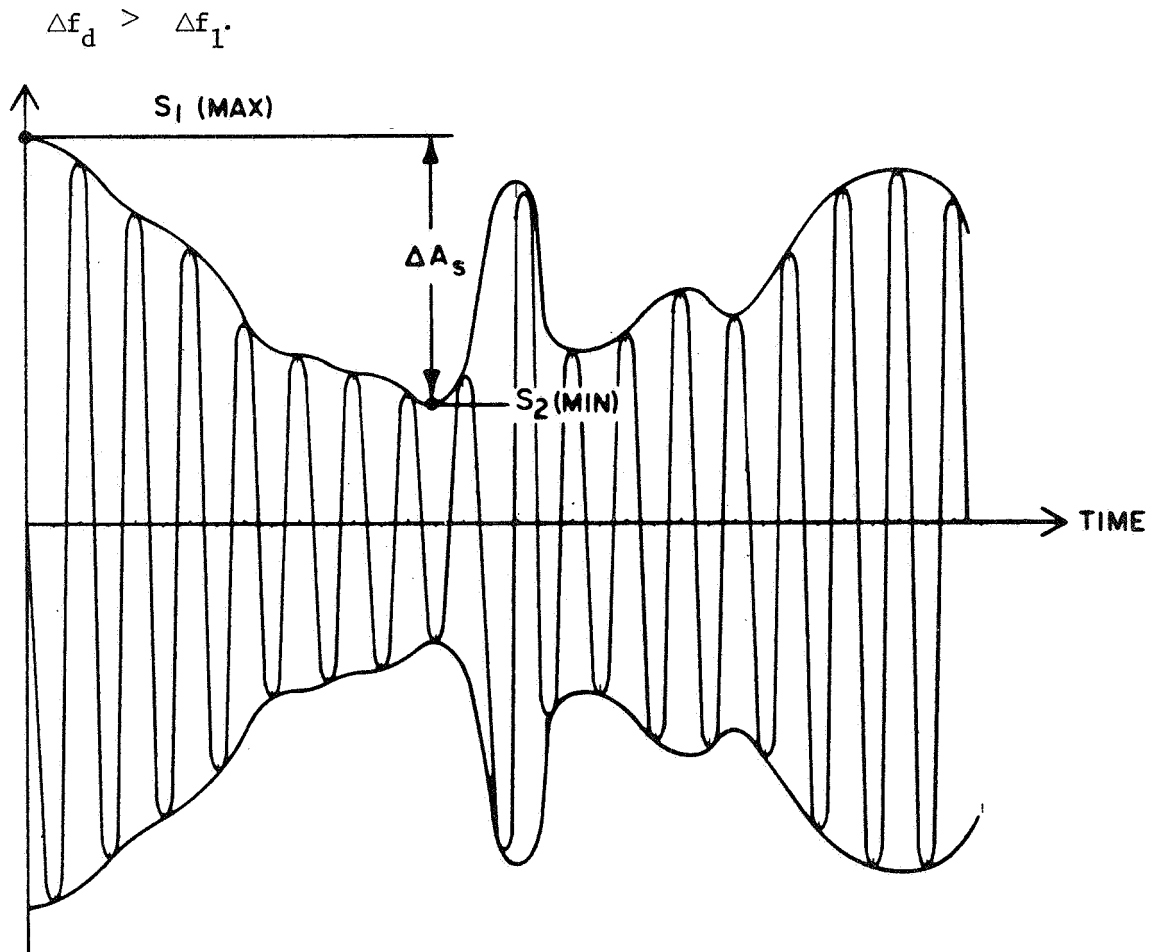


Figure 58 Multifrequency amplitude modulation.

This concerns the filters, the detector, the modulation signal amplifier, and the traveling-wave tube modulator, as well as any linearization devices. For AM with PM the limiter and preamplifier must also have adequate bandwidth, as well as the phase linearization device and the delay time.

In an Appendix the energy distributions for vestigial sideband signals for television are analyzed. This analysis illustrates the significance of vestigial sideband AM signals in a practical application.

G. REMOVAL OF HEAT

The tubes generate waste heat, which is primarily produced at the collector and to a lesser extent, at the slow wave structure due to beam interception and circuit losses. This heat must be removed while the operating temperatures are as low as possible for reliability reasons. The heat can be removed in several ways:

- 1) heat source - heat conduction- radiation into space
 - 2) heat source - heat conduction - heat pipe- radiation into space
- or
- 3) a combination of 1) and 2).

These approaches have to be evaluated with respect to the overall required weight and size of the heat transfer systems, as well as the tube reliability and life, such that prime considerations have to be given to the life and reliability. The operating temperature is the most critical factor in determining the reliability; it should be as low as possible.

It has been found that the coupled cavity temperature T_c at the ferrules should not exceed $T_c = 350^\circ\text{C}$ when PPM focusing is used and $T_c = 400^\circ\text{C}$ with a copper structure. The collector temperature should be below 500°C in a closed system. When the operating temperatures of the tube parts or components are excessively high, their outgassing rate becomes large. This may lead to ionization in the beam area and the formation of conductive coatings across ceramic insulators. Ionization can cause damage of the cathode by ion bombardment and conductive coatings will produce voltage breakdown.

The emissive power density as a function of temperature for various thermal emissivities is given in Figure 59. From this figure the required area to radiate a given amount of power can be calculated. Assuming a radiating surface emissivity of .8, we find that a radiator with a temperature of 100°C would need $12,500\text{ cm}^2$ of radiator area per 1000 watts of dissipated power. A radiator operating at 400°C would require 1095 cm^2 of radiator area per 1000 watts of dissipated power. Assuming that different radiators are used for the circuit and the collector, the heat transfer from the heat source (collector or circuit) must be accomplished with a low enough temperature gradient, so that the specified temperature limits at the heat source are not exceeded.

Higher collector temperatures would be permissible, when the collector is not designed with vacuum seals, but with electric insulators (separators) only, such that the vacuum seal is provided by a thermally transparent envelope as shown in Figure 60. This system uses a low temperature dielectric heat pipe cooling for circuit and gun, while the collector is radiation cooled. The collector envelope cover would be removed in space to achieve space vacuum pumping. This tube could be processed and pretested on ground,

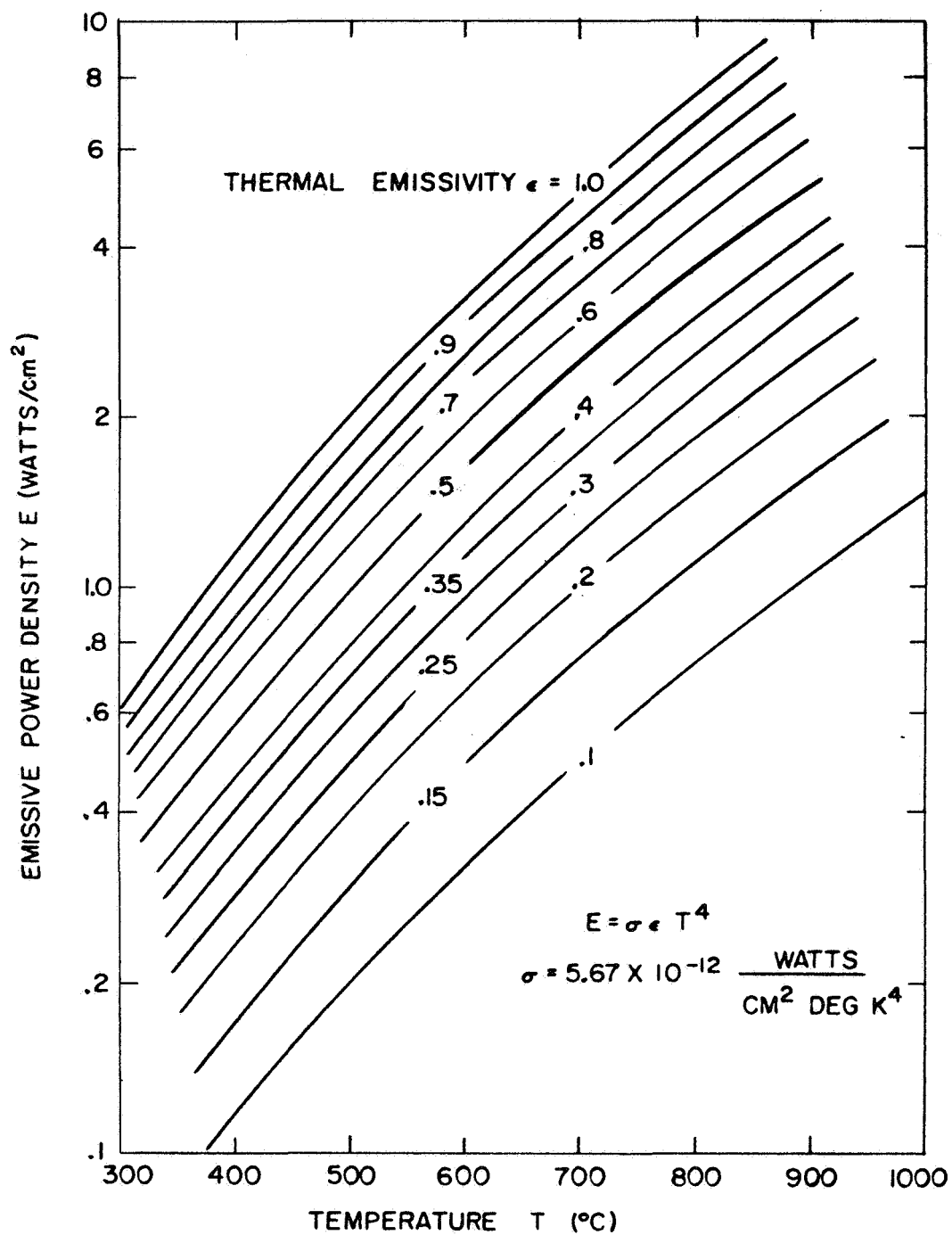


Figure 59 Emissive power as a function of temperature for various thermal emissivities.

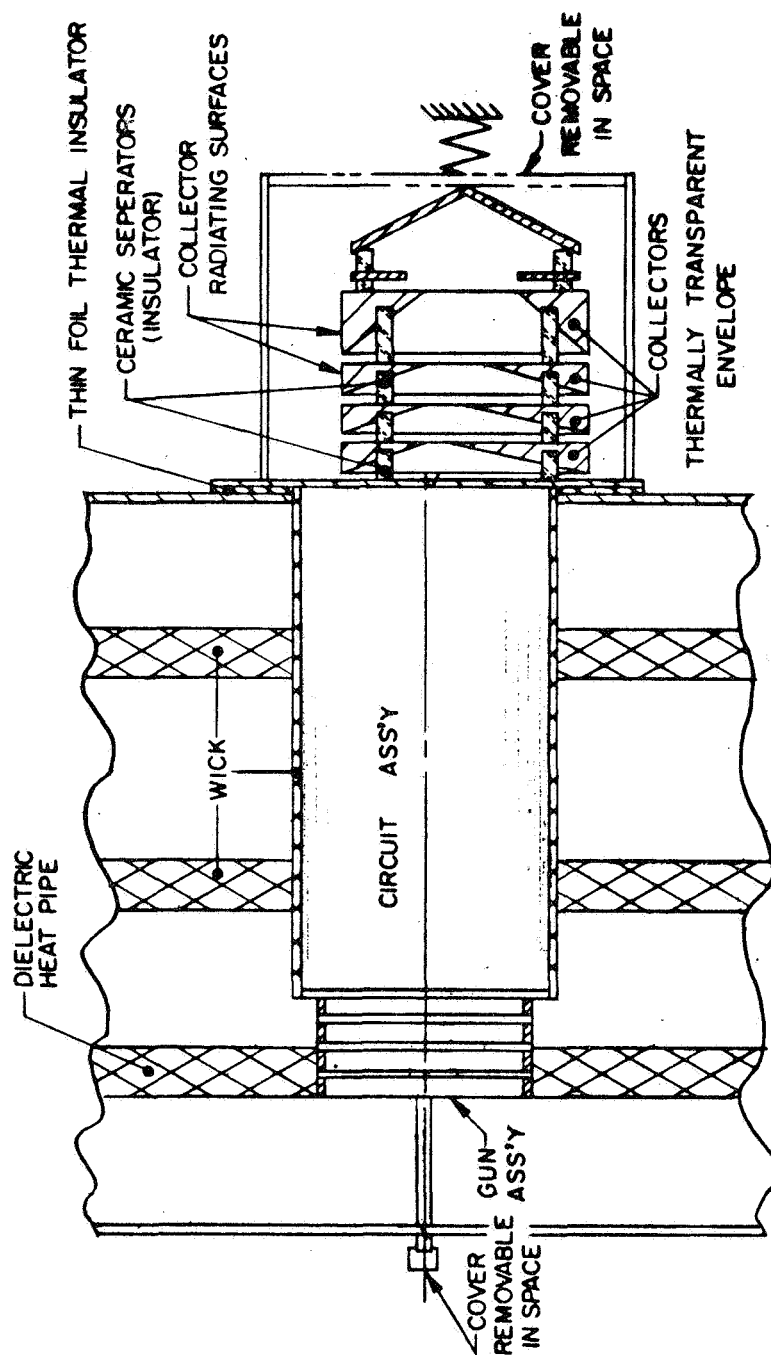


Figure 60 Tube with dielectric heat pipe for circuit cooling and radiating collector.

since the thermally transparent vacuum envelope will protect the tube during ground processing and testing. The ceramic insulators consist only of ceramic separators leaving large gaps between different potential collector plates for maximum pumping. The circuit can be protected from the collector heat by thin foil thermal insulators. This system appears to be quite promising for small tubes with a collector heat dissipation of up to 200 watts.

For higher power levels, however, this system could become rather bulky and unreliable, at least at the present state of technology. For example, in the 850 MHz tube, the dissipated thermal power in the first collector plate is approximately 1000 watts. Assuming a thermal emissivity of .8 at all temperatures, the required collector diameter to radiate 1000 watts would be:

TEMPERATURE	COLLECTOR PLATE DIAMETER
500°C	16.4 cm (63.7 in)
700°C	64.4 cm (25.4 in)
900°C	33.5 cm (13.2 in)

The diameter of the thermally transparent envelope, such as quartz or sapphire, should be at least twice as large as that of the collector in order to protect it against overheating and thermal stress fractures during ground testing. In order to keep the size of the envelope sufficiently small, a radiating collector temperature of approximately 1000°C would be required. However at these temperatures the outgassing rates would be too high even for space pumping and the tube operation could not be considered reliable. An alternative for direct radiation collector cooling would be to process and to activate the tube in space. This technique, if at all possible, would require extensive equipment for the spacecraft, and the mission reliability would be reduced considerably.

Heat pipe cooling appears to be the most promising and reliable for the high power levels of the tubes. Depending on the choice of radiator temperature, two different heat pipe systems for the internal heat transfer from the tube to the radiator can be designed, a low temperature or a high temperature system.

Low temperature heat pipe systems use primarily organic liquids, with operating temperatures in the range of 100°C to about 400°C , while high temperature heat pipe systems use primarily liquid metals, with operating temperatures of approximately 500°C to 1000°C or even higher. The high temperature systems appear more attractive from a size and weight point of view, since the radiator size can be much smaller for higher radiation temperatures. Liquid metals also have generally better heat transfer properties in such systems. Nevertheless, only low temperature heat pipe systems are considered because of their expected superior reliability and life potential. Low temperature systems can use dielectric fluids and all tube components can be operated at a uniform temperature. Such low temperature heat pipe systems can be designed without the additional weight burden of a large radiator, since they can be designed as an integral structural part of the spacecraft.

V. ELECTRONIC DESIGN

A. BASIC CIRCUIT INTERACTION CONSIDERATIONS

1. Choice of Design Parameters

Detailed experimental¹⁵ and theoretical^{1,16,17} studies on traveling-wave tubes have shown that maximum conversion efficiencies η_1 for conventional designs can be achieved when

- i. the value of the gain parameter C ^{15,18} is high, since η_1 is proportional C
- ii. the (radial) propagation parameter γr_a has a value of approximately

$$\gamma r_a \approx .8$$

with

r_a = beam hole radius

$$\gamma = \frac{2\pi f}{v_p} \quad \text{(radial) propagation constant of slow-wave structure}$$

v_p = phase velocity of circuit.

The gain parameter C is defined as¹⁸

$$C = \left(\frac{KI_o}{4V_o} \right)^{1/3}$$

with

K = interaction impedance of circuit on electron beam

I_o = dc beam current

V_o = beam potential (voltage)

The interaction impedance K should therefore be as high as possible to achieve good conversion efficiencies.

The interaction impedance of coupled cavity circuits can be shown to be proportional to

$$h \cdot \left(\frac{\Delta f}{f_o} \right)^{-1} f_o \quad \text{or}$$

$$\left(V_o \right)^{1/2} \left(\frac{\Delta f}{f_o} \right)^{-1} \left(\frac{h}{l_c} \right)$$

where

h = cavity height

l_c = cavity period

$\frac{\Delta f}{f_o}$ = (cold) bandwidth of circuit

The interaction impedance can therefore be greatly increased when the bandwidth is narrow. However, the bandwidth must be large enough to meet the phase linearity requirements as discussed in the next section.

The cavity height h can be increased when a large value for the design voltage V_o is chosen. It should be noted, however, that the gain parameter C varies with the choice of the voltage as

$$C = \text{proportional } (P_o)^{1/3} (V_o)^{-1/2}$$

with

P_o = beam power.

The conversion efficiency therefore increases with lower values of the beam voltage. A lower limit for the voltage is given by the degrading effect of the space charge, which increases with lower beam voltage values (assuming constant beam power). Optimum efficiencies can be obtained with

a value of the space charge parameter $QC^{15,18}$

$$QC \approx .2 .$$

This corresponds to a beam perveance of approximately 1 μp . This is true only for a conventional design. When velocity resynchronization is used, the beam voltage should be higher, with a lower space charge parameter value of approximately

$$QC \approx .05 \text{ to } .10 .$$

The corresponding beam perveance is then also found to be lower.

With velocity resynchronization the conversion efficiency depends also on the gain parameter C. However, with collector depression the efficiency varies very little with the voltage choice (within the optimum space charge parameter values) and design rules for velocity resynchronization circuits have not yet been established. An optimum design has to be determined by the trial and error approach.

It was found that the 850 MHz and 2 GHz tubes could be designed with high enough voltages to permit a PPM focusing design without degradation of efficiency, and their voltage choice was determined by stability requirements of the PPM focusing.

This was not the case, however, for the 8 GHz and 11 GHz tubes; their voltage was chosen to achieve optimum efficiency, and these tubes have to be solenoid focused. PPM focusing for these tubes would have required excessively high voltages to assure focusing stability, with a resulting degradation in efficiency. PM focussing is not feasible because of its rather low field limitations.

The interaction impedance K can further be increased by choosing a phase angle \emptyset (for one period) very close to the lower cut-off frequency of the circuit. However, phase linearity considerations impose a minimum phase angle requirement as discussed in the next section. However, there are other design parameters of the coupled cavity structure which can be optimized for a high interaction impedance.

One is a choice of the gap to period ratio of

$$g/\ell_c \approx .2.$$

The cavity height h can be maximized by reducing the wall thickness of the circuit. The cavity height reduction, however, is limited by

- a. structural considerations
- b. thermal considerations to achieve good heat flow from the ferrules
- c. for PPM focusing by magnetic saturation effects of the cavity wall, which also serves as a magnetic pole piece.

The propagation parameter γr_a determines the rate of the radial circuit field (impedance) reduction in the beam cross section. With lower γr_a values the field reduction becomes smaller; however, space charge debunching effects become stronger and there is an optimum choice for γr_a of .8.

With velocity resynchronization the choice of the relative beam velocity (voltage) of the driver section deserves special consideration. This parameter determines the efficiency of the driver section, but also the beam modulation which enters the resynchronization section. This beam modulation is a rather important factor in making the velocity resynchronization effective. The beam modulation of a modulated electron beam

at large signal levels is generally rather complex, but of significance is primarily the beam modulation current at the fundamental frequency. This is the only component of the beam modulation which is capable of energy transfer to the slow-wave circuit.

In Figure 61 the computed fundamental and harmonic beam modulation current at saturation have been plotted as a function of the velocity parameter b for typical tube conditions. The velocity parameter b is defined by¹⁸

$$b = \frac{1}{C} \left[\frac{u_o}{v_p} - 1 \right]$$

where

u_o = dc beam velocity

v_p = circuit phase velocity.

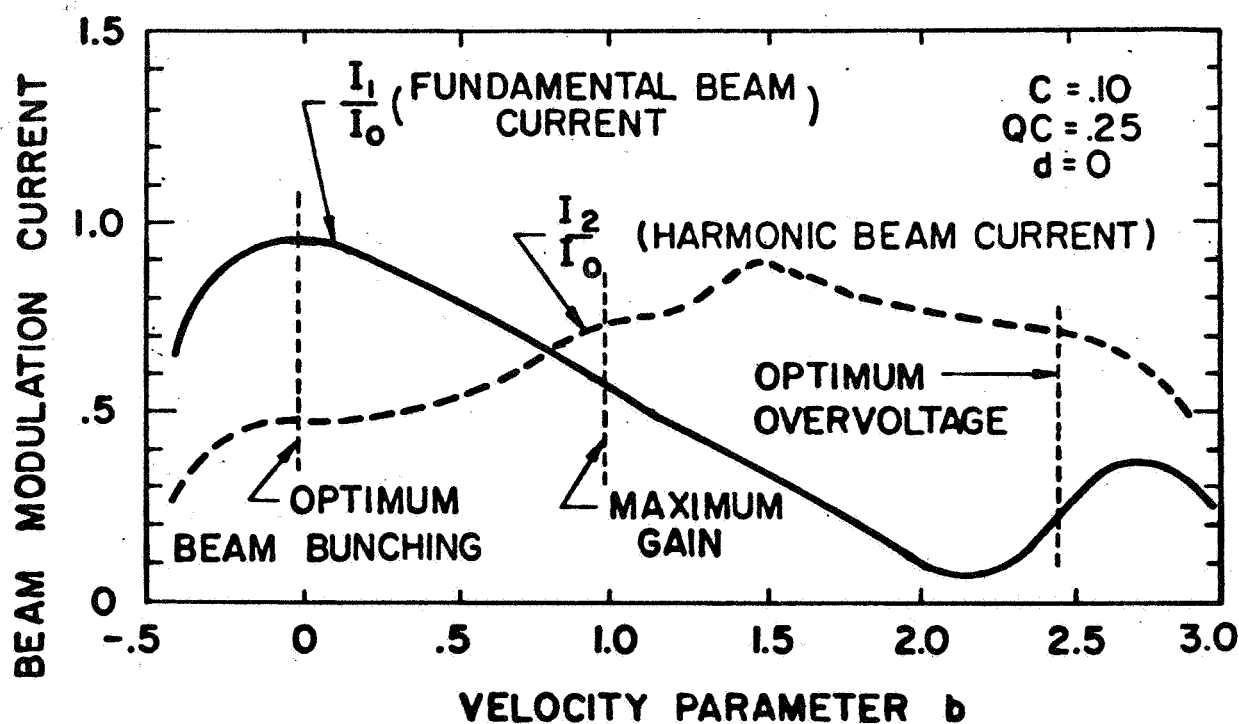


Figure 61 Fundamental and harmonic beam modulation current at saturation (computed).

It can be seen that the magnitude of the fundamental beam modulation current increases with smaller b values, until it reaches a maximum at the "optimum beam bunching voltage," which is lower than the maximum gain voltage. This "optimum beam bunching voltage" in the driver section provides indeed the largest efficiency enhancement with velocity resynchronization, even though the initial efficiency is then rather low. At this voltage the harmonic beam current is comparatively small. At the "optimum overvoltage," on the other hand, the fundamental beam current is rather small, and practically no further efficiency improvement is possible with velocity resynchronization, at least not with the methods described here. At this voltage the harmonic beam modulation current is comparatively large.

For the tube designs the propagation parameter was chosen to be

$$\gamma r_a = .80$$

and the velocity parameter b to be

$$b = 0.$$

2. Phase Linearity and Bandwidth Considerations

Transmission of television signals requires a very high degree of phase linearity of the transmission system. The phase characteristics of a slow-wave structure can readily be derived from its equivalent circuit.

The coupled cavity circuit can be represented by an equivalent lumped circuit as shown in Figure 62.

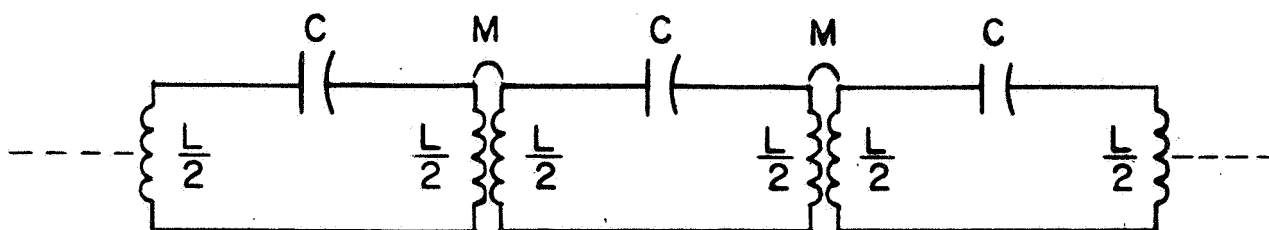


Figure 62 Equivalent circuit for coupled cavity structure.

L and C are the elements of the cavity alone while M is the mutual inductance of the coupling hole.

The network shown in Figure 62 can be transposed into an equivalent ladder network consisting of T-sections as shown in Figure 63.

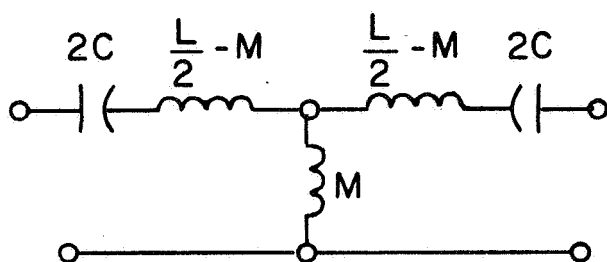


Figure 63

Equivalent T section of coupled cavity circuit.

The phase characteristics of a T-section network as shown in Figure 64 are generally given by

$$\cos \varphi = 1 + \frac{Z_1}{Z_2}.$$

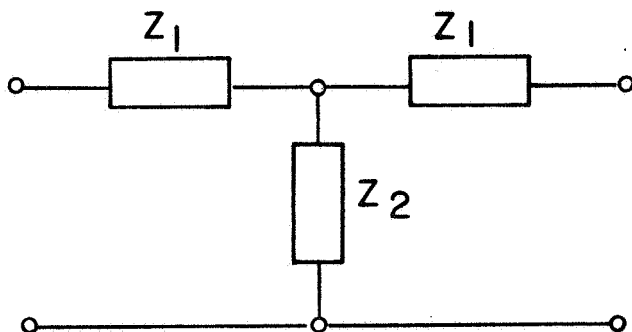


Figure 64

T section ladder network.

The dispersion characteristics of the equivalent circuit of Figure 63 are therefore

$$\cos \psi = \frac{L}{2M} - \frac{1}{2\omega^2 CM}.$$

The cut-off frequencies are determined by the conditions:

$$\text{Lower cut-off frequency } f_1: \frac{2}{Z_1} + \frac{1}{Z_2} = 0$$

$$\text{Upper cut-off frequency } f_2: Z_1 = 0$$

For narrow-bandwidth circuits, the phase characteristics can be approximated by

$$\cos \psi = \frac{f_m}{\Delta f_c} \left[1 - \frac{1}{2} \left(\frac{f_m}{f} \right)^2 \right]$$

with

$$f_m = \frac{f_1 + f_2}{2}$$

$$\Delta f_c = f_2 - f_1$$

$\psi = \beta \ell_c$, phase angle per period.

β = circuit propagation parameter

The phase deviation $\frac{d\psi}{df}$ is therefore

$$\frac{d\psi}{df} = \left(\frac{f_m}{f} \right)^3 \frac{1}{\Delta f_c \sin \psi}.$$

The phase deviation has been plotted in Figure 65 for a circuit with a cold bandwidth Δf_c of

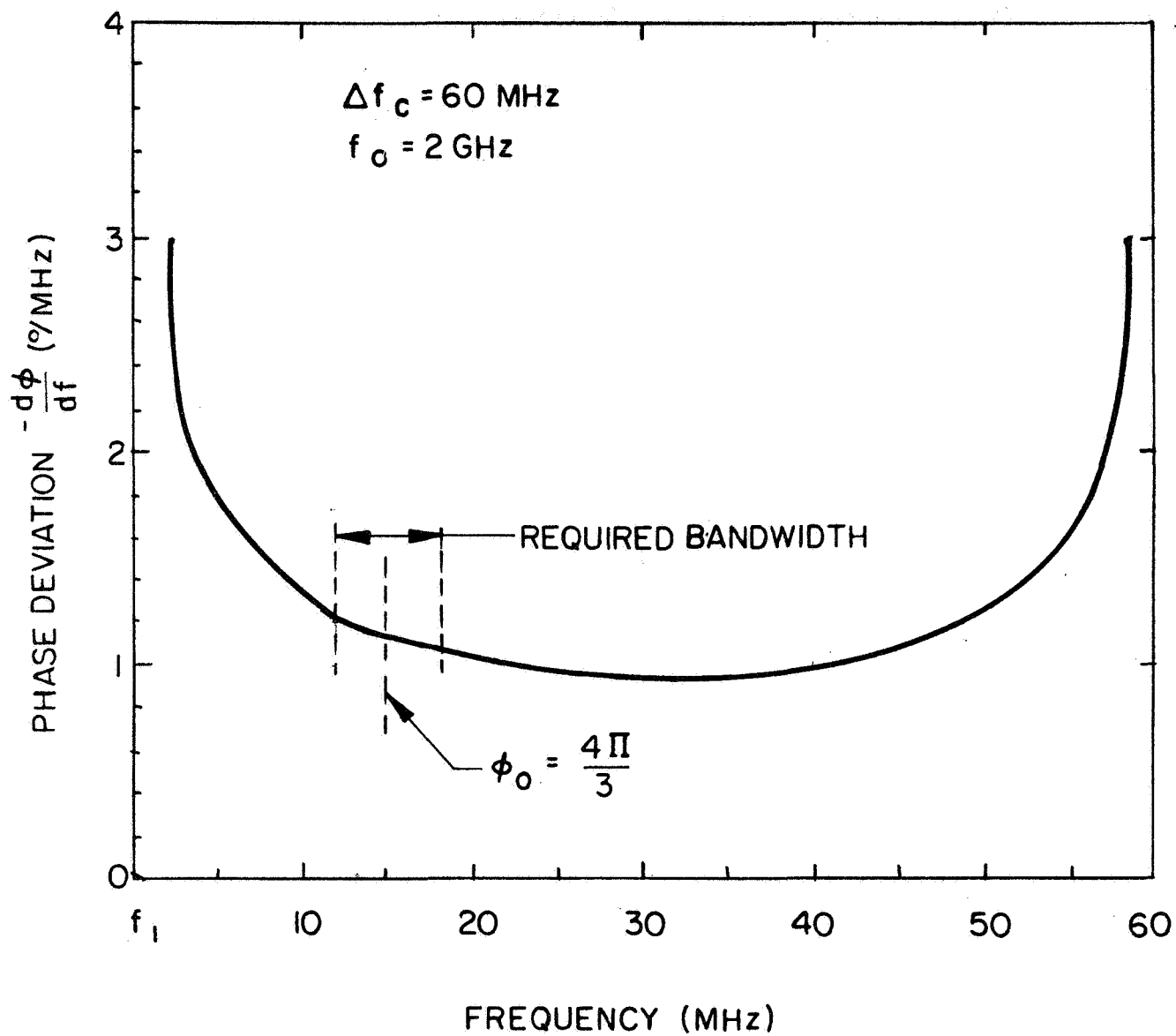


Figure 65 Phase deviation of coupled cavity circuit.

$$\Delta f_c = 60 \text{ MHz}$$

for the 2 GHz tube.

These data suggest choosing a phase angle ϕ_o for the center frequency of

$$\phi_o = \frac{4\pi}{3}$$

in order to keep the phase deviation within a specified maximum value of

$$\frac{d\psi}{df} \text{ (max.)} = -1.2^\circ/\text{MHz}.$$

The phase deviation at the center frequency f_o is found to be

$$\frac{d\psi}{df} \text{ (850 MHz)} = -1.16^\circ/\text{MHz}$$

$$\frac{d\psi}{df} \text{ (2 GHz)} = -1.12^\circ/\text{MHz}.$$

In Figure 66 the phase deviation at the center frequency ($\psi_o = 4\pi/3$) has been plotted as a function of the cold bandwidth. It can be seen that a cold bandwidth Δf_c of less than 60 MHz is inadequate to meet the phase deviation requirements for amplitude modulation.

The AM tubes are therefore designed for a cold bandwidth Δf_c of

$$\Delta f_c = 60 \text{ MHz}$$

with a center frequency phase angle of

$$\psi_o = \frac{4\pi}{3}.$$

For the FM tubes the specified second order phase deviation $\frac{d^2\psi}{df^2}$ is

$$\frac{d^2\psi}{df^2} = .05^\circ/(\text{MHz})^2 \text{ maximum}$$

$$\frac{d^2\psi}{df^2} = < .015^\circ/(\text{MHz})^2 \text{ desired.}$$

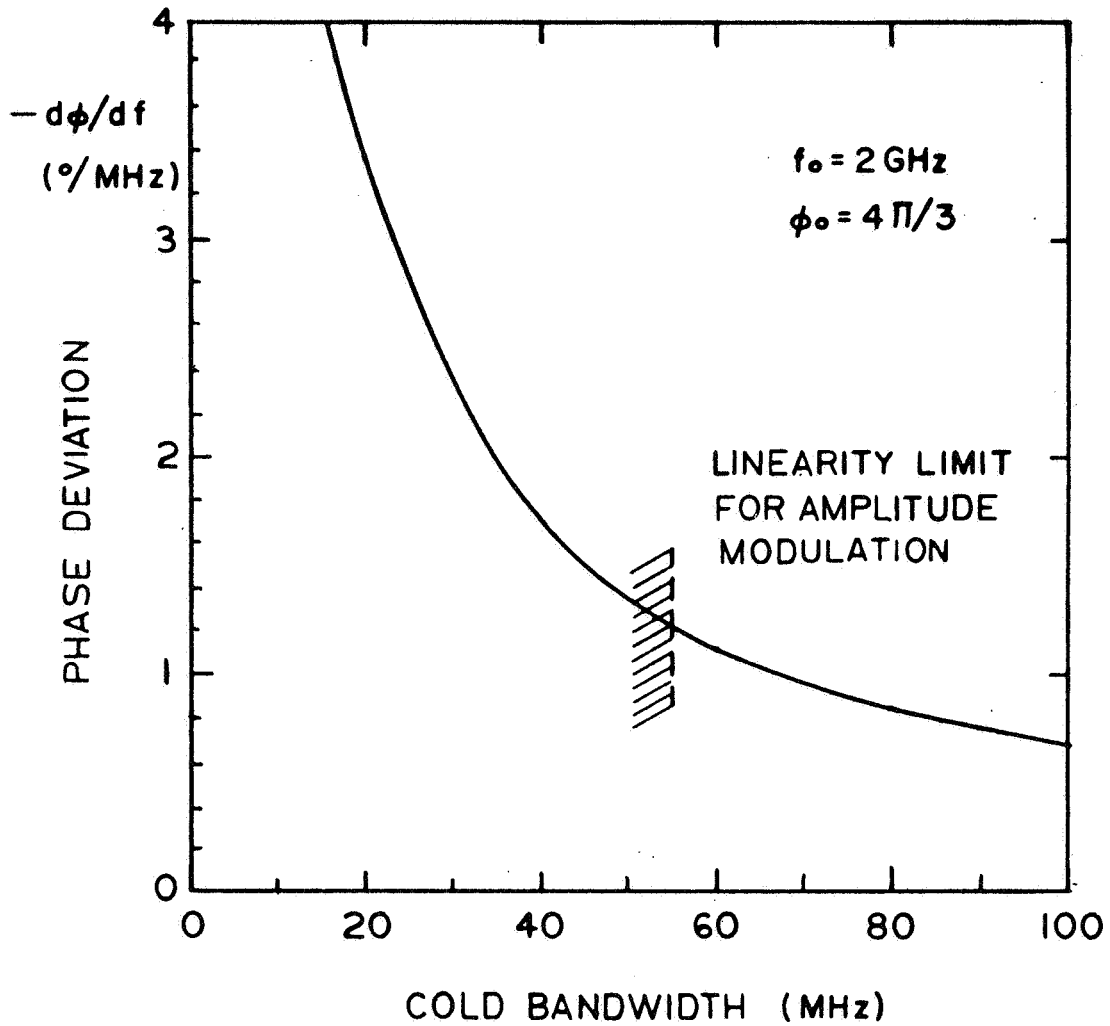


Figure 66 Phase deviation and bandwidth for coupled cavity circuit.

For narrow bandwidth coupled cavity tubes the second order phase deviation can be expressed by

$$\frac{d^2\phi}{df^2} = \left(\frac{f_m}{f}\right)^3 \frac{3}{f \Delta f_c \sin \phi} - \left(\frac{f_m}{f}\right)^6 \frac{\cos \phi}{\Delta f_c^2 \sin^3 \phi}$$

This has been plotted for the 2 GHz tube with $\Delta f_c = 60$ MHz cold bandwidth in Figure 67. These data also suggest to choose a phase angle ϕ_o for the center frequency of

$$\phi_o = \frac{4\pi}{3}$$

in order to keep the second order phase deviation small enough.

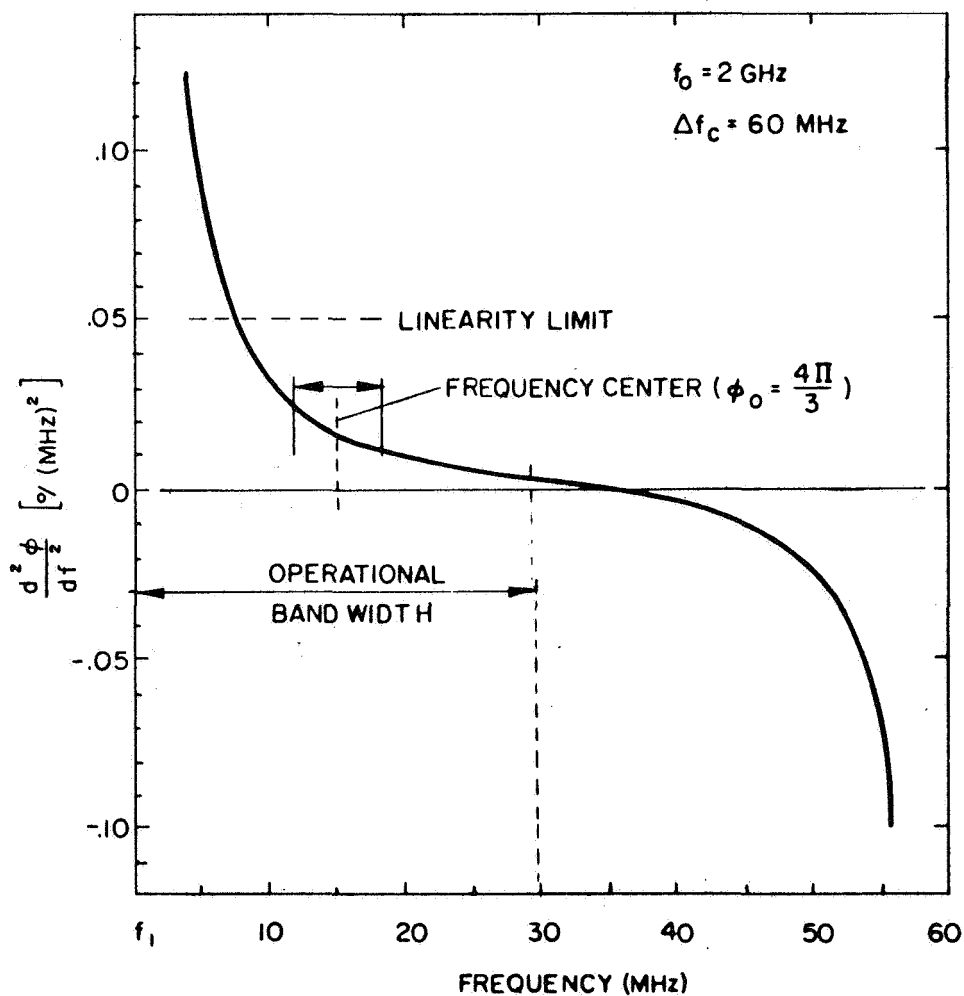


Figure 67 Second order phase deviation for coupled cavity circuit.

At the center frequency ($\phi_0 = \frac{4\pi}{3}$) the second order phase deviation is found for a 60 MHz cold bandwidth to be

$$\frac{d^2\phi}{df^2} (2 \text{ GHz}) = .0145^\circ / (\text{MHz})^2$$

$$\frac{d^2\phi}{df^2} (8 \text{ GHz}) = .0130^\circ / (\text{MHz})^2$$

$$\frac{d^2\phi}{df^2} (11 \text{ GHz}) = .0128^\circ / (\text{MHz})^2.$$

In Figure 68 the second order phase deviation is shown at the center frequency as a function of the cold bandwidth Δf_c . A cold bandwidth choice of

$$\Delta f_c = 60 \text{ MHz}$$

appears to be adequate to meet the phase linearity requirements of the FM tubes and has therefore been used as a design basis for these tubes.

The phase linearity considerations given above do not include the effects of beam loading on the circuit. These effects cannot as yet be analyzed. Should these effects be found to be detrimental to the phase linearity, it would be easy to restore the required linearity by an appropriate increase of the cold bandwidth, however, at some expense of interaction impedance and electronic efficiency.

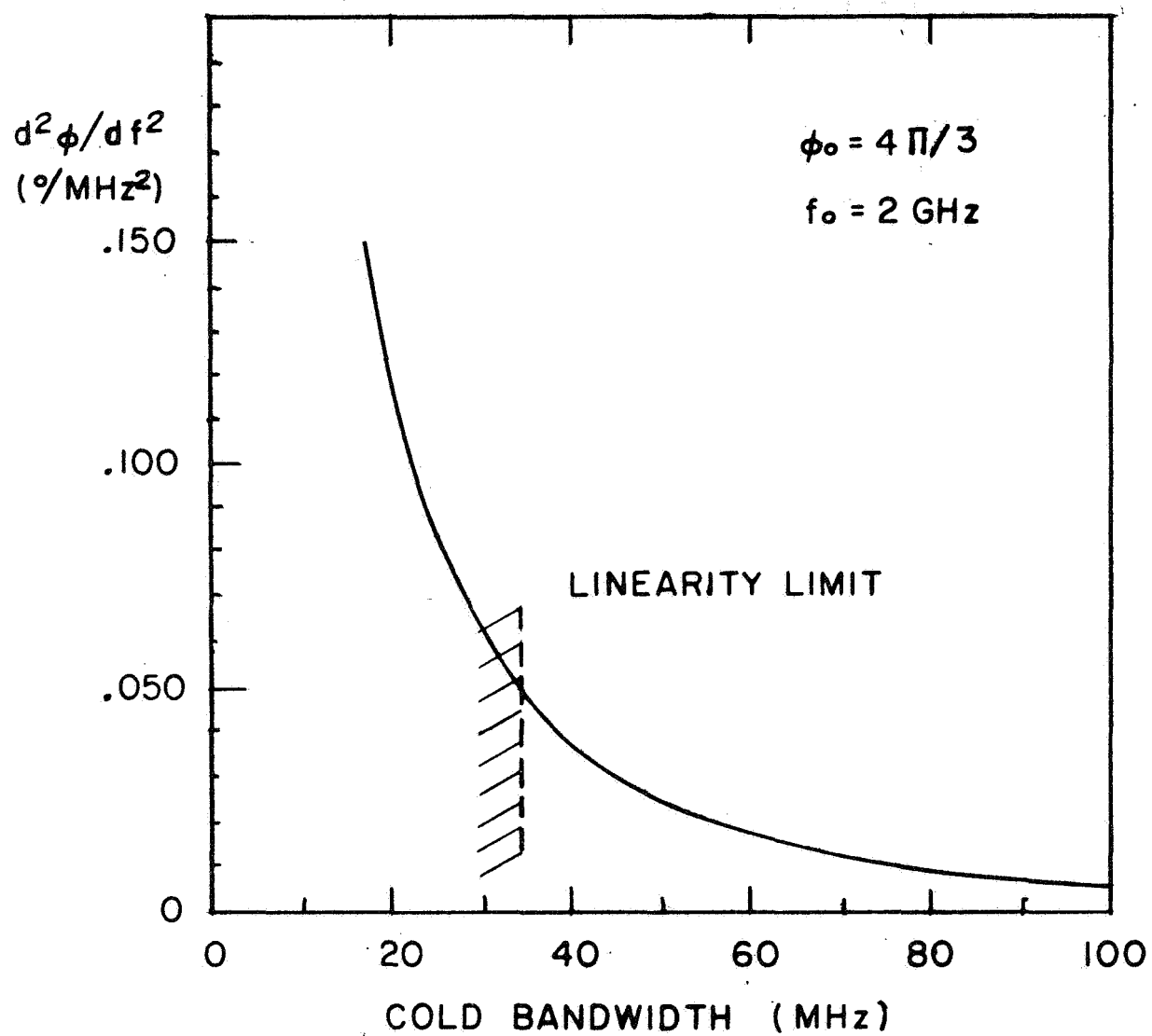


Figure 68 Second order phase deviation and bandwidth for coupled cavity circuit.

3. Cold Tests on Coupled Cavity Circuit Structures and Evaluation of Dielectric Loading

Cold Tests Without Dielectric Loading

The interaction impedance of the slow wave structure is an important parameter in designing a high efficiency traveling-wave tube. In order to obtain more realistic data for these designs, cold test circuits were designed and built to evaluate the interaction impedance empirically. The circuit design was based on the procedures outlined in the previous sections. The final dimensions of the cavity radius r_3 and the slot width W (Figure 69) were adjusted empirically to achieve the desired cut-off frequency and bandwidth. These dimensions agree closely with the predicted design dimensions. The empirical frequency and bandwidth adjustments were discontinued when an approximate frequency and bandwidth performance was obtained. The resultant cavity dimensions are given in Table XII.

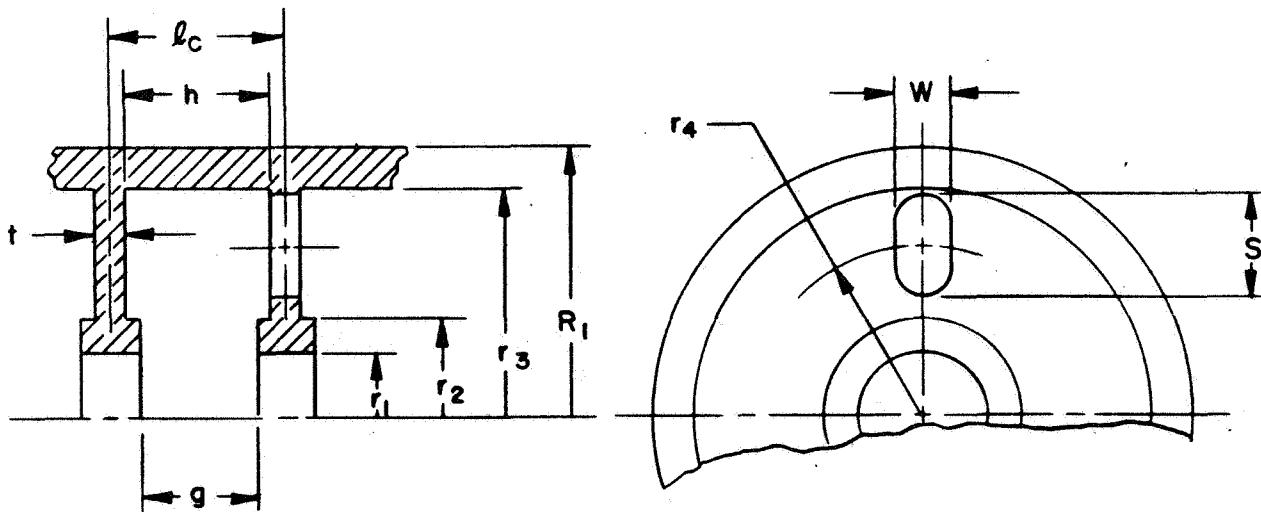


Figure 69 Schematic of coupled cavity circuit.

Table XII Coupled cavity dimensions for cold tests.

	S-BAND	X-BAND
V_o	8.8 kV	10.5 kV
f_o	2.03 GHz	8.05 GHz
Δf_c	55.3 MHz	44.6 MHz
$2r_1$.75 cm (.295 in)	.203 cm (.080 in)
$2r_2$.952 (.375 in)	.355 cm (.140 in)
$2r_3$	10.17 cm (4.000 in)	2.465 cm (.970 in)
$2r_4$	5.84 cm (2.300 in)	1.485 cm (.585 in)
ℓ_c	1.853 cm (.730 in)	.508 cm (.200 in)
t	.203 cm (.080 in)	.127 cm (.050 in)
h	1.65 cm (.650 in)	.381 cm (.150 in)
g	.371 cm (.146 in)	.102 cm (.04 in)
S	4.32 cm (1.700 in)	.98 cm (.385 in)
W	2.92 cm (1.150 in)	.381 cm (.150 in)

The resultant frequency versus phase diagram for the S-band circuit is shown in Figure 70.

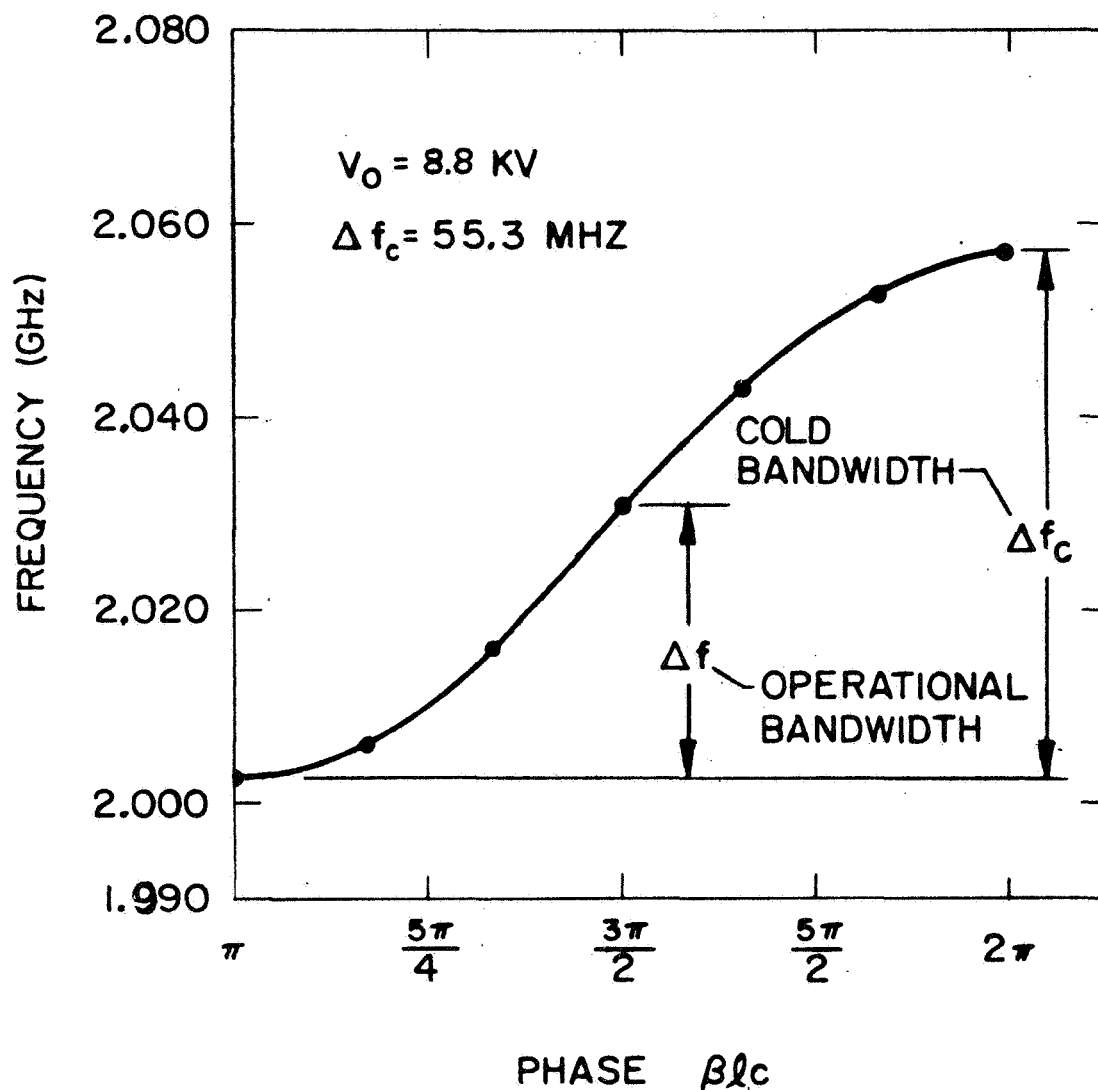


Figure 70 Dispersion diagram for 2 GHz coupled cavity circuit (measured).

The measured interaction impedance K of these structures, as obtained with a perturbation method, are shown in Figures 71 and 72.

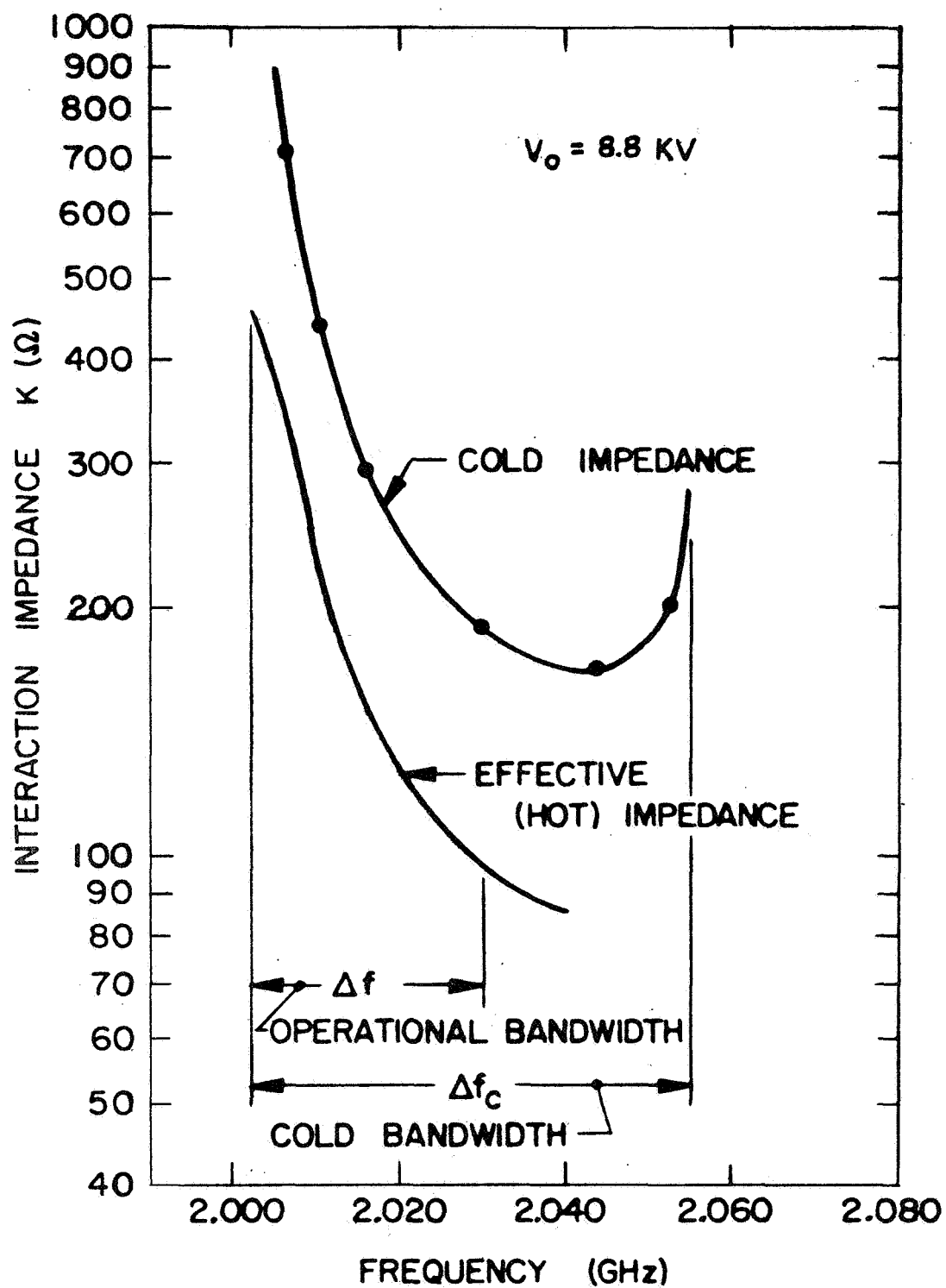


Figure 71 Interaction impedance of 2 GHz coupled cavity circuit (measured).

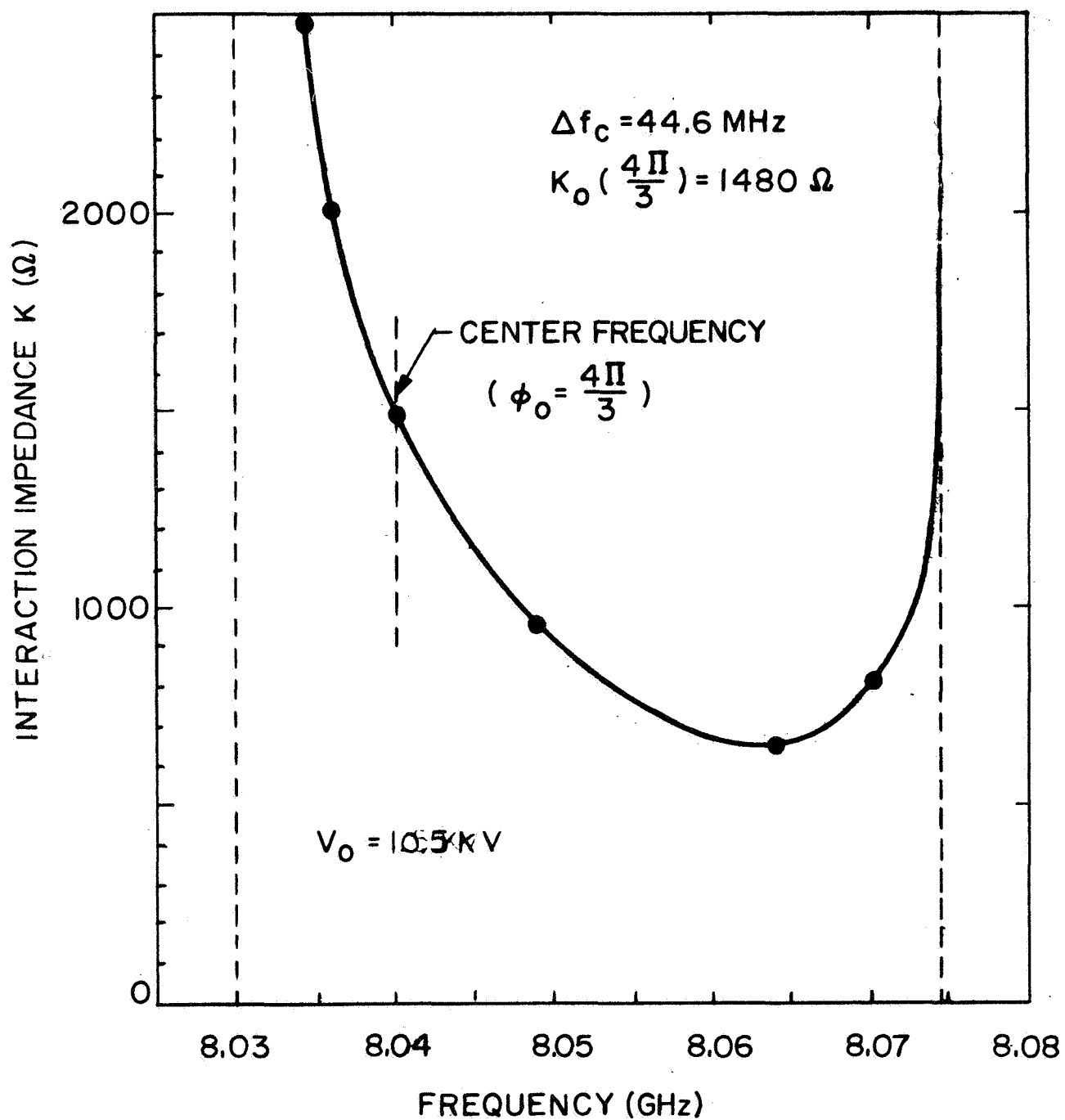


Figure 72 Cold interaction impedance of X-band circuit (measured).

In a number of previous experiments, it has been established, that the effective interaction impedance K' of a coupled cavity tube is reduced by a factor of approximately 2 due to electronic beam loading effects, or

$$K' \text{ (effective)} \approx 1/2 K \text{ (cold)}$$

as illustrated in Figure 71 for the S-band circuit. It is also well established that the effective interaction impedance remains finite at the lower cutoff frequency. High efficiency has been demonstrated with many coupled cavity tubes at this frequency.

Following conventional design procedures, the cold bandwidth Δf_c of a coupled cavity circuit is designed to be twice as large as the operational bandwidth Δf of the tube, such that the lower half of the frequency range is used, with the center frequency producing a phase angle $\beta_o \ell_c$ of

$$\beta_o \ell_c = \frac{4}{3} \pi$$

in one cavity.

The effective interaction impedance K' at the operational center frequency ($\varphi = \frac{4}{3}\pi$) is therefore for the two testers:

	2 GHz	8 GHz
$K' (\varphi = \frac{4}{3}\pi)$	148 Ω	740 Ω

From these data the interaction impedance can be scaled to other circuits by

$$K = \text{proportional } (V_o)^{1/2} \left(\frac{\Delta f}{f_o} \right)^{-1} \cdot \left(\frac{h}{\ell_c} \right).$$

Evaluation of Dielectric Loading on Coupled Cavity Circuit

The diameter of coupled cavities can be significantly reduced, when the cavity is filled with a dielectric material. Such dielectric loading, may, therefore, accomplish a considerable size and weight reduction, especially for lower frequency tubes, provided the interaction impedance and consequently the efficiency does not become degraded.

Cold tests were therefore undertaken to evaluate the effect of dielectric loading, using the X-band circuit described above as a test vehicle. "Stycast" material with a dielectric constant ϵ of

$$\epsilon = 6$$

and

$$\epsilon = 9$$

was used to simulate the dielectric properties of Beryllia (BeO) and Alumina.

This material can be machined, and therefore it is easy to fabricate. The higher losses of this material do not significantly affect the properties to be evaluated (impedance and phase velocity). The coupling slot width W (bandwidth) was increased to facilitate the measurements. The size of the dielectric discs was chosen to completely fill the cavity space between the outer radius (r_2) of the ferrule and the wall (r_3) of the cavity. The coupling slot between cavities was not filled with dielectric. The frequency versus phase data of these experiments are shown in Figure 73.

The resultant circuit characteristics with dielectric loading have to be compared to those of an equivalent unloaded circuit with the same frequency, bandwidth, and voltage (period). One obtains an effective dielectric constant ϵ' , which determines the cavity radius r_3' ($\epsilon = 1$)

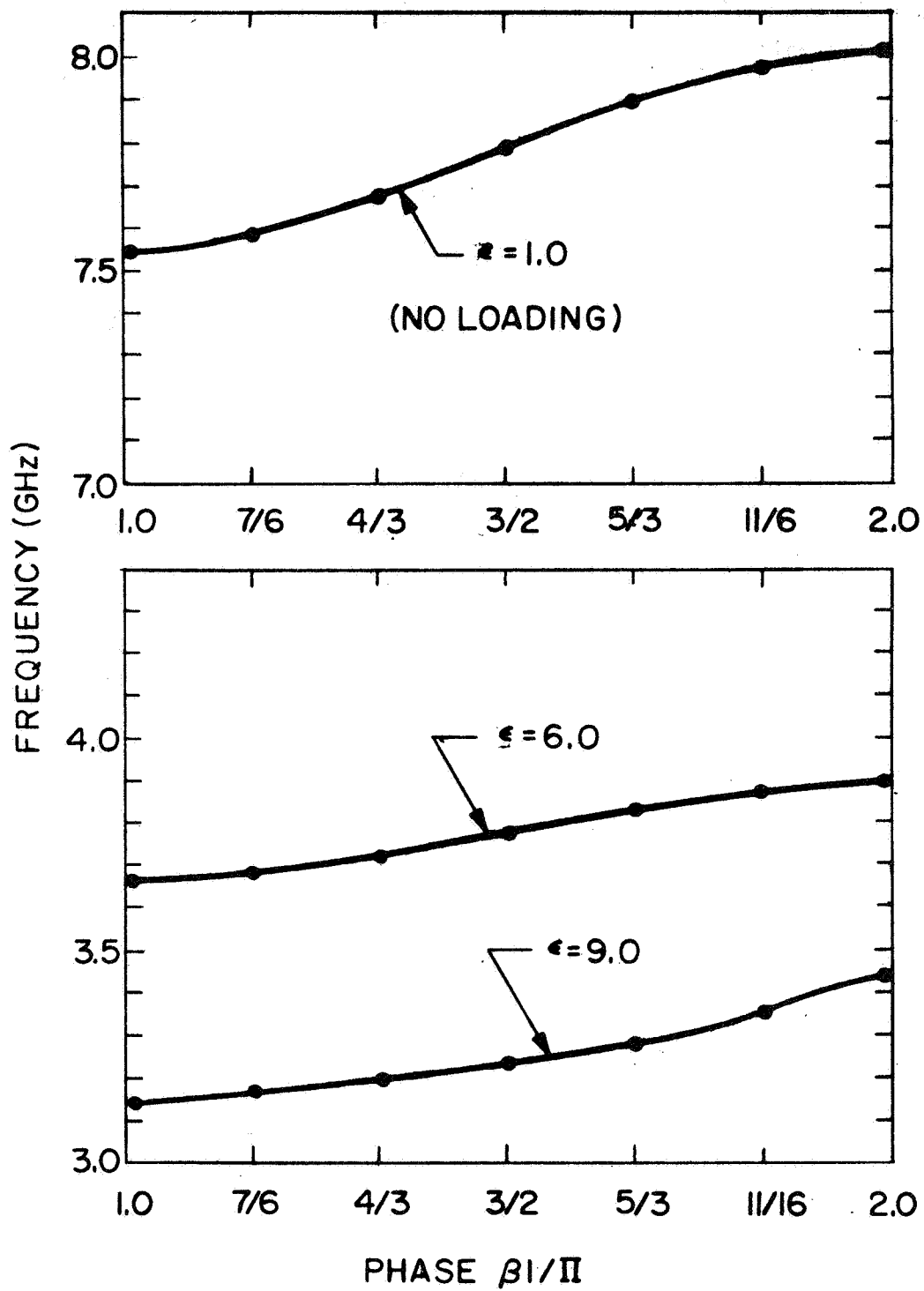


Figure 73 Phase diagrams for dielectrically loaded coupled cavity circuits (measured).

of the equivalent unloaded circuit, or

$$\frac{r_3(\epsilon)}{r_3'(\epsilon = 1)} = (\epsilon')^{-1/2}.$$

Of particular concern is the comparison of the interaction impedance K (at a given phase angle θ_0) with that of the equivalent unloaded circuit K' , expressed by an impedance factor F_k :

$$F_k = \frac{K'(\epsilon)}{K(\epsilon = 1)}.$$

These comparison data have been compiled in Table XIII below:

Table XIII Comparison of dielectrically loaded circuit with equivalent unloaded circuit.

		$\epsilon = 1.0$	$\epsilon = 6$	$\epsilon = 9$
Upper Cutoff Frequency	f_2 (GHz)	8.005	4.007	3.371
Lower Cutoff Frequency	f_1 (GHz)	7.530	3.715	3.114
Bandwidth	$\frac{\Delta f}{f_0}$	6.15%	7.70%	8.11%
Interaction Impedance	$K(\varphi = 4\pi/3)$	120.8 Ω	51.2 Ω	45.4 Ω
Circuit Voltage	$V(\varphi = 4\pi/3)$	9.78 kV	2.37 kV	1.66 kV
Cavity Radius Reduction	$\frac{r_3(\epsilon)}{r_3'(\epsilon = 1)}$	1	.442	.373
Effective Dielectric Constant	ϵ'	1	5.10	7.18
Interaction Impedance of equivalent circuit	$K'(\epsilon = 1, \varphi = 4\pi/3)$		47.4 Ω	37.8 Ω
Impedance Factor	F_k	1	1.08	1.20

These data show that a significant diameter reduction of the coupled cavity can indeed be accomplished with dielectric loading. This dielectric loading is accomplished with a slight increase of the interaction impedance.

The dielectric loading method is therefore applied to the design of the 850 MHz and 2 GHz tubes to reduce their diameter and weight.

It is therefore proposed to use Alumina ($\epsilon = 9$) as a dielectric loading material for the design of the 850 MHz and 2 GHz tubes. This material provides a larger diameter reduction compared to Beryllia loading.

Such dielectric loading will also significantly improve the heat flow from the cavity ferrule to the outside of the tube, primarily because the radial conduction path in the cavity wall is much shorter.

The dielectric loading will however increase the losses due to the dielectric losses in the ceramics, but only to an insignificant extent for the 850 MHz and 2 GHz tubes.

The interaction impedance K' , including the effect of the beam loading and of the dielectric loading with Alumina, are therefore for the tubes at $\varphi = \frac{4\pi}{3}$ and for $\Delta f_c = 60$ MHz:

	850 MHz	2 GHz	8 GHz	11 GHz
K' (ohms)	89	189	550	820
ϵ	9	9	1	1

4. Experimental Evaluation of Circuit Losses

The efficiency of traveling-wave tubes can be significantly affected by the intrinsic losses of the slow wave structure, especially at higher frequencies. The effect of the circuit losses is therefore included in the large signal computer program. The loss is generally expressed by the loss parameter d , defined as:

$$d = \frac{\alpha}{\beta_e C}$$

with

α = loss constant

β_e = electronic propagation parameter.

A realistic evaluation of the coupled cavity circuit losses is only possible experimentally with cold tests. The loss L of an existing coupled cavity circuit at C-band was therefore measured. The circuit consisted of an unbrazed stack of coupled cavities made of copper with an input and output coupler.

The loss constant is then determined to

$$\alpha = \frac{L(\text{dB})}{8.69\ell}$$

with

ℓ = circuit length.

For the measured circuit the loss constant was

$$\alpha_c = 3.88 \cdot 10^{-3} / \text{cm} \quad (f_o = 4.7 \text{ GHz} , K' = 22 \text{ ohms}).$$

It can be shown, that the loss constant α_c of a coupled cavity circuit varies with frequency as

$$\alpha_c = \alpha (f)^{1/2} (K)^{-1}.$$

With this scaling the loss constant can be estimated for all tube designs.

The dielectric loading of the 850 MHz and 2 GHz tube circuits will increase these circuit losses by those of the dielectric α_d , or

$$\alpha = \alpha_c + \alpha_d.$$

The dielectric losses α_d can in good approximation be expressed by

$$\alpha_d = \frac{\pi f}{c} (\epsilon)^{1/2} \tan \delta$$

with

$\tan \delta$ = loss tangent of dielectric material

c = velocity of light .

The dielectric losses increase proportional to the frequency and thus become quite significant with higher frequencies.

A number of low loss dielectric materials are available, which can be used in vacuum tubes. Among these, Alumina and Beryllia are frequently used in tubes. Their dielectric properties at microwave frequencies are known as follows:

	ϵ	$\tan \delta$
Beryllia (BeO)	6	.0005
Alumina (Al ₂ O ₃)	9	.0003

Neither the dielectric constant ϵ nor the loss tangent change significantly with frequency or with temperature (up to about 500°C).

The loss constants for the tubes, assuming dielectric loading, are therefore estimated to

	850 MHz	2 GHz	8 GHz	11 GHz
α_d (cm ⁻¹)	$8.5 \cdot 10^{-5}$	$1.88 \cdot 10^{-4}$	---	---
α_c (cm ⁻¹)	$4.7 \cdot 10^{-4}$	$3.37 \cdot 10^{-4}$	$2.3 \cdot 10^{-4}$	$1.82 \cdot 10^{-4}$
α_{total} (cm ⁻¹)	$5.5 \cdot 10^{-4}$	$5.25 \cdot 10^{-4}$	$2.3 \cdot 10^{-4}$	$1.82 \cdot 10^{-4}$

It can be seen, that the dielectric losses at the low frequencies are relatively small compared to the ohmic losses.

5. Coupled Cavity Structure Design

The design parameters of the tubes, primarily the choice of the beam voltage V_0 , were varied, and the efficiencies were computed with a large signal computer program to arrive at an optimum efficiency design within the thermal and focusing constraints. For a given set of tube parameters the cavity dimensions for a required frequency and bandwidth can be calculated from the field equations of a coupled cavity, which include the effect of the ferrule and the coupling slot.

The cavity dimensions (Figures 69 and 74) are obtained from the solution of a transcendental equation (Bessel functions)^{20,21}. In practice these dimensions are found to be accurate to about 5%, and empirical corrections of the cavity radius r_3 and of the coupling angle θ are required to obtain the desired frequency and bandwidth.

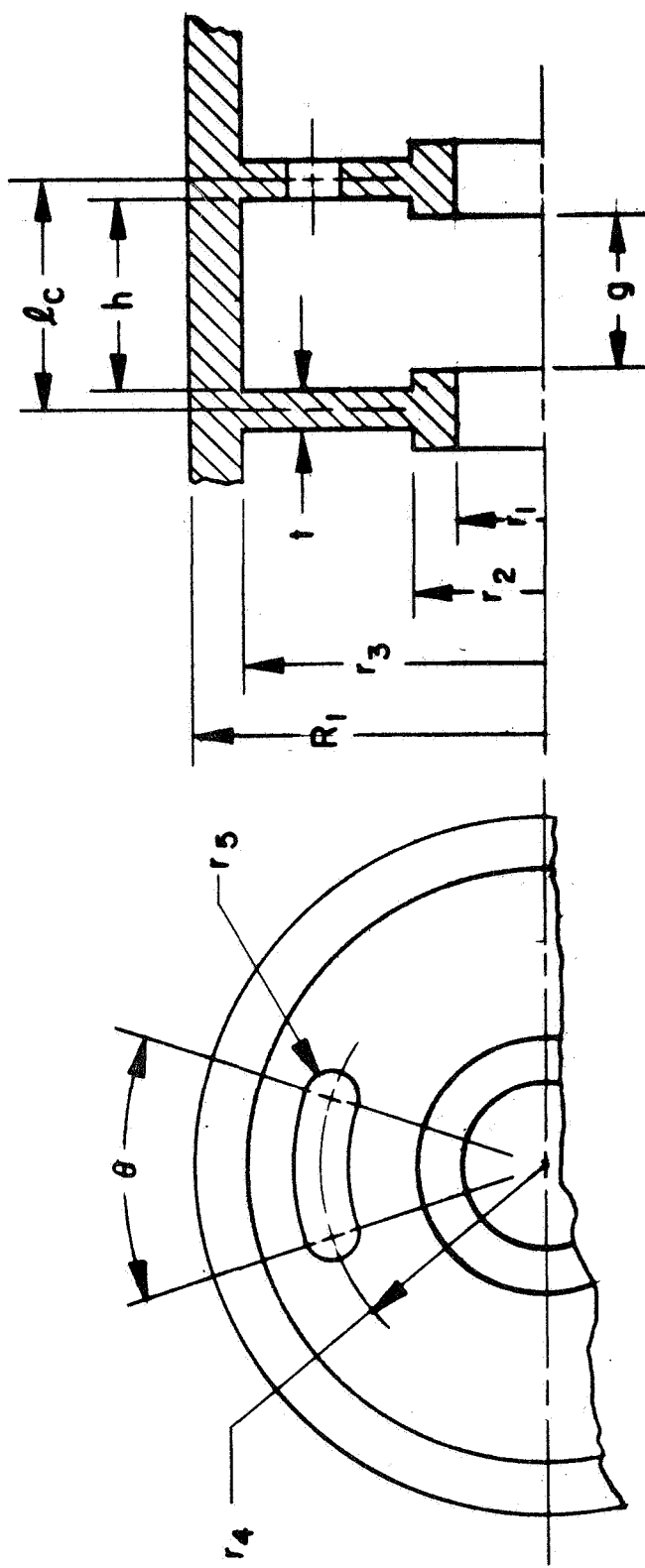


Figure 74 Schematic of coupled cavity circuit.

The outside radius R_1 of the cavity has to be chosen to provide adequate structural strength to the structure. A wall thickness of .050" to .100" can be considered sufficient for this purpose. For the voltage jump cavity, however, provisions must be made to incorporate a choke in the cavity wall to eliminate RF perturbations by the insulation as shown schematically in Figure 75.

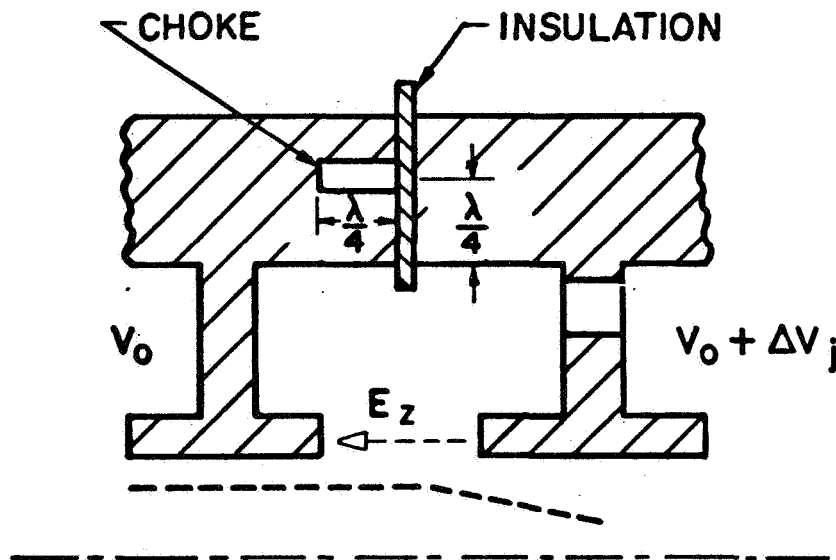


Figure 75 Voltage jump transition in coupled cavity circuit.

For this cavity a circuit wall thickness of $\lambda/2$ will be provided. It is assumed that Alumina ($\epsilon = 9$) is used for insulation and for dielectric loading. This will reduce the required electric lengths for the choke design by $(\epsilon)^{1/2}$, and the wall thickness can be reduced to $\lambda_0/6$. The outer cavity radius R_1 is then given by

$$R_1 = r_3 + \lambda_o/6.$$

For coupled cavity circuits with PPM focusing (Figure 76) the wall thickness t has to be increased to keep the magnetic flux density in the pole pieces low enough and to provide an adequate thermal path to the outside. The resultant cavity dimensions (Figure 74 and 76) are listed in Table XIV.

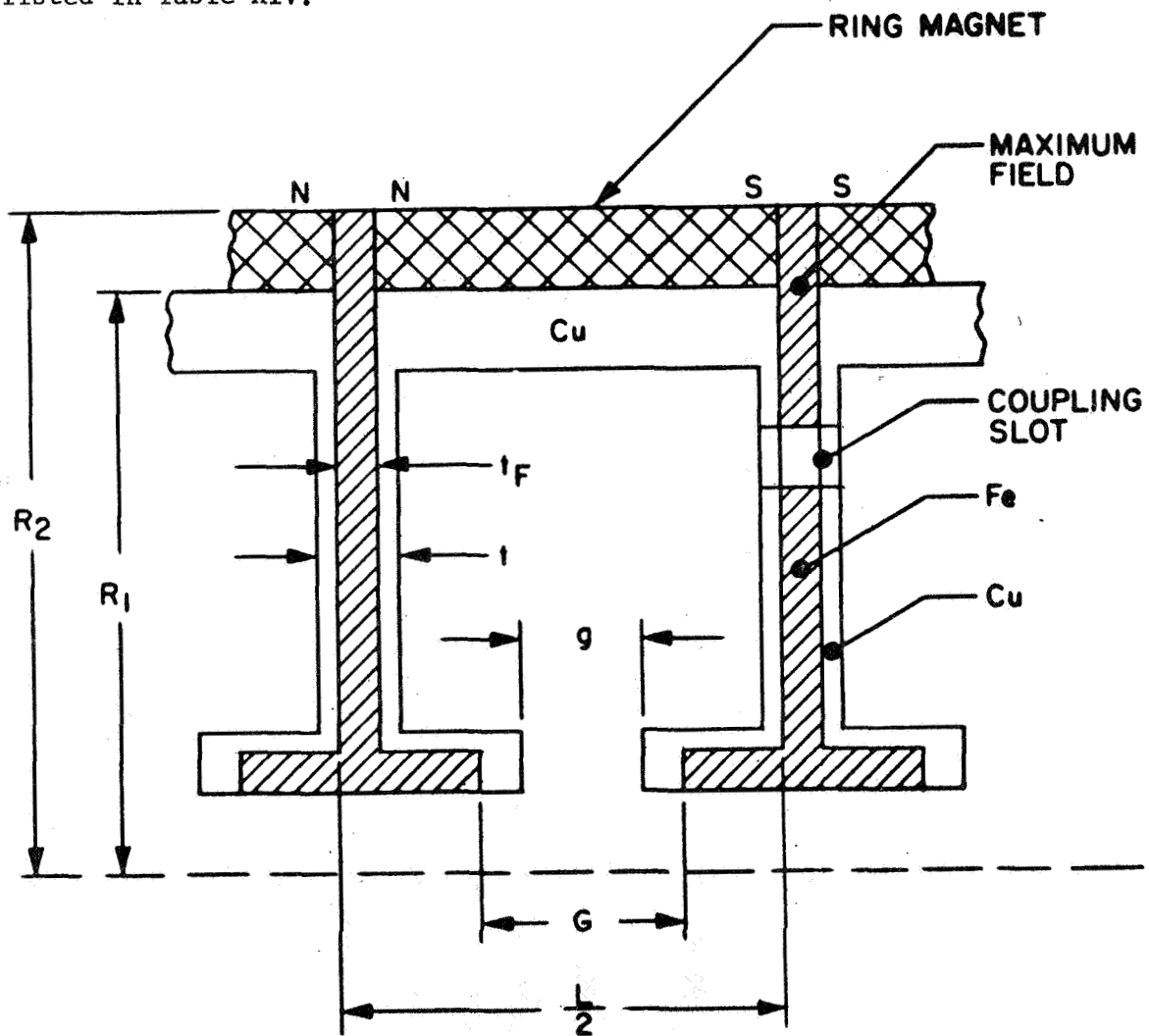


Figure 76 Schematic of permanent periodic magnet focusing structure with coupled cavity circuit.

Table XIV Dimensions of coupled cavity structures ($\Delta f_c = 60$ MHz).

f	850 MHz	2 GHz	8 GHz	11 GHz
ϵ	9	9	1	1
V_o	16 kV	13 kV	12 kV	14 kV
$2r_1$	2.25 cm (.886 in)	.864 cm (.340 in)	.208 cm (.082 in)	.162 cm (.064 in)
$2r_2$	2.505 cm (.986 in)	1.117 cm (.440 in)	.3605 cm (.142 in)	.315 cm (.124 in)
$2r_2$ (Fe)	2.403 cm (.946 in)	1.015 cm (.400 in)	---	---
ℓ_c	5.92 cm (2.33 in)	2.26 cm (.890 in)	.542 cm (.213 in)	.427 cm (.168 in)
g	1.182 cm (.466 in)	.452 cm (.178 in)	.109 cm (.043 in)	.086 cm (.034 in)
G_m (Fe)	3.942 cm (1.553 in)	1.51 cm (.593 in)	---	---
t	.419 cm (.165 in)	.292 cm (.115 in)	.127 cm (.050 in)	.127 cm (.050 in)
t_F (Fe)	.216 cm (.085 in)	.191 cm (.075 in)	---	---
$2r_3$	8.75 cm (3.444 in)	3.758 cm (1.48 in)	2.46 cm (.970 in)	1.772 cm (.698 in)
$2R_1$	23.05 cm (9.072 in)	11.30 cm (4.448 in)	6.26 cm (2.462 in)	5.21 cm (2.056 in)
r_4	2.82 cm (1.110 in)	1.22 cm (.480 in)	.744 cm (.293 in)	.552 cm (.217 in)
r_5	1.55 cm (.610 in)	.6475 cm (.255 in)	---	---
θ	67.1°	34.6°	---	---
W			.437 cm (.172 in)	.297 cm (.117 in)
S			.978 cm (.385 in)	.67 cm (.264 in)

B. CIRCUIT CONFIGURATIONS WITH MULTIVOLTAGE OF JUMP TAPER

A new efficiency enhancement method, the ~~multivoltage~~ jump taper, has been introduced for the high efficiency design of the tubes. This scheme was found to be superior to the previously used voltage jump velocity taper method in efficiency, ability to focus and flexibility of adjustment. In contrast to other velocity resynchronization schemes, its design is less critical with respect to the optimum length. There is also design flexibility in the choice of the maximum overvoltage. A maximum overvoltage V_j of approximately twice the basic voltage V_o , or

$$V_j \approx 2 V_o$$

was chosen in order to keep the voltage gradients in the cavities within acceptable limits.

The tubes with FM modulation (tubes III, IV and V) are designed for 40 dB saturation gain, while the AM tubes (tubes I and II) are to be operated in the modulator chain from zero to 20 dB gain. The high gain tubes have to be designed with a sever to prevent feedback oscillations, while the modulator tubes are designed as feedthrough tubes without attenuator. However, care must be taken in the design of their input and output couplers to assure stability at the peak values of output.

The severs are either internal or external cavity terminations located approximately in the center of the circuit length. For the power levels considered internal cavity terminations appear adequate. These internal severs consist of very lossy ceramic material, which partially fills one cavity. These severs completely absorb the power of the circuit wave, and the RF energy is coupled from the input section of the circuit to

the output section by the beam modulation only. Such RF coupling in a sever between the circuit sections can only be accomplished at the expense of some power loss. That is not of great concern, since the power (gain) loss of the sever can be recovered by increasing the tube length to provide additional gain.

This is only true, however, if the sever is located in the small signal region of the tube; this can be assured by designing the output section of the tube with high enough gain. If this is not the case, the sever is found to degrade the beam modulation, and sever efficiency losses are observed. These requirements are also to be satisfied for a tube with velocity resynchronization. The gain between sever and the velocity resynchronization section must be high enough in order to avoid a degradation of the beam modulation. This important design consideration in conjunction with a sever has been evaluated with the large signal computer program, which is capable of analyzing sever problems.

The tube parameters and characteristics are generally expressed in terms of the small signal parameters and linearized gain characteristics.¹⁵ The gain G (in dB) can then be expressed by

$$G = BCN_1 - A - L_s - \Delta G_1 + \Delta G_j$$

as illustrated in Figure 77,

where

- BCN_1 = small signal gain over N_1 number of wavelengths
- BC = small signal gain per wavelength
- A = launching loss
- L_s = sever loss
- ΔG_1 = gain compression (at saturation)
- ΔG_j = gain in multi-voltage jump taper.

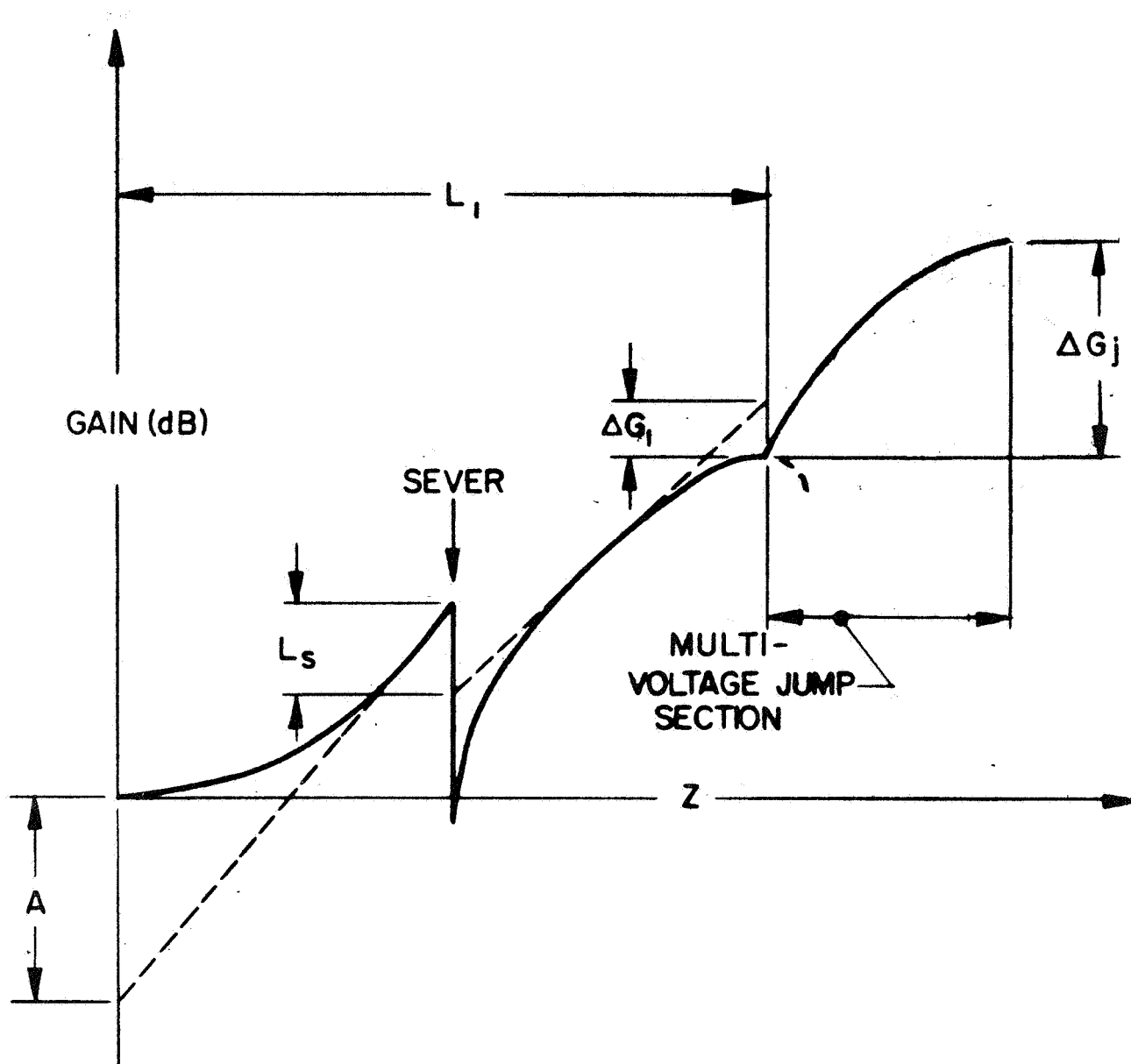


Figure 77 Linearized gain profile in multi-voltage jump taper traveling-wave tube with sever.

These parameters have been obtained by the large signal analysis. They are listed in Table XV together with the other small signal parameters and the number of cavities in the various tube sections.

The voltage profile of the multi-voltage jump taper was optimized with a new computer design technique. It was found that the optimum voltage profile did not exhibit a linear increase as expected. The optimum voltage jump taper configurations are listed in Table XVI together with their voltages V_n (above cathode potential) and voltage gradients ΔV_n .

The resultant efficiencies are in the range from 75% to 80% with multi-stage collector depression. Their values are listed in the next section.

C. EFFICIENCY ENHANCEMENT WITH MULTI-STAGE COLLECTOR DEPRESSION

A significant part of the efficiency enhancement can be achieved with a multistage depressed collector. It will be shown that for tubes employing velocity resynchronization schemes, resulting in very high conversion efficiencies, multistage depressed collectors become very effective for further efficiency enhancement. In this section the feasibility of multistage collector depression is therefore evaluated for all tubes. The optimum number of collector stages is determined, taking collector deficiencies of velocity sorting and secondary suppression into account.

The collector performance evaluation is based on a new design approach, which incorporates magnetic refocusing, transverse magnetic and electric velocity sorting, and electric suppression of secondaries as described in Section IV. D. These techniques are considered an optimum design approach for multistage collectors, but this has yet to be substantiated by analysis and experiments.

Table XV Small signal parameters for tubes.

FREQUENCY		850 MHz	2 GHz	2 GHz	8 GHz	11 GHz
Modulation		AM	AM	FM	FM	FM
Gain (dB)		20	20	40	40	40
C		.0895	.1025	.1025	.1583	.163
QC		.0812	.0513	.0513	.035	.0243
b		0	0	0	0	0
d		.009	.003	.003	.0002	.0001
Gain/cavity (dB)		2.73	3.18	3.18	4.98	6.07
A (dB)		11.03	10.8	10.8	10.31	10.12
B (dB)		45.8	46.5	46.5	47.3	55.7
L_s (dB)		5.4	5.0	5.0	2.7	2.2
ΔG_1 (dB)		4.61	4.13	4.13	3.68	4.04
ΔG_j (dB)		3.3	+3.5	3.56	2.56	2.40
Input section		12	10	19	12	12
Beyond sever		--	---	5	5	5
Multivoltage jump taper		10	7	7	6	5
Total		22	17	26	18	17
Number of Cavities						

Table XVI Multivoltage jump taper configurations.

FREQUENCY	850 MHz		2 GHz		8 GHz		11 GHz	
	16 kV		13 kV		12 kV		14 kV	
CAVITY NUMBER	V (kV)	ΔV (kV)	V (kV)	ΔV (kV)	V (kV)	ΔV (kV)	V (kV)	ΔV (kV)
1	21.15	5.15	17.66	4.66	16.8	4.8	19.6	5.6
2	21.15	0	17.66	0	16.8	0	19.6	0
3	21.15	0	19.95	2.29	19.9	3.1	23.56	3.96
4	22.62	1.47	22.24	2.29	23.0	3.1	27.52	3.96
5	24.08	1.46	24.53	2.29	26.1	3.0	31.5	3.96
6	25.55	1.47	26.82	2.29	26.0	0	---	---
7	27.01	1.46	29.10	2.28	---	---	---	---
8	28.48	1.47	---	---	---	---	---	---
9	29.94	1.46	---	---	---	---	---	---
10	31.40	1.46	---	---	---	---	---	---

This evaluation is based on the computed energy distribution of the spent beam, which has been obtained from the large signal analysis of the high efficiency designs. Such computed spent beam energy distributions have been compared in detail with velocity distribution measurements with a velocity analyzer in previous studies¹. Very good agreement of these data has been found.

Such velocity distributions are usually presented in an integrated form:

$$\frac{I(V)}{I_0} = \frac{1}{I_0} \int_V^{\infty} \frac{\partial I}{\partial E} dE$$

where

$$\frac{I(V)}{I_0} = \text{fraction of beam current with kinetic energy larger than or equal to } V.$$

$$\frac{1}{I_0} \frac{\partial I(E)}{\partial E} = \text{"current energy density" (fraction of beam current with kinetic energy } E \text{ per unit energy range).}$$

The computed spent beam energy distribution of the 2 GHz tubes and the 8 GHz tube is shown in Figure 78 and 79 for the multivoltage jump taper designs and for the previously used velocity taper - voltage jump combination and the voltage jump method.

The multi-voltage jump taper designs are found to have a larger velocity spread and are therefore better suited for multistage collector operation.

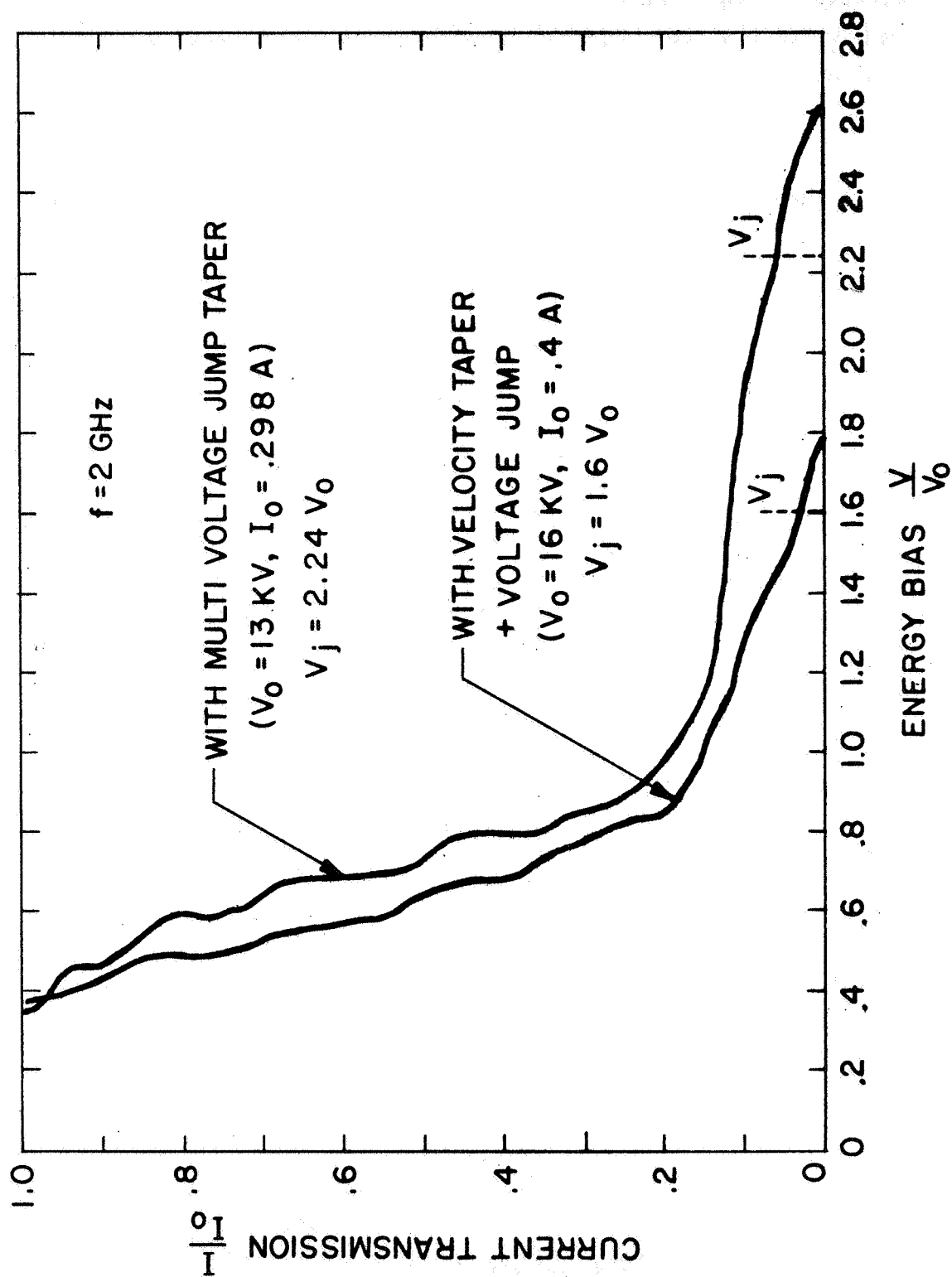


Figure 78 Spent beam energy distribution with multivoltage jump taper and with velocity taper - voltage jump for 2 GHz tube (Computed).

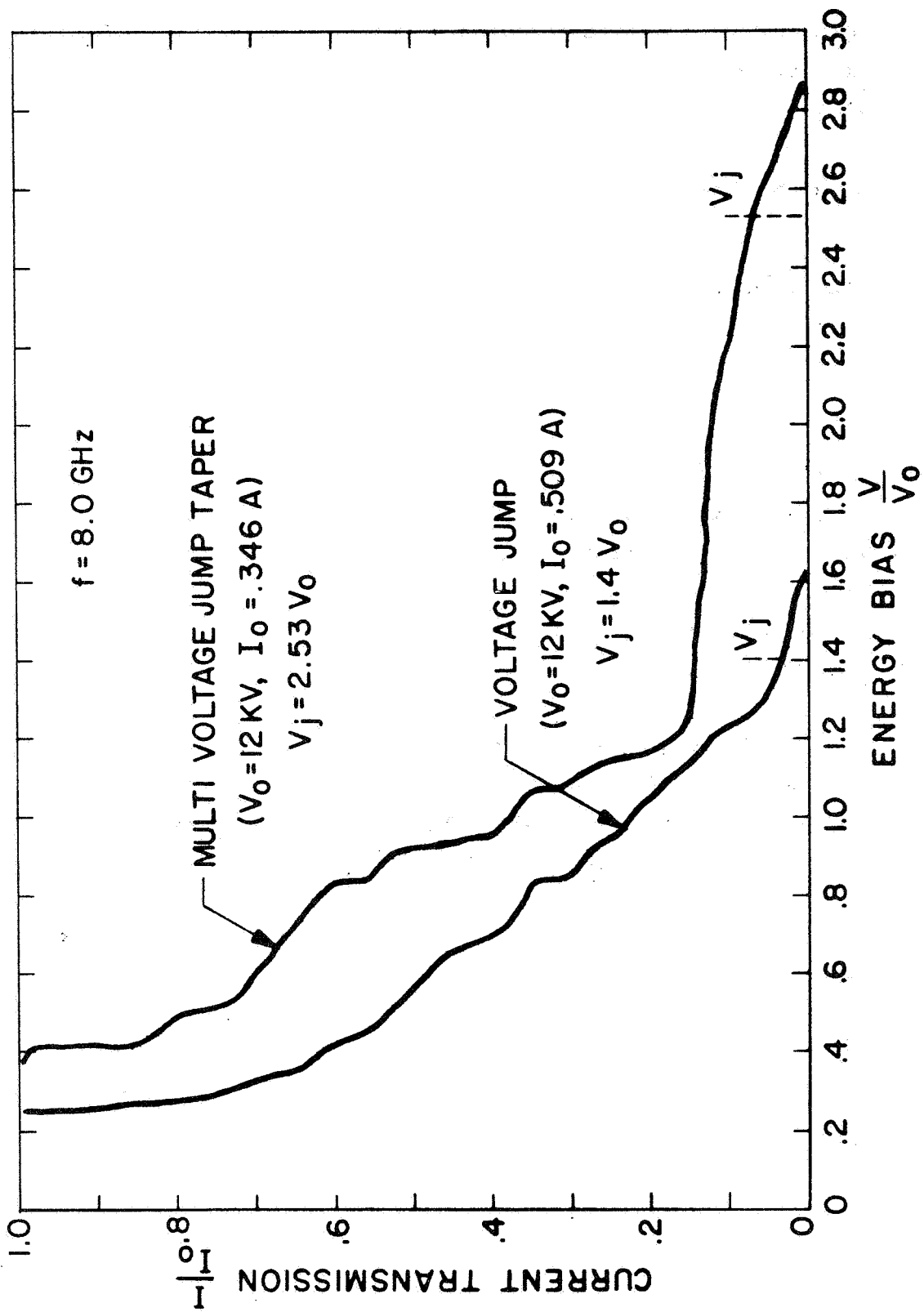


Figure 79 Spent beam energy distribution with multivoltage jump taper and with voltage jump for 8 GHz tube (Computed).

With these spent beam current energy distribution data, it becomes possible to evaluate the efficiency improvement which can be obtained with multi-stage collector operation. With n collector stages the efficiency improvement F_c , as compared to a single collector at the highest beam potential V_j , can be expressed by:

$$F_c = \frac{V_j I_o}{\sum_{k=1}^n (V_j - \Delta V_k) \Delta I_k}$$

where

V_j = beam potential at output

I_o = beam current

ΔV_k = collector bias of stage k

ΔI_k = beam current with energies between V_k and V_{k+1}

This assumes an ideal collector with perfect velocity sorting and no other degrading effects.

It can be shown that for k stages there exists an optimum selection of the collector potentials V_k (and collector currents ΔI_k) for which the efficiency improvement becomes a maximum. These optimum collector potentials V_k are given by the conditions:

$$\frac{\partial P_c}{\partial V_k} = 0 \text{ for all } k$$

with

$$\text{collector power } P_c = \sum_{k=1}^n V_k \Delta I_k$$

$$\text{and } V_k = V_j - \Delta V_k$$

These relations have been used to determine the optimum collector potentials V_k and corresponding beam currents ΔI_k for all tubes. The number of collector stages was varied from one to five stages to determine the possible efficiency improvements as a function of the number of collector stages.

These ideal collector data were corrected for some of the more significant degrading effects, specifically:

1. Space charge potential depression
2. Imperfect velocity sorting
3. Secondary electron backstreaming

The magnitude of these degrading effects was estimated optimistically, assuming that improved collector design techniques will be developed compared to the present state of the art. With these corrections it was found that the maximum tube efficiency is achieved with four collector stages, while additional collector stages will not improve the efficiency anymore.

With more conservative assumptions for these corrections a maximum (slightly lower) efficiency is achieved with three collector stages.

These corrections are estimated as follows:

The space charge depression ΔV_c was assumed to be 5% of the beam potential V_o , or

$$\Delta V_c = .05 V_o.$$

This value has been chosen because well designed collectors can be depressed with a dc beam as much as 95% before space charge blocking is observed.

In the multi-stage collector designs, the ideal collector potentials V_k are therefore increased to

$$V_k' = V_k + .05 V_o$$

to take this effort into account.

Velocity Sorting Efficiency η_s

It is assumed that each of the velocity sorting mechanisms of the n collector stages has a velocity sorting efficiency η_s of less than 100%.

These imperfections of velocity sorting can be caused by non-laminar flow conditions of the electron trajectories and by inadequate configurations of the sorting fields. As a result, the current ΔI_k of stage k is modified to:

$$\Delta I_k' = (\eta_s)^{k-1} \Delta I_k + \sum_{m=k+1}^n \eta_s^{k-1} (1 - \eta_s) \Delta I_m.$$

In Figure 80, the efficiency improvement of the 850 MHz tube is shown for one to five collector stages and varying values of the velocity sorting efficiency, including secondary backstreaming of 10%.

In this case the current ΔI_k to stage k is reduced by a current I_s of backstreaming secondaries of

$$I_s = -.10 \Delta I_k$$

This backstreaming current is assumed to flow to the next higher collector stage $k - 1$.

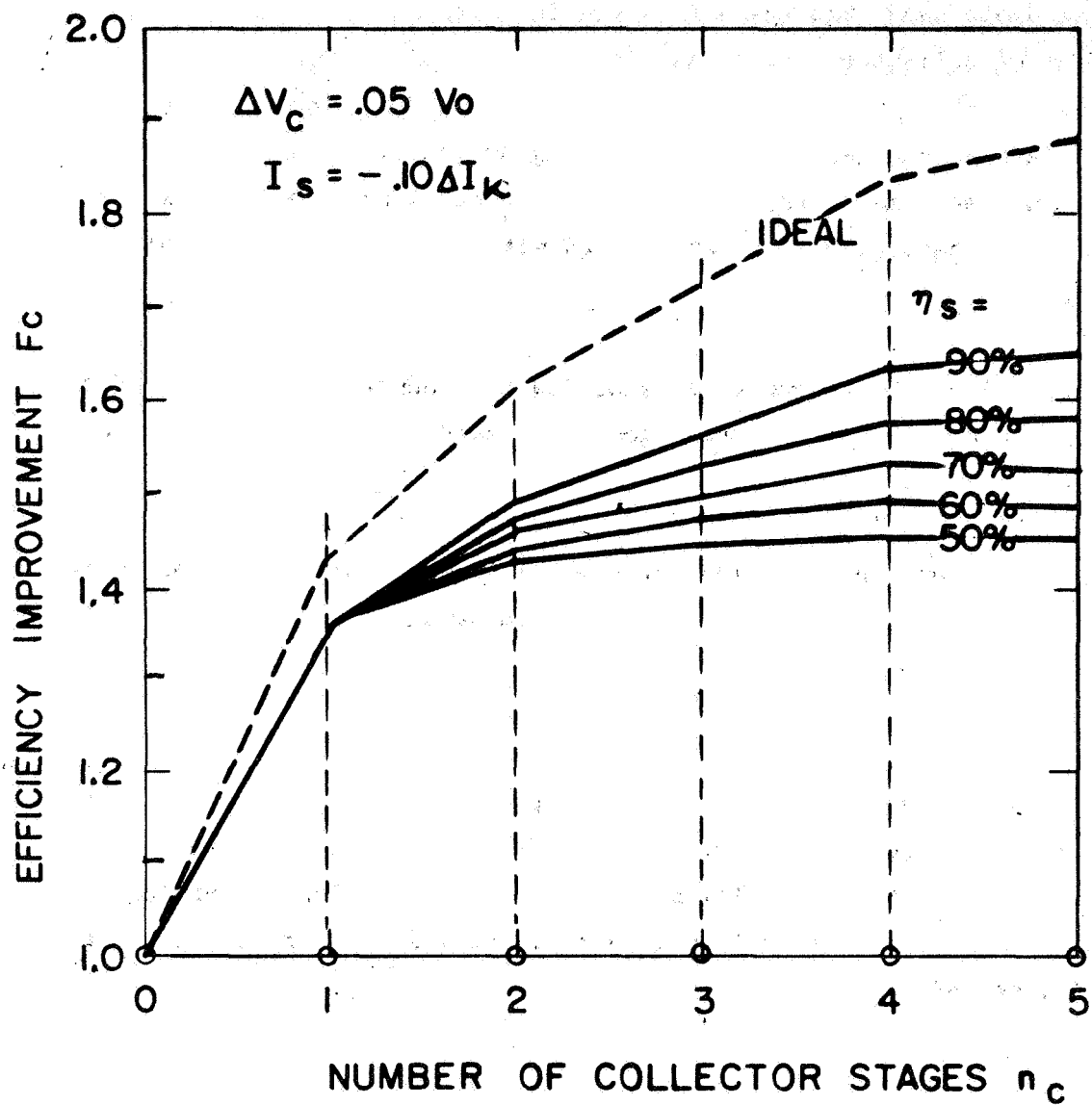


Figure 80 Effect of velocity sorting efficiency in multistage collector operation (computed for 850 MHz tube).

These plots show that the efficiency improvement is higher with a larger number of collector stages reaching a factor of nearly 1.9 with 5 stages (ideal) corresponding to a tube efficiency of 89%. However, the improvement becomes smaller with an increasing number of collector stages. The ideal ultimate multistage collector efficiency, when the beam energy is completely recovered, is then reached with a large number of collector stages.

The efficiency improvement is significantly reduced when a reduced sorting efficiency is taken into account, especially for a larger number of stages.

In previous multistage collector studies on two stage collectors with radial velocity sorting (Section IV. D) a sorting efficiency of

$$\eta_s = 70\%$$

was achieved, as compared to the measured spent beam energy distribution. The proposed transverse magnetic and electric velocity sorting scheme is not subject to the deficiencies of the radial velocity sorting scheme (Section IV. D.). It is therefore believed that an improved sorting efficiency of

$$\eta_s = 80\%$$

should be feasible with careful evaluation and development.

Computations show (Figure 81), that a multistage collector with

$$n = 4$$

stages would then provide maximum efficiency improvements.

Backstreaming of Secondaries

Backstreaming secondaries have been the subject of considerable attention in depressed collector design. Effective design methods are available to keep the backstreaming current from secondaries small.

In this evaluation, it is assumed that each collector stage loses a fraction f_B of its current due to backstreaming secondaries:

$$I_s = -f_B \Delta I_k.$$

This current is assumed to be collected at the adjacent collector stage with the higher collector potential. The collector current ΔI_k in stage k is then modified by the secondaries to:

$$\Delta I_k' = \Delta I_k + f_B (\Delta I_k + I - \Delta I_k)$$

Only the first collector stage (beyond the output coupler) is assumed not to lose secondaries, because this stage provides more design freedom for the suppression of secondaries.

The efficiency improvement has been evaluated for a variable amount of backstreaming current I_s of secondaries. It is assumed, that this backstreaming current

$$I_s = -f_B \Delta I_k$$

is collected at the next higher collector stage $K-1$. In Figure 82 the resultant efficiency improvements F_c have been plotted for the 850 MHz tube as a function of the number of collector stages, assuming a sorting

efficiency of $\eta_s = 80\%$ and a space charge depression of $\Delta V_c = .05 V_0$ for each stage. It can be seen, that with these assumptions the number of useful collector stages is primarily determined by the effectiveness of the velocity sorting mechanism, while the effect of the backstreaming secondaries remains relatively minor.

In previous multistage collector studies¹ on two stage collectors with radial velocity sorting and secondary suppression by shielding (Section IV. 8) a backstreaming current of 5% was observed.

With a larger number of collector stages the reduction of backstreaming secondaries depends primarily on the accuracy of the velocity sorting mechanism. With perfect velocity sorting, practically no backstreaming secondaries are expected to occur, since only the collector aperture edges may contribute to them. With inaccurate velocity sorting, however, some trajectories will strike the wrong side of the collector electrodes (Figure 42), which have no field suppression, and backstreaming of secondaries will result. In the following analysis it will be assumed, that the backstreaming of secondaries for each collector stage can be kept to 10%, or

$$I_s = -.10 \Delta I_k$$

Without more detailed studies, this has to be considered an arbitrary assumption. The data of Figure 81 show however, that the effect of secondaries is not very significant.

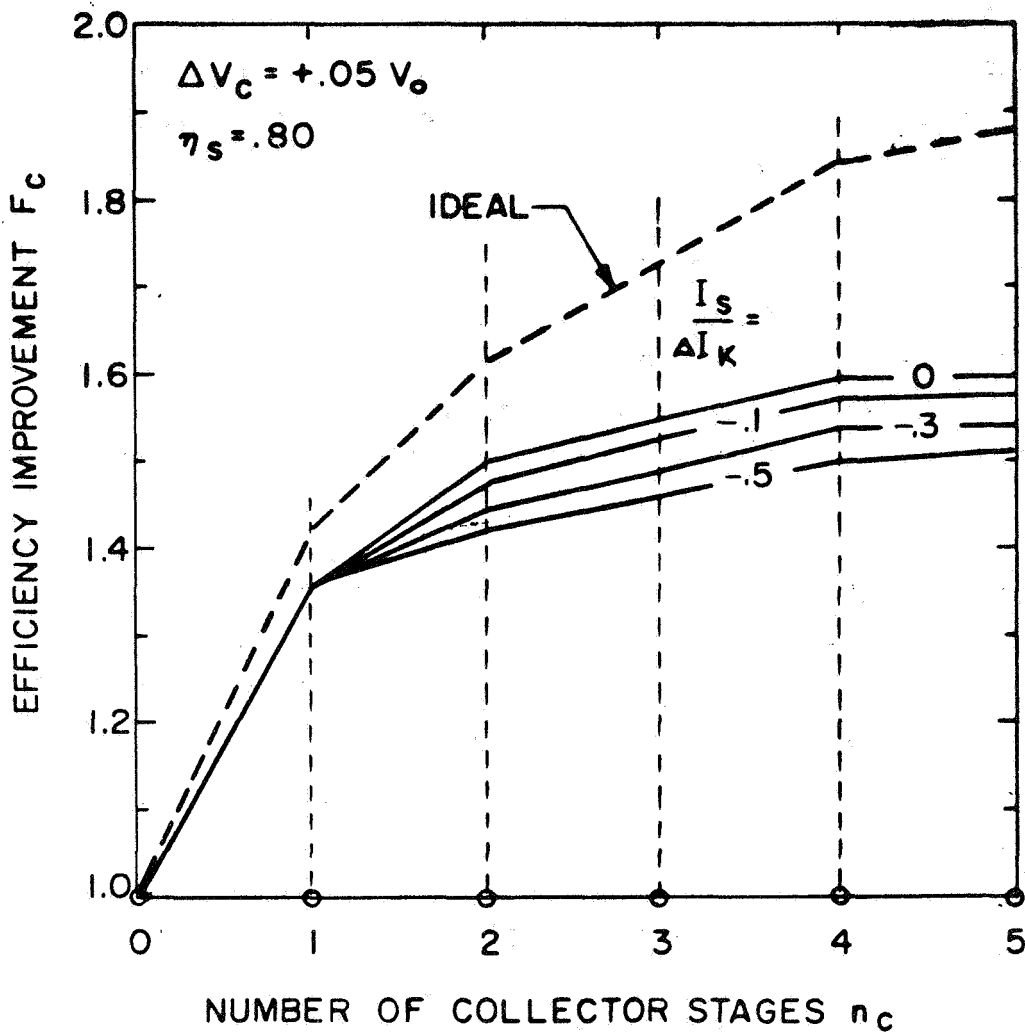


Figure 81 Effect of backstreaming secondaries on multistage collector operation (computed for 850 MHz tube).

In Table XVII the computed optimum collector voltages and currents have been listed for all tubes. These data include the corrections described above.

These data show that typically the first and second collector stage potential is higher than the driver section potential V_o , while the potential of the third stage is approximately the same as that of the driver section. The fourth collector stage potential generally is much lower than that of the other stages.

The collector currents decrease quite substantially with the number of stages. The first stage collects about 40 to 50% of the beam current, while the fourth stage collector current is only about 5 to 10%.

The thermal load distribution on the collector stages is of concern for the cooling design. The collector load has been evaluated with the computed spent beam energy distribution also. The thermal load, which includes the effects of the space charge depression, velocity sorting and backstreaming secondaries, as described above, has also been listed in Table XVII.

These data show that a major portion of the thermal collector load, about 40 to 50%, is dumped into the first collector stage, while the thermal load of each of the following stages is significantly reduced. The last (fourth) stage has to absorb only about 10% of the beam dissipation.

If these collectors were to be radiation cooled a problem would arise as to how to provide adequate heat shielding for the circuit and to remove the heat from the inner collector stages, since the inner stages closest to the circuit would be hottest.

The efficiency data of Table XVII include also the efficiency for the solenoid focused tubes and the efficiency for the AM tubes, when the audio FM tubes and the driver tubes are included in the in the calculation of system efficiency.

Table XVII Four stage collector operation for multivoltage jump taper designs.

FREQUENCY		850 MHz	2 GHz	8 GHz	11 GHz
OUTPUT POWER (kW)	P_{out}	7.6 kW	5.2 kW	5.1 kW	5.1 kW
Driver Section Potential (kV)	V_o	16.0	13	12	14
Final Voltage Jump Potential (kV) (Above Ground)	V_j	31.4	29.1	26.1	31.5
Optimum Collector Potential (kV) (Above ground)	V_1	22.5	25.3	20.9	26.6
	V_2	19.1	22.2	18.95	19.1
	V_3	16.3	19.8	15.75	13.1
		0	5.3	1.31	1.45
Collector Currents (mA)	I_j	0	0	22	0
	ΔI_1	208	114	136	191
	ΔI_2	143	100	125	66
	ΔI_3	135	70	48	28
	ΔI_4	19	14	17	13
Thermal Collector load (watts)	P_{cj}	0	0	72	0
	P_{c1}	1010	513	450	915
	P_{c2}	607	327	371	414
	P_{c3}	720	382	403	208
	P_{c4}	87	137	124	133
Ideal Collector Efficiency	$\eta_{c\ ideal}$	88%	90%	88%	85%
Collector Efficiency Efficiency with Solenoid	η_c	75.1%	79.1%	78.2%	75%
	η_{cs}	---	---	73.5%	71.3%
For AM Amplifiers: Efficiency with helix driver tube and audio FM tube (estimated)	η	67%	70%	---	---

VI. FOCUSING AND BEAM OPTICS

A. FOCUSING

The required focusing field for an electron beam increases with the space charge density of the beam and with the fraction of the magnetic beam flux which penetrates the cathode surface. A magnetically shielded cathode will therefore permit focusing of the beam with the lowest possible magnetic field. This type of focusing produces a beam flow defined as "Brillouin flow." On the other hand, the beam flow with magnetic cathode flux is defined as "confined flow" or "immersed flow." Although confined flow requires a higher magnetic focusing field than does Brillouin flow, it is preferable when uniform magnetic focusing fields (such as those produced by solenoids) are available. This is because confined flow produces a stiffer beam which is less sensitive to focusing perturbations and RF defocusing effects.¹³ Confined flow focusing is now generally applied to solenoid focused high power tubes. Very high quality beam focusing can be achieved with this method when the gun launching conditions into the focusing field are optimized, and when the focusing field is highly uniform. These focusing fields can be produced with foil solenoids of copper or aluminum. The transverse fields of these solenoids can be kept as small as a fraction of 1% of the axial fields. However, solenoids require electrical power and thus degrade the efficiency. They are usually larger and heavier than periodic permanent magnet focusing systems.

Unlike uniform field focusing, periodic focusing will inherently produce a scalloping beam contour. The period of this beam scalloping is related to the focusing system period. With proper gun launching conditions, and a good focusing design, the magnitude of the scalloping beam ripples can be rather small, i.e., on the order of only a few percent of the mean beam diameter. Unlike uniform focusing systems, periodic focusing systems

require magnetically shielded cathodes and thus provide "Brillouin flow" for the best focusing. The plasma frequency reduction factor is then smaller than with confined flow.

The focusing stiffness of Brillouin flow is relatively weak;¹³ the beam radius r_b will vary with the current I and beam velocity u as

$$r_b = \alpha \left(\frac{I}{u} \right)^{1/2}.$$

In determining the required focusing field for either a uniform or periodic focusing system, the beam conditions at saturation (full RF power) must be taken into account. In this case, the beam is strongly bunched; its current density is therefore strongly increased locally -- generally by a factor of about three compared to the uniform dc beam.¹⁵ In addition, the average beam velocity is considerably reduced as a result of the energy extraction by the amplified RF wave. The mean energy reduction of the spent beam is proportional to the electronic efficiency, and the average beam bunch velocity \bar{u} at the output is therefore

$$\bar{u} = u_o \left[\frac{V_j}{V_o} (1 - \eta_1) \right]^{1/2}$$

with

- u_o = dc beam velocity in driver section
- V_j = dc beam potential at output
- V_o = dc beam potential in driver section
- η_1 = electronic efficiency at output

The local current density concentration in the beam bunches and their velocity reduction will significantly increase their space charge density (at least locally) in RF beams. In addition, the RF fields of the circuit wave produces perturbing radial fields, which cause beam focusing perturbations. Therefore, the RF focusing requirements are considerably more severe than those for the dc beam. The focusing system must, therefore, be designed to meet the RF requirements.

The magnitude of the focusing field is designed to produce a beam diameter sufficiently small to take even strong RF defocusing effects into account.

The PPM focusing design will therefore provide twice as large a peak focusing field B as for a dc beam, or

$$B = 2 (2)^{1/2} B_0$$

with B_0 "Brillouin" field, while the solenoid focused tubes will provide a uniform field of

$$B = 2 B_0$$

with confined flow ($K_c = .85$). With these field magnitudes the average beam diameter will only fill .6 of the circuit hole diameter $2 r_a$, even with RF defocusing, or

$$\left(\frac{r_b}{r_a} \right)_{\max} = .6$$

and excellent beam transmission into the collector is then assured.

The stability of the periodic magnetic focusing is also severely affected by the bunching and energy extraction from the beam with very high efficiency. Therefore the $\frac{\lambda_p}{L}$ ratio, which determines the stability margin, was chosen large enough with a value of

$$\frac{\lambda_p}{L} > 4$$

with (Figure 77)

λ_p = plasma wavelength

L = magnetic period

to assure stable focusing with high efficiencies.

The focusing design for PPM utilizes the coupled cavity structure for the pole piece configuration, Figure 76. The close proximity of the pole pieces to the beam assures a very high quality PPM focusing system. It requires, however, a magnetic period L of twice the cavity period l_c . The magnetic gap G is chosen to $G = 2/3 l_c$ to eliminate the third harmonic of the axial magnetic field for improved focusing. The magnetic gap of the ferrule is thus larger than its electric gap. The electric gap is provided by copper spacers. In addition, the ferrules and pole pieces are copper clad to provide adequate thermal conduction.

The required magnetic flux is calculated by taking the external and internal leakage flux between pole pieces and between ferrules into account. The thickness of the pole pieces t_f is chosen to limit the maximum field B in the pole pieces (at R_1) to

$$B_{\max} = 10,000 \text{ gauss}$$

to avoid saturation effects. The required pole piece thickness has been listed in Table XIV.

The required magnetic flux is to be provided with a conventional ring magnet (radius $R_1 - R_2$). Several magnet materials have been considered:

Ceramic magnetics ("Indox")

Alnico 5

Alnico 8

Platinum-Cobalt (Pt - Co)

For each tube a magnet material has been selected which provides the smallest magnet radius R_2 for an assumed operating temperature of

$$T = 200^{\circ}\text{C}.$$

The chosen materials and the resultant magnet radii R_2 (for voltage jump cavities) are listed in Table XVIII.

The focusing design for the solenoid has been evaluated both for aluminum and for copper foil solenoids (with teflon insulation) for an operating temperature of

$$T = 200^{\circ}\text{C}.$$

A packing factor of the solenoid of

.85

was assumed.

Table XVIII Focusing design parameters .

Frequency		850 MHz	2 GHz	8 GHz	11 GHz
Focusing		PPM	PPM	Solenoid	Solenoid
Material		Alnico 5	Alnico 5	Copper	Copper
Magnetic Field B	gauss	213 (peak)	480 (peak)	1490	1720
Driver Section		4.25	4.40	---	---
$\frac{\lambda_p}{L}$ Voltage Jump Section		7.2	8.2	---	---
R_1	cm (in)	11.5 (4.536)	5.64 (2.224)	3.13 (1.23)	2.62 (1.03)
R_2	cm (in)	11.8 (4.636)	5.9 (2.324)	6.73 (2.65)	6.48 (2.55)
Magnet Length	cm (in)	130. (51.3)	38.3 (15.1) (20 dB) 59 (23.2) (40 dB)	9.73 (3.83)	7.26 (2.86)
Magnet Weight	kg (lbs)	20.4 (44.9)	3.3 (7.3)	8.58 (18.9)	6.35 (14.0)
Solenoid Power (T = 200°C)	watts	---	---	409	348

A wrapped-on solenoid design is used to achieve a light weight and efficient solenoid design. The inner diameter D_1 is then limited by the extruding voltage jump seals. The outer solenoid diameter D_2 was optimized to provide a minimum effective solenoid weight W_{eff} (Figure 45). This includes the weight for the solenoid W_s and for the solenoid power supply W_p , using the conversion factor

$$\frac{100 \text{ lbs wt.}}{1 \text{ kW power}}$$

with

$$P_s = \text{solenoid power}$$

and

$$W_{eff} = W_s + W_p.$$

The resultant solenoid diameter D_2 , power P_s , and weight are also given in Table XVIII.

B. GUN AND HEATER

The cathode loading and the cathode life can be affected by the gun design. When a high cathode-to-beam area convergence is chosen, the cathode loading can be kept low. There are, however, design restrictions on the choice of the gun area convergence ratio. This is because the electron-optical performance deteriorates with increasing area convergence ratios. This deterioration manifests itself in non-uniform cathode emission and in increasing non-laminarity of the beam in such a way that some electron trajectories are found to cross over each other. The focusing of such beams with translaminar trajectories is generally degraded. The design of high convergence guns becomes more difficult with guns for high perveance beams.

Good quality guns can readily be designed for area convergences up to about 60 to 80 with moderate beam perveance (up to about $2\mu p$).

In these gun design considerations the voltage breakdown limitations which may occur at high voltages, have to be considered.

The gun design follows well established procedures, based on Pierce's theory¹² and empirical methods (electrolytic tank, gun tester, trajectory program). The beam area convergence ratio has been chosen to achieve a low enough current density i_c at the cathode of

$$i_c < 500 \text{ mA/cm}^2$$

to assure long cathode life (20,000 hours minimum).

To achieve long heater life, the heater voltage was chosen relatively low, but within the presently available heater supply regulation techniques. The required heater power is determined by the heater efficiency, defined as

$$\text{heater efficiency} = \frac{\text{radiated power from cathode surface}}{\text{heater power}}$$

The heater efficiency is known from empirical data to be for

coil heaters	20%
pancake heaters	30%

The radiated power P_R from the cathode surface is related to the required cathode temperature T_K ($^{\circ}K$) by:

$$P_R = e_T \sigma (T_K^4 - T_O^4)$$

where

$$\sigma = 5.735 \cdot 10^{-12} \text{ watts/cm}^2/\text{°K}^{-4}$$

$$e_T = (\text{emissitivity}) \text{ for oxide cathodes} = .31$$
$$\text{for tungsten cathodes} = .18$$

$$T_o (\text{°K}) = \text{temperature of cathode environment}$$

The gun and heater design parameters have been compiled in Table XIX. It can be seen that the gun and heater design will be capable of providing reliable operation and long life. The maximum field strength in the gun is well within safe limits ($E_{\max} = 150 \text{ kV/cm}$).

C. LAUNCHING CONDITIONS FOR THE GUN

Good beam focusing can only be achieved when the entrance conditions of the gun trajectories into the focusing field are optimized.

It is then possible, at least in concept, to achieve a smooth beam flow without ripples with a uniform magnetic focusing field, and with very small beam ripples of only a few percent with PPM focusing. This is especially important for high efficiency tubes where the beam perturbations due to RF defocusing become more significant. Good beam transmission is not only desirable for effective depressed collector operation, but also for the thermal protection of the slow wave structure, thus contributing to the tube reliability and life.

The optimum beam launching conditions can be determined with a trajectory computer program, or a beam tester, but it is also possible to estimate these launching conditions. The optimum gun launching condition is generally found such that the electrostatic beam minimum position Z_{\min} (Figure 82) is located where the magnetic field has reached a value of approximately 70% of its maximum in the interaction region.²²

Table XIX Gun and heater design parameters.

FREQUENCY		850 MHz	2 GHz	8 GHz	11 GHz
Perveance	μP	.25	.202	.262	.18
Cathode Voltage	(kV)	16	13	12	14
Cathode Current	mA	505	298	346	298
Cathode Diameter	cm (in)	2.87 (1.13)	1.64 (.645)	.967 (.381)	.880 (.346)
Cathode Current Density	mA/cm ²	78	142	470	490
Beam Area Convergence		4.5	10	60	85
Cathode Curvature R_c	cm (in)	8.93 (3.52)	4.3 (1.69)	1.98 (.781)	1.84 (.724)
Anode Curvature R_a	cm (in)	4.4 (1.73)	1.85 (.731)	.77 (.304)	.616 (.243)
Maximum Electric Field in Gun	kV/cm	8.2	16.2	75	94
Shadow Grid		Yes	Yes/no	no	no
Cathode Type		Oxide Coated Cathode		Impregnated Tungsten Cathode	
Cathode Temperature	°C	700	730	950	950
Heater Type		Pancake		Coiled wire	
Heater Efficiency	%	30	20	20	20
Heater Power	Watts	33.3	15.3	7.5	6.4
Heater Voltage	V	12	9	6.3	6.3
Heater Current	A	2.77	1.70	1.19	1.01

For confined flow the pole piece hole diameter d_p must also be large enough to provide the desired amount of magnetic flux K_c to the cathode surface. The magnetic cathode flux K_c has been defined as

$$K_c = \frac{r_c^2 B_c}{r_o^2 B_o}$$

where

r_c = cathode radius

r_o = dc beam radius

B_c = axial magnetic field at cathode surface

B_o = axial magnetic in focusing region

The estimated optimum gun launching conditions and pole piece hole sizes for the tubes have been listed in Table XX.

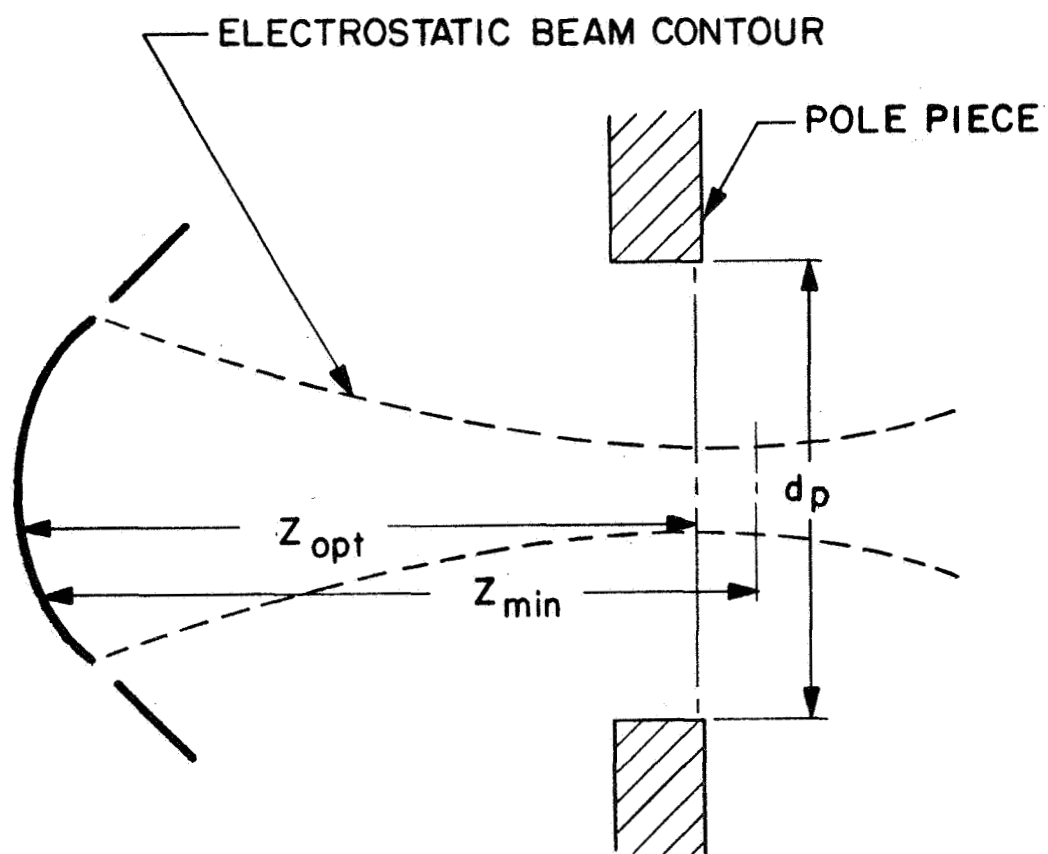


Figure 82 Launching conditions for gun.

Table XX Estimated optimum gun launching conditions (Figure 82).

TUBE FREQUENCY		850 MHz	2 GHz	8 GHz	11 GHz
Beam minimum distance Z_{\min}	cm (in)	9.95 (3.92)	5.82 (2.29)	2.87 (1.13)	2.67 (1.05)
Opt. gun position Z_{opt}	cm (in)	9.27 (3.65)	5.56 (2.19)	2.28 (.900)	2.25 (.895)
Pole piece hole diameter d_p	cm (in)	2.25 (.886)	.864 (.340)	1.98 (.780)	1.40 (.550)
Cathode field B_c	gauss	0	0	21	17
Magnetic cathode flux	K_c	0	0	.85	.85

VII. COLLECTOR DESIGN

A new approach for the design of the multistage collector has been used. This approach uses magnetic refocusing of the spent beam and transverse magnetic and electrostatic velocity sorting with electrostatic suppression of backstreaming secondaries, as described in Section IV. D. and illustrated with Figures 39, 40 and 41. This is considered an optimum design approach, however, analytical and experimental evaluations will be required to establish this.

In Section V. C. an estimate has been made on the optimum number of collector stages using the computed velocity spread of the spent beam and also considering the effects of space charge depression, velocity sorting deficiencies and backstreaming secondaries. It was found that the useful number of collector stages is primarily limited by velocity sorting deficiencies for given velocity spread conditions, such that for larger velocity sorting deficiencies the useful number of collector stages (for efficiency improvement) becomes smaller. For this analysis it is assumed, that a fairly good sorting efficiency ($\eta_s = 80\%$) can be achieved for the design of the multistage collector, even though the required design methods have not yet been developed. With this assumption the optimum number n of collector stages has been determined to

$$n = 4$$

The collector design given here uses therefore four collector stages.

The design of a multistage collector with the described configuration has to be based on a spent beam trajectory analysis. An accurate trajectory analysis requires a general three dimensional (non-symmetric) computer trajectory program, which includes space charge effects, transverse fields and trajectory crossover and reversals. In addition the

launching conditions of the spent beam at the output have to be known with reasonable accuracy. Such a collector design analysis is presently not yet available.

The collector design given here is therefore based on simplified methods to estimate the spent beam collector trajectories. To make this possible, a number of simplifying assumptions were made as follows:

1. The magnetic refocusing configuration (Figure 39) achieves a laminar beam with parallel trajectories. Velocity sorting errors originating from the initial beam trajectories are then eliminated.
2. The magnetic deflection field is uniform over the chosen deflection length ℓ_m (Figure 40) and field edge effects are ignored. Under these conditions the magnetic deflection field could not produce any velocity sorting errors. The choice of the initial deflection strength affects the collector design in two ways: with larger deflection angles the transverse kinetic energy of the deflected electrons is increased. This reduces the collector efficiency, since the transverse kinetic energy cannot be extracted by a longitudinal deceleration field. A larger initial deflection angle, on the other hand, permits to design a shorter and smaller velocity sorting section of the collector, since the deceleration field can then be higher. However, the power density on the collector electrodes will then be larger.

Therefore a compromise in the choice of the initial deflection must be made to achieve good collector efficiency with a reasonable collector size and acceptable power densities on the collector.

For the collector designs given here, the deflection angle was chosen to

$$\frac{dr}{dz} = .2$$

for the average energy electrons of the spent beam. This deflection corresponds approximately to the magnitude of the radial RF defocusing in the output coupler. This magnitude of the deflection was found to result in reasonable collector dimensions. The collector (deceleration) length L_c was chosen large enough to keep the power density on the collector surfaces small enough ($< 100 \text{ watts/cm}^2$).

3. The axial electrostatic deceleration field was assumed to be constant throughout the deceleration region, which starts at the termination point of the magnetic deflection field. The field is produced by a series of parallel and plane collector electrodes plus one additional deceleration electrode which are located at their respective equipotential positions. (Figure 41). Field perturbations caused by the collector apertures and in the transition region at the beginning of the deceleration field are ignored. Such field perturbations may produce velocity sorting errors.
4. The collector trajectories are calculated for each spent beam velocity group in two steps: First, the trajectories are determined without space charge. A space charge correction is then applied to these electrostatic trajectories. The electrostatic trajectories (parabolas) are readily obtained in a uniform deceleration field, when the launching slope is known. The space charge correction uses the paraxial beam spread curves Δr_s of an electron beam with space charge in a uniform deceleration field to correct the tilted electrostatic trajectories by Δr_s as indicated in Figure 83.

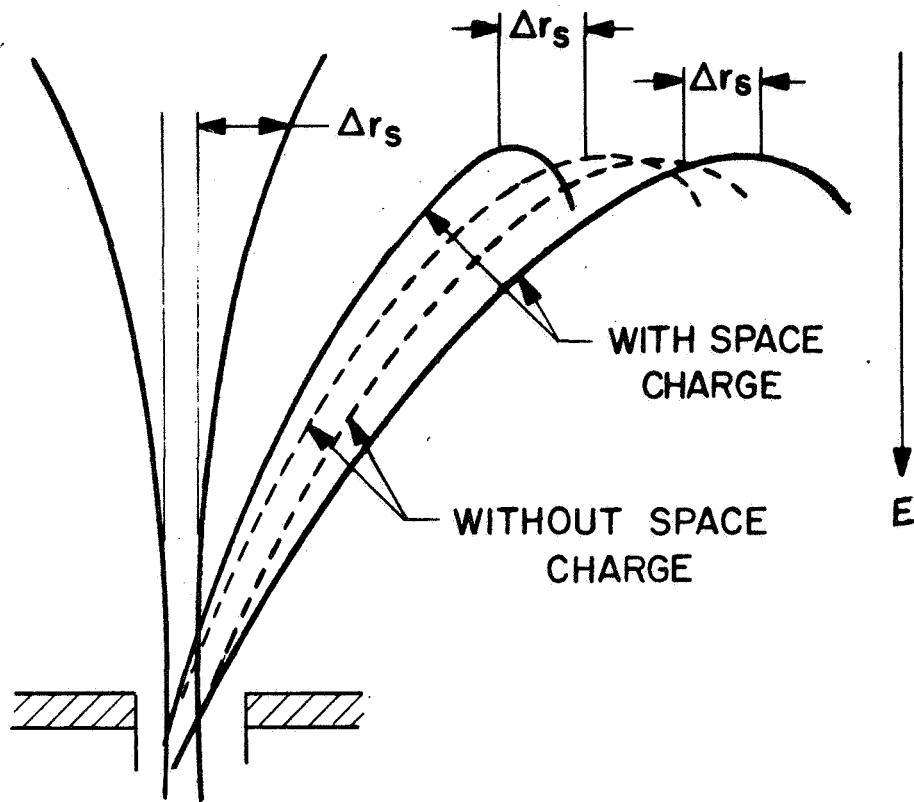


Figure 83 Beam spread of tilted beam in electrostatic deceleration field with space charge correction.

The space charge conditions are derived from the estimated RF beam current and the average beam velocity for each velocity group.

Trajectories have been determined for the two extreme beam radii in the transverse direction and for the two beam radii perpendicular to the direction of deflection for each velocity group. These trajectories have been calculated for both the slowest and the fastest velocity in each velocity group.

5. The collector apertures were determined from these trajectories as follows:

The collector apertures were made circular, such that their "left" edge is lined up with the "left" edge of the entering beam, as shown in Figure 84.

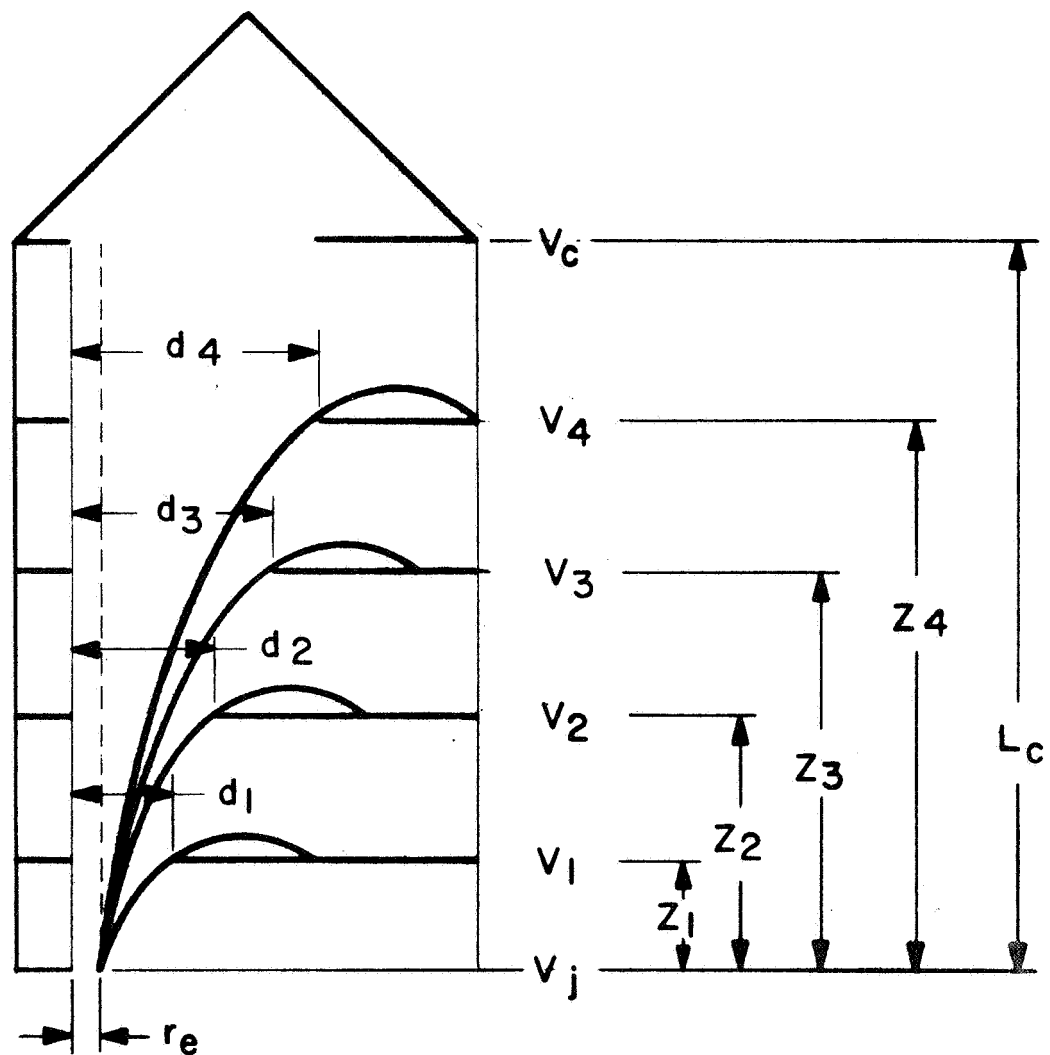


Figure 84 Schematic of four-stage collector

The collector aperture diameter (d_K) are determined by the "right" edge electron trajectory with the slowest velocity in each velocity group as shown in Figure 84. It was found, that with these assumptions the fastest "left" edge trajectory of each velocity group was also intercepted by its respective collector electrode, indicating perfect velocity sorting.

The design data for the resultant collector configurations are listed in Table XXI. These data include an estimate of the thermal power density on the first collector stage.

These design data will have to be modified with a more accurate collector trajectory analysis based on realistic spent beam launching conditions. Such an analysis will also yield data to evaluate velocity sorting deficiencies, secondary backstreaming and the effective efficiency improvement with the multistage collector.

Table XXI Four stage collector design parameters (Figure 38, 39, 84).

FREQUENCY		850 MHz	2 GHz	8 GHz	11 GHz
Refocusing length $\lambda_s/4$	cm (in)	6.9 (2.72)	2.52 (.993)	.259 (.102)	.256 (.101)
Beam diameter at output pole piece	cm (in)	2.01(.790)	1.04 (.408)	.203 (.080)	.178 (.070)
Length of deflection pole piece (ℓ_m)	cm (in)	.127 (.50)	.127 (.50)	.542 (.213)	.427 (.168)
Magnetic deflection field B_T	gauss	72	60	141	200
Collector spacings	Z_1	7.1 (2.80)	1.48 (.582)	1.80 (.708)	1.03 (.405)
	Z_2	10.08 (3.96)	2.86 (1.125)	2.55 (1.004)	3.73 (1.071)
	Z_3	12.52 (4.93)	3.97 (1.57)	3.83 (1.508)	4.30 (1.692)
	Z_4	24.30 (9.56)	10.46 (4.115)	9.46 (3.729)	7.14 (2.805)
	L_c	27.42 (10.8)	12.12 (5.16)	10.18 (4.0)	7.63 (3.0)
Collector apertures	d_1	6.85 (2.70)	2.642 (1.04)	1.60 (.630)	1.17 (.460)
	d_2	7.88 (3.10)	3.28 (1.29)	2.13 (.840)	1.65 (.650)
	d_3	9.23 (3.63)	3.66 (1.44)	2.31 (.910)	1.93 (.760)
	d_4	10.4 (4.08)	4.57 (1.80)	3.30 (1.30)	2.39 (.940)
Estimated thermal power density on first collector	watts/cm ²	8.8	26	27	86

VII. THERMAL DESIGN

The tube will be mounted into a dielectric heat pipe assembly as shown in Figure 85. For the purpose of thermal analysis the heat flow of three sections is considered: The gun assembly, the circuit assembly and the collector assembly. The contribution of heat generated in the gun assembly is very small and can therefore be neglected. The thermal analysis of the circuit and the collector follows.

The thermal analysis of the coupled cavity structure evaluates and determines the required copper cladding of the pole pieces (for PPM focusing, Figure 76), or the required circuit wall thickness (for solenoid focusing) for a specified maximum temperature gradient ΔT between ferrules and outer surface of the circuit and for a specified maximum temperature T_f of the ferrule. This provides information on a suitable operating temperature and fluid material for the heat pipe cooling system. The operating temperature and size of the radiator are then also determined.

A. THERMAL CIRCUIT ANALYSIS

For the thermal circuit analysis it is assumed that a major part of the thermal loading is produced by beam interception. The circuit losses are found to be small compared to the power produced by the expected beam interception (Section VA 4). The thermal contribution from losses is therefore neglected in this analysis. It is assumed that the beam interception of each ferrule P_f is 1% of the dc beam power, or

$$P_f = .01 I_o V_o$$

This assumption provides a considerable safety margin, since the total beam interception on the circuit in well focused high power tubes is less than 3 to 5%, even for high efficiency tubes. This interception occurs near the output end of the tube and is distributed over several cavities.

The thermal analysis of the circuit assumes radial heat flow from the ferrule to the outside of the tube. The heat path is divided into 6 radial disc sections with changing thickness (Figure 86) such that the coupling slot is replaced by an equivalent (thinner) disc segment.

The temperature gradient ΔT_n in each segment is given by:

$$\Delta T_n = \frac{P_f \ln \left[\frac{r_n}{r_n - 1} \right]}{2\pi \left[K_f T_f + K_{cu} (t - t_f) \right]}$$

where

- r_n outer radius of disc segment
- $r_n - 1$ inner radius of disc segment
- K_f thermal conductivity of iron (for PPM focusing)
- K_{cu} thermal conductivity of copper
- t_f thickness of iron in disc segment (for PPM focusing)
- $t - t_f$ thickness of copper in disc segment.

The total temperature gradient ΔT between the inner ferrule surface and the outer vacuum barrel surface is therefore (Figure 86):

$$\Delta T = \Delta T_1 + \Delta T_2 + \Delta T_3 + \Delta T_4 + \Delta T_5 + \Delta T_6$$

The thickness of the copper cladding was adjusted to keep this temperature gradient to less than 100°C or

$$\Delta T_{\max} \leq 100^\circ\text{C}$$

with the exception of the 850 MHz and 2 GHz tubes, where it was allowed to reach 150°C.

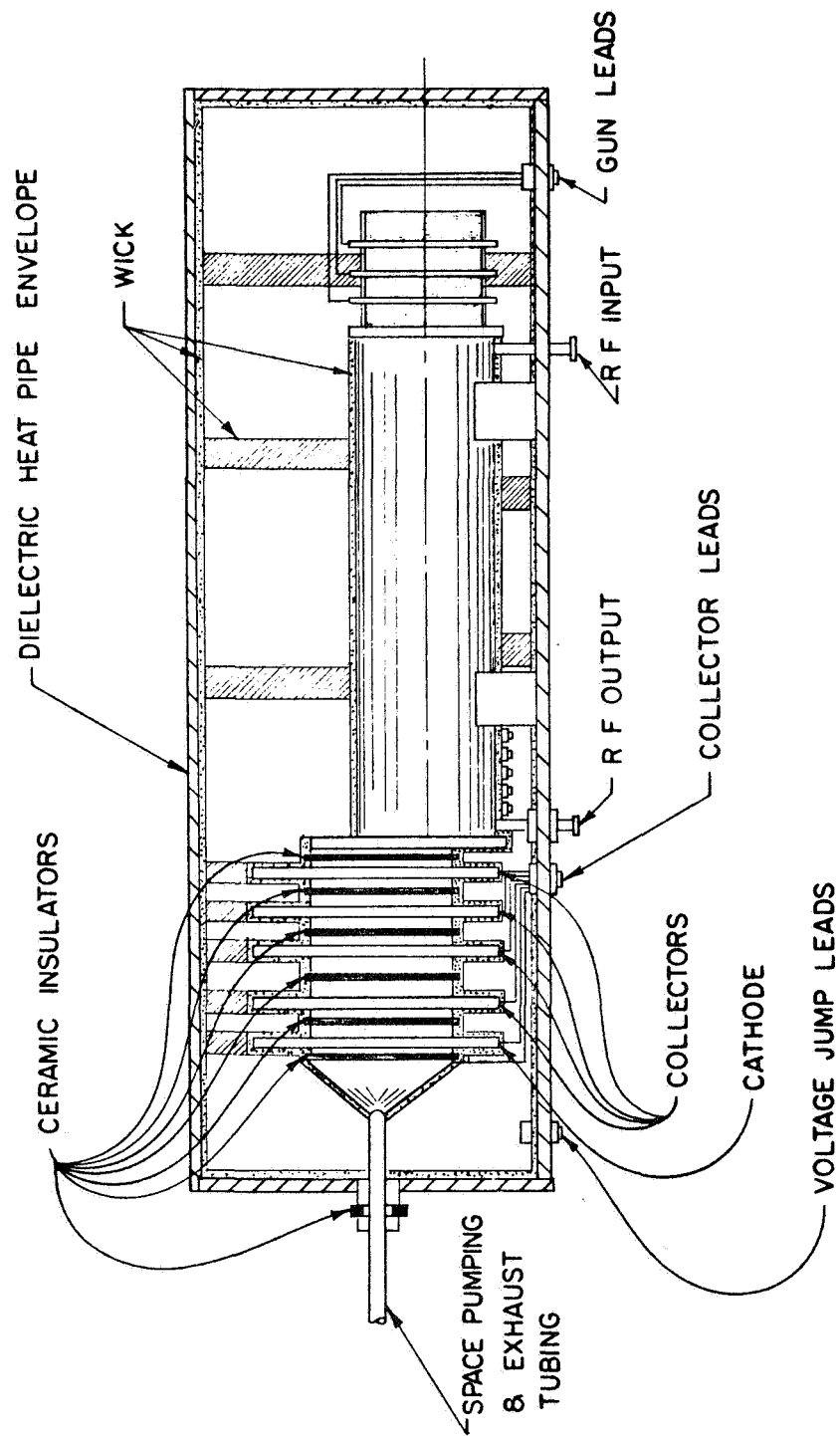


Figure 85 Schematic of tube with dielectric heat pipe cooling.

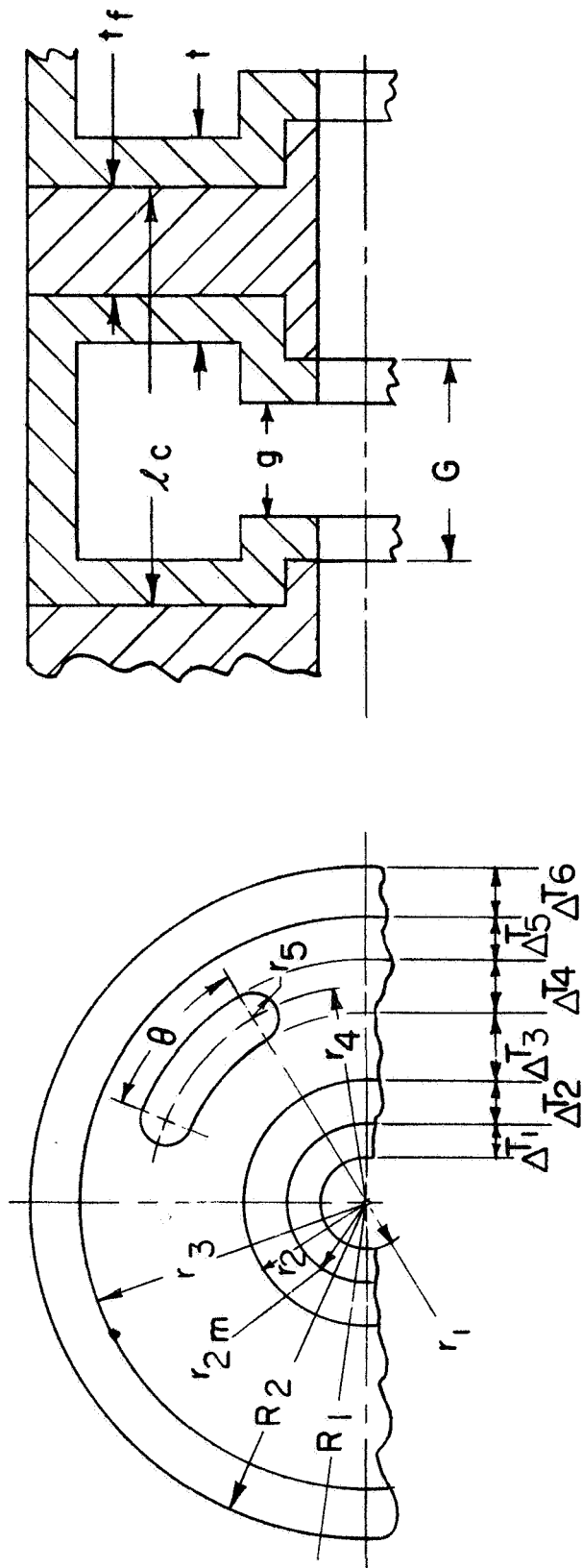


Figure 86 Thermal analysis of coupled cavity structure.

The computed data for ΔT are listed in Table XXII for all tubes.

The required operating temperature T_H of the heat pipe fluid at the vacuum barrel surface is determined, when the maximum temperature T_f at the ferrule is specified. It is given by

$$T_H = T_f - \Delta T - \Delta T_H$$

where

ΔT_B = interface temperature drop at barrel surface

ΔT_H = temperature drop from cooling surface (evaporation)
to radiating surface (condenser) in heat pipe.

The maximum temperature of the pole piece ferrule (for PPM focusing) has been specified to

$$T_{f \text{ max}} (\text{PPM}) = 150^\circ\text{C}.$$

This provides a safety margin of more than 500°C against destructive overheating (Curie-temperature $\approx 700^\circ\text{C}$). For solenoid focusing the maximum permissible ferrule temperature has been specified to

$$T_{f \text{ max}} (\text{solenoid}) = 200^\circ\text{C}.$$

This provides a safety margin of more than 500°C against destructive overheating.

The resultant maximum temperature gradients have been listed in Table XXII.

With the chosen heat pipe temperature T_H the temperature of the radiator T_r is determined

$$T_r = T_H - \Delta T_H - \Delta T_r$$

Table XXII Thermal circuit analysis (Figure 86).

TUBE	FREQUENCY	MODULATION	FOCUSING	MAXIMUM FERRULE TEMPERATURE (°C)	CIRCUIT TEMPERATURE GRADIENT ΔT (°C)	COLLECTOR TEMPERATURE (°C)	COLLECTOR PLATE EXTENSION ΔR_t (cm)	WORKING FLUID
L-band	850 GHz	AM	PPM	150	29.5	100	.8	DC 200
S-band	2 GHz	AM	PPM	150	49.2	100	.53	DC 200
		FM	PPM	200	103.0	100	1.32	DC 200
X-band	8 GHz	FM	Solenoid	200	88.0	100	1.21	DC 200
Ku-band	11 GHz	FM	Solenoid	200	84.4	100	3.44	DC 200

with

ΔT_r = interface temperature drop at radiating surface.

The interface temperature gradients at the heat pipe surfaces ΔT_B and ΔT_r and the temperature drop through the heat pipe ΔT_H are small compared to the temperature gradient in the circuit. Their magnitude is in the order of $\Delta T_B + \Delta T_r + \Delta T_H \approx 10^\circ$ to 20°C .

With the known radiator temperature T_r and the known dissipated power P_r ,

$$P_r = P_o (1 - \eta) + P_s$$

with

P_o = applied dc power to the tube

η = tube efficiency

P_s = solenoid power (for solenoid focusing)

the required working fluid of the heat pipe can be determined. These data are also shown in Table XXII.

B. COLLECTOR COOLING

Figure 87 shows schematically the heat pipe cooled collector assembly. The collector plates are extended outside the vacuum envelope by ΔR_t to provide adequate heat transfer areas for heat pipe cooling. The extension ΔR_t was chosen to provide adequate heat transfer area for the total thermal collector power on one collector.

The power density for heat pipes with organic fluids is generally chosen as 60 watts/in² (9.3 watts/cm²).

The required extension ΔR_t is then found:

$$\Delta R_t = \frac{Q}{2\pi d_k (PD)}$$

d_k = collector diameter

Q = power absorbed by the collector

PD = average power density of working fluid.

The collector disc extensions and the vacuum envelopes are covered with wick material of .100 in (.254 cm) thickness. It was found in experiments with dielectric heat pipe wicks, that the evaporator wick thickness should not exceed .200 in (.508 cm) to prevent localized film boiling. A wick thickness for the evaporator of .050 in to .100 in was found to be most satisfactory. Wicks for the condenser will be single layer refracil .050 in (.127 cm) thick.. The radial wick spoke length ℓ_w can be calculated from the expressions:

$$\Delta P_v = 1.855 \times 10^2 \frac{Q^2}{\rho \eta_c^2 (\Delta R_t)^2 d_k^2 \ell_t^2 (\Delta H)^2}$$

$$\Delta P_\ell = \frac{Q \ell_w \nu}{2 n_w A r_c^2 \Delta H (Cf)}$$

$$\Delta P_c = \frac{2 \gamma \cos \theta}{r_c}$$

$$\Delta P_c = \Delta P_\ell + \Delta P_v$$

ℓ_w = wick spoke length between evaporator and condenser (cm)
 ΔP_c = capillary driving pressure
 ΔP_ℓ = pressure drop in liquid flow
 ΔP_v = pressure drop in vapor flow
 ΔH = latent heat of vaporization (cal/g)
 ℓ_t = thickness of collector plate (cm)
 n_c = number of collectors
 Q = heat flow (cal/sec)
 d_k = collector diameter (cm)
 ν = kinematic viscosity (cm²/sec)
 n_w = number of wicks
 A = wick cross-sectional area (cm²)
 Cf = wick factor for reffrasil, .4 to .5
 r_c = pore radius (cm)
 ρ = vapor density (g/cm³)
 γ = surface tension (dynes/cm)
 θ = wetting angle (degrees).

The condenser surface of the dielectric heat pipe is an integral part of the demountable tube package. The package envelope will therefore serve as condenser for the tube (dielectric heat pipe), and it will also serve as an evaporator for the radiator heat pipe system to the outside. This heat pipe system is an integral part of the spacecraft.

C. SPACECRAFT COOLING SYSTEM

Two specific configurations, the "dual panel RF joint concept" (Figure 88) and the "quad panel slip ring concept" (Figure 89) have been suggested by NASA and have been considered for a heat pipe design. These two configurations differ primarily in their attitude toward the sun. The "dual panel RF joint concept" is stationary with respect to the sun, while the "quad panel slip ring concept" rotates with respect to the sun with one revolution per day.

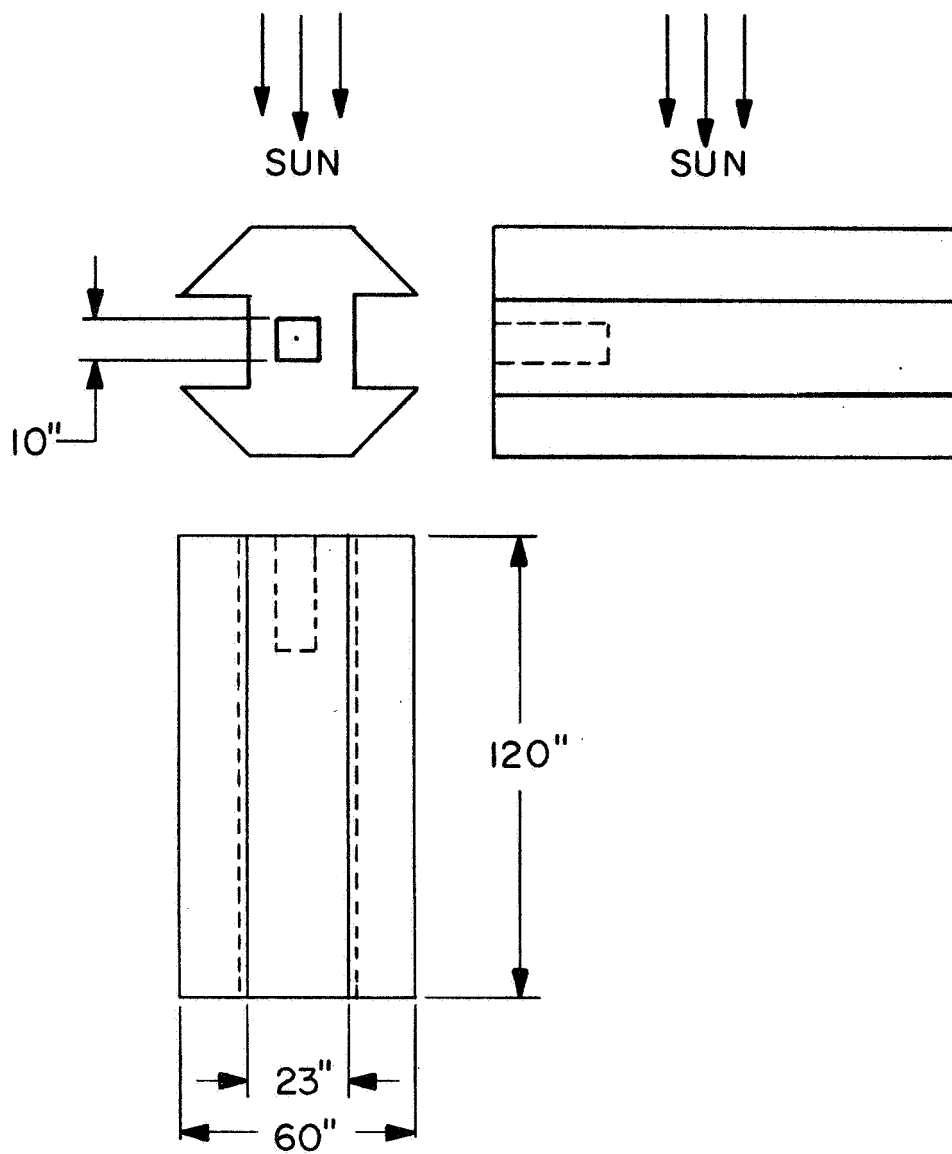


Figure 88 Spacecraft design using dual panel RF joint concept.

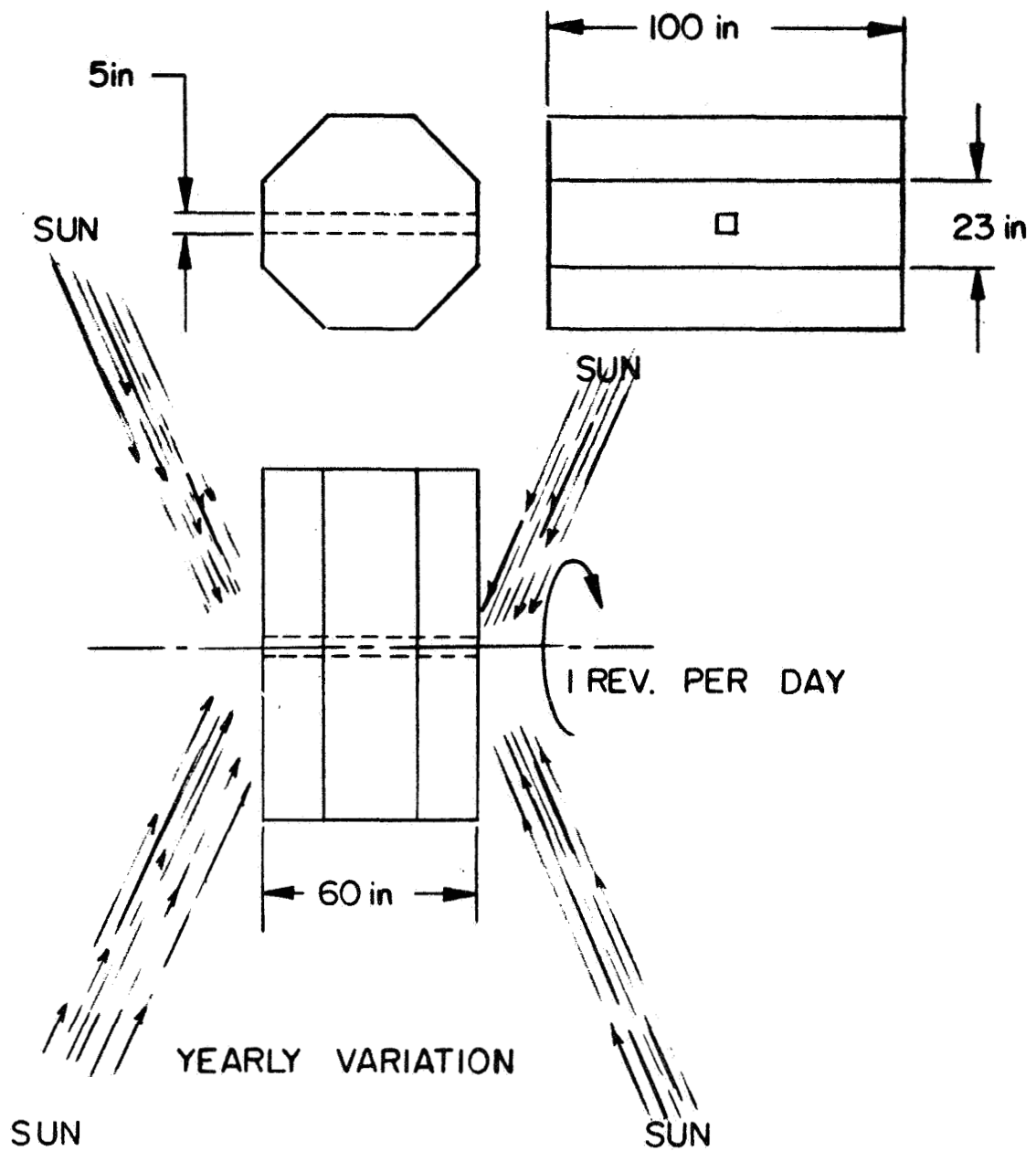


Figure 89. Spacecraft design with quad panel slip-ring concept.

For the "dual panel RF joint concept" only the spacecraft surfaces, which are not exposed to the sun, are available for heat radiation. The rotating "quad panel slip ring concept", on the other hand, permits the application of one-way heat pipes in the outer spacecraft system, and a very large portion of the spacecraft envelope can be made available for heat radiation, since the one-way heat pipes will effectively shield the spacecraft interior against sun radiation.

A calculation of the available radiator surfaces shows that these surfaces indeed permit a heat pipe operation at very low temperatures. The "dual panel RF joint concept" permits radiator and heat pipe temperatures T_R in the order of

$$T_R \approx 120^\circ\text{C}$$

while the superior one way heat pipe system of the "quad panel slip ring concept" may be operated as low as

$$T_R \approx 80^\circ\text{C}.$$

In both configurations the cooling system was conceived as an integral part of the spacecraft, such that a part of the spacecraft skin serves as a heat radiator. This approach permits to design a cooling system for low temperature operation without significant weight increase.

Of the two alternate configurations the "quad panel slip ring" concept was proposed for the cooling system design, because it provides a larger effective radiator area and thus permits lower operating temperature. A schematic of this spacecraft configuration in orbit is shown in Figure 90.

The cooling system consists of 3 heat pipe stages, as shown schematically in Figure 91.

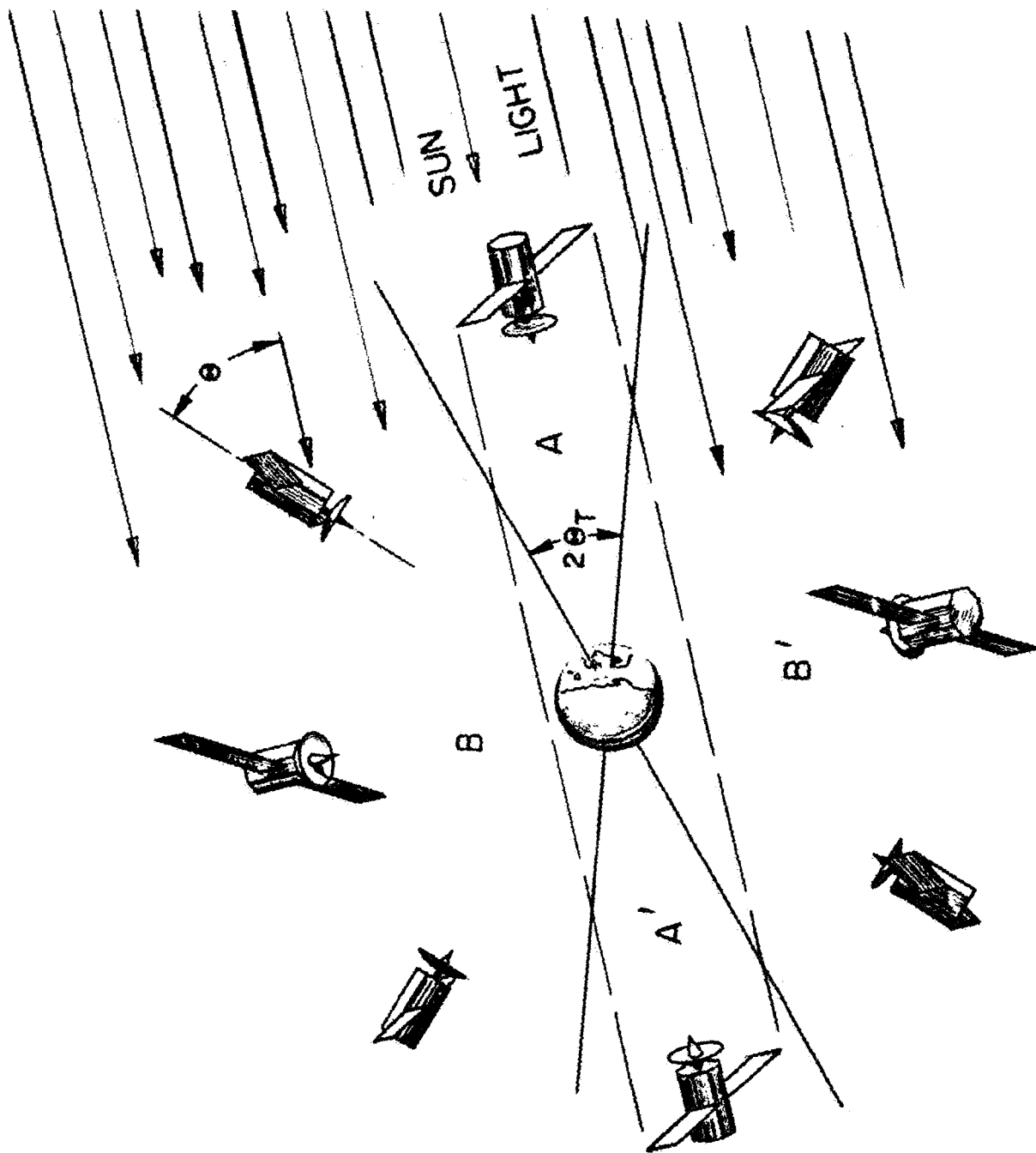


Figure 90 Spacecraft in synchronous orbit (quad panel slip ring concept).

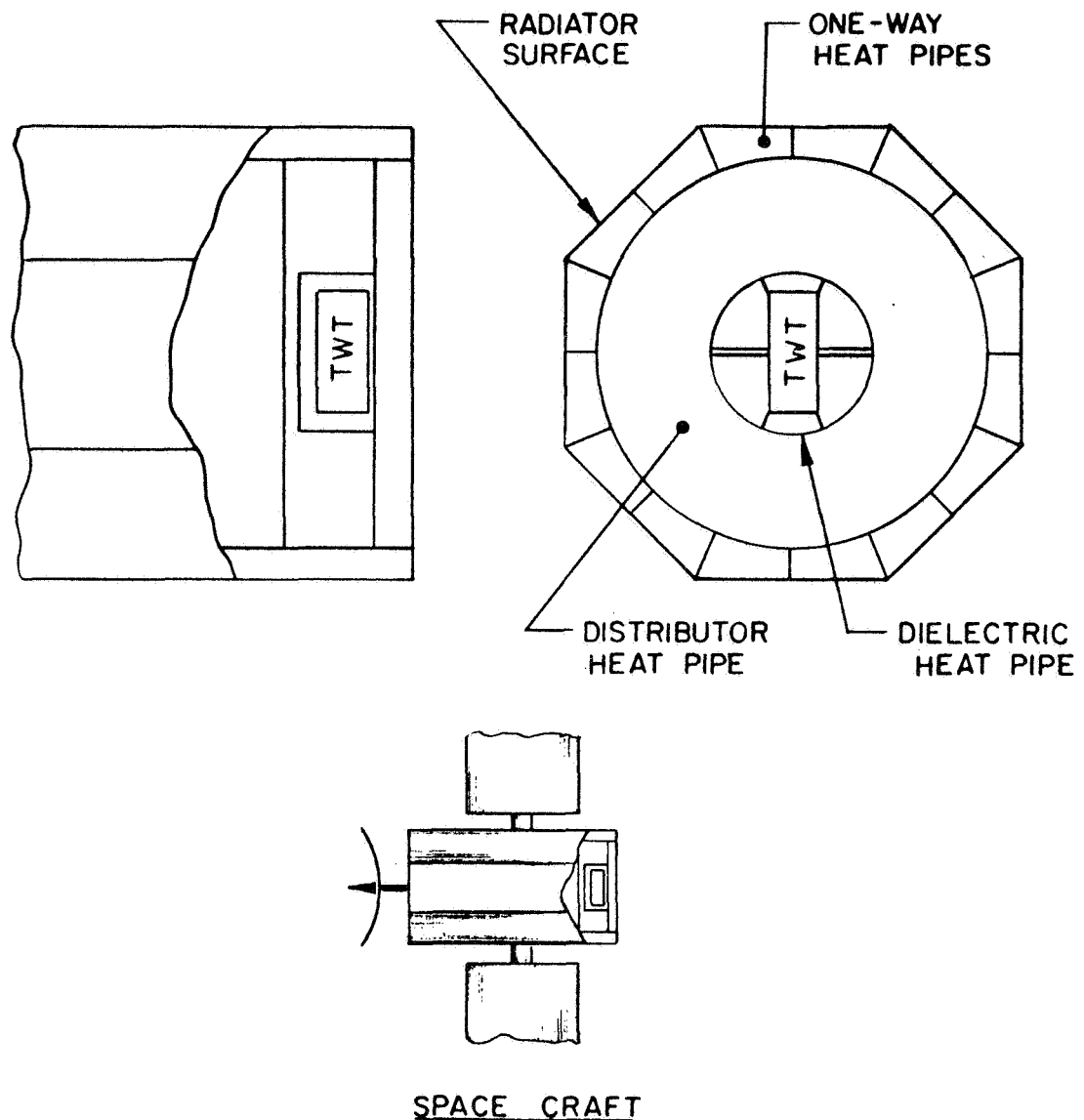


Figure 91 Schematic of heat pipe cooling system.

The tube is enclosed in a dielectric heat pipe system. This makes it possible to achieve a very effective heat transfer from all tube surfaces with different electric potentials to the distributor heat pipe. The dielectric heat pipe fluid is an electric insulator and, therefore, a more efficient heat transfer is achieved from the tube than would be possible through ceramic insulators.

The distributor heat pipe transfers the heat to the multiple one-way heat pipes. From these, the heat is dumped into the radiator surfaces of the spacecraft skin.

The one-way heat pipes automatically turn off the heat flow to those radiator panels, which are exposed to the sun and thus cannot radiate. This makes it possible to provide a larger radiator area, although a fraction of the increased area is temporarily not in operation. This one way cooling system provides an abundance of heat transfer paths and thus can be considered more reliable. The system is rather large in size and the heat flow densities are, therefore, very low. These estimated heat flow densities are substantially lower than the established heat flow capabilities of such heat pipe systems. This also will contribute to a high reliability of the design.

The estimated power flow densities and average radiator temperatures for these systems are:

RF POWER	HEAT FLOW DENSITIES			AVERAGE RADIATOR TEMPERATURE
	DIELECTRIC HEAT PIPE	DISTRIBUTOR HEAT PIPE	ONE -WAY HEAT PIPE	
5 kW	1.09 W/cm ²	.634 W/cm ²	.08 W/cm ²	57°C

The temperature of the radiator panels will vary during one period (24 hours) due to the change of exposure to the sun and due to the directional changes of the heat flow in the one way heat pipes.

These periodic temperature variations have been evaluated for the proposed spacecraft configuration.

In this analysis each of the panels have been considered as being isolated thermally from each other.

The geometry of the spacecraft (Figure 90) suggests to consider two types of panels:

- i) panels never exposed to the sun
- ii) panels periodically exposed to the sun

The periodically exposed panels go through the following four thermal conditions in one period (Figure 90):

- 1) One way heat pipe: operating; sun exposure sets in Region A(A')
- 2) One way heat pipe: off; continuous sun exposure Region B(B')
- 3) One way heat pipe: operating; sun exposure ends Region A'(A)
- 4) One way heat pipe: operating; no sun exposure Region B'(B)

The resulting temperature variations are shown in Figure 92 for a 5 kW system.

The one way heat pipes are automatically activated and inactivated by the sun exposure, and thus they protect the spacecraft cooling system against an excessive thermal load from the sun. Only during their turn-off period is there a small amount of heat being absorbed by the system from the sun. This causes only a small temperature increase of 5° to 10° of the radiation temperature (at $t = 7$ to 8.5 hours and $t = 19$ to 20.5 hours).

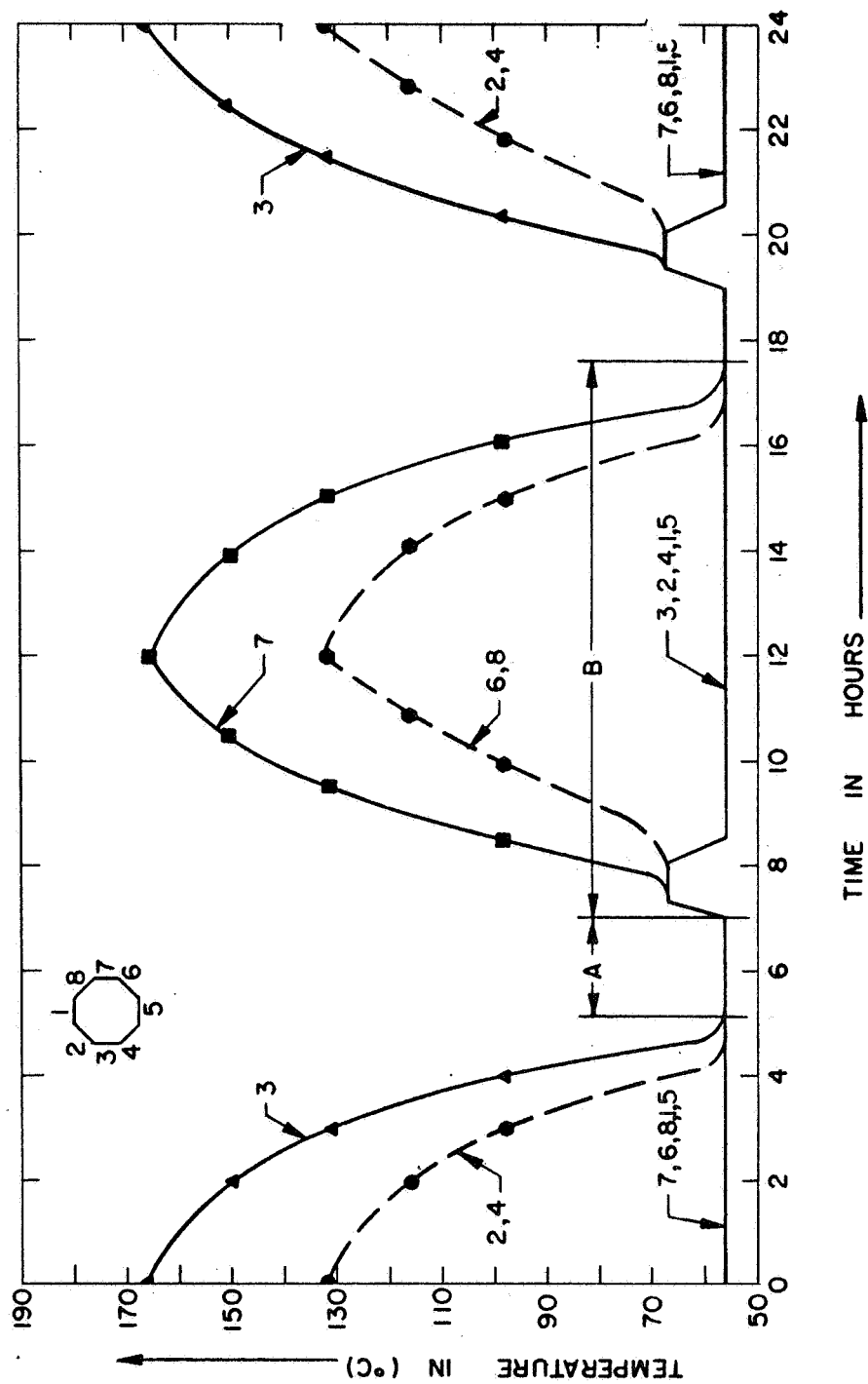


Figure 92 Temperature variations on radiator panels during orbit (one-way heat pipe system, $P = 5$ kW).

The turn-off (on) time of the one way heat pipes (angle θ_T of Figure 90) is given by the condition that the sun absorption becomes equal to the heat radiation, or

$$S\alpha_s \cos \beta = e\sigma T^4$$

where:

- S = solar constant
- α_s = absorptivity
- $S\alpha_s = .135 \text{ W/cm}^2$
- $\cos \beta$ = projection of surface to sun
- $e = .92$ (emissivity)
- σ = Stephan-Boltzmann constant

The projection angle β is related to the angle θ of the space craft axis to the sun by (Figure 92):

$$\begin{aligned}\beta &= \frac{\pi}{2} & (\text{panel 1 and 5}) \\ \beta &= \theta & (\text{panel 3 and 7}) \\ \beta &= \theta + \frac{\pi}{4} & (\text{panel 2, 4, 6, and 8})\end{aligned}$$

After the one-way heat pipes are turned off, the panels continue to absorb sun radiation and their temperature is given by the condition:

$$T = \left(\frac{S\alpha_s \cos \beta}{e\sigma} \right)^{1/4}$$

The maximum temperature increase of these panels during this period, for the 5 kW system, are found to range from (Figure 92)

$$\Delta T_{\max} = 110^\circ\text{C} \quad (\text{panel 3 and 7})$$

and

$$\Delta T_{\max} = 75^\circ\text{C}. \quad (\text{panel 2, 4, 6, and 8})$$

Although the effective radiation area is reduced during the period B (B'), the radiation temperature increase from that of period A (A') is very small (not shown in Figure 92).

A shut-off and on cycle of 1.5 hours duration has been specified during one period (24 hours). The temperature variations of the cooling system during this operation have, therefore, been estimated.

During the turn-off period of radiation the temperature of the panels is described by the equation:

$$C_{th} \frac{dT}{dt} = A \epsilon \sigma T^4$$

where

A = area of radiation surfaces

C_{th} = thermal capacitance of spacecraft

where

$$C_{th} = \sum W c_p$$

and

W = weight of material

c_p = specific heat of material.

The temperatures of the heat pipe system are given by the small temperature gradients produced in the heat pipe system. However, at a lower temperature limit T_L

$$T_L \approx 25^\circ\text{C} \quad (\text{room temperature})$$

the heat pipes become inoperative and the heat transfer from the inner heat transfer surfaces to the external radiators is primarily by radiation.

For each radiation heat transfer a temperature gradient will be produced. This temperature gradient, however, is found to be small.

The resultant temperature variations of the spacecraft during the shut-off time are shown in Figure 93. In Figure 94 the temperature drop is shown for an extended shut-off period. It can be seen that the temperature of the spacecraft drops so rapidly after shut-off that the heat pipes become inoperative after only a few minutes of the turn-off. At the end of the turn-off period, the temperature of the radiation panels has dropped to about

$$T_{\min} \approx -173^{\circ}\text{C}$$

while the spacecraft system has cooled down to nearly -148°C .

The total temperature variation ΔT_{\max} of the spacecraft during one period is, therefore, only about

$$\Delta T_{\max} \approx 200^{\circ}\text{C}$$

including the turn-off period. This temperature variation will keep thermal stresses relatively small. The maximum temperature gradient ΔT_s within the cooling system at any time is only about $T_s \approx 25^{\circ}\text{C}$.

During most of the shut-off period the heat pipe fluids will be frozen. However, immediately after turn-on the heat pipes will start to function. The tube heat will primarily be used to melt the heat pipe fluids, since the evaporation heat of these fluids is much larger than their melting heat. The operational temperatures of the cooling system is reached very rapidly after turn-on (Figure 93).

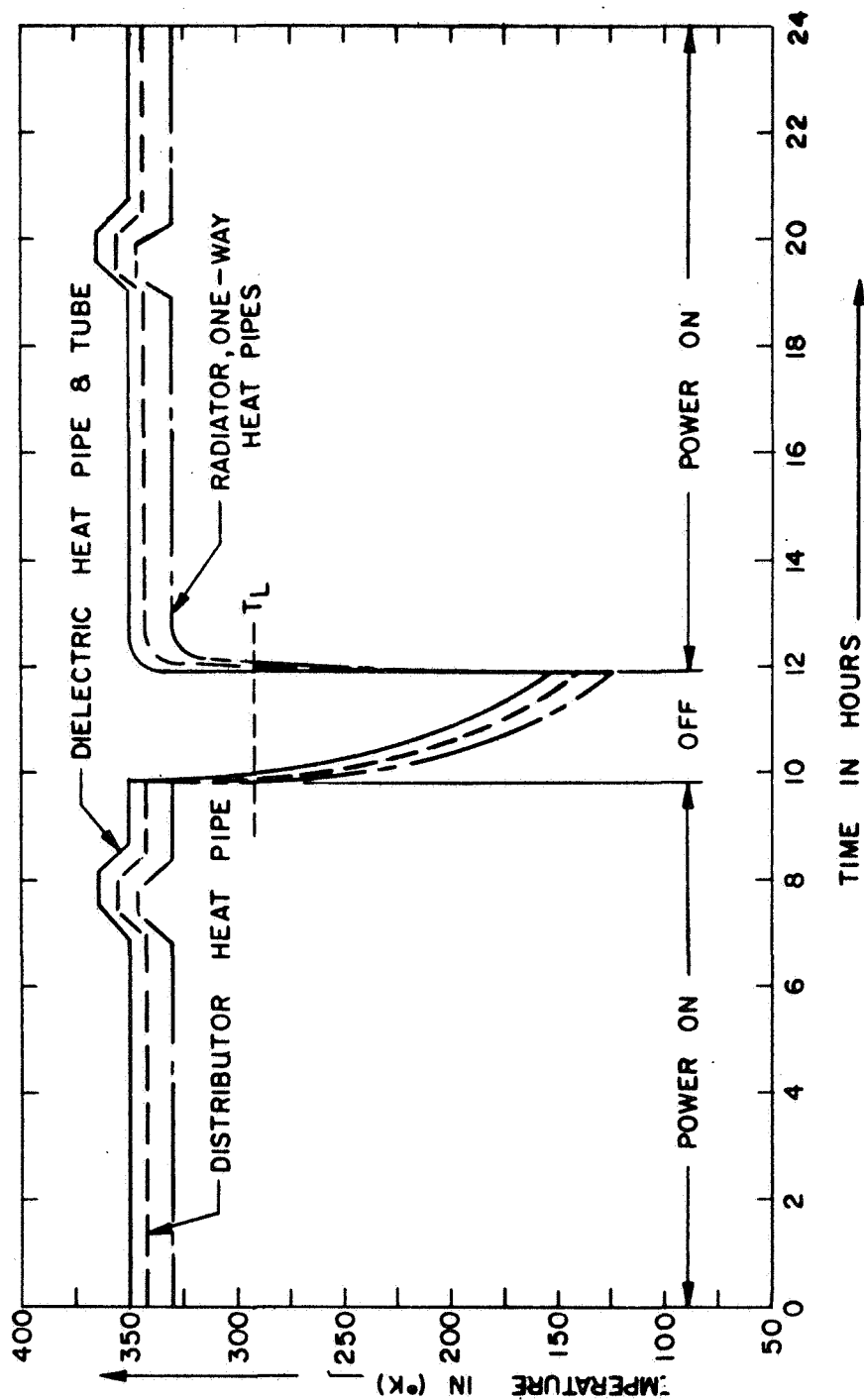


Figure 93 Temperature variations of heat pipe cooling system during orbit with 1.5 hours turn-off period.

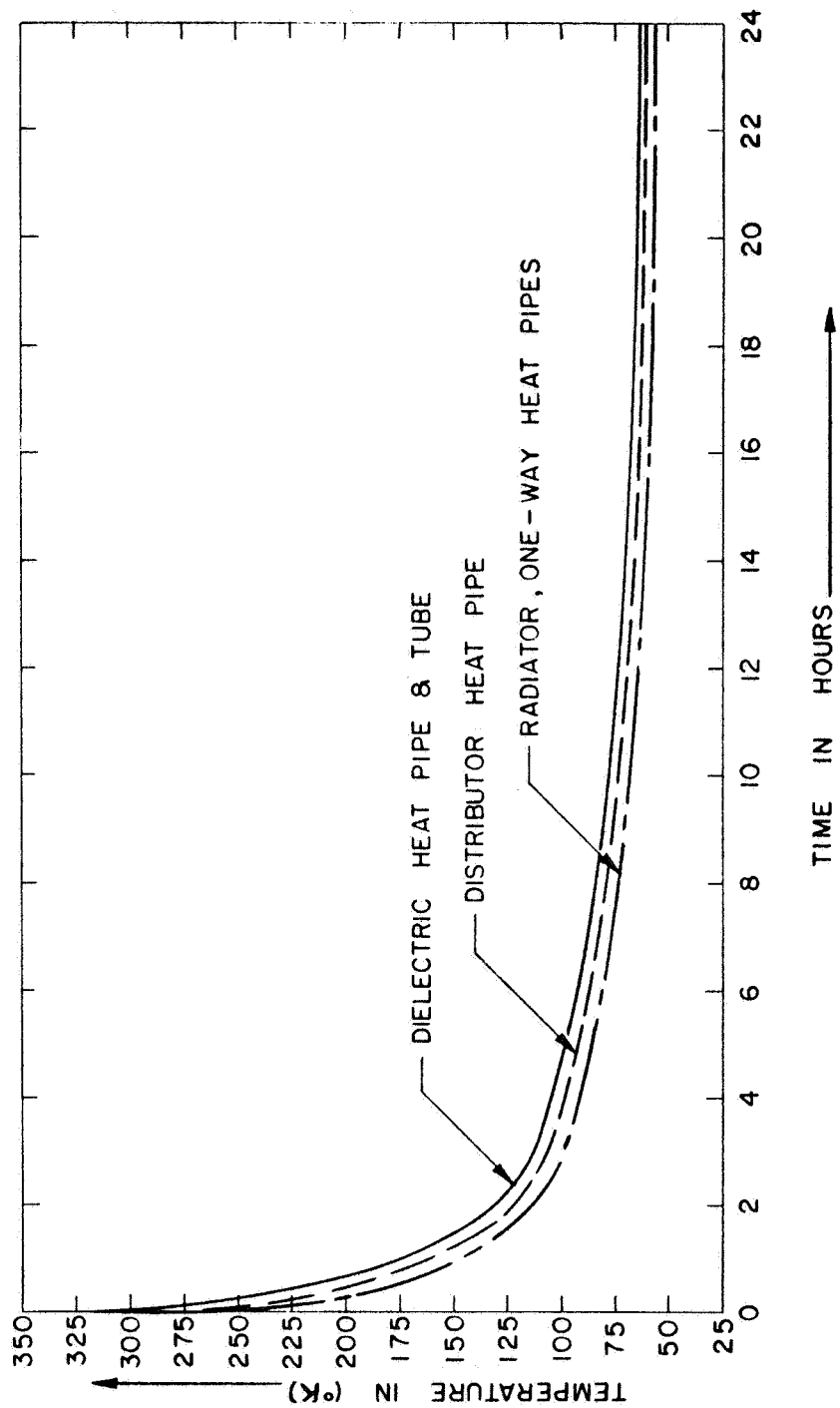
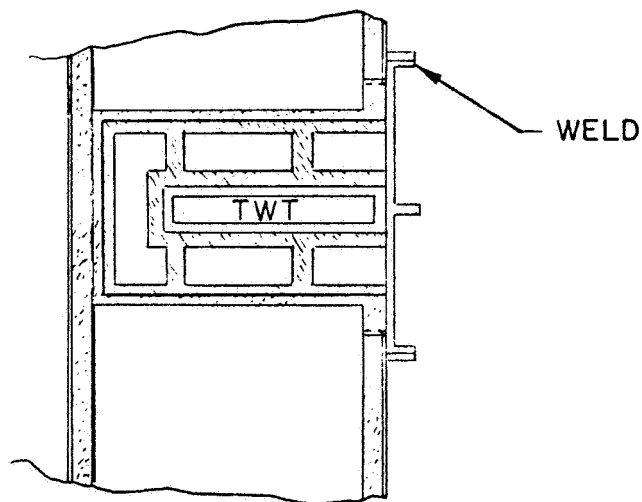
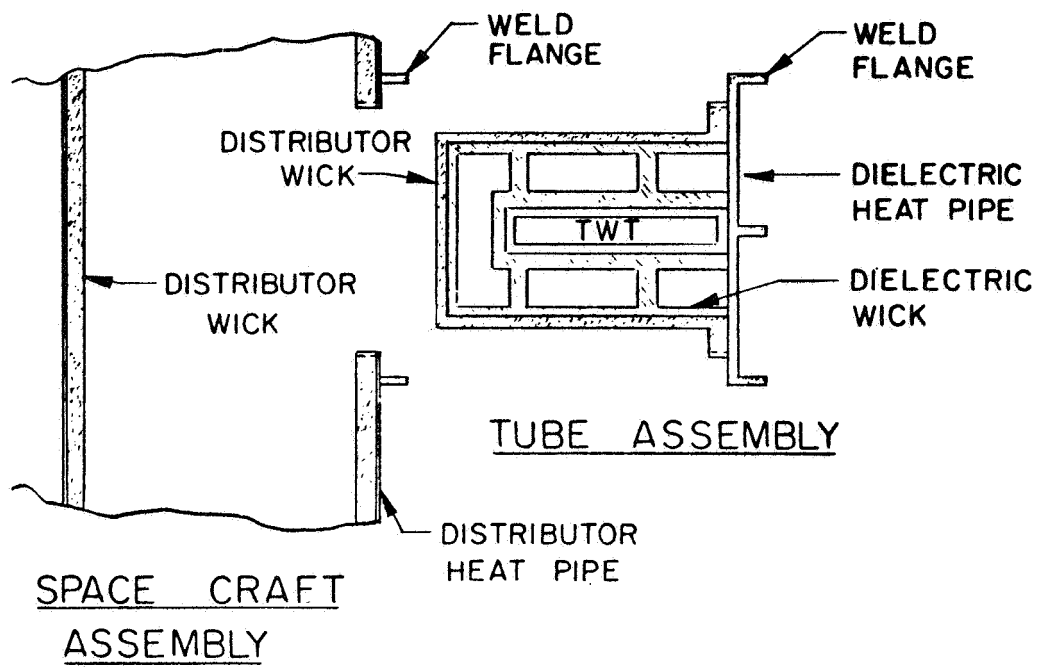


Figure 94 Rate of temperature drop of heat pipe cooling system after turn-off.

In Figure 95, a schematic of the spacecraft cooling system assembly is shown. This schematic shows the advantages of the proposed three-stage cooling system. The tube with the dielectric heat pipe is built and assembled as a separate unit, and the tube performance, including its heat transfer characteristics, can readily be evaluated outside the spacecraft.

The distributor heat pipe and the one-way heat pipes are an integral part of the spacecraft. The assembly of both parts is accomplished with a final weld.



FINAL ASSEMBLY

Figure 95 Schematic of distributor heat pipe system assembly.

IX. MECHANICAL DESIGN

A. CIRCUIT CONSTRUCTION

In this section some of the details of the mechanical designs that are peculiar to the proposed high power traveling-wave tubes for this space application will be outlined. The coupled cavity interaction circuit was chosen. At the power levels and bandwidths required, it provides a high impedance, which is desirable for the requirements of high efficiency and high gain per unit length. It is also a superior circuit from the standpoint of dissipating the heat which is generated by intercepted beam power. Since the vacuum envelope can be constructed entirely of metal and ceramic materials, high temperature processing techniques are possible with a coupled cavity tube to assure improved life and reliability. Complete circuit subassemblies from typical coupled cavity tubes are shown in Figure 96.

These are X-band tubes incorporating PPM focusing. For this type of tube the cavity walls are made of iron to serve as magnetic pole pieces. They are the larger diameter portion of the circuit. The pole pieces are copper plated to facilitate brazing of the assembly. The outer diameter wall of the coupled cavity is made of copper which is brazed between the pole pieces and serves to complete the vacuum envelope. The input and output RF match assemblies are located at each end. On the tubes shown the coupler is connected to a reduced height waveguide and then through a step transformer to a "poker chip" ceramic waveguide window. These are high gain tubes (approximately 50 dB), which incorporate internal circuit severers with matched terminations to divide the circuit into separate sections to assure stability. The final

assembly of the circuits shown is made in a controlled atmosphere furnace using a high temperature copper-gold brazing material between each circuit element. The vacuum assembly is completed by connecting the circuit with the electron gun and the beam collector by heliarc welding.

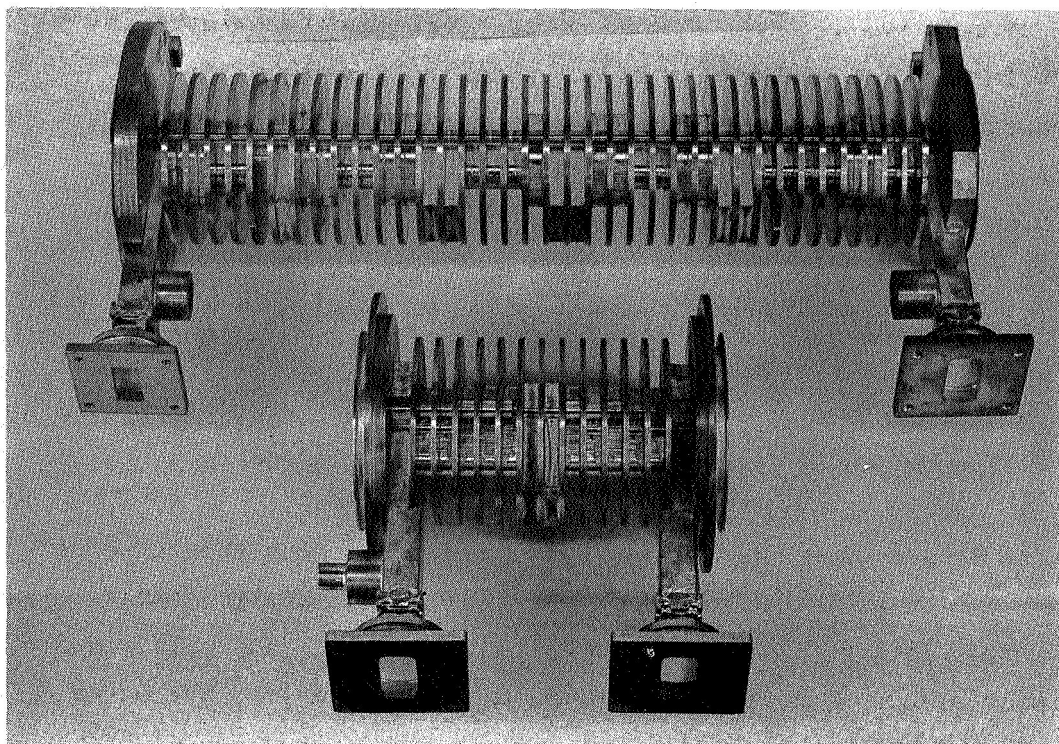


Figure 96 Typical coupled cavity circuit assemblies for periodic permanent magnet focused X-band tubes.

The magnets are split rings and are mounted on the tube after the processing has been completed. They are not part of the vacuum envelope. Circuit parts from a typical Ku-band tube are shown in Figure 97. The dark half ring pieces are the Alnico focusing magnets. The two holes through the larger pole pieces are used for alignment and to provide coolant pipes in the tubes.

Figures 98 and 99 show typical parts for coupler assembly of a coupled cavity tube with solenoid focusing. This type of tube uses only copper for the circuit, yielding excellent thermal conductivity as well as low electrical loss. The RF match between the circuit and the external waveguide is optimized by adjusting the dimensions of the stepped coupler cavity. The four holes near the outer edge of the circuit provide alignment during assembly and also coolant passages for forced liquid cooling in operation. The input waveguide is bent to facilitate mounting in the solenoid. The rectangular cutouts at the outer diameter of the circuit are provided to mount the waveguide. In the proposed tubes with solenoid focusing, the solenoids will be wrapped directly onto the circuit, which will result in a much smaller and lighter package and a more efficient solenoid. The final tube design will be similar to a typical PPM focused design rather than the usual solenoid focused coupled cavity tube.

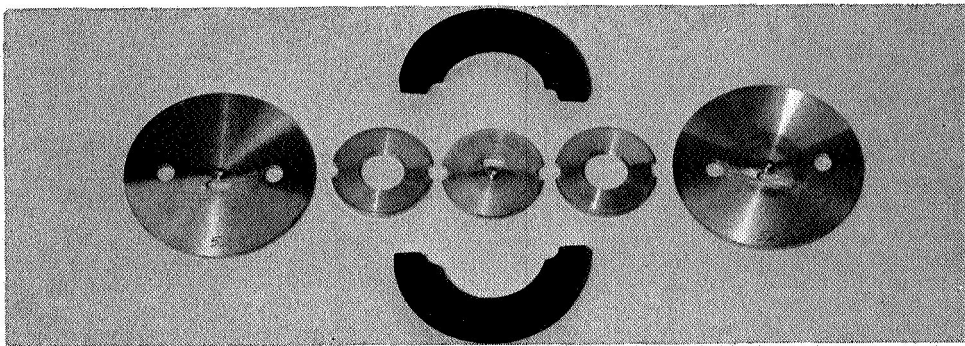


Figure 97 Typical circuit parts for a PPM focused coupled cavity tube.

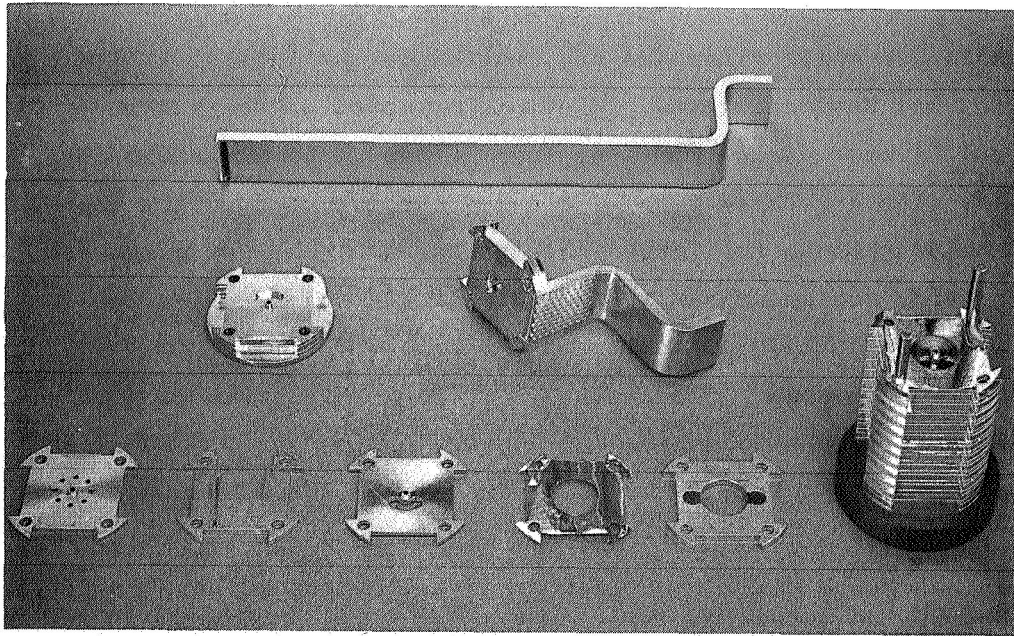


Figure 98 Typical circuit parts of solenoid focused coupled cavity tube.

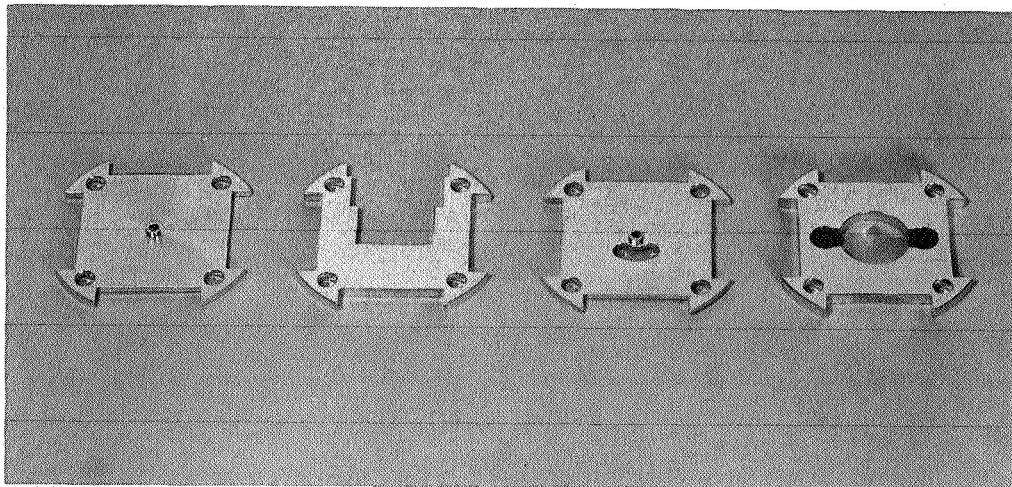


Figure 99 Typical waveguide coupler parts for solenoid focused coupled cavity tube.

Parts for a typical sever termination assembly are shown in Figure 100. These are parts from a PPM focused Ku-band tube. The sever consists of a cavity web with the kidney-shaped coupling hole eliminated. The RF circuit wave is, therefore, completely blocked from the following circuit section. The termination at the sever is provided by a wedge shaped piece of a lossy ceramic material. This material is specially designed to operate at high temperatures and to provide the proper dielectric and loss properties required to produce a satisfactory termination. It may be brazed to the cavity wall for high power dissipation. The dimensions of the termination itself and of the termination cavity are chosen to provide a good RF match to the circuit.

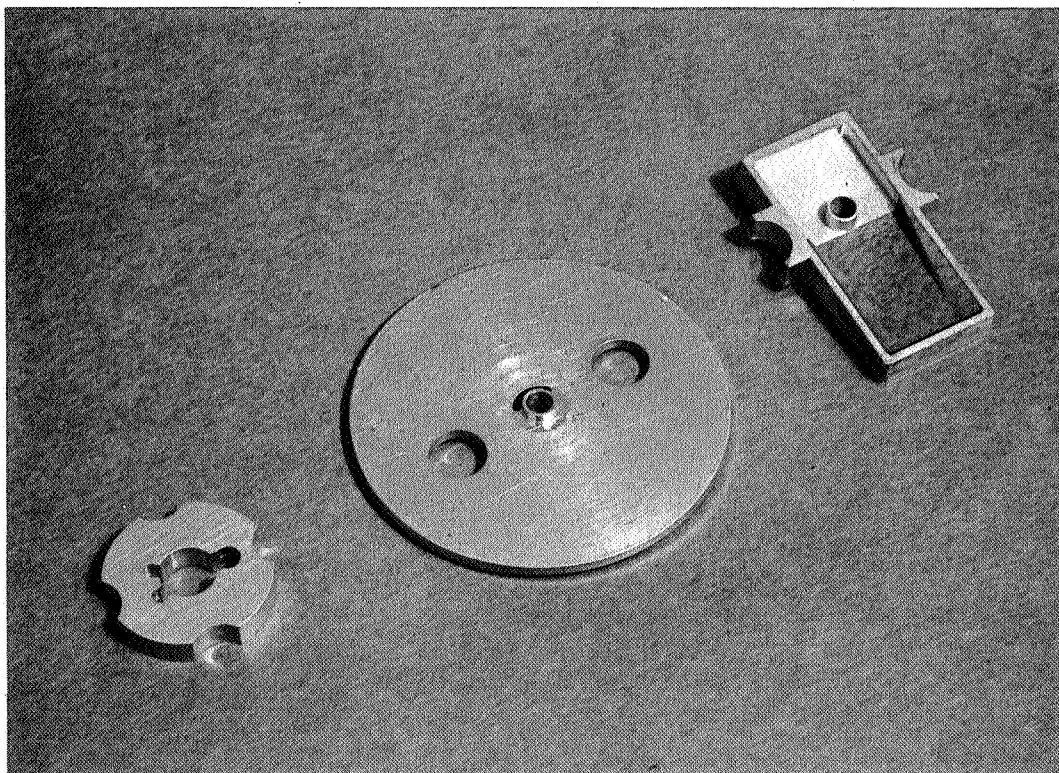


Figure 100 Typical sever transition components for coupled cavity tube.

B. GUN CONSTRUCTION

A typical shadow grid electron gun assembly and its anode are shown in Figure 101. The anode and the focus electrode, which is the element at the end of the gun assembly with eight circularly located holes, are fabricated of highly polished molybdenum. Beyond the focus electrode a pair of precisely aligned target grids can be seen. The top grid serves as a control element. The lower one is the shadow grid which is located very close to the cathode. It shields the control grid from electron interception. This double grid technique provides extremely low grid current interception (of the order of one-tenth of 1% of the total beam current) and consequently results in long grid life and reliability. The shadow grid technique is proposed to allow modulation of the beam in the traveling-wave tube modulator for AM signals.

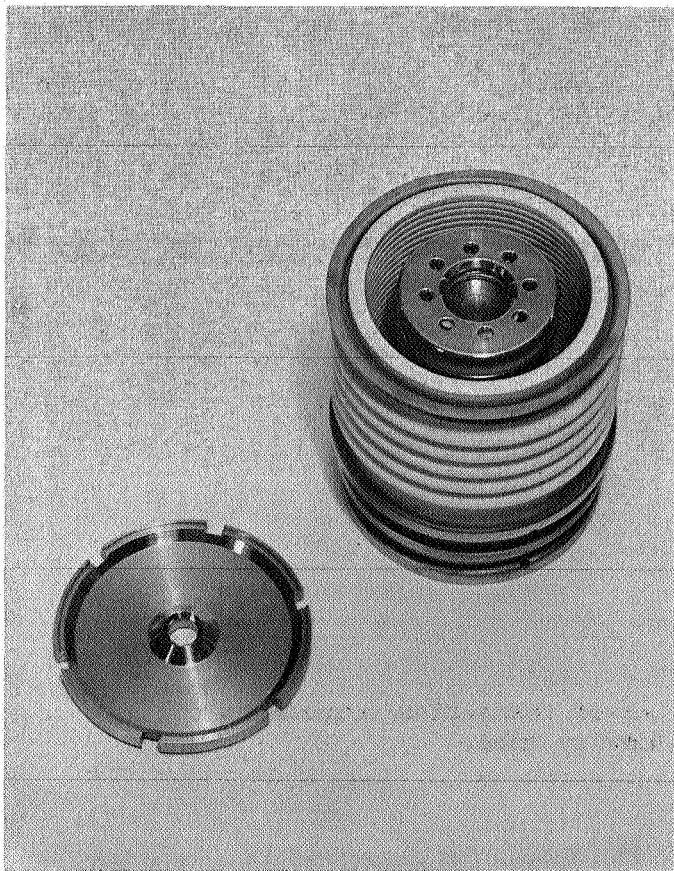


Figure 101
Typical shadow grid
electron gun assembly.

The outer stem assembly of the electron gun is made by a single high temperature braze of a stacked set of alternating alumina ceramic standoffs and kovar rings. The internal gun stem assemblies are welded to the internal flanges of the kovar rings. The ring at the end serves as a weld flange to attach the completed electron gun to the body of the tube. For the proposed tubes the anode will be isolated from the tube body, so that a small positive potential can be applied to it to serve as an ion trap. For that case, the gun stem will have one more insulator ring than is shown in the photograph, and the anode will be sealed to it.

For the FM tubes, grid modulation will not be required. The basic gun construction will be similar, except for the omission of the grid components.

C. SPECIAL DESIGN REQUIREMENTS

The preceeding paragraphs have outlined the basic mechanical features of typical high power coupled cavity traveling-wave tubes that have been developed in the past. The proposed application will require novel approaches in some of the construction details. The major areas are as follows:

1. A heat pipe coolant system is used. In the past, coupled cavity tubes have usually been cooled by forced liquid flowing through a series of ducts distributed through the tube body and collector. Heat pipe techniques have recently been applied to tube elements such as the collector. However, the proposed application will cool the entire tube. The heat pipe cooling system requires primarily changes in the outer packaging of the tube. However, the construction techniques for fabricating the vacuum envelope will not be different from that for conventional cooling.

2. A multi-voltage jump taper will be used in the output section to provide efficiency enhancement. The voltage jump technique requires that successive circuit cavities be insulated from one another. The insulation must be capable of holding the jump voltage and also providing a mechanically strong vacuum seal. Figure 102 shows a cross-sectional layout sketch of an insulator assembly designed for PPM focused tubes. The insulator assembly is similar to one section of an electron gun ceramic insulator assembly. It consists of the dc block ceramic ring between a pair of kovar weld flange rings with metalized back-up ceramic rings. The back-up ceramic rings provide greater strength and reliability of the metal to ceramic seal. High purity alumina ceramic will be used. This material has good mechanical and electrical properties. To prevent RF radiation an RF choke is incorporated within the cavity structure. The use of an alumina ring which has a high dielectric constant, inside the choke groove as well as for the dc block insulator, provides high dielectric loading and permits therefore a small choke assembly design. The final assembly of a series of voltage jump cavities is made by means of a peripheral weld between the ceramic assembly weld flange and the outer edge of the iron pole piece. The outer diameter of the pole piece is stepped, as shown in Figure 102, to provide thermal isolation during the welding operation and to locate the split ring pole piece extension which is installed after processing of the vacuum assembly. Insulation material such as teflon is installed between the focusing magnet and the adjacent pole piece which is at a higher potential. Electrical lead connection to the individual circuit section can be made by welding a lead to the circuit and stringing it through a groove in the pole piece extension to the outside of the tube package.

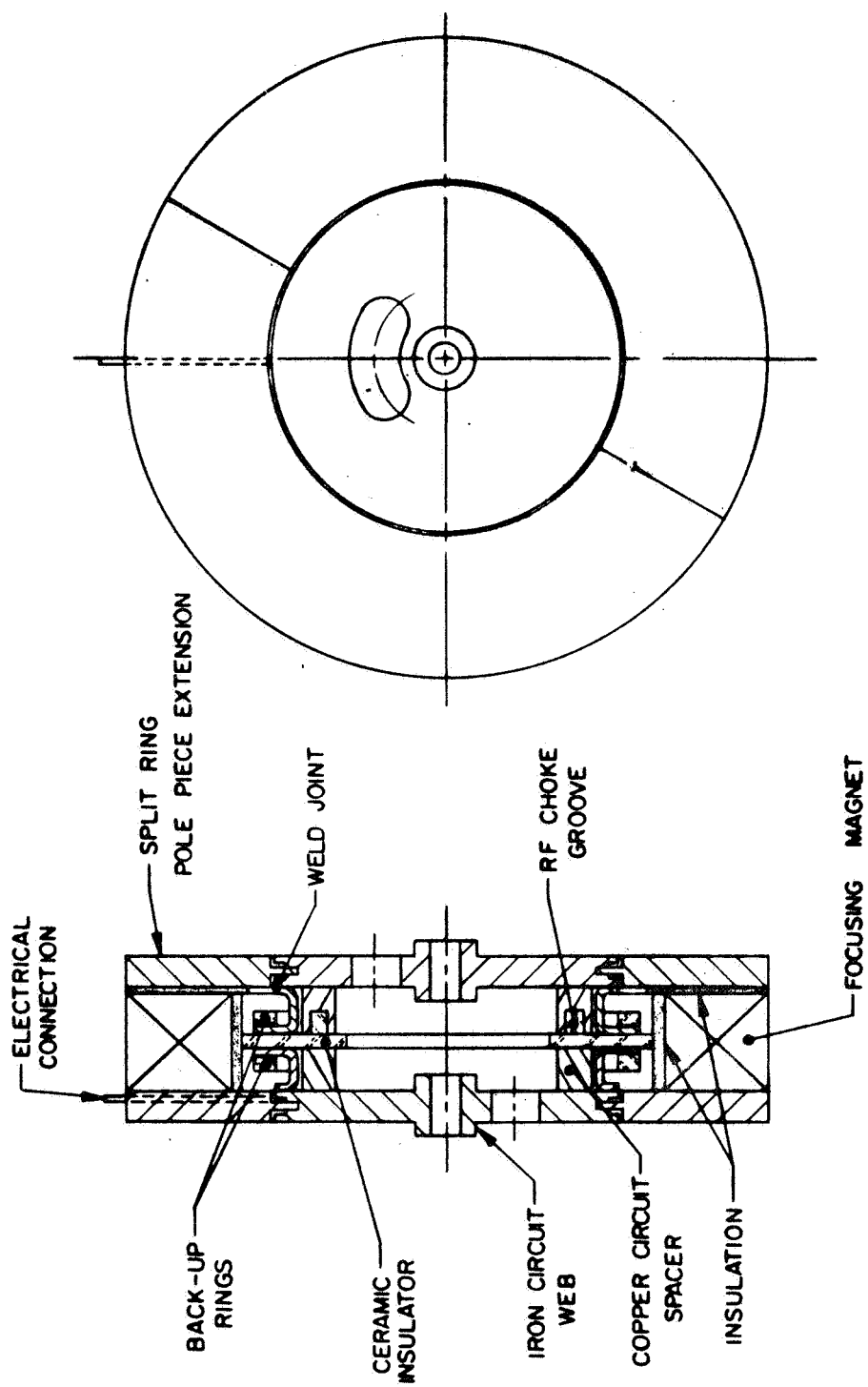


Figure 102 Voltage jump insulator assembly with iron cavity walls.

Solenoid focusing is proposed for the higher frequency tubes. Because the space is more limited than on the larger lower frequency tubes, and because iron pole pieces will not be used, a voltage jump insulator assembly as shown in Figure 103 will be used. The ceramic insulator assembly is similar to that described above; however, the weld flange is arranged so that the final peripheral weld can be made between successive flanges. The copper circuit cavity sections are located radially between the successively stacked insulator assemblies. A split insulator tubing (this can be a wick of the heat pipe coolant system) through which the dc leads to the individual cavity sections can be run, is placed around the assembly circuit. The solenoid pipes are then wrapped around this tubing. These solenoid windings must be axially aligned with the individual cavities.

With the voltage jump efficiency enhancement technique, the output coupler section is generally operated at an elevated voltage above ground. Therefore, the output section must be electrically isolated from the body, and a dc block must be incorporated in the output waveguide line. A possible output waveguide assembly is shown in Figure 104. The transition between the RF interaction circuit and the external waveguide consists usually of a reduced height waveguide with a step transformer. The narrow bandwidths of the proposed tubes will permit a quarter wavelength rectangular block window in conjunction with an abrupt step in waveguide height for a good match over the required bandwidth. The window is metalized on the periphery and brazed to the inside of the waveguide to complete the vacuum envelope. To form the dc block, an insulator assembly incorporating an RF choke, similar to the ones described above for the voltage jump circuit sections, will be welded on to the window assembly as shown in Figure 104. The output end of this flange will mate directly to a standard waveguide flange for the frequency band of the tube.

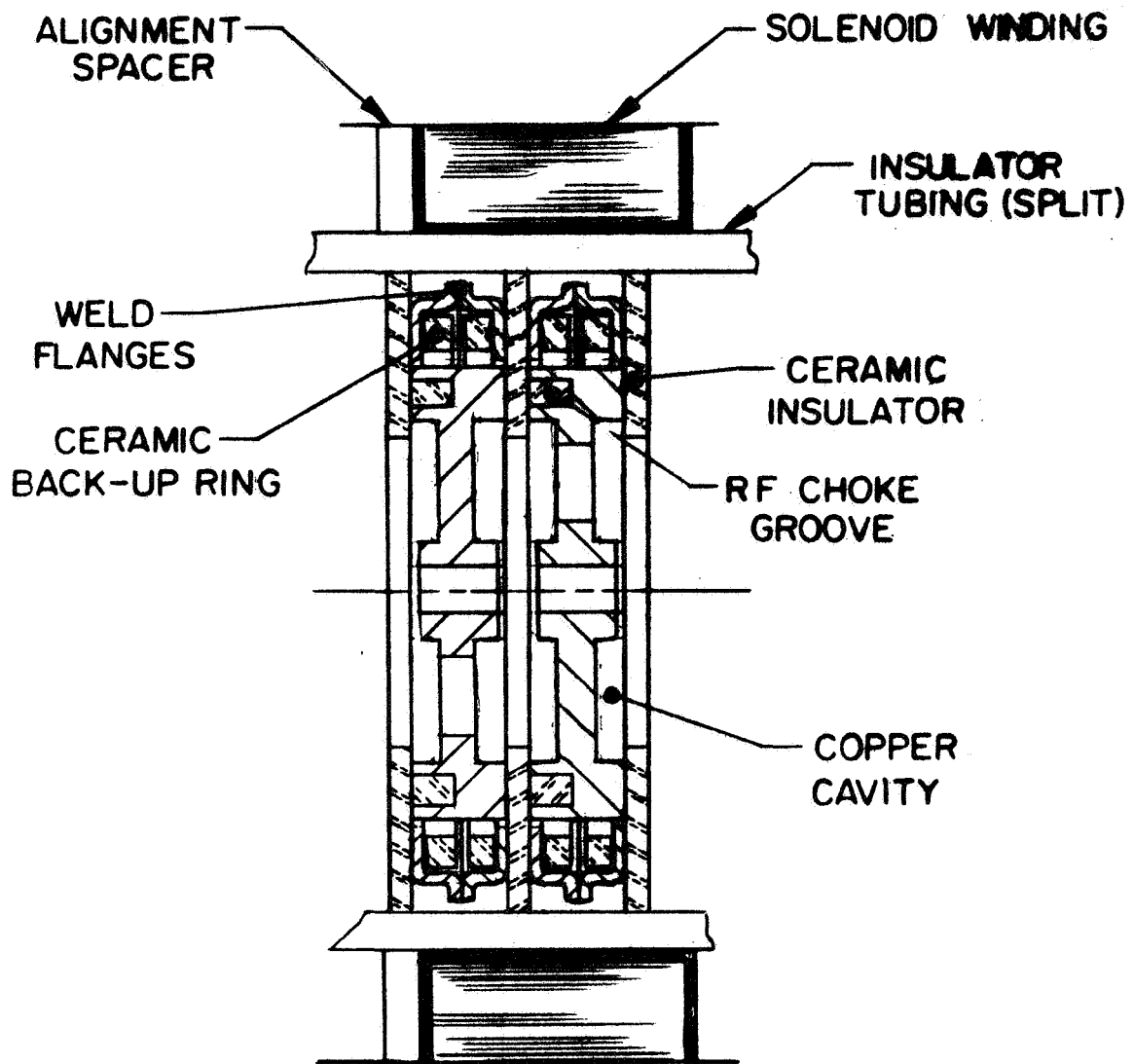


Figure 103 Voltage jump insulator assembly for solenoid focused tube.

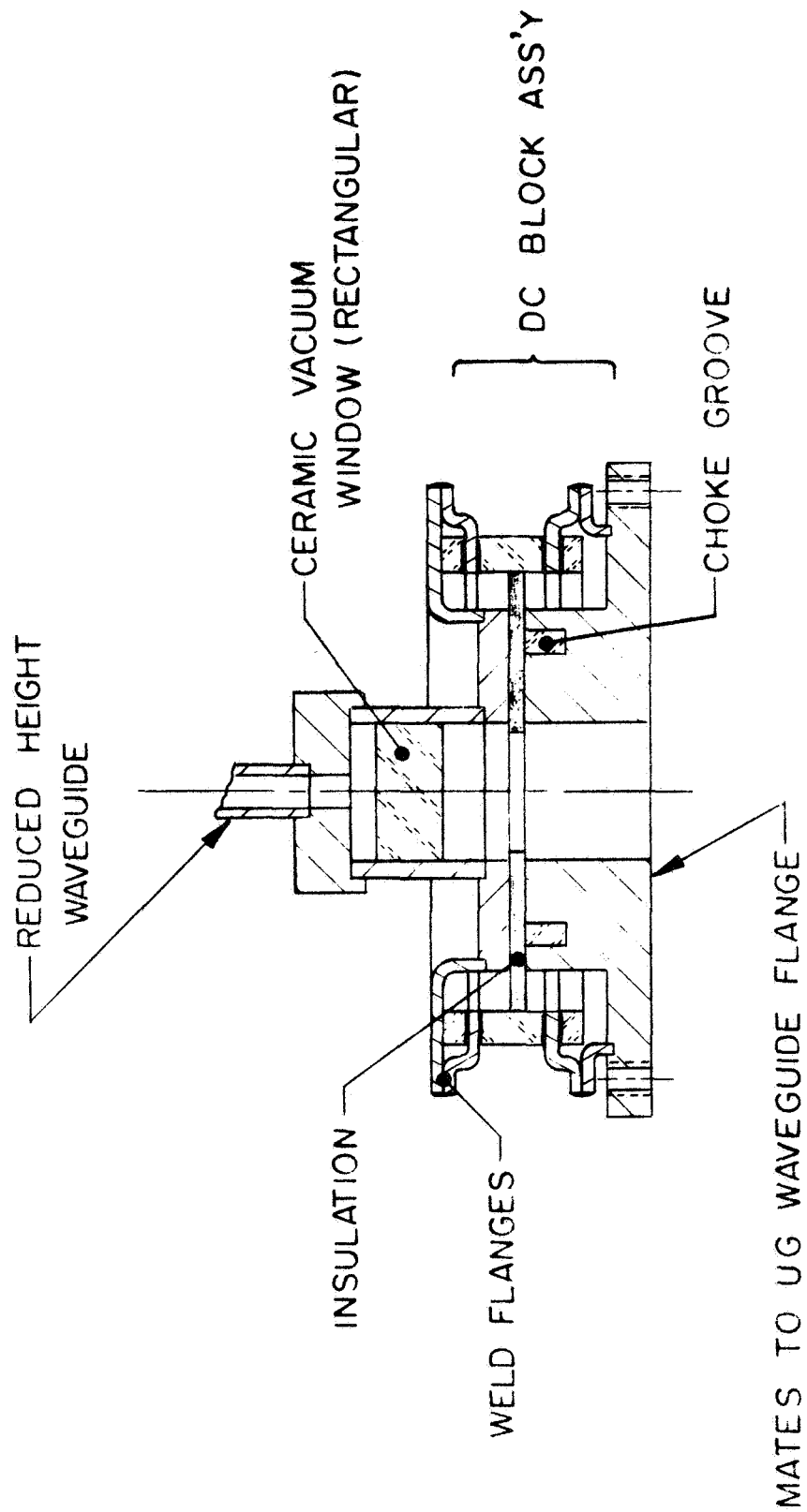
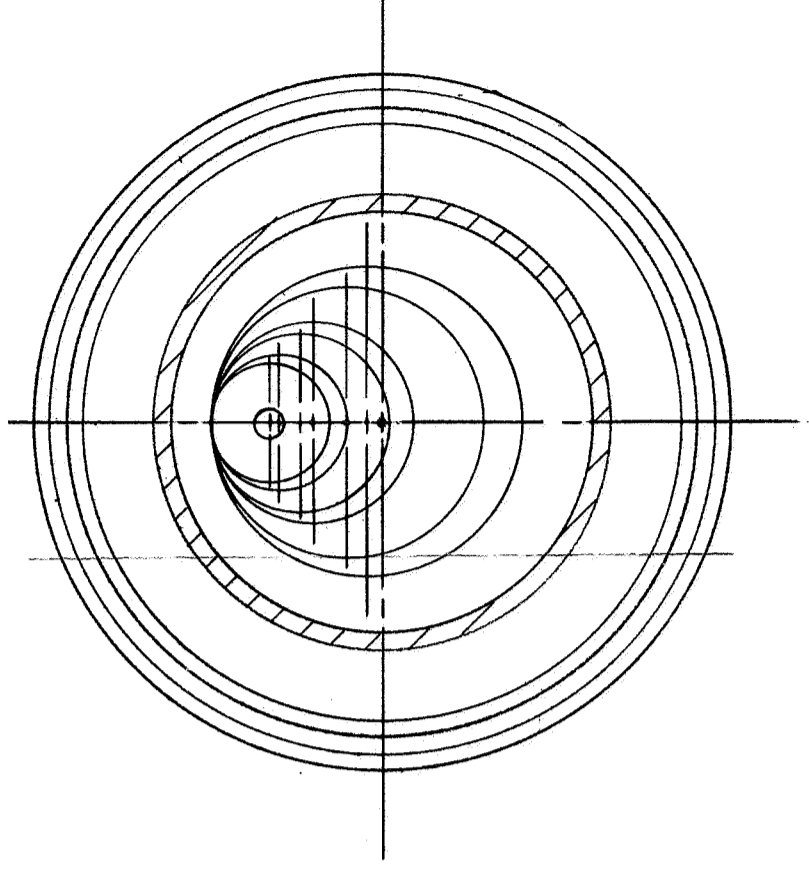
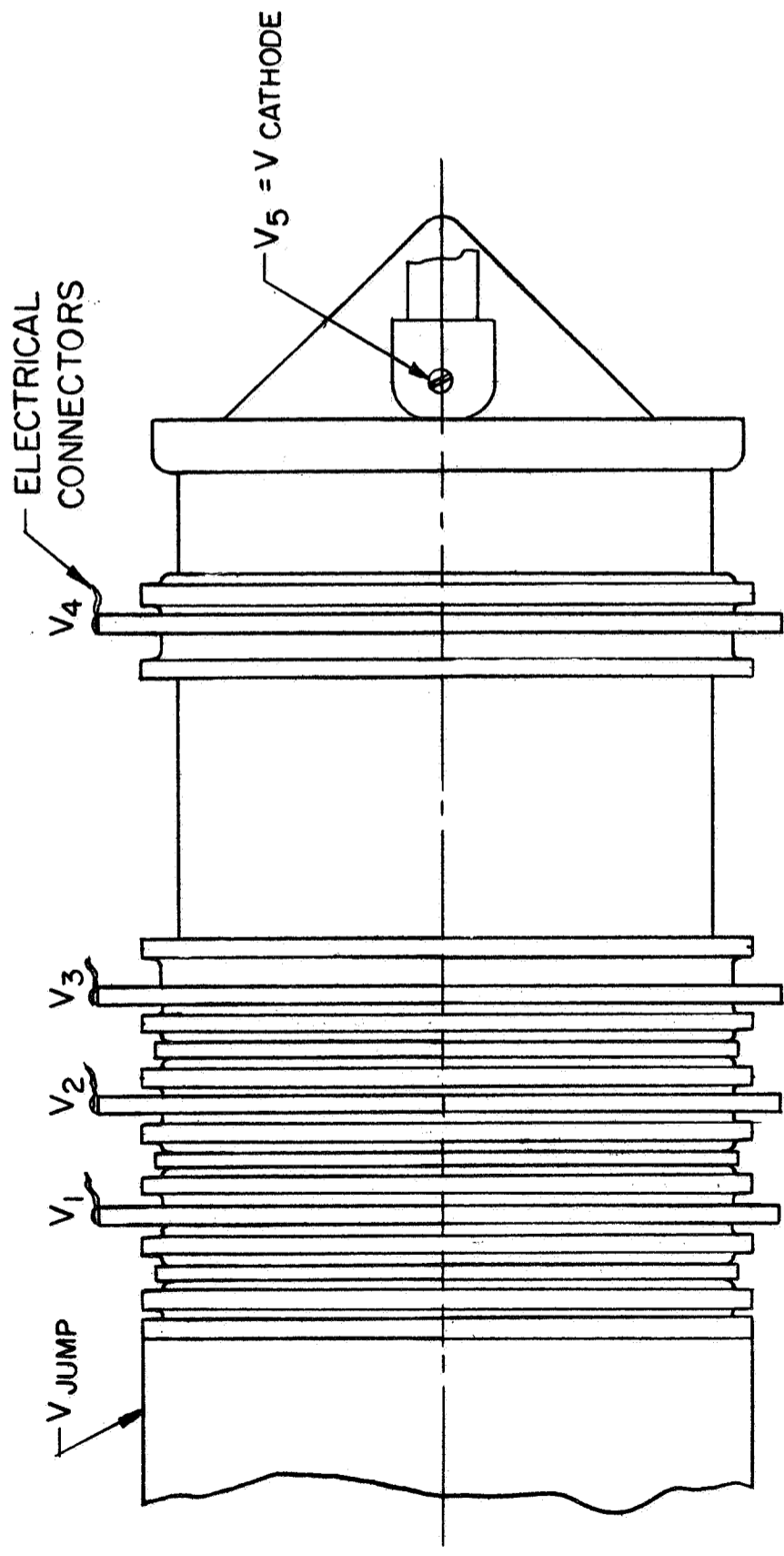


Figure 104 Output RF window and dc block assembly.

If a coaxial line is to be used on the lower frequency tubes, similar considerations can be taken to provide a coaxial vacuum window coupler and dc block.

3. A multi stage depressed collector will be used on the proposed tubes. The electrical parameters of this unique collector were described in the electrical design section for each of the different tubes. A schematic of the mechanical layout of the collector for the S-band tube is presented in Figure 105. The basic design consists of a series of copper discs with transversely displaced center holes of gradually increasing diameter proceeding in the direction of beam travel. The discs are operated at successively lower potentials to optimally collect velocity groups of the spent beam electrons. The discs are separated by a series of ceramic insulating rings. Each insulator ring is part of a brazed insulator and weld flange assembly similar to those used in the electron gun stem and the circuit voltage jump insulators. Each collector disc also will have a weld flange brazed to both sides. The final assembly of the collector is made by welding the series of peripheral weld flanges of the succeeding collector disc and insulator assembly. The collector is attached to the circuit output flange by a similar weld.

After the fabrication of the subassemblies of the vacuum envelope has been completed, the tube is mounted in its external package and integrated with the heat pipe cooling section as described in the section on thermal design. In addition to providing proper cooling and electrical insulation for the various voltage elements, the package will be sturdily designed to support the tube and its tube components to withstand the stringent requirements of shock and vibration associated with the launch and space environments.



SECTION A-A

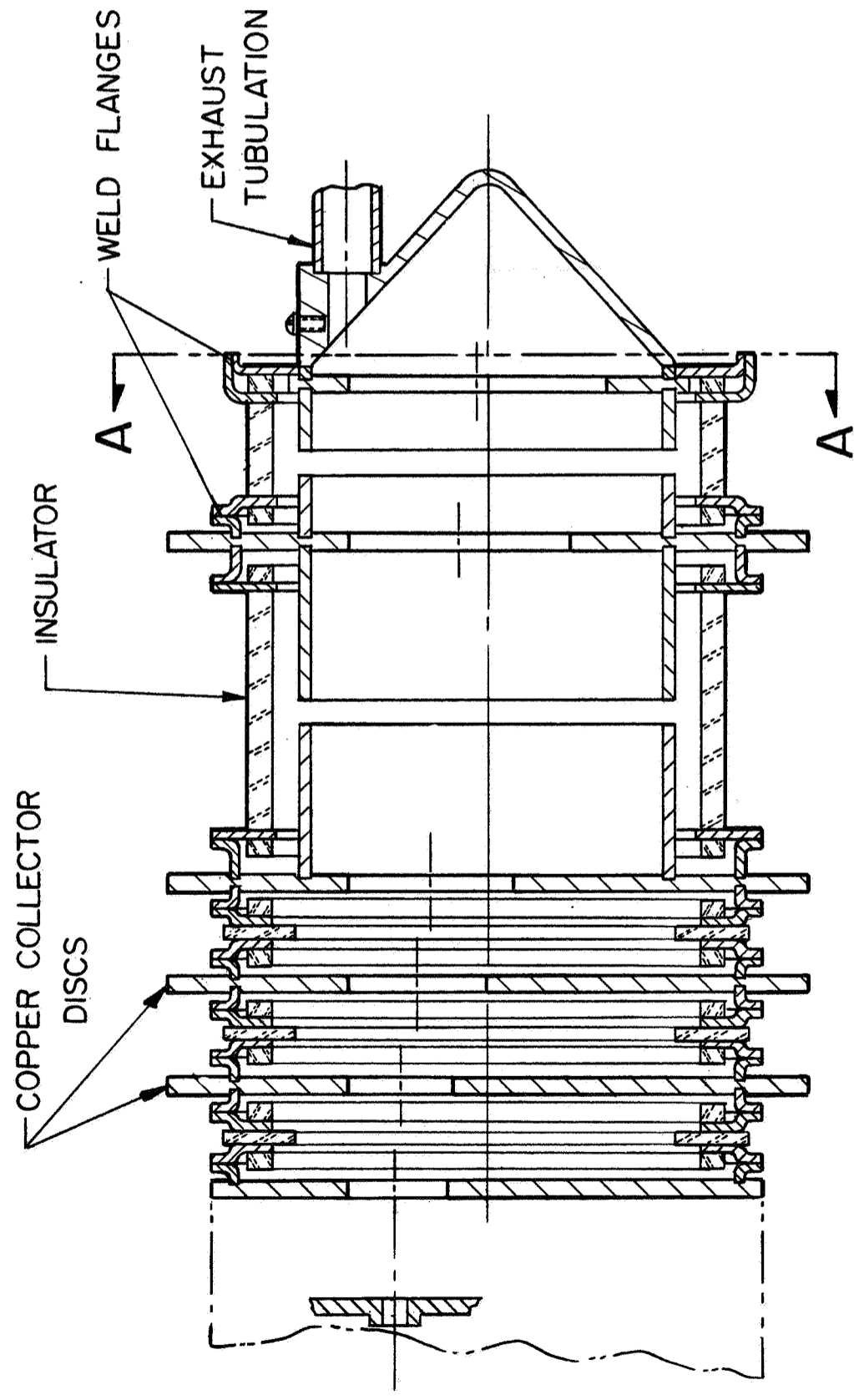


Figure 105 Multistage collector design.

X. LONG LIFE DESIGN

A. TUBE LIFE

The life of properly designed vacuum tubes is limited by the wear-out time of the cathode. The cathode of long life tubes must therefore be designed for long life operation and it must be protected during its life against damages. The cathode can be damaged primarily by ion bombardment, if the tube vacuum is inadequate and residual gases are present inside the tube. The gases are ionized either by the electron beam or by accidental discharges. Such damages can be avoided as long as an adequately low pressure is maintained inside the tube during its life by ion traps and pumps. Only materials with very low outgassing rates can therefore be used. All materials and components must carefully be outgassed during the processing by well established cleaning, outgassing and bake out procedures at high temperatures.

During the operation, however, the tube temperature must be as low as possible in order to keep the outgassing rate small. The tube should, therefore, be designed so that the thermal loading (power density) of any tube component is kept small in operation. In addition, the operating temperature of the cooling system should be chosen as low as possible.

These requirements become more critical for high power tubes. The local thermal loading is likely to be higher with resultant higher local temperatures. In addition, the higher voltages for such tubes are likely to increase the ionization rate and the kinetic energy of the ion bombardment becomes larger and thus more destructive.

The tubes have, therefore, been designed with a heat pipe cooling system, which operates at rather low temperatures.

The major part of the thermal loading occurs in the collector. A large size collector geometry was therefore chosen to assure low beam power densities at the collector surfaces.

The slow wave structure (coupled cavity circuit) is also exposed to some thermal loading primarily due to some electron beam interception. Such interception can be minimized by a careful gun and focusing design and by the choice of a comparatively small beam diameter with respect to the beam hole size. The tubes have therefore been designed with a relative beam size of .6 of the beam hole size.

1. Tube Life and Vacuum

The operational pressure in various sections inside the tube is a complex function of the design parameters of the tube, of the materials and their processing history, and of the operational conditions.

In order to keep the pressure low, the outgassing rate of any tube component must be as low as possible, and continuous vacuum pumping with a larger rate than the outgassing rate must be available during the tube life. Such vacuum pumping is provided in low power tubes by the pumping action of the cathode surface and by getters. In high power tubes, however, these pumping means are inadequate and appendage vacuum pumps are generally provided to maintain sufficient pumping speed.

Nevertheless, the outgassing rate of all tube components should be as low as possible.

2. Maintaining the Vacuum

The traveling-wave tubes require a vacuum of less than 10^{-6} torr. In order to maintain such a vacuum, getter materials and ion pumps are often used. However, these materials are very selective gas pumping devices; also they may lose their efficiency during long

life operation. Therefore, another approach is considered where the tube vacuum envelope is opened to the space environment. The approach has merit since the space environment has a pressure less than 10^{-12} torr, is nonselective in pumping any gas, and acts as an everlasting pump. Such an opening in the tube can be in the form of tubulations from the collector sections and from the electron gun section, as shown in Figure 106.

The tube vacuum is such that the mean free path of the gases exceeds the internal dimensions of the traveling-wave tube; therefore, such flow is termed molecular flow, with the Knudsen number

$$\frac{L}{a} > 1.00$$

where L is the mean free path and a is the characteristic dimension. Since the mean free path of air at 25°C is related to the pressure, P_{μ} , in microns of Hg by

$$L = \frac{5.09}{P_{\mu}},$$

the Knudsen number can be written as

$$\frac{L}{a} = \frac{5.09}{a P_{\mu}} > 1.00$$

or $a P_{\mu} > 1.00$ for molecular flow.

Thus at 1×10^{-6} torr, the mean free path of air at 25°C is 50.9 meters, or far greater than the characteristic dimensions of the traveling-wave tube.

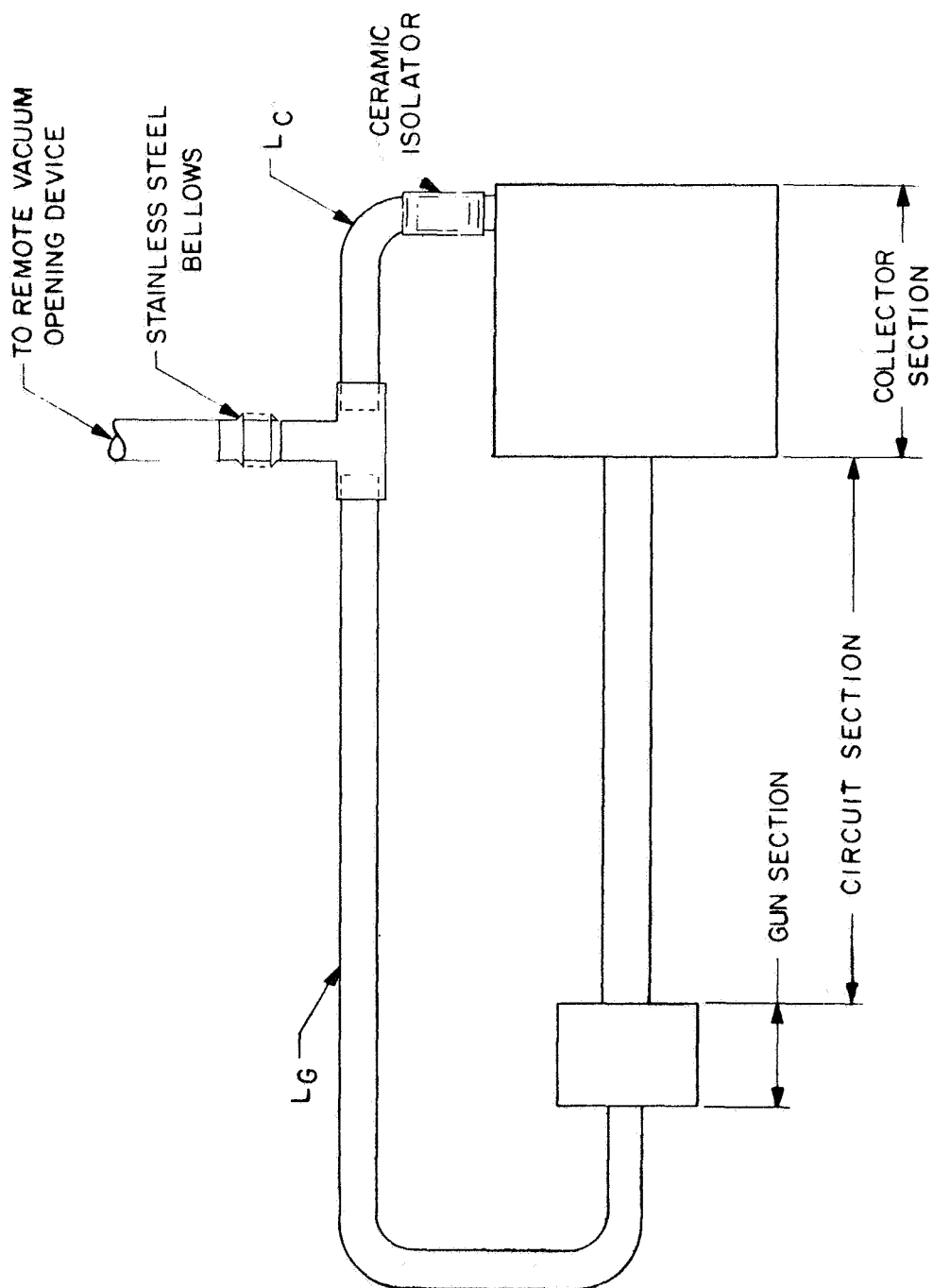


Figure 106 Schematic of traveling-wave tube and gas pumping tubulations.

The equation of gas flow rate is

$$-\frac{d(PV)}{dt} = Q = F(P - P_o)$$

where Q is the flow rate in micron liters per second, F is the gas conduction in liters per second, P is the upstream pressure, and P_o is the downstream pressure (in microns of Hg).

For molecular flow, the gas conductance is defined as

$$F = \frac{8}{3} \left(\frac{2 R_o T}{\pi M} \right)^{1/2} \left(\int_0^{\ell} \frac{H}{A^2} d\ell \right)^{-1}$$

where R_o is the universal gas constant, M is the molecular weight of the gas (grams/mole), T is the temperature in $^{\circ}K$, ℓ is the length of gas travel in cm, H is the perimeter at any ℓ , and A is the cross-sectional area at any ℓ . Thus, for a cylindrical tube of radius a (cm),

$$F = 30.48 \frac{a^3}{\ell} \left(\frac{T}{M} \right)^{1/2} \text{ liters/second}$$

and for a circular orifice of radius a

$$F = 11.42 a^2 \left(\frac{T}{M} \right)^{1/2} \text{ liters/second}$$

The computations of gas conductances inside the tube were somewhat more complex than the above examples (e.g., the slow wave circuit section consists of cylindrical cavities each linked by extended ferrules). The computed gas conductances for each of the five tubes along the gun section, circuit section, and collector section are given in Table XXIII.

TABLE XXIII Gas conductances (liters/second) of the three sections of the tubes.

TUBE FREQUENCY	GUN SECTION	CIRCUIT SECTION	COLLECTOR SECTION
AM 850 MHz	1900	1.1	350
AM & FM 2 GHz	600	0.2	25
FM 8 GHz	14	0.008	31
FM 11 GHz	2.5	0.005	16

The computed gas conductances throughout the collector region, and also from the face of the cathode throughout the ceramic enclosure around the electron gun section, are 30 to 1600 times higher than the computed gas conductances along the circuit section. As a result these regions are considered negligible impedances to gas flow if gases evolving from the circuit section are significant and are expected to be pumped either through the collector or gun section.

During the operation of the tube, the cathode temperatures will approximate 800°C and 1100°C for oxide type and dispenser type cathodes respectively; also, the collector region may exceed 200 or 300°C in small local regions; and the circuit section of the tube will not exceed 200°C. Therefore the traveling-wave tube will experience greatest gas evolution in the cathode and collector regions.

Table XXIII shows that the gas conductance along the circuit region is extremely low, especially for the two high frequency tubes. If only one pumpout tubulation is used in the tube, sizeable gas pressures might result in the opposite end of the traveling-wave tube due to the low gas conductance of the circuit section. It is therefore important to place gas pumping tubulations onto both the collector section and the gun section as shown in Figure 106.

In order to provide sufficient pumping speeds, the gas pumping tubulations must have a sufficient diameter so that gas bursts will be pumped quickly (within seconds). Referring back to the equation for gas flow rate:

$$-\frac{d(PV)}{dt} = Q = F (P - P_o)$$

the solution for the required gas conductance, F, is

$$F = \frac{V}{t} \ln \left(\frac{P_i - P_o}{P_m - P_o} \right) = \frac{V}{t} \ln \left(\frac{P_i - 10^{-12}}{10^{-6} - 10^{-12}} \right)$$

where P_o is the vacuum of space equal to 10^{-12} torr, P_i is the initial gas burst pressure, P_m is the maximum safe operating pressure equal to 1×10^{-6} torr, t is the time required to pump the gas from a pressure of P_i to P_m , and V is the volume of the cavity initially containing the gas burst. The computed volumes of the gun and collector cavities for each traveling-wave tube are listed in Table XXIV.

Table XXIV Calculated volumes of gun and collector cavities (liters).

TUBE FREQUENCY	GUN CAVITY	COLLECTOR CAVITY
AM 850 MHz	1.8	13.0
AM & FM 2 GHz	.550	1.6
FM 8 GHz	.040	.82
FM 11 GHz	.025	.35

Assuming that a gas burst attaining a pressure of 1×10^{-3} torr must be pumped within 10 seconds from either the gun section or the collector section, then the gas conductances of the pumping tubulations must exceed the values in Table XXV

Table XXV Required tubulation gas conductances (liters/sec).

TUBE FREQUENCY	GUN SECTION	COLLECTOR SECTION
AM 850 MHz	1.25	8.90
AM & FM 2 GHz	.395	1.11
FM 8 GHz	.275	.57
FM 11 GHz	.182	.24

Table XXVI shows the maximum permissible lengths of 1/2 inch and 1 inch diameter tubulations required for the gun sections and the collector sections for each traveling-wave tube.

Table XXVI Maximum permissible tubulation lengths for gun and collector sections, cm (inches).

TUBE FREQUENCY	L_G (GUN SECTION)		L_C (COLLECTOR SECTION)	
	1/2 inch Dia.	1 inch Dia.	1/2 inch Dia.	1 inch Dia.
AM 850 MHz	20.0 (8)	<u>162</u> (<u>64</u>)	2.84 (1.12)	<u>22.8</u> (<u>9.0</u>)
AM & FM 2 GHz	<u>63.5</u> (<u>25</u>)	508 (200)	<u>24.8</u> (<u>9.0</u>)	182 (72)
FM 8 GHz	<u>91</u> (<u>36</u>)	740 (290)	<u>44.5</u> (<u>17.5</u>)	355 (140)
FM 11 GHz	<u>140</u> (<u>55</u>)	1110 (440)	<u>106</u> (<u>42</u>)	890 (330)
The underlined lengths will be used in designing these tubulations.				

These tubulations are connected as shown in Figure 106. L_G and L_C are the respective tubulations for the gun section and the collector section. L_C is composed of a ceramic isolator to insulate the collector voltage.

L_C and L_G are brazed to a "T" junction, which in turn is brazed to a stainless steel bellows. This bellows will attenuate shock from the remote vacuum opening device which is shown in Figure 107.

The remote vacuum opening device is the device intended to open the tube to the space vacuum. It is mounted on a fixed supporting plate (A). The pump-out tubulation (B) is firmly mounted to this plate by two nuts (C), which are tightened around the brazed threaded sleeve (D).

At the desired moment, a hermetically sealed squib is detonated within the power cartridge (E), causing the piston (F) to strike the yoke (G) with considerable force. The yoke, which is tightly fixed to the upper portion of the breaking collar (H), breaks the tubulation off at the groove (I), using the point (J) as a fulcrum. The yoke and broken tubulation are sent off into space by this action, thus providing the tube with space pumping of any internal gases.

The tube can be baked out with its tubulation assembly using this design. The yoke (G) is put in place after bake-out. In order to facilitate opening of the tubulation, a groove (I) is cut through the collar (H) so that the finished wall thickness is one-third of the original wall thickness of the tubulation (B). The power cartridge and piston unit is a commercially obtainable device, available with squibs of any desired detonating force, which are hermetically sealed to prevent any possible gas contamination of the tube in space.

This remote vacuum opening device is successfully used in sounding rockets.

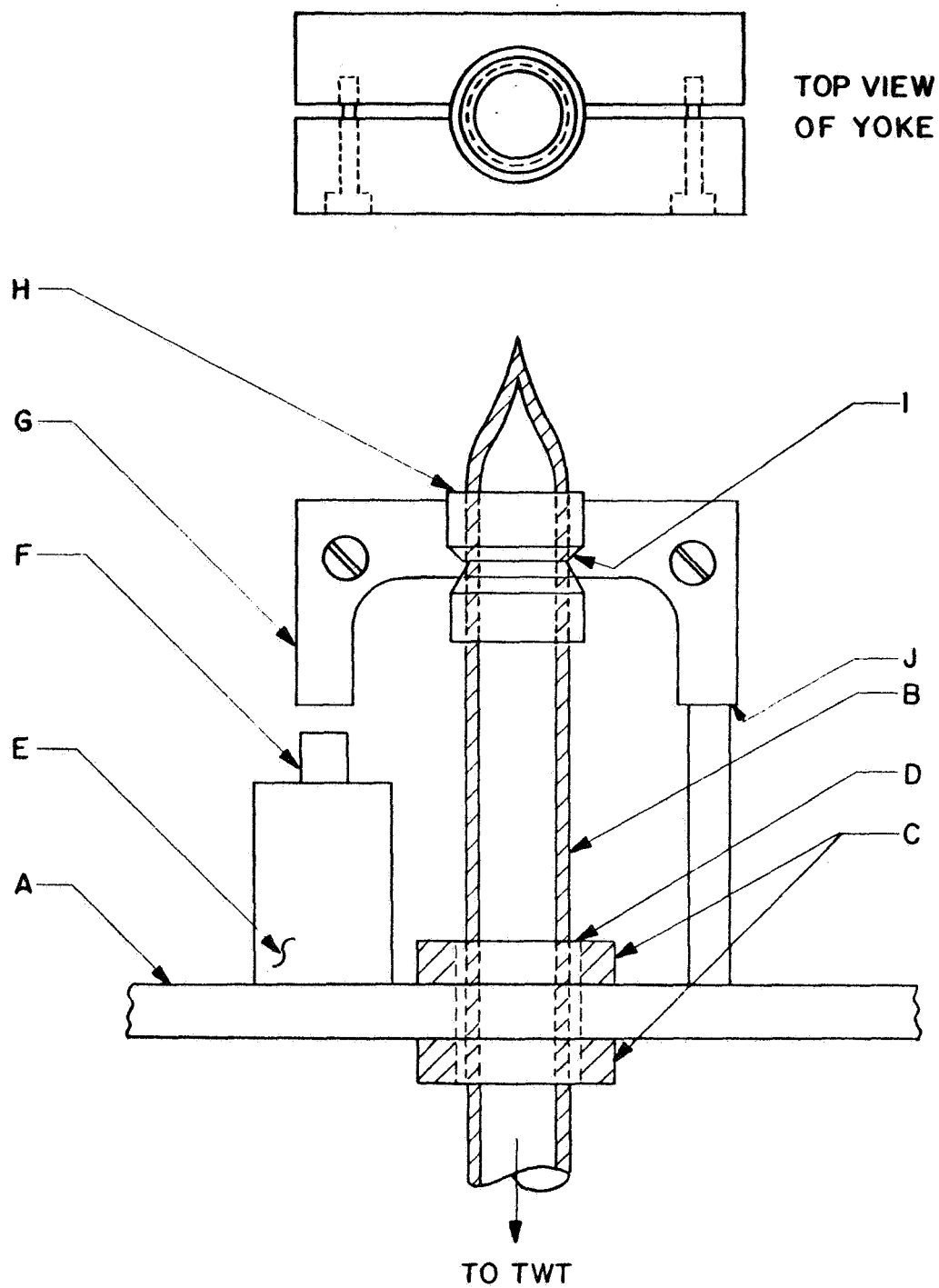


Figure 107 Remote vacuum opening device.

3. Materials and Processing

The vacuum environment of a traveling-wave tube contains a finite residual level of gases from the materials used for tube construction. The level of residual gases within the tube envelope is increased with higher operating temperatures.

The tube design life can be optimized, when only materials with inherently low vapor pressures at the operating temperatures are used. These materials must be mutually compatible to assure rugged mechanical design as well as provide heat transfer to the cooling surfaces with a thermal margin of safety.

In Table XXVII a list of materials for vacuum tubes and their application is given.

The component having the highest temperatures within the gun will be heaters (900°C to 1200°C) and the cathode (700°C to 950°C). The highest temperatures within the slow wave structure will occur at the last few cavities of the structure, with expected maximum temperatures of 300°C to 400°C . These temperatures depend primarily on the focusing quality. The highest temperatures within the collector are expected at the first collector stage, with temperatures up to 300°C to 400°C .

A plot of vapor pressure as a function of the operating temperature for various tube materials is shown in Figure 108. This figure indicates that at the ambient vacuum envelope pressure of 10^{-8} to 10^{-9} mm Hg a reasonable margin between the highest operating temperatures and the evaporation temperature is available. Therefore the selected materials and temperatures will not significantly raise the residual gas level of outgassing, particularly after bake-out.

Table XXVII Materials used in vacuum tubes.

MATERIAL	APPLICATION
Alumina	Heater cooling, gun ceramics, dielectric loading, vacuum seals, windows
Alumina or Beryllia	Collector insulators, windows
Copper	Circuit structure, collector
Copper - Gold	Gun, circuit, collector, and window brazes
Iron	Pole pieces
Kovar	Seal flanges
Monel	Window supports
Molybdenum	Cathode support, pins
Nickel	Gun leads, cathode focus electrodes
Nickel - Zirconium	Cathode base
Platinum	Heater and lead welds
Stainless Steel	Support structures
Tantalum	Gun heat shields
Tungsten	Heater wire, cathode material

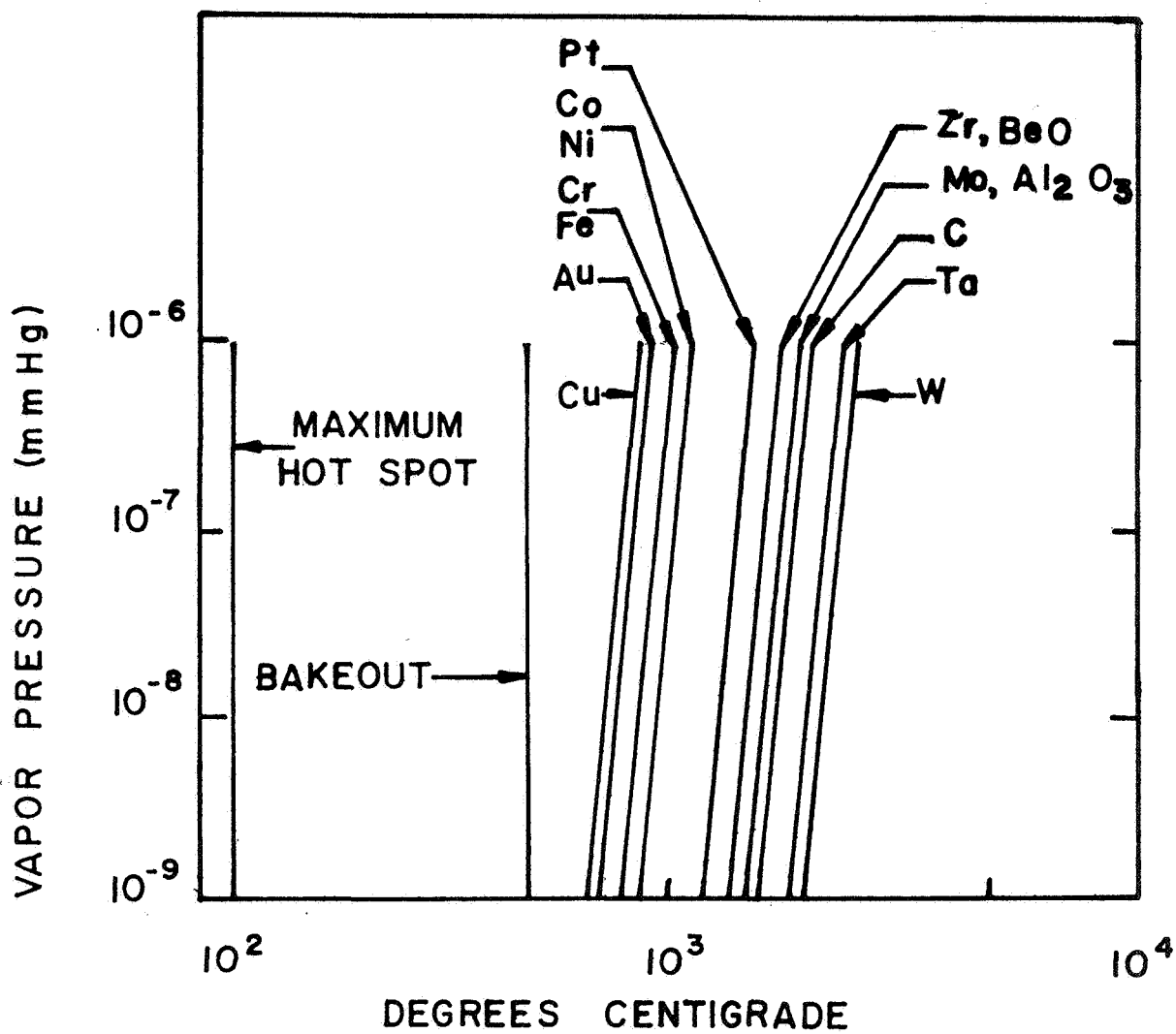


Figure 108 Vapor pressure of vacuum tube materials as a function of temperature.

It is equally important that manufacturing, processing and testing controls are implemented to obtain an initially clean vacuum envelope.

The following list gives production and processing techniques for high reliability space tubes.

1. Parts fabrication under controlled cleanliness conditions.
2. Special preparation and cleaning procedures for vacuum envelope parts.
3. Parts traceable to raw material and manufacturer's lot.
4. Preaging on vac ion pump to remove initial outgassing.
5. Bake-out in vacuum to avoid small leaks caused by external oxidation.
6. Vac ion pumping to remove outgassing products throughout the initial tube testing phase.

4. Ion Trapping

The flow of positive ions toward the cathode can be stopped with a positive potential barrier at the anode. A positive anode potential of about 100 volts with respect to the potential of the input section of the slow wave structure is generally adequate to prevent positive ions from entering the gun region. This method is generally used in long life space tubes and is therefore incorporated in the tube designs. In addition, the depressed collector also provides an ion trap for positive ions. The collector has to absorb a major part of the applied power and thus will produce most of the outgassing and ions. Depressed collector operation will trap most of the positive ions generated in the collector region.

The potential profile of the tubes is shown schematically in Figure 109. Thus, the driver section of the circuit and the collector region constitute positive ion traps.

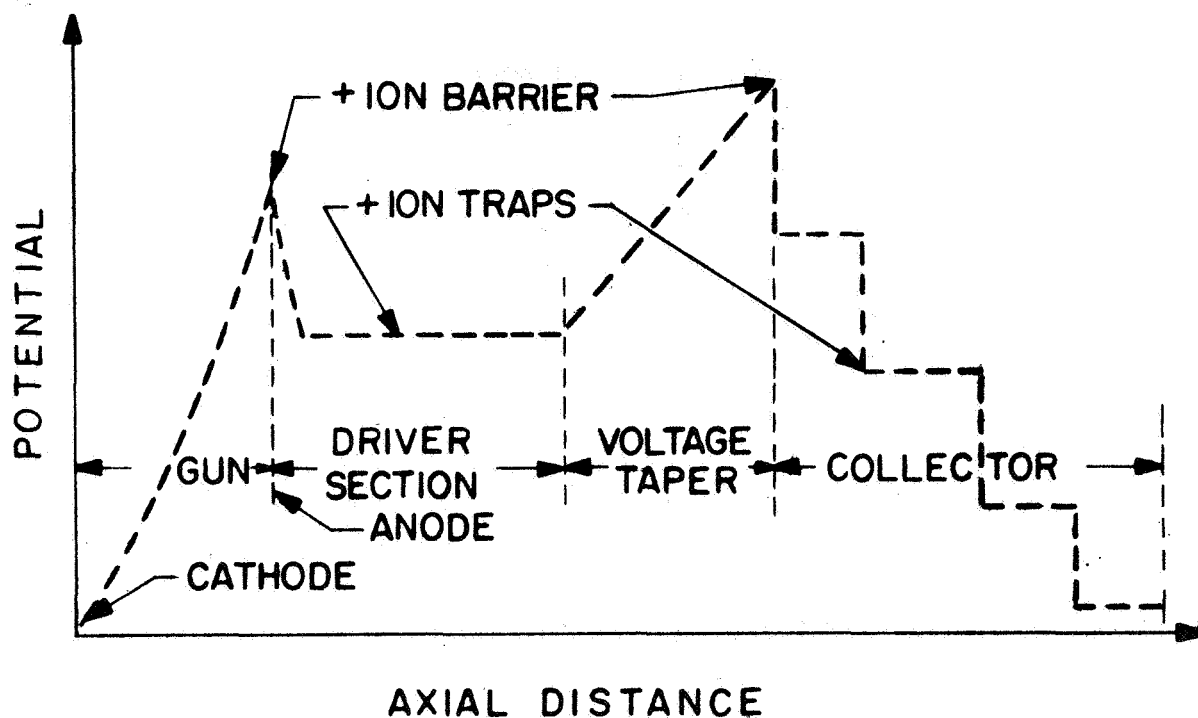


Figure 109 Axial potential profile of tube.

5. . . Long Life Cathodes

Several types of long life cathodes are available which can be considered for the tube design. These include:

- a. The oxide coated cathode
- b. The nickel matrix cathode
- c. The coated nickel powder cathode
- d. The impregnated tungsten cathode

These cathodes utilize primarily the property of low work function values of Barium (or Barium oxide) for their emission. The characteristics and life capabilities of these cathode types are fairly well established, especially those of the oxide coated cathode.

Cathodes must be operated at space charge limited emission during their useful life. In this case, the current density drawn from the cathode is much smaller than the available electrons from the temperature emission of the hot cathode. The excessive electrons form a space charge cloud in front of the cathode surface, which acts also as an electric shield for the cathode.

When the current density is increased (by increasing the anode potential), the space charge cloud is removed from the cathode surface and the emission becomes temperature limited. Temperature limited emission, however, cannot be sustained very long in these cathodes. Electro-physical processes within the cathode lead to a rapid loss of emission (cathode "poisoning") and, after some time, to permanent damage to the cathode. The cathode temperature is a critical factor for these operational conditions of the cathode. With higher cathode temperatures more electrons are emitted and space charge limited emission can be maintained with higher current densities. The required cathode temperature to maintain space charge limited emission depends on the type of cathode, as shown in Figure 110. This plot shows that each of the cathode types

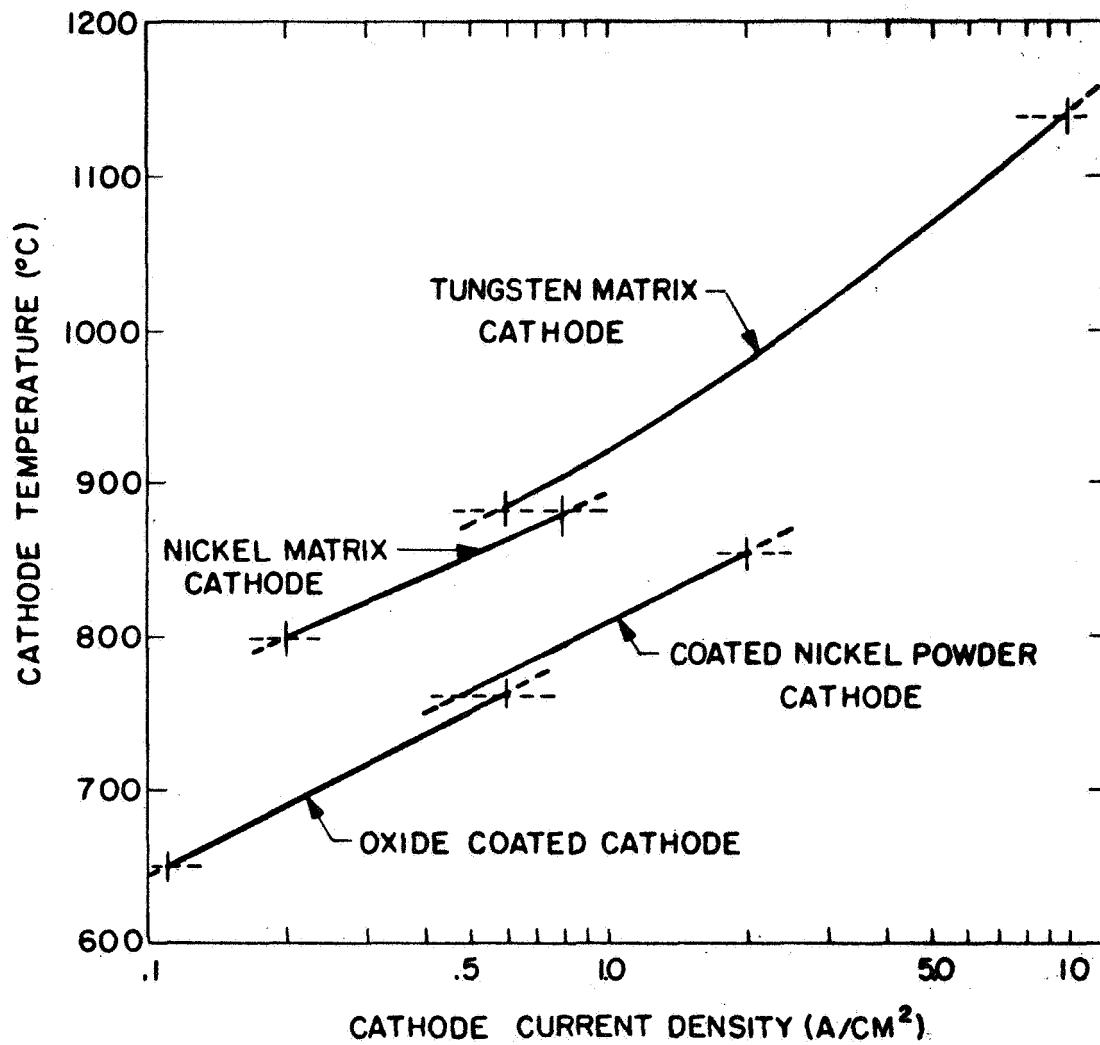


Figure 110 Cathode temperature for space charge limited emission.

have to be operated above a minimum temperature and emission density for space charge limited emission. In Figure 110 an upper temperature and current density limit for each of the mentioned cathodes are shown. Above this higher temperature limit the cathode life is quickly terminated due to excessive evaporation of active material from the cathode. The oxide coated cathode can thus be operated at rather low temperatures up to about 760°C , but at relatively low current densities of approximately 600 mA/cm^2 . The tungsten matrix cathode, on the other hand, needs temperatures ranging from at least 880°C to approximately 1140°C , yielding current densities from approximately 600 mA/cm^2 up to about 10 A/cm^2 . The life varies greatly for these cathodes as a function of the temperature and thus also as a function of the current density. With higher temperatures (and higher current densities) the cathode life is rapidly reduced due to increased evaporation rates and other processes which lead to earlier depletion of active cathode materials. Life predictions for the cathodes as a function of their current density are shown in Figure 111. These life predictions are derived from an analysis of the processes involved in the operation of the cathode. These processes have been investigated most extensively for oxide coated cathodes. These cathodes have, therefore, been used almost exclusively for long life tubes and especially for space tubes. Life test data and tubes in the field have confirmed the life predictions for oxide coated cathodes. These data indicate that the predictions shown in Figure 111 for these cathodes can be considered conservative and the actual life expectancy is likely to be higher.

Recently, development efforts have been devoted to the more advanced cathode types. Some of these cathode types show great promise for very long life at higher current densities, especially the tungsten matrix.

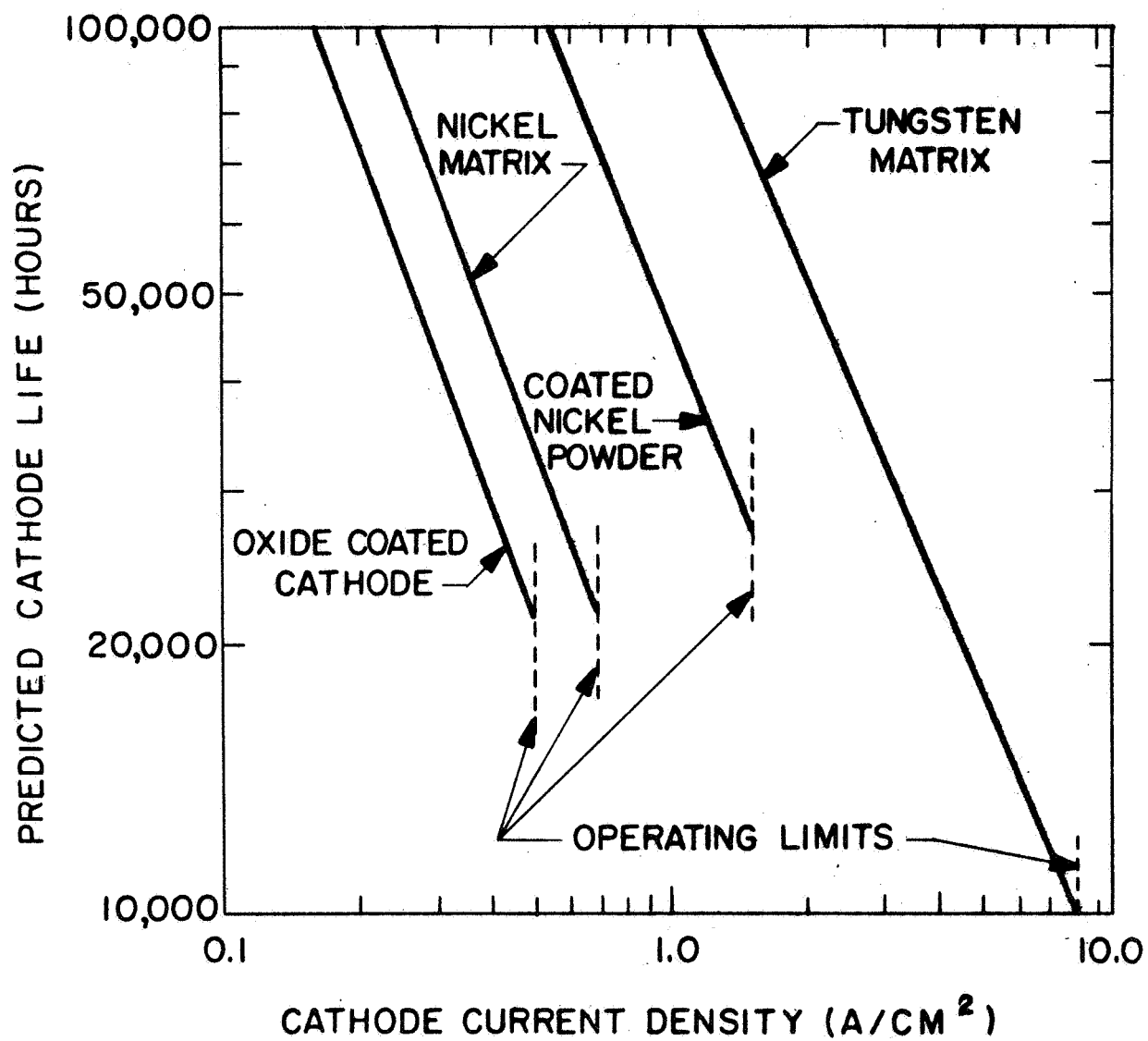


Figure 111. Life predictions for cathodes as a function of the cathode current loading.

In evaluating the capabilities of these cathodes, the heater and its life must be considered too. The heater temperature generally has to be approximately 150°C to 200°C higher than the cathode temperature. Excessively high heater temperatures can reduce the heater life. At heater temperatures higher than 1350°C , the heater wire (tungsten) recrystallizes and becomes very brittle. At these temperatures the insulating heater coating (alumina) reacts with the heater wire, resulting in gas evolution and oxide reduction. The insulation is then destroyed and short circuits within the heater coil may occur, leading to hot spots and to heater destruction. At higher temperatures, tungsten sublimation also becomes significant.

The heater temperature should therefore be below 1350° for long life cathodes.

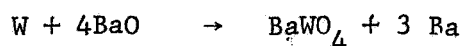
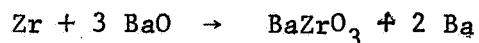
A description of the oxide coated cathode and the other types of cathodes follows:

Oxide Coated Cathode ^{23,24}

The oxide coated cathode consists of a nickel alloy base which is coated with a mixture of Barium oxide (BaO) and strontium oxide (SrO) crystals. Its superior emission properties are due to the very low work function of the oxide coating. However, this is true only if an excess of oxygen vacancies exists in the lattice sites of the oxide crystals. These oxygen vacancies act as electron donors in the oxide coating, which represents an n-type semiconductor. The work function of the crystal is then considerably lower than that of pure barium or strontium. A perfect oxide lattice structure (without oxygen vacancies) would be a rather poor emitter. The condition of excess oxygen vacancies in the crystal does not exist by itself, since there are an almost equal number of barium (and strontium) vacancies in the lattice sites of the oxide crystals. These barium vacancies act as electron acceptors and thus tend to cancel the emission enhancement of the oxygen vacancies. The

excess oxygen vacancies are produced by chemical reduction processes. The nickel alloy base metal contains reducing agents, such as zirconium (Zr) and tungsten (W), which diffuse toward the interface surface of the metal base. At the interface surface the reducing agents react chemically with the oxides and free barium becomes available. The barium donors fill the barium vacancies in the lattice structure so that the desired excess oxygen vacancies are produced and the coating becomes an n-type semiconductor.

The reduction processes at the interface surface can be described by:



Barium however has a rather high evaporation rate at cathode temperatures, and therefore the reduction process must continue during the life of the cathode in order to maintain the excess oxygen vacancies in the crystal. Cathode emission therefore depends on the dynamic balance of barium evaporation and the diffusion of the reducing agents.

The cathode life is terminated when either the barium supply of the oxides or the supply of the reducing agents is exhausted. The thickness and density of the oxide coating is limited by its adherence to the metal base. However, at low cathode temperatures, the coating thickness is adequate to supply enough barium during the cathode life. In this case the cathode life is terminated by the depletion of reducing agents. The diffusion rate of the reducing agents (Zr and W) to the interface surface is much slower than the chemical reduction process and the evaporation of barium. The production of barium by this process is diffusion limited rather than reaction limited. The slow diffusion rates of the reducing agents makes it therefore possible to achieve long life. However, the diffusion rate does not remain constant but decreases with time. This is illustrated in Figure 112 with the computed

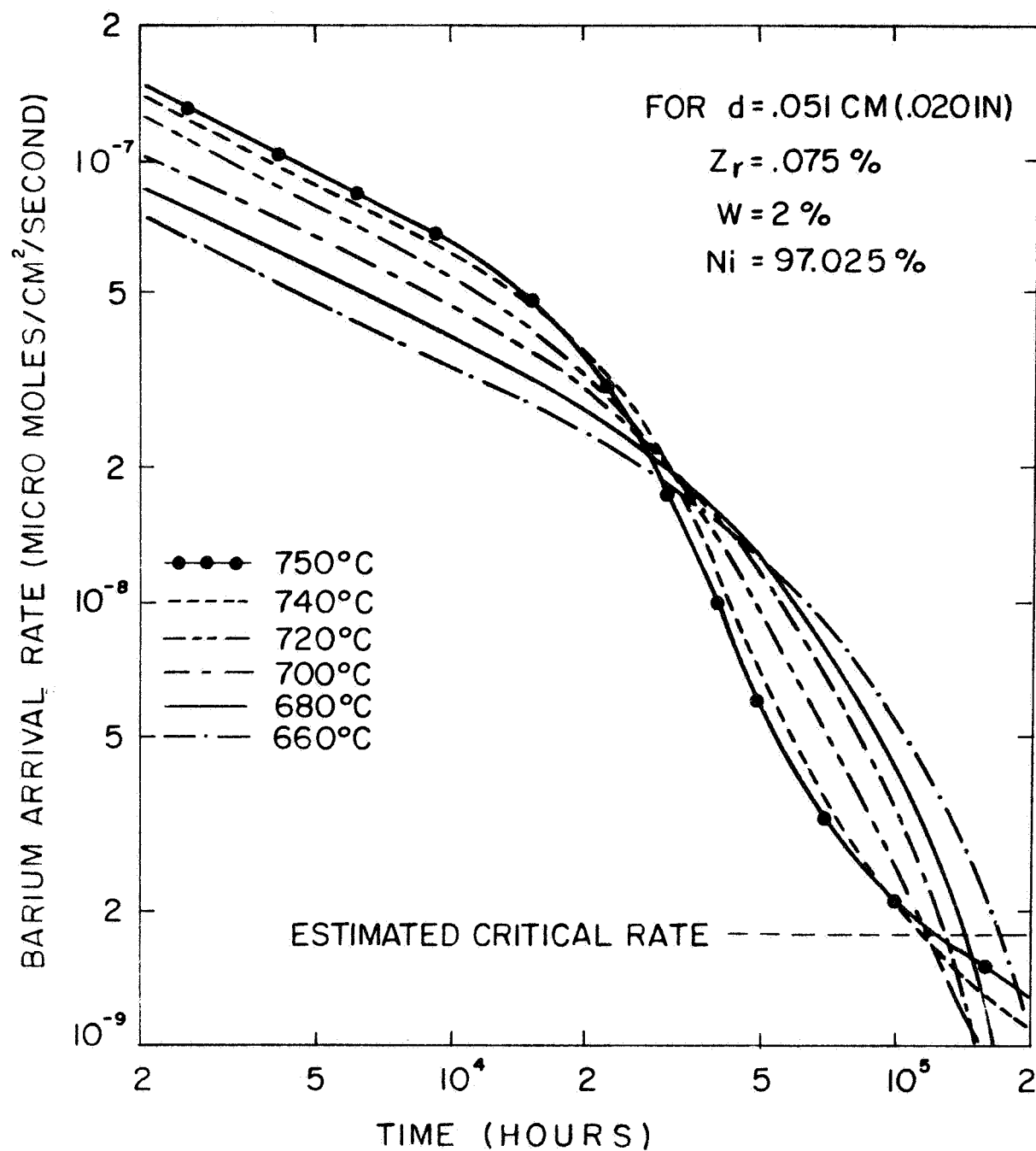


Figure 112 Barium arrival rate in oxide coated cathode (computed for 235H cathode).

barium arrival rates as a function of the cathode temperature for a nickel base with $d = .051$ cm (.020 in) thickness. The zirconium concentration in the nickel base is rather critical for the arrival rate of barium. A too small zirconium concentration will produce a too small barium arrival rate to sustain emission, while a too high zirconium concentration will deplete the barium reservoir in the coating too soon. The absence of any impurities in the nickel base, which may act as additional accidental reducing agents, is therefore important for long life cathodes. Impurities of the nickel alloy base should, therefore, be limited to less than .01% by weight. A high concentration of zirconium or of impurities is also undesirable because an interface resistance layer is formed at the nickel base surface. This interface resistance reduces the mechanical adhesion of the coating after several thousand hours of operation, and it causes additional cathode heating which may become excessive. Values of the interface resistance may range from .1 to 100 ohms. Silicon has been found to be the most harmful impurity, building a BaSiO_4 resistance layer. The base metal must, therefore, be especially pure with respect to silicon.

The reducing agent tungsten in the nickel base has a substantially lower diffusion rate than zirconium:

Diffusion constant (at 740°C)	W:	$3.8 \cdot 10^{-16}$	cm^2/sec
	Zr:	$1.7 \cdot 10^{-11}$	cm^2/sec

Moreover, the reaction of tungsten is so slow at cathode temperatures that the barium production by tungsten is reaction limited rather than diffusion limited. Therefore, the barium arrival rate is entirely determined by the zirconium diffusion up to about 15,000 hours of operation. Thereafter, however, the barium production by tungsten becomes more effective and improves the life of the cathode (Figure 112).

The end of the cathode life occurs when the barium arrival rate has become too small to sustain an adequate number of oxygen vacancies in the oxide lattice. The emission drops then from space charge limited to temperature limited levels and further deterioration will follow. The necessary minimum barium arrival rate depends not only on the barium evaporation rate, but also on the vacuum environment of the cathode. The residual gases released from other tube parts during operation are ionized by the electron beam, and some of the resulting positive ions tend to cause damage to the cathode by bombardment or by oxidizing the electron donors, an effect known as cathode poisoning. The most effective gasses in poisoning the cathode are H_2O , CO_2 , SO_2 , CO , and O_2 . The barium arrival rate must therefore be large enough to replace evaporated barium as well as barium losses due to poisoning. The poisoning rate tends to decrease with increasing operating time since the poisoning has a pumping effect on the tube vacuum and the vacuum pressure tends to harden with time.

The gas pressure is likely to be higher in high power tubes due to the larger tube surfaces and possibly higher temperatures in some components. Therefore, the minimum required barium arrival rate is likely to be higher for higher power tubes.

It is possible to experimentally determine the minimum required barium arrival rate for a specific tube with the dip test²⁵. With the dip test, the cathode temperature is temporarily reduced, which lowers the barium arrival rate. The critical minimum barium arrival rate, which determines the life of the tube, can be detected by observing the work function, since the work function changes at the critical barium arrival rate. With this method the critical barium arrival rate of the tube cathode shown in Figure 112 has been estimated to:

$$1.8 \times 10^{-9} \text{ micromoles/cm}^2/\text{sec} (\approx 10^{10} \text{ atoms/cm}^2/\text{sec})$$

Generally, a minimum barium arrival rate in the order of

$$10^{10} \text{ to } 10^{11} \text{ atoms/cm}^2/\text{sec}$$

is found necessary in long life tubes with oxide cathodes.

The oxide coating is unstable in the presence of atmospheric water vapor. The coating is therefore applied in the form of corresponding carbonates. The carbonate powder is mixed with an organic binder (nitrocellulose or polybutylmethacrylate) and a solvent (amylacetate). This mixture is either sprayed or brushed onto the cathode base. The binder is removed after the initial pumping during the bake-out process at approximately 200°C, when it evaporates.

The remaining carbonates are decomposed during the later cathode breakdown process. The oxides are formed after CO₂ has been removed by pumping at approximately 700°C. This is followed by the activation process of the cathode, which is accomplished at temperatures ranging from 900° to 1150°C. During activation the diffusion process of the reducing agents in the metal base is initiated, and the subsequent reduction at the interface establishes the semi-conducting properties of the coating. The activation is generally enhanced by current flow through the cathode due to the resultant electrolytic dissociation in the coating.

The activation temperature and time are critical parameters to obtain long life cathodes.

It was found that triple carbonates (Ba, Sr, and Ca) can be faster activated than double carbonates (Ba and Sr), but their adherence to the nickel base is generally poorer, and peeling of the coating may then occur. Double carbonates also are found to yield better cathode life.

Before the tube is being operated, a tube aging process is required at operating temperatures. Long life tubes generally are aged over a considerable time. The aging temperature and time are important to achieve long life.

In Table XXVIII below the most common causes of cathode failure and their prevention are listed.

Table XXVIII Failure causes for oxide coated cathodes and their prevention.

CATHODE FAILURE	CAUSE OF FAILURE	PREVENTION
Coating Evaporation	Cathode temperature too high	Redesign cathode with larger area and lower current density and temperature
Formation of Inter-face Layer	Impurities (Si) react with barium	Select base metal with adequate purity
Peeling of Coating	Formation of inter-face layer	
Cathode Destruction by Ion Bombardment	High residual gas content	Better tube processing and pumping
Loss of Emission	Cathode Poisoning	
	Depletion of reducing agents in base metal	Use thicker base metal or increase concentration of reducing agents
Heater Failure	Recrystallization of tungsten	Lower heater temperature (below 1350°C)
	Reaction with Alumina coating	

The Nickel Matrix Cathode

Two methods are known to produce a nickel matrix cathode.

The pressed cathode is made by pressing together a mixture of powdered barium-strontium-carbonates and nickel powder and sintering the pressed material at 1000°C to metal base.

The nickel powdered cathode uses nickel oxide or nickel oxalate powder, which is sintered to the metal base. The carbonate suspension is brushed or pressed into the matrix.

With both methods a porous nickel matrix cathode is produced with a porosity of approximately 50 percent. Reducing agents, such as zirconium, tungsten, or magnesium, are added to both the nickel base metal and to the nickel powder (matrix).

The nickel matrix cathode has a greatly improved electrical and thermal conductivity of the coating, as well as much better bond of the coating to the base metal, and a larger volume of the coating can be applied. As a result the cathode resistance of this oxide is very low. This provides better protection against arcing at high voltage and current density operation and improved resistance against damages by ion bombardment. This cathode is capable of long life operation with higher current densities from 600 mA/cm^2 to 1000 mA/cm^2 , but with higher cathode temperatures, in the range of 840°C .

The nickel matrix cathode requires a much longer activation time than oxide coated cathodes, approximately four to five times as long. The nickel matrix cathode has a tendency to grow relatively large single barium oxide crystals in the coating. These crystals do not exhibit oxygen vacancies and therefore degrade the emission and disturb the diffusion process, leading to inhomogeneities. Nickel matrix cathodes also tend to shrink excessively.

They produce a relatively high residual gas content. The higher cathode temperatures make the heater design more critical.

The Coated Nickel Powder Cathode (CPG)²⁷

This cathode type can be considered as a modification of the oxide coated cathode and to some extent of the nickel matrix cathode. The cathode is produced in a very similar fashion as the oxide coated cathode. However, each triple or double carbonate particle is coated with a thin nickel layer. This is accomplished by heating the barium-strontium-carbonate solution (using amylacetate or solvent) to approximately 100°C and flushing the hot solution with carbonyl nickel ($\text{Ni}(\text{CO})_4$) suspended in hydrogen gas. The carbonyl nickel powder is suspended in an inert liquid and a hydrogen flow through this liquid carries the material in suspension to the hot carbonate solution.

The carbonyl nickel is thermally decomposed and forms a nickel coating on each of the carbonate particles. The nickel coating process is followed by a dry nitrogen flush. The coating process is rather critical with respect to the temperature, the concentration of the mixtures, and the purity of the materials. After the nickel coating is applied, a binder (nitrocellulose or polybutyl-methacrylate) is added and the solution can be sprayed onto the nickel alloy base in the same fashion as for the conventional oxide coated cathode. The cathode processing and activation procedure is also the same as for conventional oxide coated cathodes. During the cathode breakdown process the continuity of the coating nickel film is broken by escaping CO_2 and the coating is sintered into a nickel frame.

This cathode exhibits superior electrical and thermal conductivity and outstanding coating adhesion to the metal base as compared to the oxide coated cathode. The work function of this cathode is almost as low as that of oxide coated cathodes, permitting low cathode temperature operation in the range of 700°C to 800°C, while the current densities can be as high as 1,000 mA/cm² for long life operation as a result of the improved properties of this cathode.

The coated nickel powder cathode achieves thermal and electrical conductivities of its coating which are comparable to those of the nickel matrix cathode, permitting equally high current densities. This is accomplished, however, with a much lower percentage of nickel in the coating frame of only approximately 3 percent by weight, compared to the 70% to 80% nickel by weight of the nickel matrix cathode. This provides the much lower work function of the coated nickel powder cathode and, therefore, its lower operating temperature compared to the nickel matrix cathode. The formation of the large single barium oxide or strontium oxide crystals during the processing generally does not occur due to the lower processing temperature and the inhibiting nickel film coating. These large single crystals are observed in nickel matrix cathodes; they cause deep donor depletion layers and degradation of the emission.

The coated nickel powder cathodes can be processed and activated within a much shorter time than nickel matrix cathodes. Their processing temperatures may be temporarily raised to 1100°C for improved outgassing of the heater and cathode.

The nickel frame of this cathode is gradually evaporated and must be replaced by sublimation of nickel from the base into the coating, which is accomplished when the vapor pressure (and temperature) of the nickel base is high enough. With insufficient nickel sublimation the coating is gradually transformed into a conventional oxide coating. The life of this cathode is generally limited by the supply of the reducing agents (Zr and W) of the nickel base, in the same fashion as for oxide coated cathodes. The barium arrival rate is also diffusion limited. Thus the C.P.C. cathode combines the advantages of the oxide coated cathode with those of the nickel matrix cathode.

The Impregnated Tungsten Cathode

The impregnated tungsten cathode is widely used in high power tubes, when high current density operation is required.

The porous tungsten body is produced by sintering pressed tungsten powder at temperatures of 2400°C . Optimum cathode performance can be obtained with a tungsten powder particle size of about $5\ \mu$ and an impurity content (iron, oxygen, and silicon) of the tungsten of less than .002%. The optimum porosity of the sintered tungsten body is found to be 17% to 19%.

The sintered tungsten ingots are then impregnated with OFHC copper at 1350°C in a dry hydrogen atmosphere. The molten copper penetrates the tungsten body by capillary action. The copper impregnated tungsten should have a density of $17.5\ \text{g/cm}^3$; it can then easily be machined, such as turned, drilled, milled, and polished. The copper serves as a filler and lubricant for the machining operations and accurately controlled sizes and dimensions can be achieved for a variety of cathode shapes without damages to the surfaces. The copper is then completely removed by evaporation at 1800°C in a vacuum furnace. This is accomplished without shrinkage as a result of the much higher sintering temperature (2400°C). The final cathode impregnation is then applied to the surface of the porous tungsten body. The impregnation consists of barium oxide, calcium oxide, and aluminum oxide powder suspended in a butyl methacrylate or benzene solution with an organic binder. These oxides have been produced by melting together 5 moles barium carbonate, 3 moles calcium carbonate, and 2 moles aluminum oxide powder at 1700° in dry hydrogen atmosphere. The amount of the calcium carbonate is not critical, but a minimum of .3 moles is required.

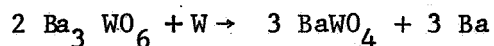
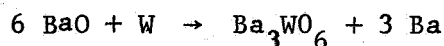
The impregnated tungsten cathode is then vacuum heated to 1700°C . This melts the impregnant and draws it into the tungsten pores by capillary action. After impregnation the cathode should have a weight increase of 5 percent.

The impregnated tungsten cathode has to be attached to a supporting structure; however, care must be taken to avoid bonding materials with reducing action on the aluminate. Platinum is also undesirable for bonding since platinum tends to migrate to the cathode surface and to increase the work function. Molybdenum is most frequently used as a support structure material, but the bonding generally is difficult to achieve.

The processing and activation of the impregnated tungsten cathode is relatively simple. After the bake-out, the cathode is activated at 1200°C with current being drawn. The cathode is then aged at 1100°C and can then be operated at 1000°C to 1080°C. Typical cathode temperatures as a function of the cathode loading are:

<u>Temperature</u>	<u>Current Density</u>
970°C	2.5 A/cm ²
1080°C	5A/ cm ²
1130°C	10A/cm ²

The emission of the impregnated tungsten cathode corresponds to a work function of 1.67 V compared to 4.54 V of tungsten. This low value of the work function and its resultant high emission is interpreted as being produced by the existence of a monoatomic layer of barium and oxygen atoms at the cathode surface. The barium atoms are produced by reduction of barium oxide by tungsten, corresponding to a reaction of:



The presence of calcium oxide is assumed to lead to an emission increase from the ends of the pores and to reduce the barium evaporation.

The barium reaches the cathode surface partly by migration over internal surfaces, but primarily by "Knudsen-flow" through the pores. The porosity of the tungsten body, therefore, influences the evaporation rate from the cathode surface.

The cathode life is terminated when the barium flow rate becomes too slow compared to its evaporation rate. In Figure 113 the evaporation rates of the materials used in an impregnated tungsten cathode are shown as function of temperature.

To achieve good emission the cathode must completely be covered with barium. It has been found that loss of emission is suffered by poisoning, when vapors of H_2O , CO_2 , SO_2 , CO , or O_2 oxidize the monoatomic layer.

Other emission damages can be caused by organic vapors, which may carbonize at the cathode or by hot metal vapors of titanium, nickel, iron, or chromium which may alloy with tungsten. It was found that a thin osmium coating at the cathode surface lowers the work function and improves the emission; however, osmium also evaporates readily.

Impregnated tungsten cathodes produce a rather high evaporation rate of barium due to their high operating temperatures. This may cause excessive deposition rates of barium on other parts of the gun, such as the focusing anode, grids, or the anode. Leakage currents and grid emission may then occur.

When coated heaters are used for higher temperatures, the heater coating can react with the tungsten filament, resulting in evaporation of cathode poisoning substances, which limits the acceptable heater temperature to $1350^{\circ}C$. However, uncoated tungsten heaters may be used up to temperatures of $1600^{\circ}C$ before severe recrystallization occurs. Coated heaters should be connected to the cathode to avoid destructive electron bombardment of the coating.

The advantages of the impregnated tungsten cathode may thus be listed as follows:

1. High current density capability

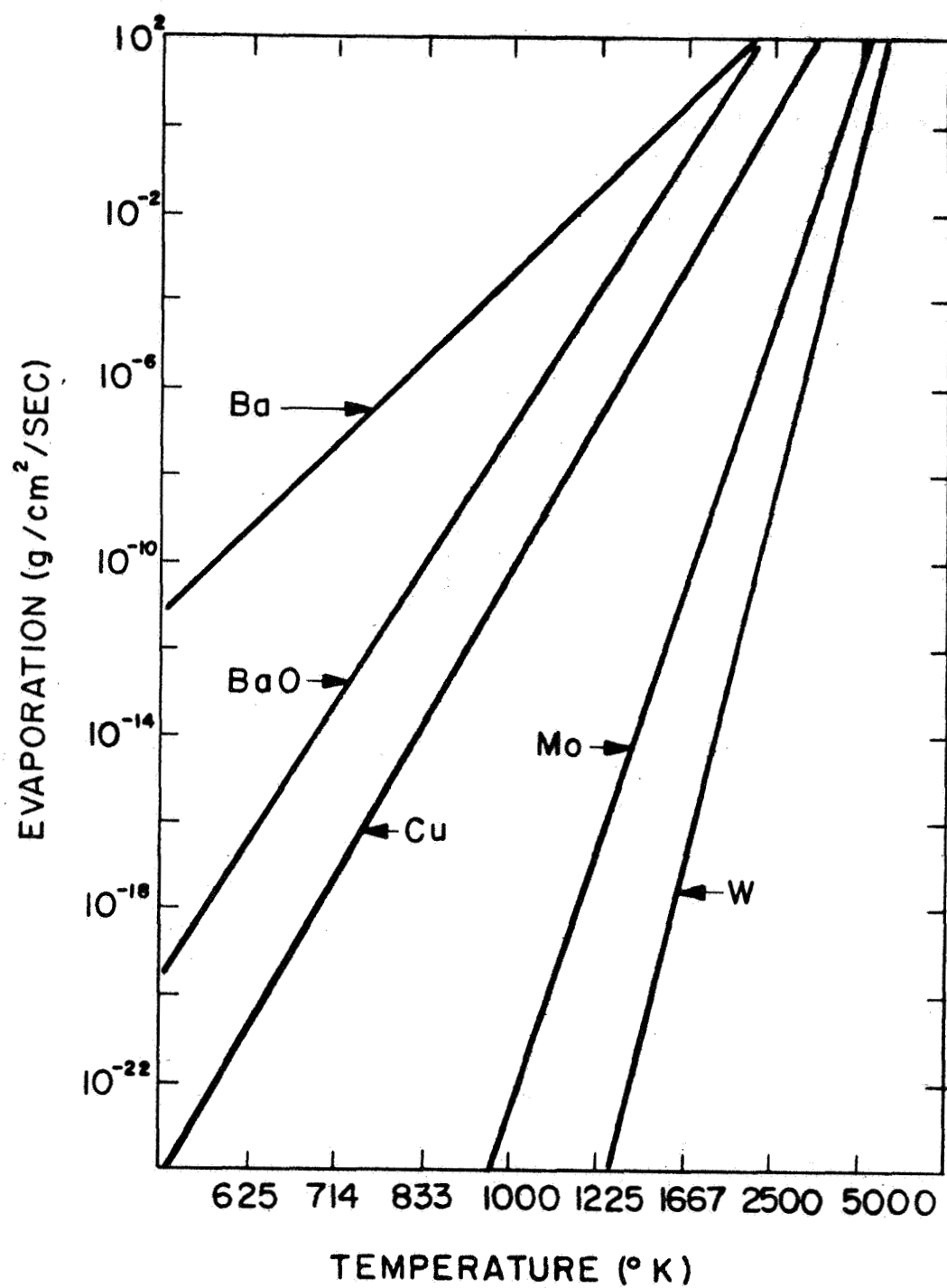


Figure 119 Evaporation rate of cathode materials of impregnated tungsten cathode.

2. High resistance of the emitting surface against ion bombardment and arcing
3. Very low cathode resistance
4. High resistance against poisoning. Cathode can be reactivated by short overheating after severe poisoning
5. The cathode can be reactivated after exposure to air.

Recommendations for the Choice of a Cathode for the Tube Designs

From the previous discussions, it can be concluded that the 850 MHz and 2 GHz tubes should be provided with oxide coated cathodes. The cathode loading of these tubes is very low and comparatively low cathode temperatures can be used, so that the barium evaporation can be kept very low. This is important in view of the grids being used in conjunction with the traveling-wave tube modulator. With low evaporation rates, the grids can be expected to maintain their characteristics during the life of the tube.

For the 8 GHz and 11 GHz tubes, an impregnated tungsten cathode is proposed. The required current densities for these tubes are relatively low for impregnated tungsten cathodes, and superior life can be expected. These tubes could also use oxide coated cathodes with shorter, but still adequate, life expectancy. The impregnated tungsten cathodes provide additional reliability due to their increased resistance against ion bombardment and poisoning. The coated nickel powder cathode could be used for these tubes too, but for this cathode type no life data are yet available.

A list of the cathode recommendations follows in Table XXIX.

Table XXIX Recommended cathodes.

TUBE	850 MHz	2 GHz AM	2 GHz FM	8 GHz	11 GHz
Shadow Grid	yes	yes	no	no	no
Cathode Loading	78 mA/cm ²	142 mA/cm ²		470 mA/cm ²	490 mA/cm ²
Cathode Type	Oxide coated cathode			Impregnated tungsten cathode	
Cathode Temperature	700°C	730°C		950°C	950°C
Cathode Life Expectancy	>50,000 hours			>50,000 hours	
Remarks	Very low cathode loading permits low cathode temperatures with low barium evaporation for grid protection and very long cathode life.			Cathode loading is low to permit very long life operation with impregnated tungsten cathode. No grids, therefore higher cathode temperatures are permissible.	

B. LIFE CONSIDERATIONS FOR HEAT PIPE

1. General

The heat pipe cooling system permits operating temperature for the high power tubes which are only slightly higher than the operating temperatures of present day medium power space tubes for communications.

The low temperature cooling system is considered essential for the long life capability of the tubes. The heat pipe system is designed for high reliability and long life, since it provides abundant heat transfer by the multiple independent parallel heat pipes in the radiator system. The radiator system is not electrically insulated and therefore all metal. This permits use of structural elements which can be easily sealed. The inner dielectric heat pipe package provides in addition to excellent heat transfer, reliable electric insulation. Such dielectric heat pipe systems are presently in development for high power traveling-wave tubes. Life tests with such systems indicate that operating life of several years can be expected with these systems. Life data in excess of 10,000 hours so far have been achieved without degradation.

The low operating temperatures further enhance system reliability. The maximum temperature change for a long term shutdown (more than 24 hours) would only be 250°C. The contraction of material would then be very small. All heat pipe parts are constructed of stainless steel to keep thermal stresses small.

Start-up of the heat pipe from a frozen state during temperature cycle is of particular interest, since heat pipes with fluids such as bismuth or water have sometimes burst at low temperatures or exhibited hot spots

during start-up. The start-up process from the frozen state to the operational liquid state of a cooling system using organic fluids, however, is not expected to interfere with the heat pipe operation. The fluid contracts upon freezing, but the evaporation heat at the melting state is much larger than the melting heat for these fluids. (For example, Dow A has a latent evaporation heat of 165 Btu/lbs compared to its latent heat of melting at 40.2 Btu/lbs.) The heated frozen fluid will therefore melt much more rapidly than it will evaporate, and hot spots due to local vapor pockets are not likely to occur. These conclusions were fully confirmed with freezing experiments of heat pipes at Hughes.

A Dow A heat pipe system was repeatedly frozen to 10°C and 100°C below its freezing temperature and restarted without any degradation or changes in the operation.

2. Meteoroid Damage

The weight of the cooling system depends on the probability of puncture by meteoroids. Extensive data are available on concentration of meteoroids in space. Typical accumulated data are shown in Figure 114³². The data on particle concentration can be combined with results obtained from tests on hypervelocity impacts. From these data the penetration probability of a material with a given thickness can be calculated. The average time to penetrate an aluminum spacecraft skin is shown in Figure 115³³. The time scale can be increased by a factor 10 for steel. Therefore a steel skin shrouding with .020 in (.0508 cm) thickness is adequate to protect the spacecraft against meteoroid penetration over a period in excess of 10 years.

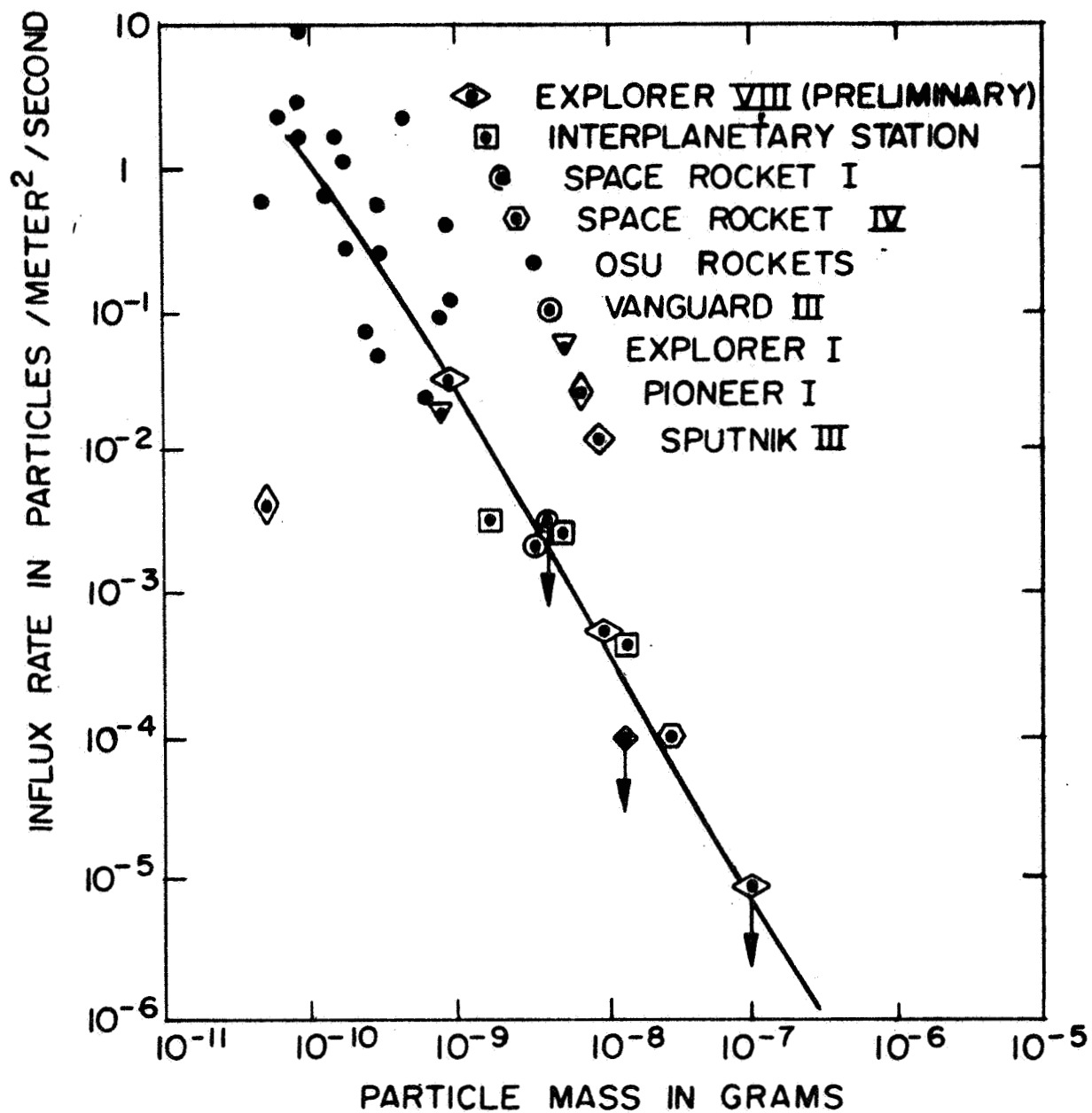


Figure 114 Average cumulative mass distribution for interplanetary dust particles in vicinity of earth.

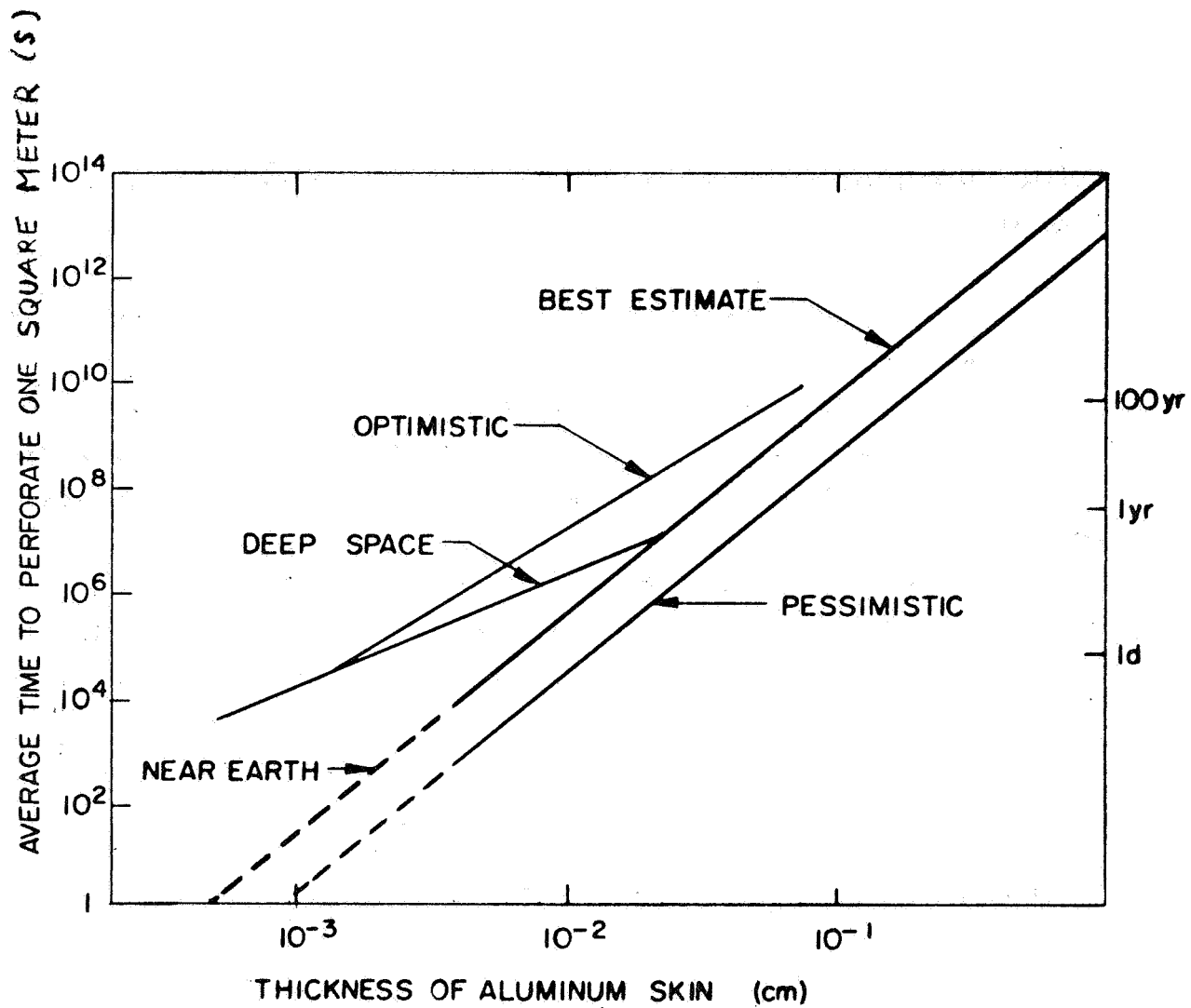


Figure 115 Penetration of meteoroids into aluminum skin³³.

XI. POWER SUPPLY REQUIREMENTS

A. GENERAL

The high efficiency of the tube designs is achieved with a multi-voltage jump taper on the circuit and a four-stage collector. A schematic of the required power supplies is shown in Figure 116.

The tube is operated with a cathode supply, circuit supply, collector supply, and heater supply with the driver section of the slow wave structure being grounded. The high frequency tubes (8 GHz and 11 GHz) also require a power supply for the solenoid. The cathode supply, anode supply, and circuit supply have to provide the required tube potentials, while the collector supply has to primarily provide the power. Both the circuit supply and the collector supply have a number of voltage taps for the circuit sections and the collector stages. In Table XXX the required tube voltages and currents for these supplies are listed. The listed tap voltages for the circuit and collector supplies are taken between the negative supply terminal and the tap terminal.

For the loading of these supplies it has been assumed that the driver section of the circuit has 3% current interception, while any of the voltage jump sections may have up to 1% current interception. The anode is assumed to intercept up to 1% of the beam current. The collector currents have been determined from the computed spent beam energy distribution, including estimated velocity sorting deficiencies and secondary backstreaming.

It should be mentioned that the listed power supply loadings for the AM tubes represent peak values. All currents (except the heater supply) will vary from these peak values to practically no current as a function of the amplitude modulation, while the relative current distribution will remain approximately constant with time, except for the collector loading. The collector loading will shift at lower modulation levels (and beam currents) to lower collector potentials.

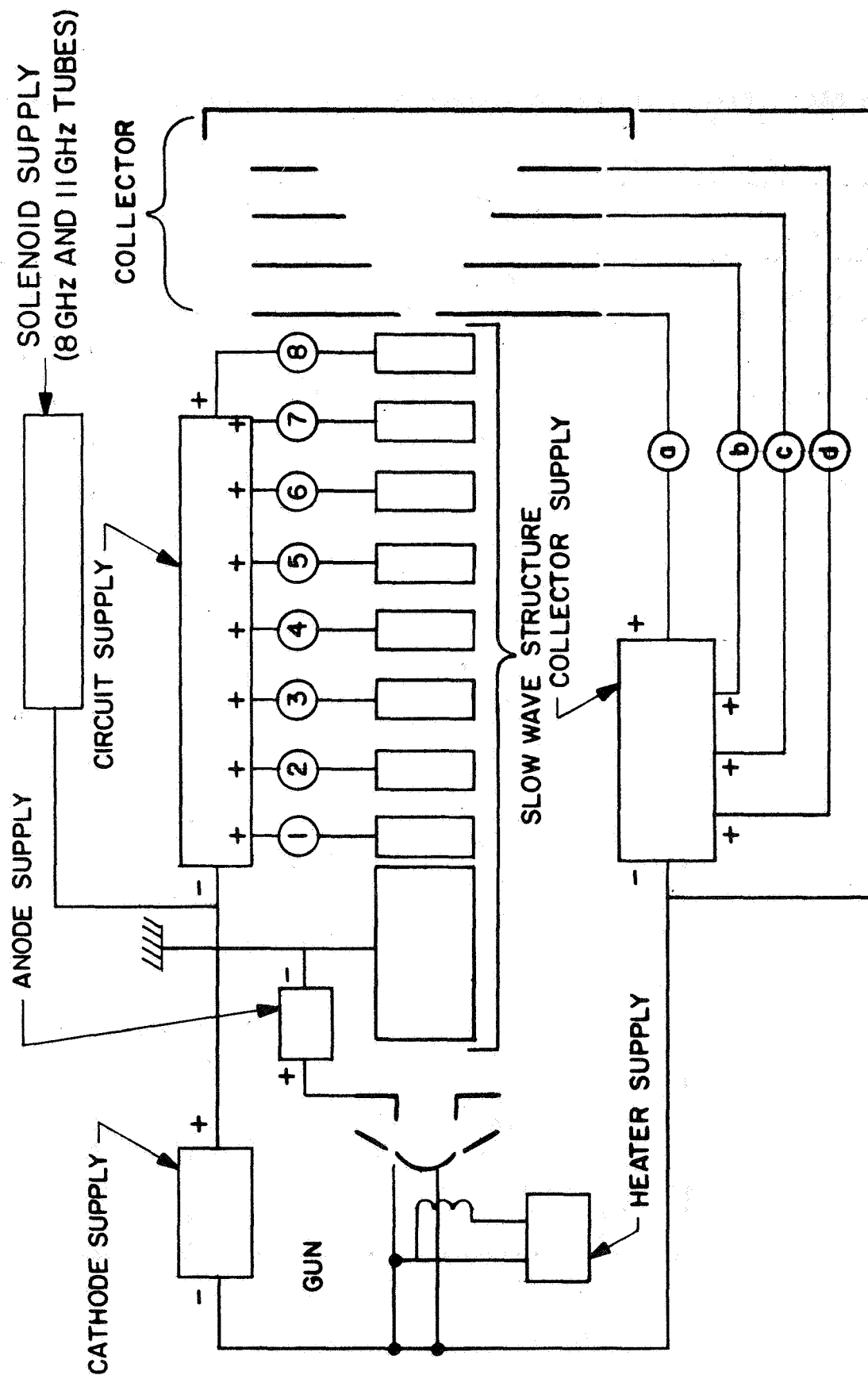


Figure 116 Power supply diagram for multi voltage jump taper tubes with four-stage collector.

Table XXX Power supplies for voltage jump taper tubes with four stage collector.

TUBE		850 MHz AM	2 GHz AM & FM	8 GHz FM	11 GHz FM
Power Out		7.6 kW	5.2 kW	5.1 kW	5.1 kW
Cathode Supply		16 kV	13 kV	12 kV	14 kV
$I_{\max.}$		15 mA	9 mA	9 mA	9 mA
Anode Supply		100 V	100 V	100 V	100 V
$I_{\max.}$		0-5 mA	0-3 mA	0-3 mA	0-3 mA
Heater Supply		12.0 V	9.0 V	6.3 V	6.3 V
		2.77 A	1.70 A	1.19 A	1.01 A
Circuit Supply	1	5.15 kV	4.66 kV	4.80 kV	5.6 kV
	2	6.62 kV	6.95 kV	7.90 kV	9.56 kV
	3	8.08 kV	9.24 kV	11.0 kV	13.52 kV
	4	9.55 kV	11.53 kV	{ 14.0 kV	17.50 kV
	5	11.01 kV	13.81 kV	22 mA	---
	6	12.48 kV	16.10 kV	---	---
	7	13.94 kV	---	---	---
	8	15.40 kV	---	---	---
I_{\max} (each)		0-5 mA	0-3 mA	(0-3 mA)	0-3 mA
Collector Supply	a	22.5 kV 208 mA	25.3 kV 114 mA	20.9 kV 136 mA	26.60 kV 191 mA
	b	19.1 kV 143 mA	22.2 kV 100 mA	18.95 kV 125 mA	19.11 kV 66 mA
	c	16.3 kV 135 mA	19.8 kV 70 mA	15.75 kV 48 mA	13.10 kV 28 mA
	d	0 19 mA	5.3 kV 14 mA	1.31 kV 17 mA	1.45 kV 13 mA
I_{TOTAL}		505 mA	298 mA	346 mA	298 mA
Solenoid Supply		---	--	14.3 V 28.6 A	15.2 V 22.9 A

The average supply loading for the AM tubes is estimated to 40% of the listed peak values. The long term stability (load regulation) requirements for these supplies have been determined to keep gain and efficiency changes by voltage variations negligibly small. The most critical long term regulation is required for the heater supply which has been specified to keep the cathode temperature variations ΔT_c with

$$\Delta T_c = \pm 20^\circ\text{C}.$$

The short term load regulation (maximum voltage ripple) takes also phase variation due to voltage ripples into account. Such phase variations are caused by voltage variations of the cathode and circuit supply. Its regulation has been determined to keep these phase variations by an order of magnitude smaller than the permissible phase variations over the frequency range. The regulation requirements for the FM tubes are therefore almost an order of magnitude smaller than those for the AM tubes.

The resultant voltage regulation requirements are listed in Table XXXI.

B. TURN-OFF AND TURN-ON PROCEDURES

The turn-on and turn-off procedures for the tubes are designed primarily to protect the cathode against temperature limited emission. The cathode must therefore be hot when the voltages are turned on or off. This can be accomplished with the Alternate I procedure listed below:

Table XXXI Voltage regulation requirements.

		MAXIMUM RIPPLE	LONG TERM
		$\frac{\Delta V}{V_o}$	$\frac{\Delta V}{V_o}$
Cathode Supply	AM	$\pm .1\%$	$\pm 1\%$
	FM	$\pm .02\%$	
Anode Supply	AM	$\pm 5\%$	$\pm 5\%$
	FM		
Heater Supply (dc)	AM	Not Critical	$\pm .1\%$
	FM		
Circuit Supply	AM	$\pm 1\%$	$\pm 2\%$
	FM	$\pm .2\%$	
Collector Supply	AM	$\pm 2\%$	$\pm 2\%$
	FM		
Solenoid Supply (8 GHz and 11 GHz only)		$\pm 5\%$	$\pm 2\%$

ALTERNATE I

A. TURN-ON

- Step 1. Turn on: heater supply
anode supply
circuit supply
collector supply
solenoid supply
(8 and 11 GHz only)
- Step 2. 5 minutes after Step 1 turn on cathode supply.

B. TURN-OFF

- Step 1. Turn off cathode supply
- Step 2. 10 ms after Step 1 turn off:
anode supply
circuit supply
collector supply
heater supply
solenoid supply
(8 and 11 GHz only)

Some coupled cavity tubes tend to break into transient oscillations during the switching periods for the cathode supply voltage. An Alternate II procedure is suggested in this case, which eliminates such transient oscillations. With this procedure the anode remains shortened to the cathode during the cathode voltage switching period.

ALTERNATE II

A. TURN-ON

- Step 1. Short cathode - anode terminals
Open anode supply connection
- Step 2. 100 ms after Step 1 open:
 - heater supply
 - circuit supply
 - collector supply
 - cathode supply
 - solenoid supply (8 and 11 GHz only)
- Step 3. 5 minutes after Step 2 open short between cathode-anode terminals
- Step 4. 100 ms after Step 3:
 - reconnect anode supply
 - turn on anode supply

B. TURN-OFF

- Step 1. Turn off anode supply
Open anode supply connection
- Step 2. 100 ms after Step 1 short cathode - anode terminals
- Step 3. 100 ms after Step 2 turn off:
 - cathode supply
 - circuit supply
 - collector supply
 - heater supply
 - solenoid supply
 - (8 and 11 GHz only)

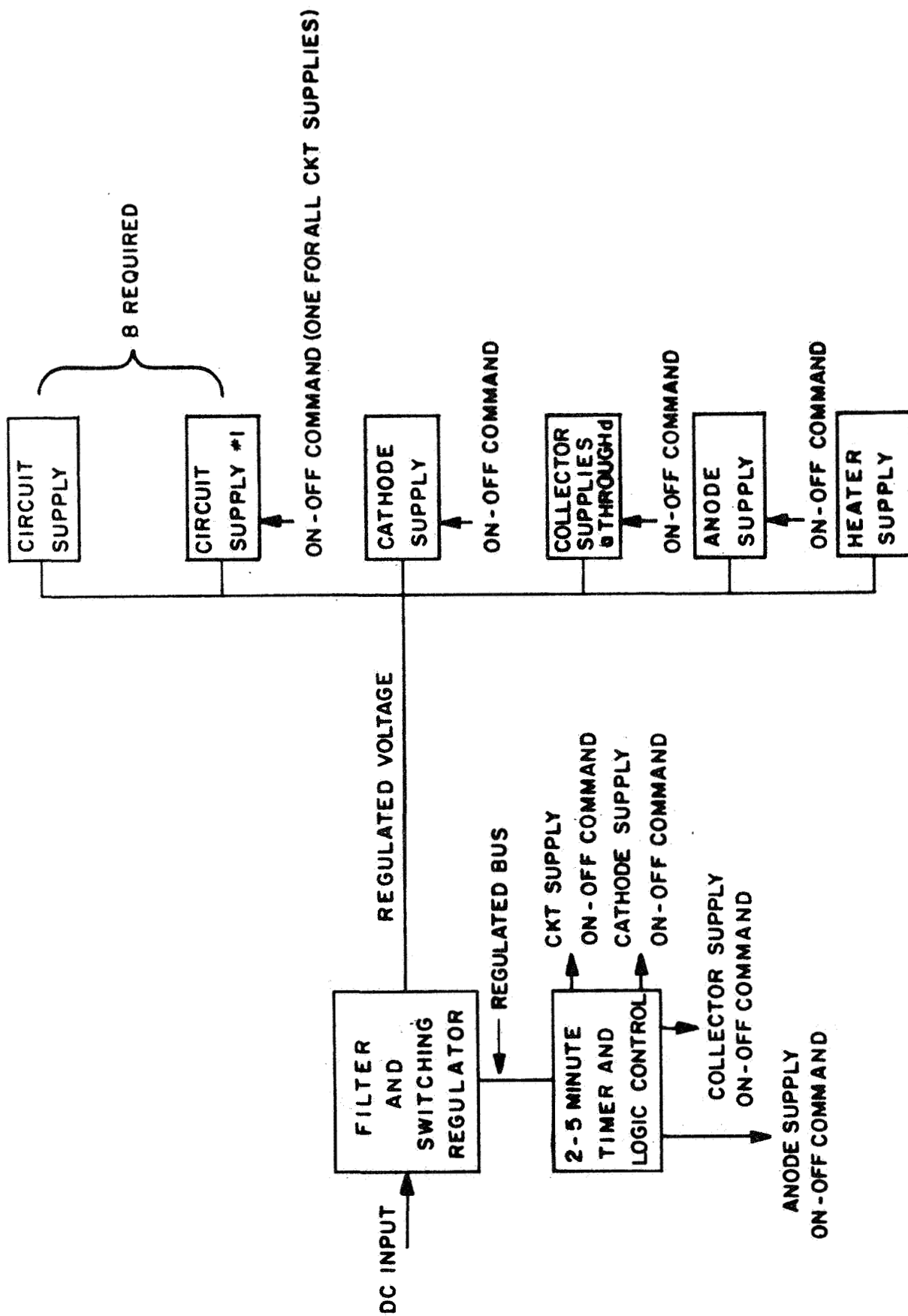


Figure 117 Diagram for switching regulator.

C. DESIGN CONSIDERATIONS FOR ELECTRONIC POWER CONDITIONER

The power requirements for a voltage jump taper traveling-wave tube with multi stage collector present some unique requirements on the electronic power conditioner design. The amount of dc power required for this tube is two (2) orders of magnitude higher than that for present space type traveling-wave tube amplifiers. The voltage levels required are an order of magnitude higher, and the number of independently regulated voltage levels needed vary from 10 to 14 depending on the output RF power. Traveling-wave tube amplifiers in space use today require 3 to 5 regulated voltage levels, some of which employ a common regulator. The requirements for the EPC for a voltage jump taper traveling-wave tube with multi stage collector are therefore unique to the extent that the dc power, voltage levels, and the number of voltage levels required are much higher than provided by current designs.

The most critical design constraint on the electronic power conditioner is the requirement of high efficiency. A high electronic power conditioner efficiency is necessary to obtain high system efficiency. A crucial requirement on efficiency may come from the thermal constraints in a spacecraft. A traveling-wave tube amplifier with 5 kW RF output and an overall efficiency of 67% would generate approximately 2-1/2 kW of heat in a fairly localized region.

Though some of the electrical parameters of the electronic power conditioner are, for high power traveling-wave tubes, more demanding than for low power traveling-wave tube amplifiers, the electrical requirements can be met with a state-of-the-art design approach. A conventional switching regulator could be used to provide a well regulated input voltage to the dc-dc as shown in Figure 117. Using this approach, the dc-dc converters would have to provide load regulation, since the

load will change with modulation (for the AM tubes). The overall efficiency of this electronic power conditioner would be between 70 and 85% depending on the required load regulation.

The conventional approach to this does not provide high efficiency and may not be optimum from a reliability point of view; the power density required in the common regulator may be excessive for reliable operation. Another approach, which would provide an improved EPC efficiency and other realizable advantages, is shown in Figure 118. This approach features a highly efficient self-regulating dc-dc converter. The converter is made self-regulating by sampling the output voltage and comparing it with a reference voltage. The error voltage resulting from this comparison determines the pulse width of the base drive control square wave. It is important to understand that the output of the base drive control circuit does not provide the base drive. The base drive, as well as the power for the inverters, is taken directly from the unregulated input. Since the control circuits in this self-regulating dc-dc converter operate at low voltages and low currents, it seems feasible that all circuitry outside the high voltage converter could be contained on one integrated circuit chip, and the same chip would be used in all converters. The high voltage converter will be the only part of this design that has to handle high currents and withstand high voltages. Several techniques have been used in high voltage design for space use. Considerable study and experimentation might be required to arrive at the best materials and techniques for the design of the high voltage converters. One approach that can provide the desired protection against corona, and be light weight at the same time, is to have high voltage converter in a vacuum with a squib that can be blown after reaching orbit.

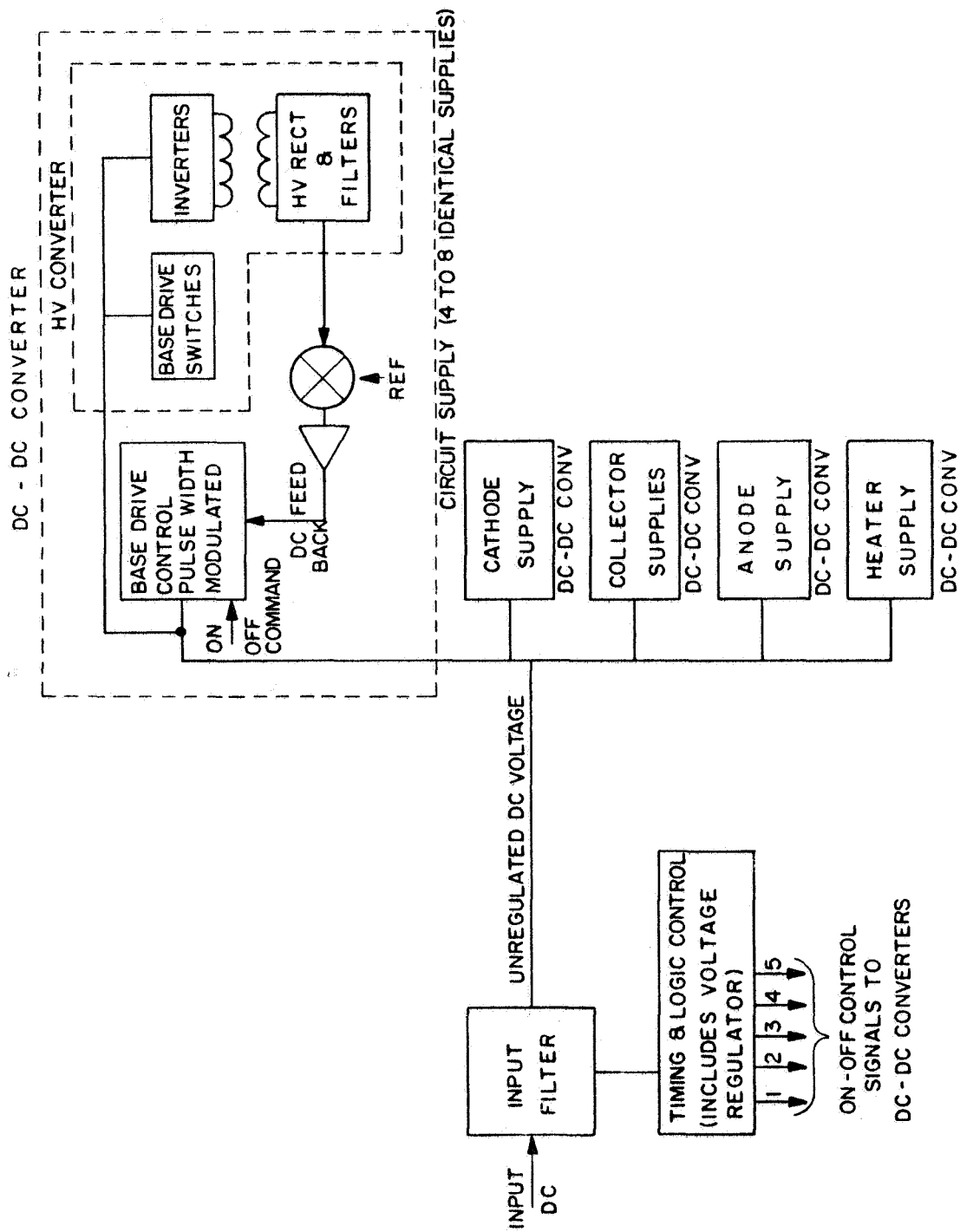


Figure 118 Electronic power conditioner with self-regulating dc-dc converter.

XII. TRAVELING-WAVE TUBE MODULATOR

In Section IV F a new scheme was described which permits linear amplification of AM signals with very high efficiency. This method uses a dual tube approach: a driver tube (preamplifier) which amplifies an FM signal, and a traveling-wave tube modulator. This traveling-wave tube modulator incorporates a modulation grid for the amplitude modulation. This system works effectively only when no (constant level) FM signals are present within the AM signal. It is therefore necessary to separate the audio FM signals with filters and amplify them separately with an FM amplifier.

The audio FM amplifier and the driver tube can operate at saturation, since they have to handle only FM signals. They can therefore be designed for very high efficiency. Their required power levels are low enough so that a light weight highly efficient helix tube can be used. In the following the design characteristics of these helix tubes is discussed, and the design considerations for the traveling-wave tube modulator grid and its characteristics are reviewed.

A. HELIX DRIVER AND FM AUDIO TUBES

Helix tubes can be designed for very high efficiency, since the helix slow wave structure may provide a high interaction impedance. Unlike the coupled cavity circuit, the helix circuit uses its fundamental mode for interaction, which is inherently stronger than the space harmonics. High interaction impedance for helices requires a small design value of γr_a . For the present tubes γr_a is chosen to

$$\gamma r_a = .8.$$

This is a value to obtain optimum efficiency and high interaction impedance. With such low γr_a choices the helix becomes more dispersive, and its bandwidth capability is then reduced. Helix circuits are therefore generally designed with larger γr_a values. For this application, however, the large bandwidth capability of the helix is not needed and the reduced bandwidth capability at the lower γr_a value, with 5 to 10% bandwidth, is more than adequate.

The interaction impedance of the helix is also a function of its configuration, including the helix support structure. Such a helix assembly is shown schematically in Figure 119. To achieve high interaction impedance, the loading by the dielectric support rods and the external metal envelope should be as small as possible. This can be accomplished by choosing a dielectric material for the support rods, which has a small dielectric constant and small losses, and by choosing a large ratio of the metal shield radius r_s to the helix radius r_a . There are several dielectric materials available for these requirements; however, the heat transfer capability of these materials is also of concern, especially for

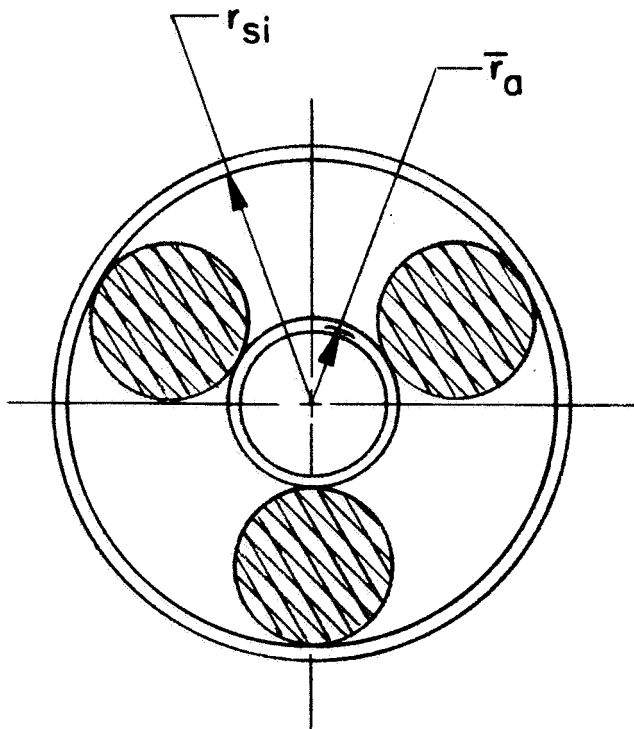


Figure 119
Helix assembly.

the FM audio tube, which has to operate at relatively high power levels. Therefore, beryllium oxide ceramic is chosen for the support rods. BeO has a relatively low dielectric constant ($\epsilon = 6$), its losses are very low, and it provides outstanding thermal heat transfer due to its excellent thermal conductivity. This material is generally used for helix tubes with high power levels. The assembly technique for the helix is also of concern for good heat transfer. For the power levels of the driver tube the conventional "triangulation technique" is entirely adequate. This technique assures good heat transfer between helix and rods, and between rods and the metal envelope, by mechanical compression. For the higher power levels of the FM audio tubes, however, the triangulation method becomes marginal. In this case the newly developed brazing technique appears to assure much better the required reliability and life. This technique achieves substantially higher power capability for helix tubes (up to several kilowatts CW at S-band) because of a greatly improved heat transfer due to an all brazed structure (helix-BeO rods and rods-metal envelope). This technique, however, is complex and difficult to achieve, primarily due to the differential thermal expansion coefficients of the rods and the metal envelope. It is therefore necessary to use a composite barrel envelope, which consists of metal rings with different thermal expansion, so that its composite expansion matches that of the rods. Life data for these types of tubes are not yet available. It is proposed to use the brazed construction for the 2 GHz FM audio tube, while the 850 MHz tube, which is much larger, is constructed with the triangulation technique. Extensive cold tests with both alumina and beryllia rods have been carried out, and it was found that a very high interaction impedance K of

$$K = 180 \text{ ohms}$$

can be achieved with beryllia rods at $\gamma r_a = .8$ and a large shield radius to helix radius ratio of

$$\frac{r_s}{r_a} = 2.3 .$$

This configuration is used for the design of the helix tubes. The loss constant α was measured at S-band to

$$\alpha = .025/\text{cm} .$$

The loss constant α is assumed to vary with the frequency and impedance as

$$\alpha = \text{proportional } (f)^{1/2} (K)^{-1}$$

for the high efficiency computer design analysis.

Helix tubes can readily be focused with a light weight periodic permanent magnetic focusing structure as shown in Figure 120. The magnetic period L is chosen to provide high focusing stability for the high efficiency design. A large value of $\frac{\lambda_p}{L}$ is therefore chosen, or

$$\frac{\lambda_p}{L} > 4 .$$

In order to obtain good beam transmission, the beam radius to helix radius ratio was chosen to

$$\frac{r_b}{r_a} = .7 .$$

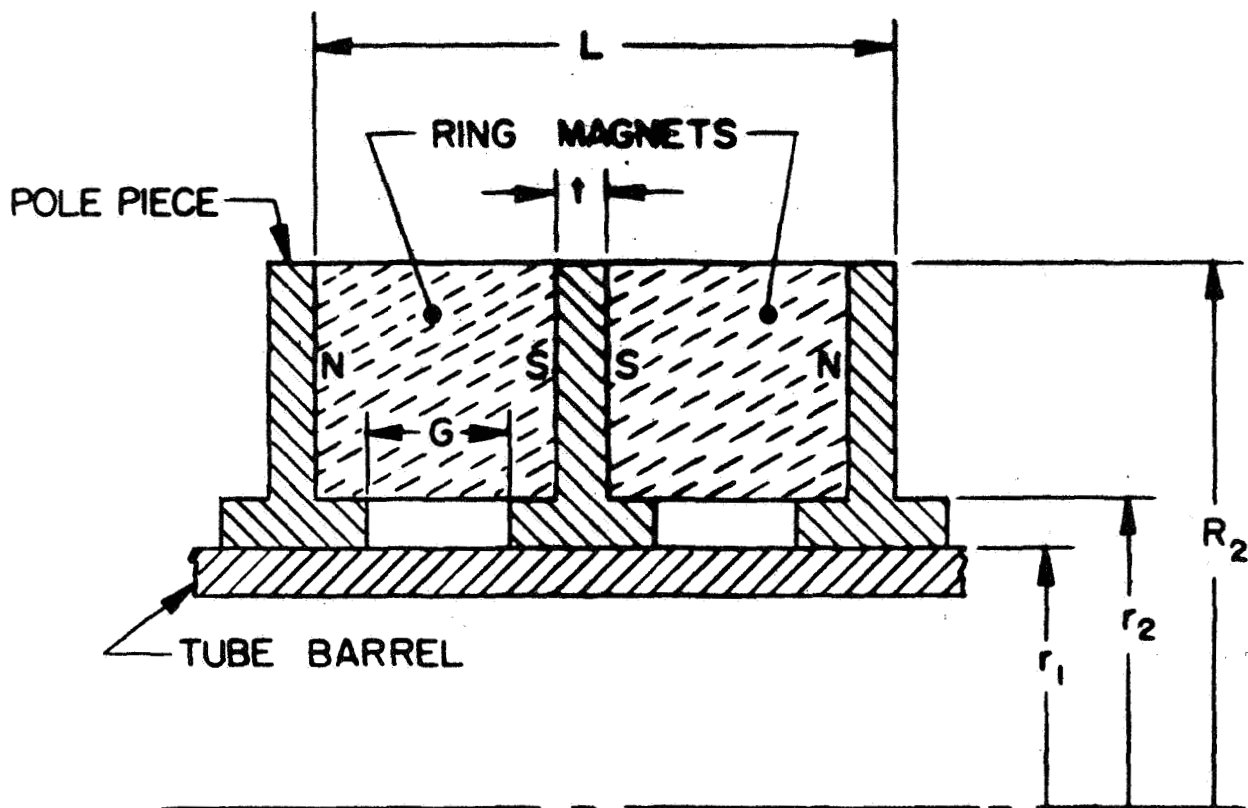


Figure 120 Helix PPM focusing configuration.

A magnetic peak field B of

$$B = 2 \sqrt{2} B_0$$

with

$$B_0 = \text{"Brillouin" field,}^{18}$$

is provided as the focusing field, taking strong beam bunching and RF defocusing into account. The cathode is magnetically shielded to assure minimum beam ripples in conjunction with optimized beam launching conditions of the gun into the focusing field.²² It is necessary, however, to use platinum cobalt magnets to achieve the required fields. The beam

area convergence of the gun can be chosen to achieve a low enough cathode loading i_c of

$$i_c < 500 \text{ mA/cm}^2$$

to assure long cathode life.

Velocity resynchronization is used for efficiency enhancement. These techniques have recently proven successful for helix tubes also, resulting in 55% efficiency with a voltage jump at S-band (Figure 10). For the helix tube designs, however, a more advanced efficiency enhancement scheme, a combination of a voltage jump and a velocity taper, is used. The design is illustrated in Figure 121. A voltage jump of $V_j = 1.4 V_o$ is followed by a velocity taper of $v_t = .6 v_o$. For this combination the computer analysis predicts efficiencies of approximately 65% with the collector grounded ($V_c = V_o$). This design approach is used for all helix tubes. The associated power supplies are illustrated in the diagram of Figure 122.

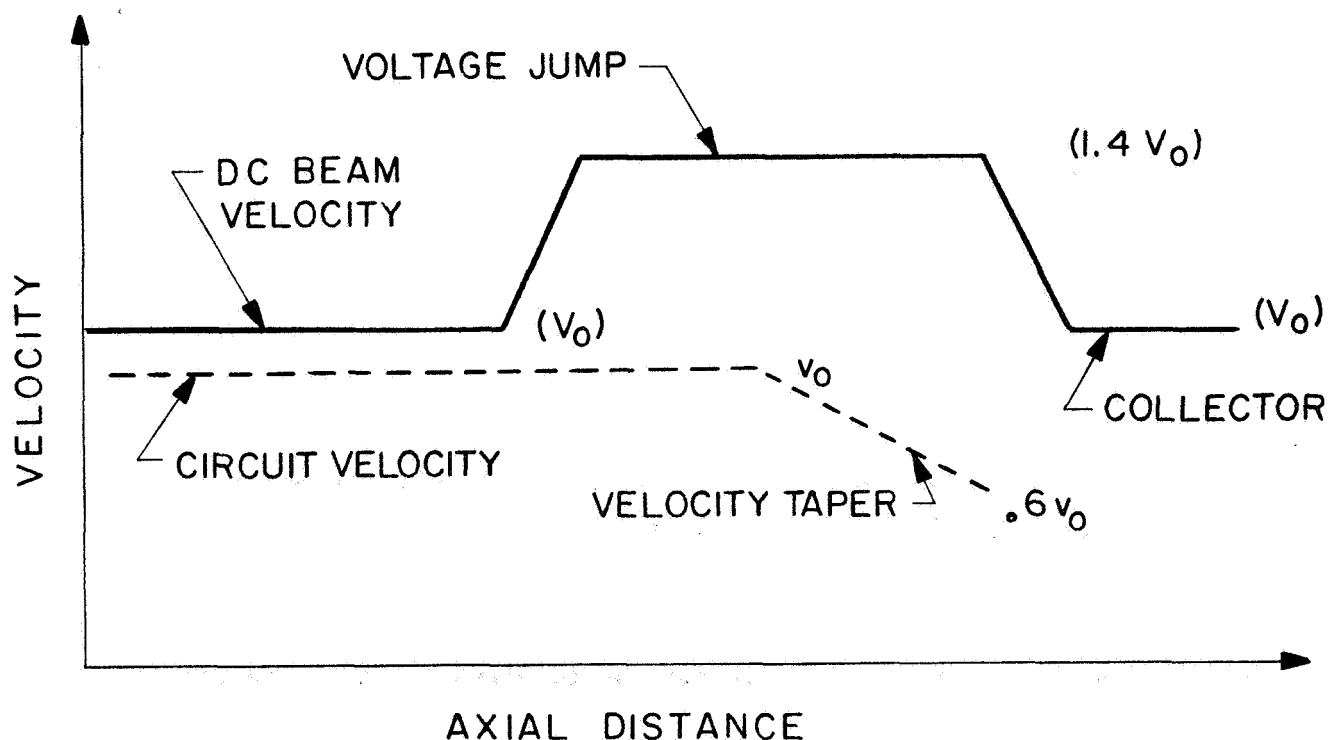


Figure 121 Velocity profiles for helix tube with voltage jump and velocity taper.

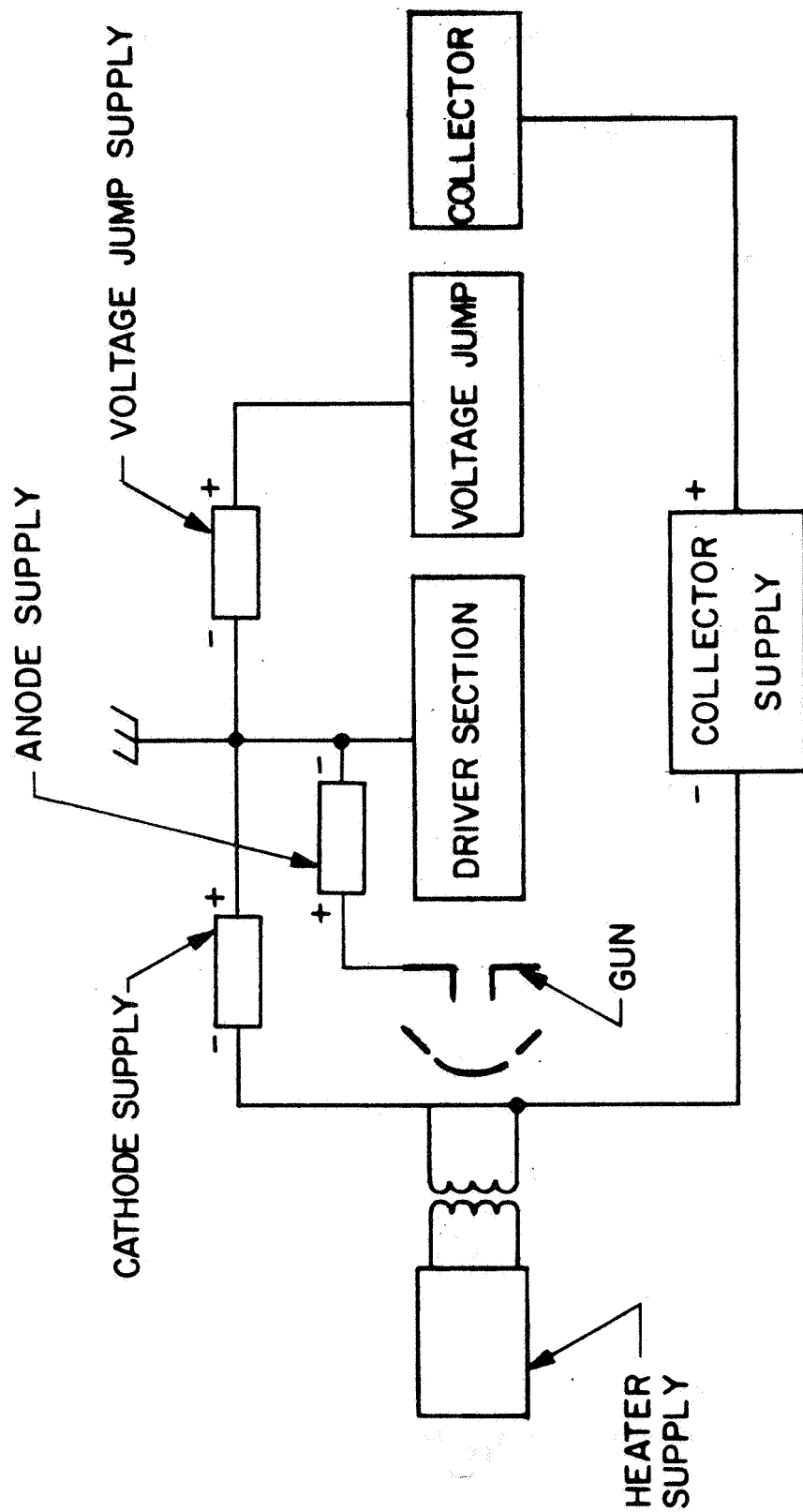


Figure 122 Power supply diagram for helix tube with voltage jump.

Helix tubes are already well proven for space applications. Design and construction techniques have been perfected to achieve rugged structures suitable for space environment and proven high reliability and long life.

In Table XXXII the design parameters for the helix tubes have been listed.

B. THE MODULATION GRID

The traveling-wave tube modulator achieves very high efficiency amplification of the AM signal. The key to its operation is the modulation grid, where the FM carrier signal and the modulation are recombined in a linear fashion. Certain characteristics are required of the modulation grid and its drive characteristics. These include its dc grid bias voltage, its frequency response, its required maximum modulation drive level, and its effects on the beam focusing.

A typical grid characteristics of a shadow grid gun used in a traveling-wave tube is shown in Figure 123. This grid characteristics is not significantly different from that of a conventional grid, and a conventional grid may be used instead for the traveling-wave tube modulator.

The design requirements for the operation of a traveling-wave modulator have been discussed in Section IV F.

At the lower modulation limit of the AM signal (20 dB below the maximum level) the grid drive becomes zero and, consequently, also the beam current produced by the grid modulation. At this condition the traveling-wave tube modulator gain is required to be zero also. However, in view of the gain characteristics of a traveling-wave tube, which produces negative gain with very small beam currents as illustrated in Figure 124, a small dc current I_0 has to be provided to the tube in order to obtain zero gain at the lower AM signal level limit. This dc current is produced by a positive grid bias voltage V_{go} (Figure 51).

Table XXXII Design parameters for helix driver and FM audio tubes.

TUBE FREQUENCY	UNIT	850 MHz	850 MHz	2 GHz	2 GHz
Application				FM audio	Driver
Output Power (CW)	watts	750	75	500	50
Gain	dB	40	40	40	40
Voltage	V	3800	1600	3600	1500
Voltage Jump ΔV_j (above ground)	V	1500	640	1450	600
Beam Current I_o	mA	310	76.5	224	55.5
Perveance	μP	1.32	1.22	1.02	1.00
Gain Parameter C		.154	.129	.143	.119
Space Charge Parameter QC		.107	.135	.101	.128
Velocity Parameter b		0	0	0	0
Loss Parameter α		.070	.060	.050	.040
γr_a		.8	.8	.8	.8
r_b/r_a		.7	.7	.7	.7
Helix Diameter	cm (in)	1.10(.432)	.715 (.280)	.454 (.179)	.294 (.116)
Barrel Inner Diameter	cm (in)	2.53(.995)	1.64 (.647)	1.05 (.413)	.678 (.267)
Magnetic Period L	cm (in)	2.44(.960)	1.712(.674)	1.204(.474)	.828 (.326)
Magnet Outer Diameter $2R_2$	cm (in)	3.91(1.54)	2.45 (.965)	3.12 (1.23)	2.00 (.788)
Magnetic Focusing Field (Peak)	gauss	427	398	885	835
λ_p/L		5.0	5.0	4.8	4.8
Magnet Material		Pt-Co	Pt-Co	Pt-Co	Pt-Co
Length Efficiency Enhancement Section	cm (in)	20.64(8.12)	15.34(6.04)	9.12(3.588)	6.78 (2.67)
Total Circuit Length (includ. Attenuator)	cm (in)	68.0(26.79)	52.4(20.65)	29.75(11.72)	22.93(9.03)
Tube Length (estimated)	cm (in)	86.0(34.0)	66.0(26.0)	40.7(16.0)	33.0(13.0)
Tube Weight (estimated)	kg(lbs)	7.0(18.0)	2.33(6.0)	3.5(9.0)	1.16(3.0)
Efficiency	%	63	61	62	60

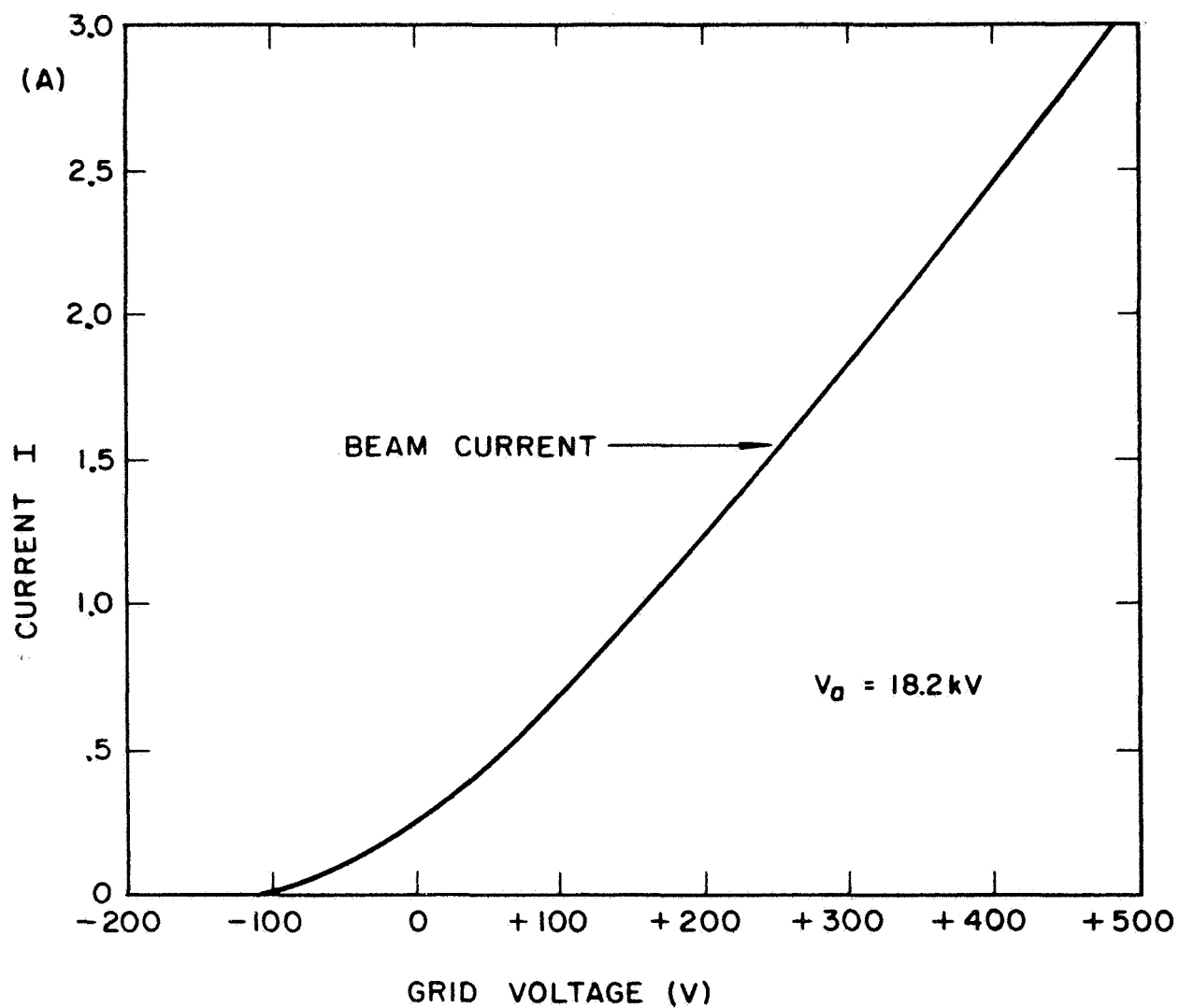


Figure 123 Typical shadow grid characteristics (Hughes 116 CG gun).

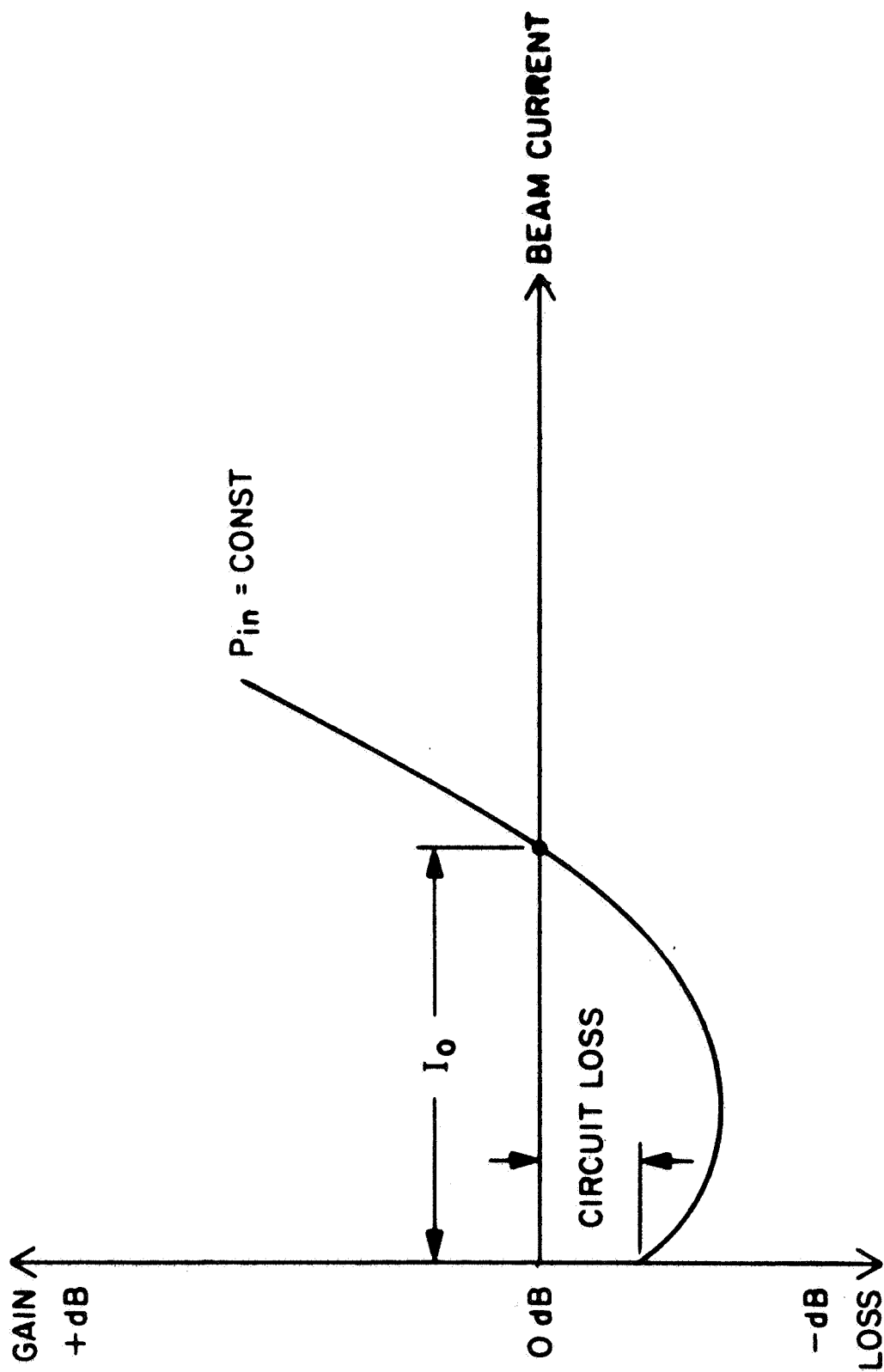


Figure 124 Gain characteristics of traveling-wave tube for very small beam currents.

The input admittance of the grid must be independent of the frequency of the modulation signal, and its phase delay is required to be constant over the modulation frequency bandwidth (6 MHz) in order to meet the linearity requirements. The input admittance of a grid can be represented by an equivalent circuit as shown in Figure 125. Its input admittance can be considered to consist of a grid capacitance C_g , which is loaded electronically by the electron beam with an electronic capacitance C_e and an electronic admittance G_e . In addition, an external admittance load G_L is applied to the grid also. This external load has to be large enough so that the input admittance of the grid is independent of frequency. The bandwidth Δf_g of the grid admittance can be considered adequate when it is much larger than the operational bandwidth Δf_m of the modulation signal or

$$\Delta f_g \gg \Delta f_m.$$

A bandwidth of the grid admittance of

$$\Delta f_g \approx 20 \text{ MHz}$$

was therefore chosen. This requires that the external load admittance G_L must be as large as

$$G_L \approx 2\pi \Delta f_g C_g.$$

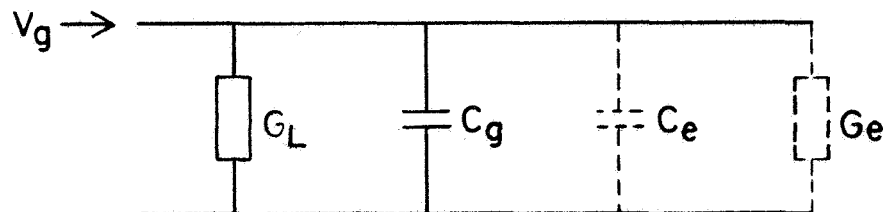


Figure 125 Grid input admittance.

The grid capacitance C_g is primarily produced by the capacitive loading of the grid support, rather than by the grid wire itself. Its value is generally found in the order of

$$20 \text{ to } 30 \text{ pF}$$

but with careful design a grid capacitance of

$$C_g = 20 \text{ pF}$$

can be achieved.

This requires a value of the external grid loading R_L of

$$R_L = 500 \text{ ohms}$$

to provide the desired bandwidth for the modulation grid.

The grid characteristics of the gun are generally defined by the μ factor. This factor defines the ratio of the anode potential (V_o) to the grid voltage for full perveance operation of the gun, or

$$\mu = \frac{V_o}{V_g}.$$

A large value of the μ factor is therefore desirable in order to keep the value of the required modulation grid modulation power small. The value of the μ factor can be larger when the gun perveance is smaller. For the low perveance designs of the traveling-wave tube modulators, the value of the μ factor is estimated to

$$\mu = 100$$

for both the 850 MHz and 2 GHz tubes. The required peak grid modulation voltages V_g are therefore

$$\begin{aligned} V_g (850 \text{ MHz}) &\approx 160 \text{ V} \\ V_g (2 \text{ GHz}) &\approx 130 \text{ V.} \end{aligned}$$

The required peak grid modulation power P_g is therefore approximately

$$\begin{aligned} P_g (850 \text{ MHz}) &\approx 51 \text{ watts} \\ P_g (2 \text{ GHz}) &\approx 34 \text{ watts.} \end{aligned}$$

The modulation amplifier (Figures 55 and 56) has therefore to provide a power gain of approximately 20 dB.

The modulation grid will affect the gun design. The insertion of a grid or shadow grid into a gun will generally have a perturbing effect on the electron optical gun characteristics. The trajectories of a gridded gun are less laminar and the beam contour is expanded, such that the beam transmission would be degraded. Therefore guns with grids or shadow grids are empirically redesigned with a beam tester. The design of a gridded gun can be derived from an ungridded gun which has a larger-than-required beam area convergence, so that the effect of the grid will reduce the beam area convergence to the desired value. The perturbing effects of a grid are generally found to be less pronounced with guns of relatively small beam area convergence, such as those of the proposed AM tubes (Table XIX), which have an area convergence of 4.5 (850 MHz) and 10 (2 GHz).

C. TRAVELING-WAVE TUBE MODULATOR CHARACTERISTICS

The gain and power characteristics of the traveling-wave tube modulators has been evaluated with the large signal computer program, which was also used for the design of the multi-voltage jump taper configurations. For these calculations the following assumptions were made:

1. The circuit configuration of the traveling-wave tube modulator incorporates a multi-voltage jump taper as described in Section V (Tables XV and XVI), with a saturation gain of 20 dB. The beam voltage is assumed to be adjusted for synchronism of the beam velocity with the circuit phase velocity, or

$$b = 0.$$

2. The beam cross-section area is assumed to vary inversely proportional with the instantaneous beam current I_i , or

$$r_{bi} = \alpha (I_i)^{-1/2}.$$

This assumption is valid for Brillouin flow, which occurs with the PPM focusing that is used for the traveling-wave tube modulators. The beam scalloping is not expected to change significantly with smaller beam currents since the electrostatic minimum beam diameter (of the gun) becomes smaller with smaller beam currents also.

3. The rectified modulation signal is proportional to the relative modulation power, corresponding to a "linear" rectifier characteristic.
4. The beam current ΔI increases proportionally with the applied grid modulation voltage ΔV_g (Figure 51 and 123), i.e., the grid current-voltage characteristics is assumed to be linear.

The beam current characteristics is shown in Figure 126 for the 2 GHz tube. It includes the dc term I_0 due to the positive grid bias voltage (in the order of 5% of the total beam current). The beam current grid characteristics for the 850 MHz is very similar.

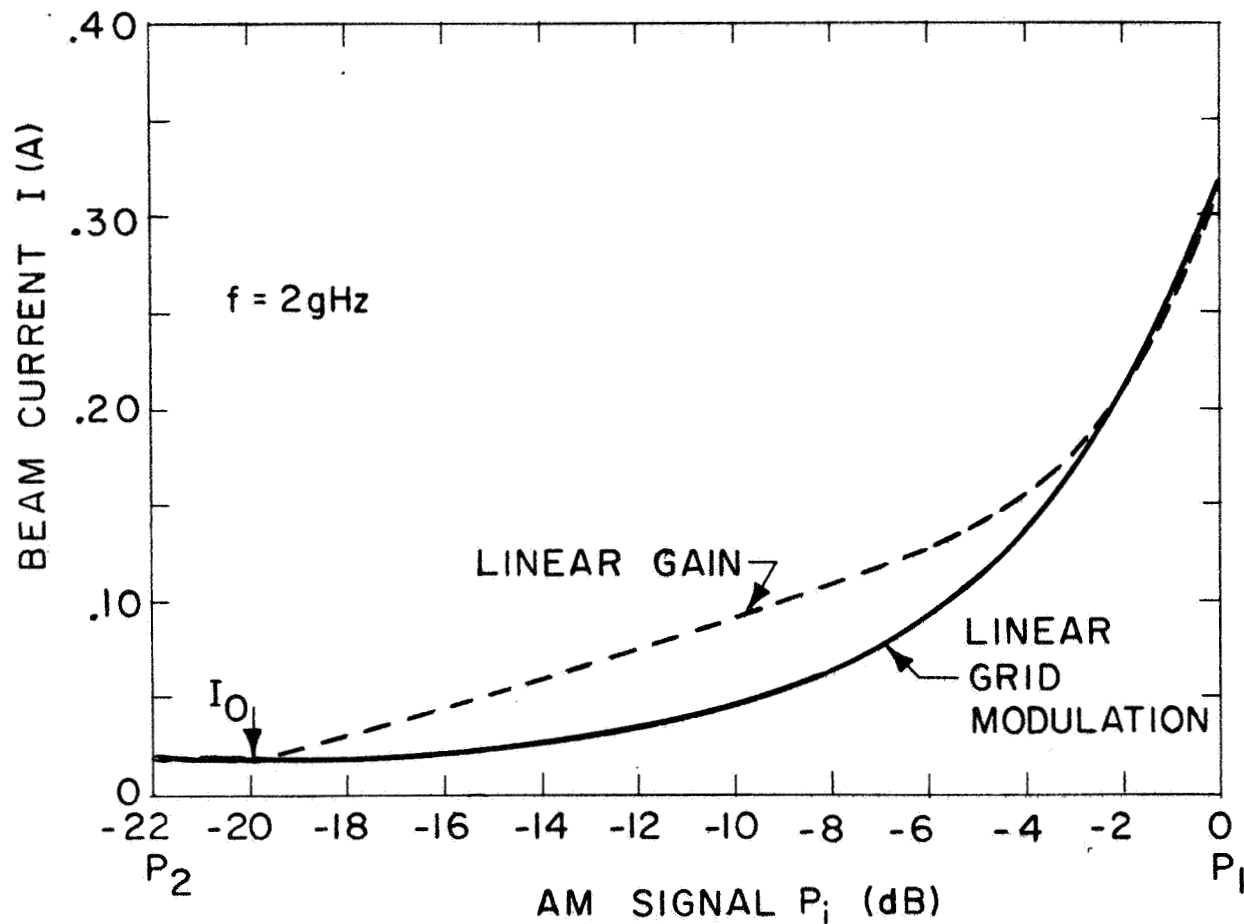


Figure 126 Beam current characteristics of (multi voltage jump) traveling-wave tube modulator (computed).

The resultant gain characteristics for the 2 GHz modulator is shown in Figure 127; a very similar gain characteristics was obtained for the 850 MHz tube. The gain characteristic is found to be linear from saturation down to 3 dB below saturation; at lower drive levels the gain is found to be lower than that for the required linear gain characteristics. The required current for a linear gain characteristics is shown in Figure 126 also. The deviations between the linear gain current and that obtained with an assumed "linear grid modulation" as described above is not very large, however. It should not be difficult to design a "linearizer" in the modulation signal chain (Figure 55) which provides the desired linear gain beam current characteristics for the traveling-wave tube modulator.

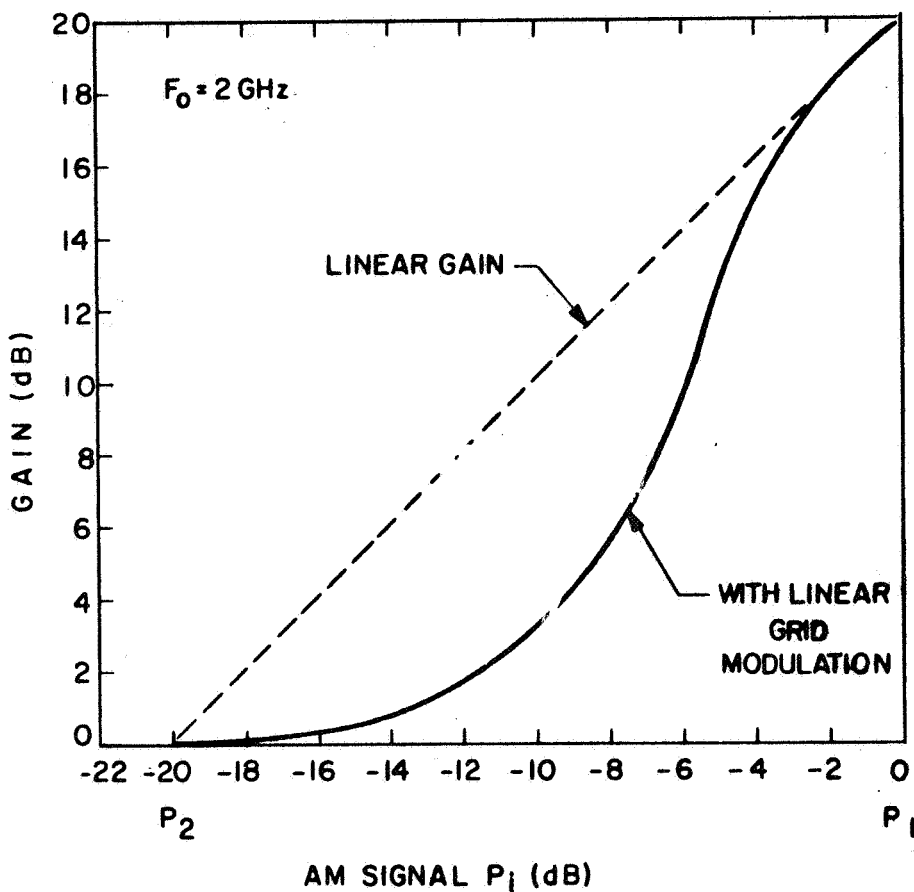


Figure 127 Gain characteristics of (multi voltage jump) TWT modulator (computed).

It should be mentioned that the resultant gain characteristics of the traveling-wave tube modulator is also a function of the circuit configuration and its efficiency enhancement design. The multi voltage jump taper configuration was designed for maximum efficiency, but it should be possible to modify its design for a more linear gain response. For instance, a single voltage jump design was found to provide considerably better gain linearity than that with the multi-voltage jump taper (Figure 127).

The spent beam energy distribution was also analyzed for the traveling-wave tube modulators at lower driver levels. It was found that the spent beam distributions at lower drive levels is such that the beam current can be collected at the two lowest potential collector stages (Section V C, Table XVI). The collector current distribution therefore shifts at lower drive levels to the lower potential collector stages resulting in increased efficiency improvements by the collector.

The dc power drain for the 2 GHz traveling-wave tube modulator is shown in Figure 128. (a similar one was obtained for the 850 MHz modulator). Even when the power requirements of the driver tube and the FM audio tube are included, the power drain drops at low AM levels to only 10% of the power drain at the peak power level. This represents a spectacular reduction of the power requirements for a traveling-wave tube modulator by more than an order of magnitude compared to a more conventional design approach.

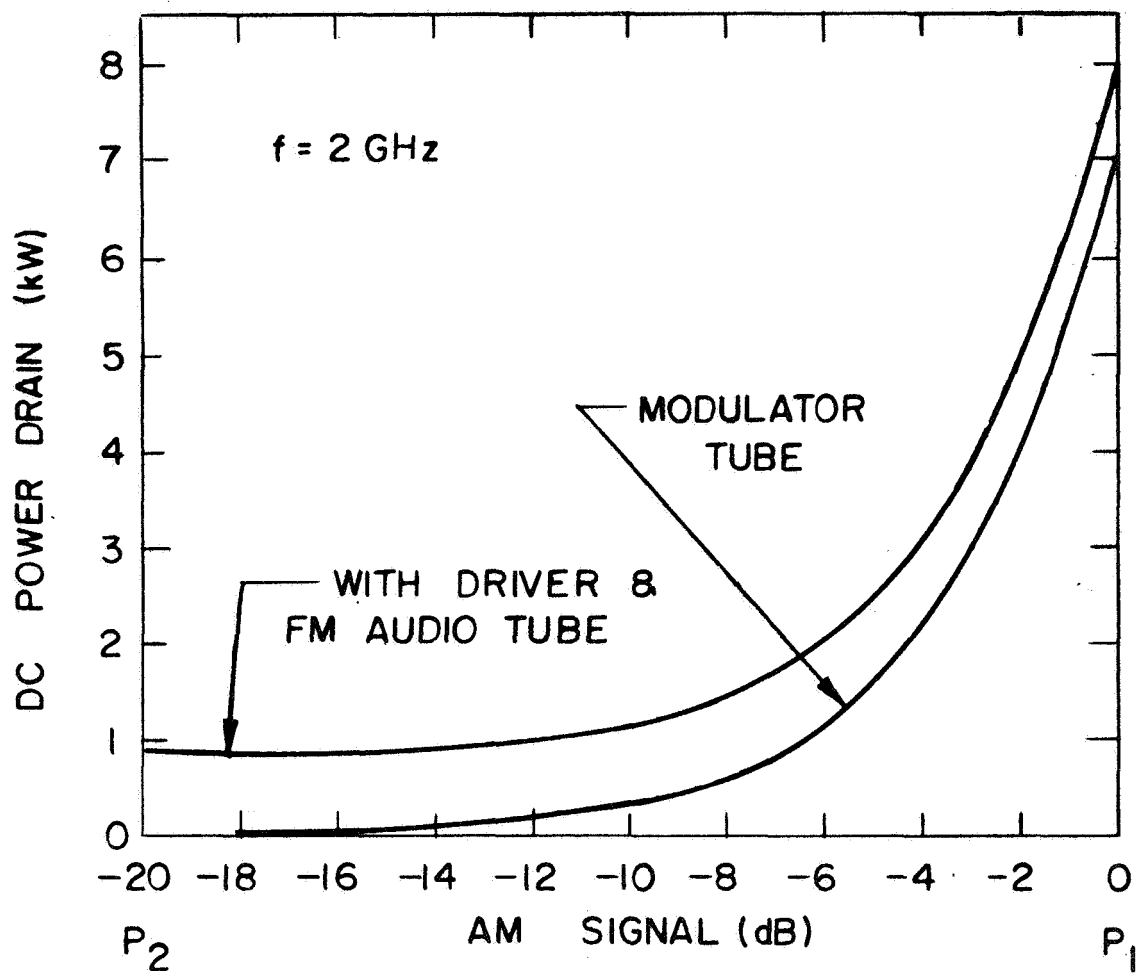


Figure 128 DC power drain of (multi voltage jump) TWT modulator with modulation drive level (computed).

XIII. SUMMARY OF TUBE DESIGN PARAMETERS

A. DESIGN CHOICES AND ASSUMPTIONS

The following design choices and assumptions were made for all tubes in order to achieve an optimum design within the requirements.

Electronic and Circuit Design

Slow Wave Structure	a. Coupled cavity circuit for high power tubes. b. Helix structure for driver and FM audio amplifier
Cold Bandwidth	60 MHz for all coupled cavity circuits.
Gap to Period Ratio of Coupled Cavity Structure	$g/\ell = .2$
Dielectric Loading of Coupled Cavity Structure	Alumina for 850 MHz and 2 GHz tubes.
Propagation parameter	$\gamma r_a = .8$
Beam to Circuit Radius	a. $\frac{r_b}{r_a} = .6$ (coupled cavity) b. $\frac{r_b}{r_a} = .7$ (helix tubes)
Velocity Parameter	$b = 0$
Efficiency Enhancement of Circuit Section	a. Multi voltage jump taper for coupled cavity tubes. b. Voltage jump and velocity taper for helix tubes.
Depressed Collector Operation	a. Four stage depressed collector for coupled cavity tubes. b. Single grounded collector for helix tubes.

Collector Configuration	<ul style="list-style-type: none"> a. Magnetic refocusing of spent beam and transverse magnetic and electric velocity sorting with electrostatic secondary suppression for coupled cavity tubes. b. Conventional for helix tubes.
Focusing	<ul style="list-style-type: none"> a. PPM for all 850 MHz and 2 GHz tubes. b. Solenoid for 8 GHz and 11 GHz tubes.
Focusing Stability	$\frac{\lambda_p}{L} > 4$ (for PPM)
Focusing Field	<ul style="list-style-type: none"> a. $B = 2 (2)^{1/2} B_o$ (PPM) b. $B = 2 B_o$ (Solenoid) with B_o = Brillouin field.
Magnetic Field at Cathode	<ul style="list-style-type: none"> a. $B_c = 0$ for PPM b. $K_c = .85$ for solenoid focusing.
Gun Design	Convergent gun (Pierce type)
Cathode Loading	$i_c < 500 \text{ mA/cm}^2$
Cathode Material	<ul style="list-style-type: none"> a. Oxide coated cathode for all 850 MHz and 2 GHz tubes. b. Impregnated tungsten cathode for 8 GHz and 11 GHz tubes.
Design Approach for AM tubes	Dual tube approach with helix driver tube and TWT modulator, separate FM amplifier for audio (helix tube)
Cooling	Heat pipe system with dielectric heat pipe (DC-200) for tube and multi one way heat pipes (Dow E) for radiator operating at approximately $T = 100^\circ \text{C}$.
Spacecraft Configuration	Quad panel slip ring configuration with integrated heat pipe and radiator system.
Ion Trapping	Anode ion trap.
Tube Vacuum	Space pumping.

B. MAJOR DESIGN PARAMETERS

In Table XXXIII a summary of the major design parameters of the coupled cavity tubes is given.

The noise figure of high power tubes can not be predicted theoretically. However, the measured noise figure of high power tubes is generally in the range of

$$25 \text{ dB} \leq \text{NF} \leq 35 \text{ dB}.$$

The noise figure of these design tubes can therefore be expected in this range.

Table XXXIII Major design parameters for coupled cavity tubes.

TUBE FREQUENCY	UNIT	850 MHz	2 GHz	2 GHz	8 GHz	11 GHz
Modulation		AM	AM	FM	FM	FM
Output Power	kW	7.6 (peak)	5.2 (peak)	5.2	5.1	5.1
Gain	dB	20 (max)	20 (max)	40	40	40
Cathode Voltage V_o	kV	16	13	13	12	14
Beam Current I_o	mA	505 (max)	298 (max)	298	346	298
Gun Perveance	μP	.25	.202	.202	.262	.18
Beam Area Convergence of Gun		4.5	10	10	60	85
Cathode Loading	mA/cm^2	78 (max)	142 (max)	142	470	490
μ Factor (Shadow Grid)		100	100	---	---	---
Cathode Type		Oxide Coated			Impregnated Tungsten	
Cathode Temperature	$^{\circ}C$	700	730	730	950	950
Heater Power	watts	33.3	15.3	15.3	7.5	6.4
Focusing Type		PPM Alnico 5			Solenoid Copper Foil	
Focusing Field	gauss	213 (peak)	480 (peak)	480 (peak)	1490	1720
Solenoid Power	watts	---	---	---	409	348
Dielectric Heat Pipe Working Fluid		DC 200	DC 200	DC 200	DC 200	DC 200
One Way Heat Pipe Working Fluid		Dow E	Dow E	Dow E	Dow E	Dow E
Estimated Temperature of Radiators	$^{\circ}C$	100 (max)	100 (max)	100	100	100

Table XXXIII Major design parameters for coupled cavity tubes (continued).

TUBE FREQUENCY	UNIT	850 MHz	2 GHz	2 GHz	8 GHz	11 GHz
Modulation		AM	AM	FM	FM	FM
Tube Diameter (with Focusing)	cm(in)	24 (9.45)	12 (4.73)	12 (4.73)	14 (5.3)	13 (5.1)
Tube Length (estimated)	cm(in)	170 (67)	66 (26)	88 (34.5)	30 (11.8)	24 (9.4)
Tube Weight, Including Focusing (estimated)	kg(lbs)	133 (300)	24 (54)	32 (70)	15.3 (34)	13 (29)
Tube Efficiency with Four Stage Depressed Collector	%	75 (peak)	79 (peak)	79	78	75
Total Required DC Power (incl. solenoid, heater driver and FM audio tubes)	kW	11.46 max 1.33 min	7.505 max .92 min	6.585	6.93	7.15
Overall Efficiency	%	66 (peak)	69 (peak)	79	73.5	71.3
Life Expectancy	hours	50,000	50,000	50,000	50,000	50,000

XIV. CRITICAL DESIGN AREAS

The tube designs of these studies are intended for an advanced satellite transmitter system. The efforts of these studies were, therefore, primarily directed to explore new design concepts and approaches for traveling-wave tubes, which appear promising to advance the state-of-the-art for such tubes. Some of these concepts have not yet been used in traveling-wave tubes, nor even been evaluated experimentally. Before a traveling-wave tube can be designed with such new approaches, however, it is first necessary to evaluate the feasibility of these concepts, to determine their limitations, and, finally, to establish design procedures.

A discussion of the critical design areas, in order of importance, follows below:

1. Multi voltage jump taper

This method has been derived and evaluated with a large signal computer program, which has provided a useful and accurate analysis for similar methods in the past. However, this scheme has not yet been demonstrated experimentally.

2. Multi stage depressed collector

The multi stage collector design involves several new concepts: magnetic refocusing of the spent beam, transverse magnetic and electric beam deflection for improved velocity sorting of the spent beam, and electrostatic potential barrier for secondary suppression. Results of advanced methods of trajectory analysis have to be evaluated experimentally before design procedures for such collectors can be established. This is expected to be a difficult task in view of the only moderate success, in the past, in the development of multi stage collectors.

3. Traveling-wave Tube modulator

All components and devices required for the design of a traveling-wave tube modulator exist or are within the present state of the art. However, the design concept is novel and has to be evaluated experimentally, before a traveling-wave tube modulator can be developed.

4. New Construction Techniques

The multi voltage jump taper and the multi stage collector require smaller, yet very reliable and strong vacuum seals for their voltage insulation. The development of such new construction techniques will therefore be required.

5. Long Life Design of High Power Tubes

Long life and reliability of high power tubes has not yet been advanced to the extent needed for the design tubes. Processing methods and techniques have yet to be developed and proven for such tubes, in order to achieve reliable performance and adequate life. The life evaluation has to include the voltage jump taper technique, the multi stage collector, and the dielectric loading method of the circuit.

6. Dielectric Heat Pipe

Dielectric heat pipes are in development for collector cooling of high power traveling-wave tubes. The heat pipe requirements for the design tubes, however, differs in some respects from those of the present development. There is a greater number of electrodes with higher potential differences, and the operating temperature will be lower. Exploratory development will be required for their design.

7. One way Heat Pipes

These types of heat pipes have been demonstrated experimentally for lower power levels. Experimental evaluation of the required power levels and operating temperatures will be necessary.

XV. CONCLUSIONS

It has been shown that the performance of traveling-wave tubes can be substantially improved when new design features are incorporated.

Efficiencies of 70 to 80 percent become feasible for coupled cavity tubes with velocity resynchronization and multi stage depressed collectors.

A new velocity resynchronization scheme for coupled cavity tubes is proposed; the multi voltage jump technique. This technique permits the use of lower perveance and lower power beams in the gun and in the driver section. The focusing requirements are then relaxed and a higher beam stability with PPM focusing becomes possible. The multi voltage jump technique also permits a reduction of the voltage gradient compared to a single voltage jump circuit. This makes it possible to extend the voltage jump technique to higher frequencies or to higher power levels.

A new design approach for multi stage depressed collectors is shown. The concept uses magnetic refocusing of the spent beam, transverse magnetic and electric velocity sorting and electric suppression of secondaries.

The diameter and weight of coupled cavity tubes at frequencies up to C-band can be substantially reduced by dielectric loading of the cavity. This has been shown to be possible without significant degradation of other tube performance characteristics. These features can be incorporated in coupled cavity tubes without restrictions to their bandwidth. Their bandwidth can be increased (within the bandwidth limitations of a coupled cavity tube) if so desired.

A new method has been presented for the design of very high efficiency linear amplifiers for AM signals. This method uses a driver tube and a

grid modulated output tube (TWT modulator) in conjunction with external circuitry for linearization. Very substantial efficiency improvements are expected with this system. The dc power requirements can then be reduced by nearly an order of magnitude compared to conventional linear amplifiers for AM signals. This method is applicable to either helix or coupled cavity tubes.

A new heat pipe system, consisting of a dielectric heat pipe and multiple one way heat pipes for cooling of high power space tubes has been described. This system is an integral part of the space-craft vehicle and permits utilization of a larger area of the space-craft surfaces for waste heat radiation. The cooling system operates at lower temperatures without weight penalty, and higher tube reliability can be expected.

LIST OF REFERENCES

1. Sauseng, O. G.: "Applied Research on Efficiency Improvement in O-type Traveling-Wave Tubes,": Technical Report No. RADC TR-67-259 (April 1967), Contract No. RADC AF-33(615)-1951.
2. Grover, G. M., Colter, T. P., Erickson, G. F.: "Structures of Very High Thermal Conductance," J.A.P. Vol. 35 (1964) pp. 1990.
3. Report SC-M-66-623 Proceedings of Joint Atomic Energy Commission/Sandia Labs. Heat Pipe Conference, Albuquerque, New Mexico (October 1966).
4. Basiulis Starr, M. C.: "Improved Reliability of Traveling-Wave Tubes Through the Use of a New Light Weight Heat Removal Device," IEEE Intern. Electron Devices Meeting, Washington, D. C. (October 1967).
5. Cobine, D. J.: "Gaseous Conductors," Dover Publication, Inc., New York (1958), pp. 163 - 167.
6. Laico, J. R., McDowell, H. L., Moster, C. R.: "Medium-Power Traveling-Wave Tube for 6,000 mc Radio Relay," B.S.T.J. Vol. 35 (November 1956), pp. 1285 - 1346.
7. Walkstein, H. J.: "Effect of Collector Potential on the Efficiency of Traveling-Wave Tubes," RCA Review, Vol 19 (June 1958), pp. 259 - 282.
8. Sterzer, F.: "Improvement of Traveling-Wave Tube Efficiency Through Collector Potential Depression," IRE Trans, Vol. ED 5, (October 1958), pp. 300 - 305.
9. Gilmour, A. S., Jr.: "The Velocity Distribution in a Velocity-Modulated Electron Beam from a Shielded Pierce Gun," RADC Report No. AF 30(602)-1696 (April 1961), Cornell University, N. Y., Res. Rept. EE 507.

10. Brewer, G. R.,
Anderson, J. R.: "Electron-Beam Defocusing Due to High-Intensity RF Fields." IRE Trans, Vol. ED-8 (November 1961), pp. 528 - 539.
11. Septier, A.: "Focusing of Charged Particles," Academic Press, New York (1967).
12. Pierce, J. R.: "Theory and Design of Electron Beams,:" D. Van Nostrand Company, New York, (1954).
13. Palmer, J. L.,
Susskind, C.: "Stiffness of Electron Beams," Journal of Electronics and Control (May 1961), pp 365 - 373.
14. Meyerer, P.: "Stepped Focusing Magnet Shrinks TWTs," MicroWaves (May 1965) pp. 24.
15. Cutler, C. C.: "The Nature of Power Saturation in Traveling-Wave Tubes," Bell System Technical Journal, Vo. 35, ED-6 (June 1959), pp. 6 - 9.
16. Tien, P. K.: "A Large Signal Analysis of Traveling-Wave Amplifiers," Bell System Technical Journal, Vol. 35 (March 1956), pp. 349-374.
17. Rowe, J. R.: "Nonlinear Electron-Wave Interaction Phenomena,": Academic Press, New York (1965).
18. Pierce, J. R.: "Traveling-Wave Tubes," D. Van Nostrand Company, New York (1950).
19. Collier, R. C.,
Helm, G. D.,
Laico, J. R.,
Striny, K. M.: "The Ground Station High Power Traveling-Wave Tube," Bell System Technical Journal, Vol. 42 (July 1963), pp. 1829 - 1861.
20. Allen, M. A.,
Kino, G. S.: "On the Theory of Strongly Coupled Cavity Chains," IRE Trans. M.T.T., Volume 8 (May 1960), pp. 362 - 372.
21. Ramo, S.,
Whinnery, J. R.: "Fields and Waves in Modern Radio," J. Wiley, Incorporated, New York (1960).

22. Molnar, J. R.,
Moster, C. R.: "Some Calculations of the Magnetic Field Requirements for Obtaining Brillouin flow in Cylindrical Electron Beams," Bell Telephone Labs Report 51-29 40-1 (1951).
23. Herman, G,
Wagner, S.: "Die Oxyd Kathode," Barth, Leipzig (1950).
24. Hannay, N. B., McNair, D.,
White, A. H.: "Semiconducting Properties in Oxide Cathodes," Journal Applied Physics, Vol. 20 (1949), pp. 699 - 681.
25. Maurer, D. W.: "Cathode Activity Measurement: A Modification of the Dip Test," Bell System Technical Journal, Dec. 1967, pp 2363 - 2374.
26. Fane, R. W.: "Some Electrical and Surface Properties of Sintered Nickel Matrix Cathodes," British Journal Applied Physics, Vol. 11 (1960), pp. 513.
27. Maurer, D. W., Pleass, C. M.: "The C. P. C; A Medium Current Density, High Reliability Cathode," Bell System Technical Journal, Volume XLVI, No. 10 (1967), pp. 2375 - 2403.
28. Lemmens, H. J., Jansen, M. J.,
Loosjes, R.: "Eine neue thermisch emittierende Katode fuer schwere Belastungen," Philips Techn. Rev., Vol. 11 (1949 - 1950), pp. 341.
29. Levi, R.: "New Dispenser Type Thermionic Cathode," J. Applied Physics, Vol. 24 (1953), pp. 233.
30. Levi, R.: "The Impregnated Cathode and its Structural Characteristics as Compared with the "L" Cathode," Le Vide Vol. 9, No. 54 (1954), pp. 284.
31. Levi, R.: "Improved Impregnated Cathode," Journal Applied Physics, Vol 26 (1955), pp. 639.
32. Dubin, M.,
McCracken, C. W.: "Measurements of Interplanetary Dust," The Astronaut Journal, June 1962.
33. Whipple, F. L.: "On Meteoroids and Penetration," Journal of Geophys. Res., September 1963.

APPENDIX

TELEVISION SIGNAL TRANSMISSION

In the most straightforward system to be considered, the video waveform is extracted from the envelope of the incoming signal by detection and used to modulate an amplified carrier in the final stage. In general, for practical reasons, the re-transmitted carrier frequency will differ from that of the received signal.

The output from the traveling-wave tube will then be passed through a suitable vestigial sideband filter to remove the unwanted part of the lower sideband, and the remaining signal conforming with the required bandwidth standards will be fed to the antenna system.

In order to assess the relative efficiencies of the signal processing systems which form the subject of this study an analysis has to be made of the amount of power which is involved in the removal of the lower part of the lower sideband, i.e., the part of the sideband furthest from the carrier.

Since the high frequency end of the sideband spectrum contains information which is related to the fine detail of the picture, the actual amount of power involved in this part is entirely dependent on the nature of the picture being transmitted.

The lower frequency part of the spectrum (below 750 KHz), on the other hand, contains almost the whole of the power associated with picture synchronization in addition to that relating to the broader areas of the picture.

The fraction of the power associated with synchronization varies with picture content but represents approximately 30% of a peak black transmission. This is therefore a minimum value, and typically the synchronizing power will be a larger fraction of the transmitted power.

In order to have its Fourier components fall entirely within the upper frequency portion of the sideband spectrum (above 750 KHz), a picture element would have to be contained in less than 2-1/2% of the horizontal width of the picture.

Based on the foregoing considerations, it would be reasonable to anticipate that, in fact, for a typical transmitted picture, the percentage of the total power removed by the vestigial sideband filter would be quite small.

DISTRIBUTION LIST FOR
FINAL REPORT
Contract NAS3-9719

	<u>No. of Copies</u>
National Aeronautics and Space Administration	
Headquarters	
Washington, D. C. 20546	
Attention: SA/L. Jaffe	1
SAC/A.M.G. Andrus	10
National Aeronautics and Space Administration	
Lewis Research Center	
21000 Brookpark Road	
Cleveland, Ohio 44135	
Attention: C. C. Conger, MS 54-1	1
R. E. Alexovich, MS 54-3	1
Dr. H. G. Kosmahl, MS 54-3	1
Technology Utilization Officer, MS 3-19	1
Spacecraft Technology Procurement Sec., MS 54-2	1
Library, MS 60-3	2
Report Control Office, MS 5-5	1
N. T. Musial, MS 501-3	1
G. J. Chomos, MS 54-3	50
Communication Systems Inc.	
5817 Columbia Pike	
Falls Church, Virginia 22046	
Attention: J. Bisaga	1
Rand Corporation	
1700 Main Street	
Santa Monica, California 90404	
Attention: Dr. J. Holt	1
National Aeronautics and Space Administration	
Electronics Research Center	
575 Technology Square	
Cambridge, Massachusetts 02139	
Attention: E/Dr. L. Vanatta	1
EM/C. Veronda	1
Library	1
National Aeronautics and Space Administration	
George C. Marshall Space Flight Center	
Huntsville, Alabama 35812	
Attention: RASTR-A/E. C. Hamilton	1
Library	1

National Aeronautics and Space Administration
 Goddard Space Flight Center
 Greenbelt, Maryland 20771
 Attention: 733/R. Pickard
 Library

1
 1

National Aeronautics and Space Administration
 Ames Research Center
 Moffett Field, California 94035
 Attention: OART-MAO/E. Van Vleck, MS 202-6
 Library

1
 1

National Aeronautics and Space Administration
 Langley Station
 Hampton, Virginia 23365
 Attention: B. Kendall, MS 173
 Library, MS 185

1
 1

National Aeronautics and Space Administration
 Manned Spacecraft Center
 Houston, Texas 77001
 Attention: Library

1

Jet Propulsion Laboratory
 4800 Oak Grove Drive
 Pasadena, California 91103
 Attention: L. Derr
 Library

1
 1

National Aeronautics and Space Administration
 Scientific and Technical Information Facility
 P. O. Box 5700
 Bethesda, Maryland

Attention: NASA Representative

3

Radio Corporation of America
 Astro-Electronics Division
 Princeton, New Jersey 08540
 Attention: R. B. Marstin

1

TRW Systems
 One Space Park
 Redondo Beach, California 90278
 Attention: W. A. Finley/Space Vehicle Division

1

General Dynamics
Convair Division
P. O. Box 1128
San Diego, California 92112
Attention: F. J. Dore/Advanced Programs

1

Hughes Aircraft Company
Space Systems Division
1194 West Jefferson Boulevard
Culver City, California 90230
Attention: H. A. Rosen/Satellite Systems Laboratory

1

General Electric Company
Missile and Space Division
Valley Forge Space Technology Center
P. O. Box 8555
Philadelphia, Pennsylvania 19101
Attention: H. Collins
P. Nadler

1

1

Federal Communications Commission
521 Twelfth Street
Washington, D. C. 20554
Attention: H. Fine

1

U. S. Information Agency
25 M Street S.W.
Washington, D. C. 20547
Attention: IBS/EF/G. Jacobs

1

General Electric Company
Tube Department
Microwave Tube Business Section
Schenectady, New York
Attention: R. Dehn

1

Litton Industries
Electron Tube Division
960 Industrial Road
San Carlos, California 94070
Attention: Dr. G. Pokorney
J. Orr

1

1

S-F-D Laboratories Inc.
800 Rahway Avenue
Union, New Jersey 07083
Attention: Dr. G. Farney

1

Hughes Aircraft Company
Electron Dynamics Division
P. O. Box 2999
Torrence, California 90509
Attention: Dr. J. Mendel

1.

Watkins Johnson Company
333 Hillview Avenue
Palo Alto, California 94304
Attention: Dr. D. Watkins

1.

Varian Associates
611 Hansen Way
Palo Alto, California 94303
Attention: F. Melzer

1.

Radio Corporation of America
Industrial Tube Division
Lancaster, Pennsylvania
Attention: W. P. Bennett

1